# STUDY OF DROPLET SPLITTING IN AN ELECTROWETTING BASED DIGITAL MICROFLUIDIC SYSTEM

by

BIDDUT BHATTACHARJEE

B.Sc., Bangladesh University of Engineering & Technology, 2004
M.Sc., Bangladesh University of Engineering & Technology, 2007

A THESIS SUBMITTED IN PARTIAL FULFILLMENT OF THE REQUIREMENTS FOR THE DEGREE OF

DOCTOR OF PHILOSOPHY

in

THE COLLEGE OF GRADUATE STUDIES
(Applied Science)

THE UNIVERSITY OF BRITISH COLUMBIA
(Okanagan)

September 2012

# Abstract

This thesis focuses on the symmetric and asymmetric splitting of droplets, which is a prominent fluidic operation in a digital microfluidic system (DMFS). The prerequisite part of the investigation of droplet splitting is to understand the electrowetting-on-dielectric (EWOD) based droplet actuation. This thesis demonstrates that not only the EWOD actuation is a self-feedback system - implying that the actuation force depends on the position of the droplet, but also the size of the droplet affects the magnitude of actuation force. However, a sensing mechanism is essential for complex operations, e.g. dispensing and splitting. One contribution of this thesis is a novel method of sensing the droplet position that requires connections to the two adjacent electrodes in the lower plate only.

For the fabrication of prototype DMFS, a new polymeric material, cyanoethyl pullulan (CEP), is proposed as the dielectric layer resulting in a simple and low-cost fabrication of DMFS. The required voltage for droplet manipulation is drastically reduced owing to high relative permittivity of CEP.

Droplet splitting is investigated both numerically and experimentally. Numerical investigation of droplet splitting in FLOW-3D®, a commercial computational fluid dynamics software, revealed that the strength of viscous forces relative to the surface tension force determines the success of splitting. For successful asymmetric splitting, performed by applying voltages of unequal magnitude to left-hand and right-hand sides of the droplet, there exists a minimum voltage for the low-voltage side that guarantees splitting. This minimum voltage increases if the aspect ratio (i.e., diameter to height) of the droplet is reduced while keeping the diameter of the droplet constant. Investigation of the asymmetric splitting with different ratios of applied voltage revealed that the ratio between the volumes of accumulated liquid on either sides increases with voltage ratio. The feasibility of asymmetric splitting as well as the effects of different ratios of applied voltages were studied in prototype DMFS. The results verify the existence of a minimum voltage for successful splitting. The ratio between the volumes of the sister droplets increases with that of the applied voltages. Moreover, the general characteristics of flow-rates and liquid accumulation were found to be similar to those in simulations.

# Preface

This thesis presents the results of research conducted in the Advanced Control and Intelligent Systems (ACIS) laboratory at the Okanagan School of Engineering, UBC, under the supervision of Dr. Homayoun Najjaran. Part of the thesis has been published in peer reviewed journals and conferences. The highlights of contributions of this thesis are as follows:

The simulation results of Section 1 of Chapter 2 were published in two journals ([a]Bhattacharjee and Najjaran 2010, [b]Bhattacharjee and Najjaran 2010). The droplet dynamic system was modelled by considering the droplet as a rigid body and incorporating the empirical functions for the resistive forces. A simple controller and generic actuation and sensing mechanisms were also considered for the control of droplet position between two adjacent electrodes. Results show the relative strength of different resistive forces, transient and steady-state response in relation to controller gain and geometrical parameters. My responsibility was to investigate the modelling, computer simulation and manuscript preparation.

Another contribution of this thesis is a novel method of droplet position sensing by measuring the capacitance between two coplanar electrodes. An analytical model of coplanar capacitance given by a quadratic function of the droplet position is proposed and verified by both numerical and experimental results, presented in Section 2 of Chapter 2. This new sensing method can be easily incorporated in feedback control of droplet operations from simple motion to complex splitting.

Results of Section 3 of Chapter 2 were published in a conference ([c]Bhattacharjee and Najjaran 2009) and my task was to analyse the EWOD-actuated droplet, develop simulation model of droplet motion, process and organize simulation results and prepare the manuscript. Under the assumption of a cylindrical conductive droplet, the EWOD-actuated droplet was demonstrated as a self-feedback system where the magnitude and direction of the generated actuation force depends on the position of the droplet with respect to the energized electrode. Moreover, the profile of actuation force also depends on the size of the droplet. Results in terms of transition time for the droplet from one electrode to the next as a function of electrode size, dielectric thickness and dielectric constant were also presented.

The results of the last section of Chapter 2 were published in another conference ([d]Bhattacharjee and Najjaran 2010). I was responsible for researching the material, fabricating the device and setting up instruments for measurement and writing the manuscript. The dielectric material, cyanoethyl pullulan, reported in this paper possesses high dielectric constant and can be

deposited using a spin-coater only. Thus, digital microfluidic devices, which are fabricated using this new material, can be operated at significantly lower voltages than the values commonly reported in the literature.

One of the major contributions of this thesis is the extensive study of the coupled electrohydrodynamics of symmetric and asymmetric splitting of droplets through CFD simulations ([e]Bhattacharjee and Najjaran 2011). Results shown in Chapter 3 elucidate the distribution of electric field, charges, pressure and velocities during symmetric splitting. The relative strength of viscous shear with surface tension force determines the result of splitting. For a given size of the droplet, material properties and geometry, there exists a voltage level below which splitting is infeasible.

Identification of the key parameters in determining the success of asymmetric splitting and the extent to which each of the parameters influence the splitting process is another major contribution of this thesis and is presented in Chapter 4. There exists a minimum required voltage for the low voltage side in asymmetric splitting for a given electrode size and aspect ratio of the droplet. The required voltage increases with increasing droplet height while the electrode size remains constant. For a given geometry and droplet aspect ratio, the ratio between the flow-rates to the right-hand and left-hand sides increases with the ratio between the applied voltages till the breakup of the neck.

The final contribution of this thesis is the experimental investigation of asymmetric splitting. The results, as presented in Chapter 5, verify the characteristic pattern of exponentially decaying liquid flow-rates and capillary numbers. The ratio between the volumes of sister droplets resulting from asymmetric splitting increases with that of the applied voltages. Moreover, the volume ratio is greater for higher base voltages on the low voltage side.

## List of Publications

Bhattacharjee B. and Najjaran H., 2012, "Droplet sensing by measuring the capacitance between coplanar electrodes in a digital microfluidic system", *Lab on a Chip* (Accepted)

Bhattacharjee B. and Najjaran H., 2010, "Simulation of droplet position control in digital microfluidics systems", *Journal of Dynamic System, Measurement and Control*, **132**, 014501.

Bhattacharjee B. and Najjaran H., 2010, "Droplet position control in digital microfluidic systems", *Biomedical Microdevices*, **12** ,115-124.

Bhattacharjee B. and Najjaran H., 2011, "Modeling and simulation of unequal droplet splitting in electrowetting based digital microfluidics", *ASME ICNMM*, Edmonton.

Bhattacharjee B. and Najjaran H., 2011, "Low-cost, low-voltage microfluidic biochip based on electrowetting actuation of droplets", *Proceedings of Microtechnologies in Medicine and Biology*, Lucerne, Switzerland.

Bhattacharjee B. and Najjaran H., 2010, "Effects of the properties of dielectric materials on the fabrication and operation of digital microfluidic systems", *Proceedings of ASME IMECE*, Vancouver.

Bhattacharjee B. and Najjaran H., 2009, "Size dependant droplet actuation in Digital Microfluidic system", *Proceedings of SPIE conference on Micro- Nanotechnology Sensors, Systems and Application, Orlando*, **7318**.

# Table of Contents

# List of Tables

# List of Figures

# Acknowledgements

I am grateful to my supervisor, Dr. Homayoun Najjaran, for providing me with the opportunity to work on the exciting field of digital microfluidics. His constant guidance and support helped me formulate the scope of this thesis and stay focused on the primary goal of this research which was mixed with a bundle of relevant other problems. I enjoyed the learning and working environment he created which constantly inspired positive and innovative thinking, and helped building the capability of independent research. I would like to thank him for everything.

I thank Drs. Hoorfar, Holzman, Stoeber for their valuable suggestions during the course of my research. I would like to thank Dr. Hoorfar for allowing me to use the scale, the hot plate and the setup for measuring contact angle. I would also like to thank fellow students in ACIS lab and others working on digital microfluidics for helpful discussions and cooperation. I thank Biddle Sawyer Inc. for providing with the sample of granular cyanoethyl pullulan (CEP) used as the dielectric material in the fabricated device.

Finally, I would like to take this opportunity to thank my wife, Banani Bhattacharjee, for the constant encouragement. It would have been extremely difficult to complete the thesis without her single-handed management of the family during the most difficult times.

# Dedication

To my parents

*Byomkesh Bhattacharjee*

*Protima Bhattacharjee*

and my daughter

*Bidita Bhattacharjee*

# CHAPTER 1

# INTRODUCTION

## 1.1 Motivation

An alternative platform for microfluidic lab-on-a-chip is realized by the manipulation of liquid volumes as discrete liquid packets rather than continuous flow of liquids of interest. Discrete-flow microfluidic systems have some inherent advantages including improved control over the liquid volume, faster reaction and mixing times and capability of sorting and detection. However, the discrete volumes of liquid in the form of plugs or droplets are driven by the flow of an immiscible phase through permanent channels. Thus, a new design of the microfluidic system is necessary for each application of biochemical and medical analyses. A new generation of microfluidic systems, where droplets are manipulated on a planar surface, has emerged with the capability of integrating all the fluidic operations such as dispensing, transport, mixing, incubation, splitting, detection, separation and waste disposal. Droplets being surrounded by air or any other immiscible phase can be transported in any direction because of the absence of any channel. A digital microfluidic system (DMFS) is an alternative platform for the manipulation of pico- to nano-liter liquid droplets on a channel-less planar surface. Among other droplet actuation methods in a DMFS, electrowetting-on-dielectric (EWOD) force based actuation has become the most popular method owing to several unique advantages such as controllability, scalability and reconfigurability, ease of fabrication and low power consumption. In a typical configuration, the DMFS consists of two plates: the lower plate comprises square electrodes coated with an insulating and a hydrophobic layer, and the upper plate providing the ground electrode is placed at a height defined by a spacer. The application of electric potential of suitable magnitude and frequency to an electrode adjacent to the droplet generates a distribution of electric potential and hence, electric field intensity at the droplet-medium interface closer to the energized electrode. The resulting electrostatic actuation force deforms the interface, reduces the wetted angle on the solid surface and pulls liquid towards that electrode. Therefore, droplets can be manipulated by proper application of the EWOD actuation force. The electrodes, arranged in linear or rectangular arrays, on the lower plate can be configured to serve as reservoirs for dispensing droplets, as pathways for transporting and as sites for mixing, splitting and detection. This thesis focuses on the EWOD-based manipulation of droplets in a DMFS.

Droplet splitting is one of the generic operations performed in a DMFS. It involves the application of voltages on both sides of the droplet and thereby elongating and pinching off resulting in two sister droplets. Diluting the content of a droplet and mixing the contents of two or more droplets typically involve repetitions of the sequence merging, transport and symmetric splitting. Dilution process through merging and symmetric splitting (i.e. splitting at 1:1 ratio), where a homogenous droplet is divided into two equal sister droplets, results in a reduction of the species concentration by a factor of two. By splitting a droplet asymmetrically (i.e. splitting at 1:1 ratio), which involves dividing the droplet into two unequal portions, a higher dilution factor can be achieved. Thus, the capability of splitting asymmetrically will not only allow accelerated mixing and dilution but also increase finer resolution in the range of achievable dilution factors. This fluidic process is governed by the bi-directionally coupled electrostatics and unsteady viscous flow. In addition to the change in topology, due to large deformation as well as break-up of droplet interface, there are other phenomena such as contact-line pinning, contact angle hysteresis and saturation which make the process highly difficult to be described by a simple model. Furthermore, there has not been any report of satisfactory theories for the above non-dominating physics involved in splitting. Thus, electrowetting based droplet splitting is not only a basic operation for a number of potential applications but also a challenging research problem.

## 1.2 Objectives

This research focused on the understanding of droplet splitting, with emphasis on asymmetric splitting, in an EWOD-based DMFS. Experimental investigation of droplet splitting requires fabrication of devices that allow for operations at reasonably lower voltages (10V-200V) in addition to being inexpensive and simple. Thus, the initial focus of this research was on searching for materials and fabrication methods that required no complex fabrication facilities including a cleanroom environment. On the other hand, droplet detection and liquid sensing are essential for accurate and reliable operations in a DMFS. In particular, the asymmetric splitting of droplets necessitates an effective sensing method for closed-loop operation. A novel method of droplet position sensing through capacitance measurement between two adjacent electrodes on the lower plate was investigated. Unlike the traditional method, which relies on capacitance measurement between electrodes on both the upper and lower plates, this new method involving coplanar electrodes significantly enhances the functionality of a DMFS. Uncertainties in experiments originating from imperfections in the properties of materials and fabrication methods as well as resource and technological constraints limit the extent of experimental investigations. Consequently, extensive numerical simulation was planned and pursued which allows for detailed investigation of droplet splitting with parametric variations. However, understanding the electrowetting actuation of droplets is a prerequisite for the development of simulation models so that the principal physics is incorporated as accurately as possible. To overcome the challenges of this research, the specific objectives of this thesis can be outlined as follows:

- Investigate the EWOD force and the dynamics of droplet motion through simulation of a lumped parameter model,
- Develop a novel method for sensing a droplet using two coplanar electrodes in the lower plate and validate the method both numerically and experimentally,
- Investigate the physics of both symmetric and asymmetric splitting of a droplet and identify the important parameters through simulation using a reliable commercial computational fluid dynamics (CFD) software program,
- Verify the concepts related to droplet splitting acquired from CFD simulation through design and fabrication of a DMF prototype for splitting experiments.

## 1.3 Literature review

Digital microfluidics is an emerging technology for lab-on-a-chip devices possessing the capability of efficiently integrating macroscale laboratory protocols (Fouillet et al. 2006, Miller and Wheeler 2009, Choi et al. 2012) into microdevices. Over the past decade, research has been continuously increasing towards various aspects of this newer generation of microfluidic systems. Alternative materials and fabrication processes, integration of auxiliary modules such as sensing and characterization, algorithms to program operations and demonstration of various bioassays are continuously being reported in the literature. The next sections present an up-to-date literature review on droplet actuation, mechanics of EWOD, fabrication of and operations in EWOD-based DMFS.

### 1.3.1 Droplet actuation

Researchers have explored several ways of actuation of droplets in microfluidic devices. Chaudhury and Whitesides (1992) reported the actuation of droplets by creating a continuous gradient of hydrophilicity on a silicon surface. By generating concentration gradient of surface-active species in the droplet Gallardo et al. (1999) demonstrated motion of droplets of aqueous and organic liquid. Utilizing the temperature-dependence of surface tension, Darhuber et al. (2003) reported an array of microheater array for thermocapillary actuation of droplets. Ichimura et al. (2000) demonstrated reversible motion of liquid drops at about 50 μm/s on a substrate surface which is modified by illuminating a photoisomerizable azobenzene monolayer. Nguyen et al. (2007) studied the magnetic manipulation of ferrofluid droplets using a pair of permanent magnets and a double sided printed circuit board (PCB) patterned for planar coils. The ferrofluid, acting as a magnetic fluid when polarized by an external uniform field, was moved along the virtual path formed by two coils generating magnetic fields of same polarity. Two other coils patterned on the backside of the PCB, energized such that their fields are of opposite sign, actuates the droplet. Due to the fact that magnetic force is a body force, larger droplets were observed to accelerate faster than smaller droplets and higher current through the actuating coils resulted in greater velocities. A two dimensional droplet manipulation chip was designed by Lehmann et al. (2006) employing the interaction between the paramagnetic particles contained in the aqueous droplet, external static magnetic field and the variable field generated by the PCB. Renaudin et al. (2006) proposed the use of a single interdigital transducer (IDT) for both actuation of a droplet and sensing the location of the droplet. The surface acoustic waves (SAW) are emitted by the IDT to move the droplet by an amount determined by the duration of the wave applied. Another SAW signal is generated and the echo from the droplet is received by the same

IDT to estimate the location of the droplet. The duration of the actuation SAW can be adjusted by knowing the droplet position with respect to the target position. An improved design has recently been demonstrated by Renaudin et al. (2009) where the piezoelectric substrate contains four IDTs for 2-dimensional localisation of a droplet. With known coordinates of the hydrophilic pads on either the bottom or top plate, the location of a droplet could be controlled with an accuracy of 200um, from the travel time between the echoes of SAWs.

Basu and Gianchandani (2007) developed a programmable 16×8 array of heaters to control two dimensional motions of microdroplets suspended in oil using Marangoni flow. Individual heaters, positioned above the oil surface generate surface flows resulting in droplets pushed away and subsurface flows resulting in droplets pulled closer. Although, droplets with diameters of 300-1000um could be moved at speeds of up to 140um/s, droplet evaporation necessitated the use of two oil layers suspending the droplets in between. A DEP based programmable fluidic processor containing 32×32 electrodes built on a scalable CMOS architecture was designed by Gascoyne et al. (2004). An aqueous droplet suspended in a non-polar medium is attracted towards higher electric fields. A non-polar droplet suspended in a polar medium can be trapped within the stronger surrounding electric fields. Thus, droplets were successfully moved and mixed irrespective of their conductivity by controlling the electrodes independently. It is reported that with the superhydrophobic surface no interactions of the electrodes with the contents of the droplet were observed. A significant improvement in terms of significantly reduced driving voltages was achieved by Hunt et al. (2008) who for the first time integrated microfluidics with CMOS process. Aqueous droplets are suspended at the boundary between a layer of low-density oil and a layer of high-density oil. Thus, contact angle hysteresis and other friction forces arising from the droplet wetting the solid surface can be avoided. The integrated prototype was successfully programmed to transport, mix, and divide 1 pL to 1 nL droplets.

Electrostatic field actuated droplet motion, sorting and mixing were demonstrated by Washizu (1998) in a device where arrays of electrodes are embedded beneath the hydrophobic and insulator layer. When an electrode next to the droplet is energized to a sufficient potential, charges are induced on the droplet surface closer to that electrode. The consequent electric field lines between the energized electrode and the induced charges generate Maxwell stress and, as a result, moves the droplet towards that direction. By sequential application of voltage to the electrodes in the array, aqueous droplets were transported continuously. In order to control the evaporation of the droplets and to incorporate two dimensional manipulation capability, Taniguchi et al. (2002) designed two microreaction devices. One of the devices has arrays of six-

phase electrodes covered with polypropylene tape. The other device contained a matrix of electrode dots for the independent control of droplets. Vegetable oil was used as the filler liquid which helps in reducing the friction between the droplet and the solid surface. Chemical reactions such as alkalization and luciferin-luciferase enzyme reaction were successfully demonstrated on both devices; however, droplets could be moved more smoothly on the former device.

An electrostatic droplet manipulation device with two dimensional arrays of electrodes on the bottom plate was proposed by Lebrasseur et al. (2006). In addition, a disposable plastic film card was developed to save the cost of electrode panel when the dielectric layer and the hydrophobic layers are degraded. The card contains the liquid medium supported by the hydrophobic coated dielectric layer as the bottom of the card. The card is then placed directly on the electrodes. The arc-electrodes allowed droplets to be mixed and the orthogonal arrays allowed the two dimensional droplet transport. However, the design lacks the capability of controlling droplets independently along one direction. The transport mechanism of liquid droplets on an insulator coated electrode array was investigated by Kawamoto and Hayashi (2006). Droplets of conductive and insulating liquid were successfully moved using the travelling electric field, although it was found that the maximum speed of the travelling field was greater for insulating liquids than that for conductive liquids. With the help of LEDs attached to the electrodes, it was observed that a droplet covering more than three electrodes cannot be transported. Moreover, there exists a threshold voltage for the actuation of droplets and a maximum synchronous travelling speed of the electric field beyond which the droplet falls behind, continuously.

A significant improvement in the speed of polarizable and conductive liquid droplets was achieved by Pollack et al. (2000) by applying the EWOD effect. In their device a droplet is sandwiched between a top plate containing the ground electrode and a bottom plate containing a linear array of square-shaped (1.5 $mm^2$) control electrodes. Control electrodes are coated with 700 nm Parylene C to provide the insulation and 200 nm Teflon AF 1600 to increase the contact angle of a droplet on the surface. The ground electrode is formed by transparent Indium-tin-oxide (ITO), which is also coated with 50 nm Teflon AF 1600. When an electrical potential is applied to a control electrode covered by a droplet which partially covers an adjacent zero-voltage control electrode, the solid-liquid interfacial tension, $\gamma_{SL,}$ decreases by the accumulated charges according to the following relation

$$\gamma_{SL} = \gamma_{SL}^{0} - \frac{\varepsilon_0 \varepsilon_R V^2}{2T} \tag{1.1}$$

where $\varepsilon$ and $t$ are the permittivity and the thickness of the dielectric layer, respectively and $\gamma^{o}_{SL}$ is the interfacial tension at zero voltage. The reduced interfacial tension reduces the contact angle at the interface between the droplet and the activated electrode according to the following relation

$$cos\theta(V) = cos\theta(0) + \frac{\varepsilon_0 \varepsilon_r V^2}{2t\gamma_{LG}}. \quad (1.2)$$

The resulting difference in contact angle between two sides of the droplet generates a pressure gradient in the bulk liquid inducing droplet motion towards the activated electrode. For 0.7-1.0 µL droplets of 100 mM KCl, the required minimum voltages for actuation are found to be 30-40 Vdc. This minimum voltage is attributed to the contact angle hysteresis of the droplet. Droplets are successfully transported continuously along the linear array of electrodes by energizing successive electrodes at 20 Hz switching frequency corresponding to an average droplet velocity of 3.0 cm/s. In order to reduce the required voltage for EWOD actuation of droplets, Moon et al. (2002) investigated the effects of dielectric thickness and dielectric constant. It was experimentally verified that electrowetting effect (i.e., the reduction of contact angle) is strengthened by reducing the dielectric thickness. A significant contact angle change (from 120° to 80°) was observed with a thin layer (70 nm) of barium strontium titanate (BST) having a dielectric constant of about 180 with a voltage of 15 Vdc where this voltage was sufficient to move a 460 nL water droplet. Pollack et al. (2002) demonstrated that droplets of 100 mM KCl can be moved with 60 Vdc at a faster speed (10 cm/s) by using low-viscosity (1 cSt) silicone oil as the filter liquid. The use of an immiscible liquid medium prevents the evaporation of droplets, reduces the threshold voltage by reducing the contact angle hysteresis, and reduces the friction between the droplet and the solid surface by providing a thin layer of lubrication.

Although digital microfluidics may not be the complete alternative for a continuous flow-based system, it has some obvious advantages such as i) reduced volume of sample and reagents, ii) minimum dead volume, iii) no need for mechanical pumps, valves and permanent channels, iv) better controllability in mixing and dilution, v) shorter reaction times for an increased surface to volume ratio, vi) scalability and vii) high throughput (Fair 2007, Teh et al. 2008, Choi et al. 2012). In fact, EWOD is the only actuation method for manipulating droplets on a planar surface with the capability of efficiently performing all the basic fluidic operations necessary for a lab-on-a-chip. For instance, droplet splitting on a planar surface is either infeasible or too complicated using other actuation methods. The following sections present relevant literature on the design, fabrication, operations and applications of EWOD-based DMFS.

### 1.3.2 DMFS design and fabrication

Design and fabrication of a DMFS are the two important aspects of the proposed research. Low cost and simple fabrication of the device capable of actuating droplets with lower voltages, generating noise-free feedback signal is always desirable. A hypothetical digital microfluidic system (EWOD-based) consists of a two dimensional array of square electrodes on a single plate. In order to exploit the full capability of the device in terms of reconfigurability, each electrode must be independently addressable. An N×M array control electrodes needs N×M electrical connections. This results in a complicated and costly fabrication process of multiple metallisation layers. An alternative design has been proposed by Fan et al. (2002) where two sets of orthogonal electrode rows, one set of row electrode on the top plate and another set on the bottom plate, are used to access the N×M array of overlapped square areas. Therefore, N+M connections are required to manipulate droplets in the N×M virtual grid. However, the significant reduction of the number of independent control electrodes may result in an unmanageable increase in the complexity of the coordination of multiple droplets.

Research on the low cost fabrication of a fully reconfigurable digital microfluidic system with independent accessibility to all the electrodes of the two dimensional array resulted in the adoption of printed circuit board (PCB) technology (Gong and Kim 2005). Due to the surface topography and roughness and the resulting high resistance to droplet motion, the coarse fabricated PCB surface requires higher actuation voltages (~500V). Later, Gong & Kim (2008) proposed three refined PCB microfabrication processes in order to be able to move a droplet surrounded by air (i.e., without filler liquid) with lower driving voltages (~80 Vac). Li et al. (2008) reported that integration of CMOS technology for multilayer metallisation with digital microfluidics can solve the problem of connectivity to electrodes in a two-dimensional array. Recently Morgan et al. (2012) demonstrated a 64×64 thin film transistor (TFT) array-based active matrix EWOD with integrated impedance sensing capability and implemented colorimetric assay for glucose detection. To eliminate the manual process of assembling two plates and the resulting inaccuracies in droplet volumes, Nelson and Kim (2011) developed a monolithic EWOD chip by surface micromachining of a thin film resulting in the control electrodes and the space between parallel plates. A hybrid system for bioanalysis in an EWOD device integrated with magnetic sensing capability was demonstrated by Brennan et al. (2011) utilizing injection molding as an alternative fabrication process.

The difficulty in connecting numerous electrodes in a two-dimensional array was eliminated by Chiou et al. (2003) who demonstrated optoelectrowetting based actuation of liquid droplets by incorporating a photoconductive material underneath the driving electrodes of an

electrowetting based system. The light intensity dependent resistance of photoconductor, in series with the impedances of the droplet and the dielectric layer, determines the voltage drop across the dielectric layer and thereby the contact angle of the droplet. A 2 mm diameter droplet of deionized water could be moved at a speed of 7 mm/s with a 4 mW laser at 532 nm wavelength. Furthermore, the requirement of multiple light sources for the manipulation of multiple droplets simultaneously is a major challenge. Later, Chiou et al. (2008) developed an improved device for optoelectrowetting droplet manipulation which allowed droplets to move at a speed of 78mm/s. Incorporation of multiple laser scanning beam and programmable scanning mirrors multiple droplets were simultaneously transported in addition to typical microfluidic operations on individual droplets such as droplet division, generation and merging. In an attempt to make the liquid droplets accessible to other devices Chuang et al. (2008) developed an open optoelectrowetting device consisting of a single plate. The driving and reference electrodes are patterned alternately and then coated with amorphous Si as the photoconductive material, $SiO_2$ and Teflon. A laser source (3 mW) resulted in droplet speed of 3.6mm/s. The minimum size of the droplet that can be manipulated is limited by the width of the electrode. The feasibility of this method has not been appraised for droplet generation and division. Krogmann et al. (2008) proposed that using an appropriate selection of amplitude and frequency of the bias voltage, liquid droplets can be pushed forward with the light source illuminating the back of the droplet. The proposed theoretical analysis based on a lumped parameter electrical circuit analysis revealed that due to the presence of a finite parasitic resistance, mostly from the droplet, there exists range of bias voltage frequency, actuation of the droplet by pushing is possible. In that frequency range, the contact angle of the illuminated side of the droplet is higher than that on the dark side. The experimental result verified the proposed actuation of a droplet by pushing in addition to the usual actuation by pulling. For droplets with negligible resistance, addition of an external resistor allows the push actuation and thereby enhancing the flexibility in manipulating droplets.

The dielectric material plays a very significant role in digital microfluidics. The electrical properties, such as dielectric constant and electric-field strength, of the material determine the operating voltage for droplet manipulation in a DMFS. In addition, the time, cost and method of fabrication of the device depends greatly on the physical and chemical properties of the chosen material for the dielectric layer. Typical operating voltage in a DMFS ranges from 50 V to 100 V for successful manipulation of droplets. Moon et al. (2002) were able to move droplets of deionized (DI) water at 15 V by using a 70 nm Barium Strontium Titanate (BST) as the dielectric layer ($\varepsilon_r = 180$). Later, Kim et al. (2006) used a 100 nm thick RF reactive sputtered Bismuth Zinc Niobate (BZN) layer to move a droplet at 14 V. Berry et al. (2006) reported a contact angle

change of over 100$^{o}$ C using SDS surfactant in the droplet and dodecane oil as the surrounding medium by applying only 3 V. However, oil environment may not be suitable for a general purpose DMFS due to possible interactions between the droplet liquid and the oil. The high-temperature chemical vapour deposition (CVD) processes require very expensive setup. Also, the high deposition temperature (>600$^{o}$ C) prohibits the integration of CMOS foundry technology and the use of polymer substrates. In an attempt to reduce the working temperature Li et al. (2008) used anodic $Ta_2O_5$ ($\varepsilon_r = 18$) as the dielectric material and successful droplet movement was achieved at 14 V. Although the anodization of Tantalum could be performed at room temperature, this requires the special resource for sputtering Tantalum on the substrate. [d]Bhattacharjee and Najjaran (2010) reported the use of cyanoethyl pullulan (CEP), having high dielectric strength ($\varepsilon_r = 20$), as the dielectric material and demonstrated that droplet actuations were possible at voltages as low as 20 V. The additional advantage of using CEP is that it can be deposited using a spin-coater only, obviating the need for any costly deposition setup needed for thermally/chemically grown dielectric layer. Chang et al. (2010) demonstrated droplet motion with a very low voltage of 3 V in an open DMFS where the dielectric layer was a 127 nm thick atomic layer deposition (ALD) aluminium oxide ($Al_2O_3$). Using polyvinyledene-fluoride-trifluoroethylene (PVDF-TrFE) as the dielectric material, Zhao et al. (2009) demonstrated that droplets can be successfully transported in an open EWOD device.

### 1.3.3 Hydrodynamics of droplet motion

The response of a liquid droplet to an applied electric field is not fully understood yet. Besides, the generation, splitting and mixing of droplets actuated by EWOD are more complex than the transport of a droplet. Hence, a good understanding of the results of research on droplet hydrodynamics is essential in the development of an approximate model of fluidic operations. Investigation of the 3-D flow fields inside an EWOD-driven droplet has been studied by Lu et al. (2008). Micro particle image velocimetry (µPIV) data obtained for different horizontal planes of a moving water droplet containing red polystyrene beads revealed two internal circulations on either side of the vertical meridian plane. In order to capture the 3-D velocity field and circulations on vertical planes, the 2-D µPIV data were utilized along with the continuity equation. It was found that a strong downward flow exists near the activated electrode due to the electrowetting force. Although the flow pattern near the interface could not be revealed because of the interference of the curved surface, experiments show that reversible laminar flow results in little net displacement of particles when the droplet is moved back and forth. This implies that complex patterns of droplet motion results in better mixing of particles rather than linear back and

forth motion. A numerical model of the EWOD-driven droplet was developed by coupling the electrostatic force with the droplet hydrodynamics (Arzpeyma et al. 2007). The voltage dependent contact angle change was calculated from the Lippmann-Young equation where the input potential is obtained from solving the Laplace equation. The droplet shape and velocity were then obtained from the solution of Navier-Stokes equations. The results of simulation in terms of droplet velocity under different actuation voltages and electrode actuation frequencies were in agreement with those obtained from experiments. The EWOD force distribution along the droplet interface and the variations of the net force on the droplet were investigated by Baird et al. (2007). Their numerical scheme solved the potential distribution and charge densities on the droplet interface. The net force on the droplet obtained from integrating the charge densities matches closely with the predicted values obtained from analytical model. Results show that the EWOD force is stronger for dielectric materials with higher dielectric constants and is not affected by initial contact angles. The force distribution, however, depends on the curvature of the interface. Recently, Ahmadi et al. (2011) reported a volume-of-fluid method numerical modeling of the coupled electrohydrodynamics of droplet motion in an EWOD-based DMFS. Incorporating the empirical models of resistive forces from the filler fluid as well as from the contact line, numerical results were shown to be in good agreement with the experimental results.

### 1.3.4 Electromechanical fundamentals of EWOD

The electromechanical interpretation of the EWOD-actuation of a liquid droplet allows one a generic approach to develop a lumped-parameter model of an electrofluidic system (Jones 2005, Jones 2009, Chatterjee et al. 2009). The electrohydrodynamics of a droplet driven by EWOD or DEP was studied by Zeng and Korsmeyer (2004) and Chakrabarty et al. (2010) from the continuum electromechanics point of view. It is argued that aqueous droplets, which are not perfectly conductive, undergo a transient process of delivering the charges to the droplet-insulator interface. When the transient time scale of electroquasistatic behaviour of the droplet is comparable to the hydrodynamic time scale, conductivity of the liquid should be taken into account. Furthermore, for liquids of relatively higher permittivity than the dielectric material between the droplet and electrodes, the droplet should be modeled as a leaky dielectric material.

The traditional electrowetting theory centers on the idea that wettability dependent contact angle change acts as the driving force for the droplet motion. This interpretation fails to explain some of the characteristics of EWOD-driven droplet manipulation, for example the motion of dielectric liquid, low-surface tension liquid with no apparent change in contact angle, and the contact angle saturation (Chatterjee et al. 2006, Abdelgawad and Wheeler 2008).

Therefore, the electromechanical analysis of the EWOD-driven droplet motion aims at finding a reasonable explanation for such behaviours. Jones et al. (2003) and Jones (2009) studied the electromechanics of a generic liquid droplet by considering the lumped capacitance and conductance of the droplet, dielectric material and the surrounding medium. It is proposed that the EWOD and DEP are the low and high frequency limits of electromechanical response of the droplet, respectively. Below the critical frequency, given by $\omega_c = \frac{2g_w}{2C_w+C_d}$, a deionized water droplet has no electric field developed inside it and the entire applied voltage is dropped across the dielectric layer. When $\omega >> \omega_c$, the water droplet behaves like a dielectric and a certain fraction of the applied voltage is dropped across the droplet.

A detailed analysis of frequency-dependent electrical actuation of liquid droplets has been done by Kumari et al. (2008). Under the assumption that the droplet retains a circular footprint, the energy minimization of the electrical network (composed of the droplet, activated electrode and the dielectric layer) yields a frequency dependent expression of the actuation force. For a droplet with given conductivity, the actuation force corresponds to that of EWOD-force when the driving frequency is low. The actuation force decreases with frequency and with a sufficiently high frequency the actuation force corresponds to that for a perfectly insulating liquid. Moreover, this behaviour is shifted towards higher frequency regions as the conductivity of the droplet liquid increases. Recently, Chatterjee et al. (2009) reported a comprehensive analysis of the droplet actuation by an AC voltage. Results verified that for a given gap between the top and bottom plates the liquid dielectric property becomes more and more pronounced as the frequency of the applied voltage is increased. As the frequency approaches the critical value, determined by the electrical properties of the liquid and dielectric layer, the DEP force on the droplet increases. However, the total actuation force reduces quickly beyond the critical frequency. When the voltage drop across the droplet exceeds that of dielectric layer, the DEP force becomes stronger than the electrowetting force. In addition, due to the dependence of conductance on the gap between two plates the total actuation force acting on the droplet increases when the gap is decreased.

Recently, [c]Bhattacharjee & Najjaran (2009) showed that the EWOD actuation of a droplet can be modeled as a closed-loop system with an inherent unity feedback of droplet position. Electrode, dielectric and droplet are modeled as a capacitor with variable area as the droplet, considered as a conductor, moves over the dielectric layer. The EWOD force depends on the rate of change of droplet area over the actuated electrode, which in turn depends on the direction of motion and the position of the droplet between the actuated and previous electrode. Thus, EWOD actuation intrinsically utilizes the droplet position to generate sufficient force to

accelerate the droplet. When the droplet approaches the final position, the magnitude of force reduces automatically so the droplet decelerates. In case the droplet has sufficient momentum to exceed the final position, the EWOD force, according to the model, will act on the opposite side of the droplet in order to bring it back to the desired position. Moreover, it is also pointed out that the EWOD force and hence, the response of the droplet depends on the size of the droplet.

### 1.3.5 Electro-hydrodynamics of digital microfluidics

The spatial distribution of electric potential in the space occupied by a droplet, its surrounding fluid and the dielectric layers is given by the Poisson equation under the electro-quasistatic assumption (Chakrabarty at al. 2010, Zeng and Korsmeyer 2004):

$$\boldsymbol{\nabla}^2 V_i = \frac{\rho_e}{\varepsilon_0 \varepsilon_{ri}} \tag{1.3}$$

where $V$ is the applied potential to the control electrode, $\rho_e$ is the free charge per unit volume inside the droplet, $\varepsilon_r$ is the relative permittivity, $\varepsilon_0$ is the vacuum permittivity, $i$ stands for the respective material. Initially the droplet may not have any free charge inside. However, if the droplet possesses finite conductivity, free charges can be transported according to the following charge conservation law:

$$\frac{\partial \rho_e}{\partial t} + \boldsymbol{\nabla}.(\rho_e \boldsymbol{U}) = -\boldsymbol{\nabla}.(\sigma \mathbf{E}) \tag{1.4}$$

where σ is the droplet conductivity, $\boldsymbol{U}$ is the velocity field, $-\boldsymbol{\nabla}.(\sigma \mathbf{E})$ is the divergence of current density $\boldsymbol{J} = \sigma \mathbf{E}$ in which $\boldsymbol{E} = -\boldsymbol{\nabla} V$ is the electric field. This charge distribution in turn affects the potential distribution. However, free charges migrate towards the interface and accumulate there very fast if the transient time of charge distribution is much smaller than the hydrodynamic time scale for the liquid. Thus, a discontinuity in the electric field appears at the droplet-medium interface which is accounted for by the following boundary condition (Chakrabarty at al. 2010):

$$\hat{\boldsymbol{n}}.(\varepsilon_0 \varepsilon_{rd} \boldsymbol{\nabla} V_m - \varepsilon_0 \varepsilon_{rm} \boldsymbol{\nabla} V_m) = \rho_s \tag{1.5}$$

where $\rho_s$ is the surface charge density at the droplet-medium interface.

The net macroscopic effect on the droplet is given by the following expression of electric force per unit of liquid volume:

$$\boldsymbol{F} = \rho_e \boldsymbol{E} + 0.5 \varepsilon_0 (\varepsilon_{rd} - \varepsilon_{rm}) \boldsymbol{\nabla} (\boldsymbol{E}.\boldsymbol{E}). \tag{1.6}$$

The first term is the well-known Coulomb force on the induced free charges in the bulk of the liquid or at the interface. The second term is known as the DEP force originating from the polarization. The presence of electric field distorts the charge poles of individual molecules of the liquid and any other species present in the droplet. The resultant of all the forces on each of these

polarized particles is the net DEP force. This is the only driving force for a droplet with very low or no conductivity under electrical actuation.

Since most liquids are incompressible and Newtonian in typical digital microfluidics applications, the hydrodynamics of a liquid droplet surrounded by another fluid medium is governed by the Navier-Stokes equations (Arzpeyma et al. 2007):

$$\rho\left[\frac{\partial \boldsymbol{U}}{\partial t} + \boldsymbol{U}.\boldsymbol{\nabla U}\right] = -\boldsymbol{\nabla} p + \mu \boldsymbol{\nabla}^2 \boldsymbol{U} + \rho g + \boldsymbol{F} \tag{1.7}$$

$$\boldsymbol{\nabla U} = 0 \tag{1.8}$$

where $\rho$ is the liquid density, $t$ is the time, $\boldsymbol{\nabla}$ is the Del operator, $p$ is the pressure, $\mu$ is the dynamic viscosity, $g$ is the gravitational acceleration, $\boldsymbol{F}$ is the body force per unit of liquid volume. At the droplet-medium interface the following boundary conditions hold:

$$(\boldsymbol{\tau}_d - \boldsymbol{\tau}_m)\hat{\boldsymbol{n}}).\hat{\boldsymbol{n}} = \gamma_{dm}\boldsymbol{\nabla}\hat{\boldsymbol{n}} \tag{1.9}$$

$$(\boldsymbol{\tau}_d - \boldsymbol{\tau}_m)\hat{\boldsymbol{n}}).\hat{\boldsymbol{t}} = (\boldsymbol{\nabla}_s\gamma_{dm}).\hat{\boldsymbol{t}} \tag{1.10}$$

where $\boldsymbol{\tau} = -pI + \mu[\boldsymbol{\nabla U} + (\boldsymbol{\nabla U})^T]$ is the stress tensor, *d* and *m* stands for droplet and medium, $\hat{\boldsymbol{n}}$ and $\hat{\boldsymbol{t}}$ are the normal and tangential unit vectors at the interface, $\gamma_{dm}$ is the surface tension between droplet and medium, $\boldsymbol{\nabla}_s = \boldsymbol{\nabla} - \hat{\boldsymbol{n}}(\hat{\boldsymbol{n}}.\boldsymbol{\nabla})$ is the surface gradient operator.

### 1.3.6 Microfluidic operations

Droplet generation, merging and splitting has been performed on an EWOD-based system demonstrating its capability of serving as a practical lab-on-a-chip where all the common microfluidic operations can be perfectly accomplished. Pollack et al. (2002) successfully performed droplet splitting and merging by controlling the pattern of energized electrodes. A droplet can be dispensed from the reservoir containing a large droplet by activating a number of electrodes along a direction which results in a liquid finger/protrusion. Subsequent deactivation of the intermediate electrodes and activation of the reservoir electrode pulls back the liquid from the neck and finally leaves a droplet on the terminal electrode after the neck is broken off. Cho et al. (2002) demonstrated the droplet generation method by arranging two extra electrodes orthogonally on both sides of the electrode where necking is expected to initiate. Instead of having an electrode for the reservoir, those two electrodes facilitate the neck initiation and break off. In another study involving droplet actuation with AC voltages of various frequencies, it was found that droplets can be moved at a speed of 25 cm/s when 150 Vac is applied. The latter was a significant improvement in droplet speed on a digital microfluidic system. Microscale mixing has also been successfully demonstrated in EWOD-based DMFS by merging two droplets and transporting the merged droplet along specified paths (Fowler et al. 2002, Ren et al. 2003, Paik et

al. 2003). Results show that the efficiency of active mixing depends on the number of rolls of the merged droplet as well as the merge and split strategy.

Droplet splitting is a generic microfluidic operation which can affect the overall performance of a DMFS. The generation of a droplet from a reservoir can be regarded as a splitting process. Therefore, from the generation of a droplet of specified volume to the control of concentration of sample species, droplet splitting process plays the key role. Droplet splitting process has been physically and experimentally studied by Cho et al. (2001). Based on the study of the geometry of a droplet in splitting process, shown in Figure 1.1, taking into account the Lippmann-Young equation and the Laplace equation of pressure across the interface, it was shown that applied voltage is related to the radii of curvature of the deformed droplet. The required gap between two hydrophobic surfaces is calculated using the estimated values of the radii of curvature $R_1$ and $R_2$. A droplet cannot be split when the gap is larger than the calculated value. A required gap of 150 µm was calculated for the size of electrode and droplet, material properties used in the experiment. The above criterion for droplet splitting was verified by experiments conducted with channel gaps of 80 µm, 150 µm and 300 µm. Only the device with 80 µm gap was able to split a droplet. Recently, Clime et al. (2009) demonstrated splitting of a droplet containing magnetic beads in an electrowetting-based device.

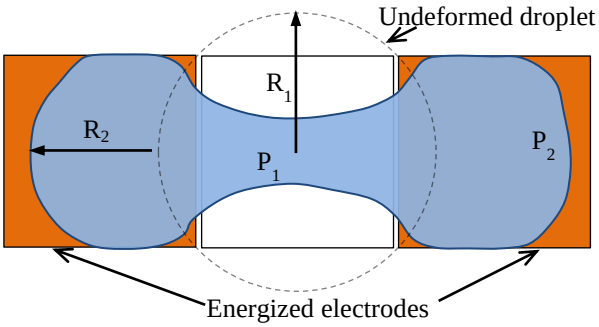


Figure 1.1: Droplet configuration for splitting (Cho et al. 2001).

### 1.3.7 Feedback control in DMFS

Recently, the need for integration of feedback control system for reliable and accurate operation on droplets has been realized and several researchers have demonstrated the benefits of closed-loop controllers in DMFS. The notion of the feedback control of droplet motion was first proposed by Gong et al. (2004) for a cross-referencing based DMFS where the droplets are driven by the EWOD force. The system consisting of a droplet, the dielectric layer and the electrodes is modeled using a network of capacitors and resistors. The position of the droplet is monitored by measuring the voltage drop across an external resistor. The simple control algorithm first

compares the measured voltage drop with a predefined/calibrated value and continues to apply the driving voltage to the target row and column electrodes as long as the measured voltage drop is smaller than the predefined value. In order to achieve high precision in droplet generation, Ren et al. (2004) proposed a control system which utilizes the capacitance feedback. The dispensed volume of a droplet can be approximated by its footprint area over the activated electrode where the footprint area can be measured using the capacitance between the droplet and electrode. The control algorithm implemented in LabVIEW® monitors the capacitance which is measured in terms of the output frequency of a ring oscillator. When the generated droplet completely overlaps the electrode, the output of the ring oscillator reaches a cut-off value and the controller shuts off the flow of liquid by closing the valve of an external continuous flow system. The reproducibility of this method was evaluated by varying the droplet volume, viscosity and generation rate. The experimental results comply with the acceptable values of the prevailing parameters in typical biomedical applications. Gong and Kim (2006) used a PID controller for the generation of droplets to eliminate the external continuous flow source of liquid and achieve higher compactness for the DMFS. Measuring the capacitance of the system, composed of the droplet-in-progress and the electrode where the droplet is to be formed, and controlling the driving voltage of the electrodes on the creation site and reservoir, successful dispensing of droplets with higher accuracy and precision was demonstrated. Droplet capacitance was shown to be related to the type and amount of contents in the liquid and utilized in mixing and concentration control (Schertzer et al. 2010). Shih et al. (2010) demonstrated that the operation of a DMFS based on the detection of a droplet on a given electrode significantly increases the reliability of bio-assays. Recently, Miguel and Najjaran (2011) have demonstrated that position of a droplet, as it moves, between two adjacent electrodes can be estimated by measuring capacitance. It is noted that all the applications of capacitance sensing in a DMFS are based on measuring between the upper electrode and one of the square electrodes in the lower plate. This method is straightforward in a sense that the measured capacitance is linearly dependent on the droplet overlap area. A major drawback of this method is the inapplicability in a single plate DMFS, where the ground electrodes are incorporated into the lower plate. Even in a two plate DMFS, the engagement of the upper plate for sensing restricts the integration of any other functionality that requires access from above. Therefore, a sensing method avoiding the connection to the upper plate would greatly enhance the functionality of a DMFS. The introduction of a coplanar sensing approach as one of the contributions of this thesis is discussed in Chapter 2.

Armani et al. (2005a, 2005b) proposed a visual feedback control system for the EWOD based DMFS. The vision algorithm isolates the pixels corresponding to the liquid/vapour interface of the droplet and then determines the location of the interface by applying the Gaussian smoothing and standard Edge Detection technique. The requirement of an external fast vision system and complex computation for image processing of multiple droplets will make the system costly as well as non-portable. Therefore, it is apparent from the above literature review that an accurate in-situ electrical signal feedback control is necessary and appropriate to attain the accuracy and precision required for the microfluidic operations such as splitting and mixing performed in the DMFS. In an attempt to avoid bulky attachments for detection in DMFS, Luan et al. (2008) reported a DMFS with integrated InGaAs-based thin-film photodetectors distributed among the electrodes. Optical fiber-based droplet sensing was demonstrated by Wang et al. (2008) for feedback control of dielectrophoretic droplet dispensing.

Recently, a general model of the closed-loop control system for droplet position between two adjacent cells in a DMFS has been presented ([c]Bhattacharjee & Najjaran, 2009). The droplet dynamic system, modeled using the semi-empirical relations of resistances to motion (Ren et al. 2002, Bahadur and Garimella 2006), is simulated for a step command in position and transient characteristics are obtained and discussed. The transient and steady-state response i.e., rise time, settling time and percentage overshoot are used to calculate the operational parameters of a DMFS such as driving frequency as well as to identify the unwanted situations. The need and utility of a feedback control system for proper functioning of a DMFS are also identified.

### 1.3.8 Bioassay applications

As mentioned in the previous paragraphs, there are a number of bio-analysis related applications that can benefit from asymmetric splitting of a droplet. For a DMFS, the particle separation and concentration control was first demonstrated by Cho and Kim (2003) by designing a separate set of electrodes for electrophoresis. Application of DC voltage between the electrodes facing a droplet can concentrate charged particles near the cathode or anode. With two oppositely charged particles in the droplet, both the cathode and the anode will attract particles of positive and negative charge, respectively. The EWOD driven splitting of the droplet, then, results in two droplets of equal volume but different concentration or different particles. Separation of negatively charged carboxylate modified latex and polystyrene particles using an electric field of 3.3 V/mm followed by the application of 60 Vac (10 kHz) resulted in droplets with mostly the desired particles. An efficient particle concentration and separation method was developed by Zhao et al. (2007) by designing the electrodes for the travelling-wave dielectrophoresis (twDEP) on the bottom plate and those for EWOD on the top plate. A droplet containing target particles

(e.g., aldehyde sulfate (AS) beads) is brought to the target location and the particles are concentrated to one side of the droplet. A subsequent splitting of the droplet into two equal size droplets results in one daughter droplet with almost all (98%, as reported) of the target particles. Results support that separation of different particles is also possible. A droplet containing two types of particles (AS and glass beads) was successfully split into two equal droplets with one having 97% of AS beads and the other having 77% of glass beads. However, the efficiency and speed of separation and concentration control through splitting is limited because with the reported methods the mother drop will be always halved. It can be noted that with the capability of splitting a droplet into two unequal droplets higher concentration of one type of particle and hence a better separation efficiency can be obtained in the smaller droplet. By modulating the applied signal and designing multiple strip electrodes within the array of usual square electrodes, the DEP manipulation of neuroblastoma cells and polystyrene beads has been successfully shown (Fan et al. 2008). Analysis of the system of droplet sandwiched between two plates, by considering as a network of resistors and capacitors, revealed that an electric field is established inside the droplet above a cut-off frequency of the applied signal. Since the width of a strip electrode is very low compared to a square electrode, the field inside the droplet is non-uniform. This non-uniform electric field has been utilized in separating the particles with positive or negative DEP depending on the proposed weighted Clausius-Mossotti factor.

Moon et al. (2006) designed a multiplexed proteomic sample preparation device for high throughput Matrix Assisted Laser Desorption/Ionization Mass Spectrometry (MALDI-MS). Figure 1.2 shows the device that consists of electrode arrays of two different sizes with transition sites where the smaller electrodes denoted by × are inscribed within the larger electrodes. The sample containing both the protein and impurities are dispensed from the reservoir, transported to the transition site using the array of smaller electrode and left there to dry. A rinsing droplet is brought over the dried sample through the array of larger electrodes. The impurities are washed away by the rinsing droplet which is then disposed into the waste reservoir. The larger electrode at the transition site is designed to overcome the difficulty in moving a droplet past the smaller electrode containing the dried protein rendering the surface hydrophilic and rough. Next, the droplet containing the MALDI-MS reagent is delivered to the spot for further analysis. However, the requirement of two arrays of unequal electrodes imposes a burden of extra time and cost in the design and fabrication. As a result, it is greatly desirable to have a device with equal-sized electrodes in the array and dispensing a droplet of the proteomic sample having a footprint area smaller than the electrode area. The EWOD actuation cannot move a droplet smaller than the size of the electrode since certain amount of overlap on the adjacent electrode is required for

continuous motion. In contrast, a regular-sized droplet can be transported to the target location and a droplet smaller than the electrode can be generated by splitting the mother droplet into 1:x ratio by EWOD.

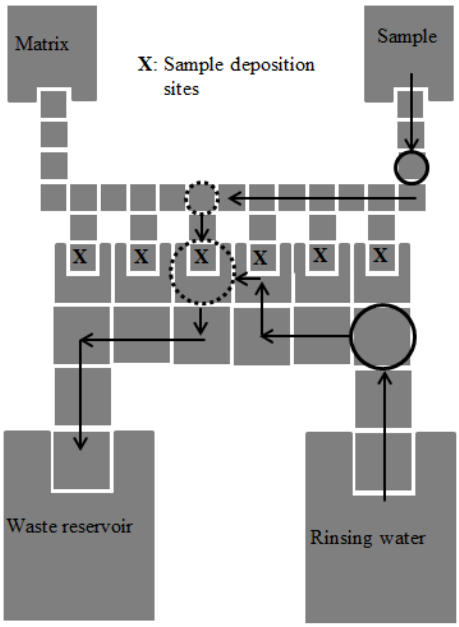


Figure 1.2: Schematic of the integrated EWOD-MALDI-MS device (Moon et al. 2006).

Clinical diagnostics of human physiological fluids, such as whole blood, serum, plasma, sweat, saliva, urine and tear, have been demonstrated on a EWOD-driven droplet-based lab-on-a-chip (Srinivasan et al. 2004). Glucose assay was performed on all the above mentioned fluids in a device integrated with reservoirs, transportation bus, detection spots and a mixing area. The results obtained agree with the reference measurements, except for the urine where interference by the uric acid affected the result. However, the glucose assay in a DMFS is performed with only a twofold dilution of the droplet containing the sample, while the bench-scale assay requires dilution factors greater than 100. With a 1:1 splitting process it will take many steps to achieve the desired dilution making the process time-consuming and susceptible to error. In a DMFS with the capability of higher dilution factors can be achieved faster than with a 1:1 splitting. The proposed method of splitting a droplet into a 1:x ratio is explained in Section IV.

The compatibility and feasibility of EWOD-based microfluidic systems for polymerase chain reaction (PCR) has been investigated by researchers (Pollack et al. 2003). Pollack et al. (2003) observed that the PCR reagent can be successfully manipulated without cross-contamination through the oil medium or the solid surface. Chang et al. (2006) implemented the

PCR in an EWOD-based device incorporating a microheater and thermal sensor for feedback controlled thermal cycling. Droplets of cDNA samples and PCR reagent are generated, merged, mixed and transported to the PCR chamber. The final results of fluorescent signal are comparable to those obtained from a bench-scale device. It is noted that the process of PCR can be enhanced with an EWOD-based DMFS capable of diluting samples to arbitrary factors and of mixing samples fast and accurately.

## 1.4 Thesis outline

This thesis is organized as follows:

Chapter 1 presents the objectives of this research, the review of relevant literature and contributions of the research.

Simulation results of droplet position control are presented in Chapter 2. A lumped parameter model of a moving droplet is developed based on the empirical theories of resistances. Results of multiple simulations considering a range of material properties and geometric parameters are discussed. Two dielectric materials possessing higher dielectric constants are investigated to reduce to the operational voltage and cost of fabrication. Experimental results of this investigation are also shown. Finally, a novel method of droplet sensing using only the control electrodes along with results is presented.

In Chapter 3, the capabilities and limitations of computational fluid dynamics software packages in simulating liquid with free surface are evaluated. The general electrohydrodynamics of droplet splitting and the role of key parameters in determining the success of splitting are explained based on the simulation results obtained from FLOW-3D®. The results of simulation based investigation of asymmetric splitting are presented in Chapter 4. The role of minimum voltage, droplet size and aspect ratio, viscous shear, surface tension and the ratio between applied voltages in determining necessary conditions for successful splitting are discussed. The required voltages for successful asymmetric splitting of droplets of various aspect ratios are determined and the parameters that characterize splitting such as flow rates, capillary numbers are presented. Finally, the simulation results of asymmetric splitting with different voltage ratios are discussed.

Chapter 5 describes the design and fabrication of the digital microfluidic system as well as the experimental setup and the results of droplet splitting experiments. The minimum voltages required for both symmetric and asymmetric splitting of a droplet of deionized water in the fabricated device are identified. Experimental results in terms of volumetric flow rates and accumulated volume of liquid in asymmetric splitting with different voltage ratios are discussed. Finally, the sources of error in experiments and of variability in results are discussed.

Chapter 6 presents the conclusions of this research along with opportunities for further research on the problem.

# CHAPTER 2
# DIGITAL MICROFLUIDICS – OPERATIONS AND ENHANCEMENTS

Accurate and reliable operations in digital microfluidics require either a feedback control system having all the parameters tuned appropriately or extensive study of the open-loop droplet operations such as motion, dispensing and splitting. The open-loop dynamic system in digital microfluidics typically consists of a moving or deforming droplet and the actuation mechanism. A mechanism for sensing the position of a droplet and the volume of liquid is essential to control droplet operations in a closed-loop fashion. This chapter begins with the study of closed-loop control of droplet position assuming generic actuation and sensing mechanisms, and lumped parameter models of the opposing forces. Simulation results reveal the significant underlying relations between the droplet response and the parameters of the controller as well as the geometry. In the next section, a novel droplet sensing mechanism is proposed which not only facilitates the realization of closed-loop control of operations in digital microfluidics, but also eliminates the limitations of traditional droplet sensing methods. This new sensing method can potentially be used for closed-loop control of droplet splitting. Since EWOD-actuated droplet splitting is central to this thesis, understanding the fundamentals of EWOD is essential. Therefore, a lumped-parameter analysis of EWOD-actuated droplet motion is performed to identify the critical factors determining the effectiveness of EWOD. Since the magnitude of EWOD force is directly related to the dielectric properties of the insulating layer, a material with high dielectric constant, CEP, is investigated in terms of contact angle change as well as droplet actuation. Results, presented in the final section, prove that droplet operations can be reliably performed with significantly lower voltages in addition to the fact that DMFS can be quickly fabricated using an inexpensive equipment.

## 2.1 Droplet Translocation and Control

### 2.1.1 Dynamics and Control of Droplet Motion:

In this study, a confined digital microfluidic system with a planar array of cells (electrodes) is considered. In this system, liquid droplets are submerged in a filler fluid (e.g., silicone oil) to prevent evaporation of droplets and to lubricate the solid surface at the contact line, and hence, to reduce the force of friction. Figure 2.1 shows the free body diagram of a

droplet moving from one cell to another in a confined DMFS. A greatly simplified model of the droplet motion in a DMFS can resemble a mass and damper system without the stiffness term. In this way, the displacement of the droplet is the output of the system and the driving force is the input to the system. In the present study, it is assumed that the driving force may be either a surface-force (e.g., electrowetting force) or a body-force (e.g., magnetic force), provided that the magnitude and direction of the force can be controlled.

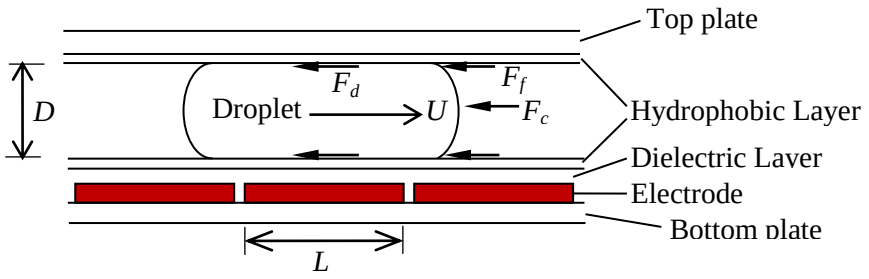


Figure 2.1: Side-view of droplet motion showing the sources of resistance to motion.

Hence, if the total resistive force against droplet motion can be modeled as a viscous friction force, which is linearly related to droplet velocity, the dynamic equation of the droplet motion is given by:

$$m\frac{d^2x}{dt^2} + c\frac{dx}{dt} = F_{dr} \tag{2.1}$$

where $x$ is the displacement of droplet, $m$ is the droplet mass, $c$ is the coefficient of friction and $F_{dr}$ is the driving force. Thus, the transfer function $G(s)$ of this simplified DMFS is given by:

$$G(s) = \frac{X(s)}{F_{dr}(s)} = \frac{1}{ms^2+cs} \tag{2.2}$$

where $X(s)$ and $F_{dr}(s)$ are the Laplace transforms of the displacement and driving force respectively. The block diagram of droplet dynamic system is shown in Figure 2.2. Now, consider the droplet actuation mechanism is such that the position of the droplet between two adjacent cells is not intrinsically utilized to generate the magnitude and direction of the driving force. In absence of external feedback on position of the droplet, the above mentioned driving force cannot produce the desired final position of the droplet despite the fact that its magnitude and direction can be controlled. For instance, a pulse of driving force will result in droplet displacement as a function of the magnitude and duration of the pulse whereas a constant driving force will continue to move the droplet. This implies that the DMFS is an open loop system and there is no control over the final position of the droplet. It can be mentioned here that in an EWOD-based DMFS, the EWOD force is a function of the droplet position. Hence, the system inherently utilizes droplet position feedback and the droplet finally settles down on the destination cell.

Nevertheless, position feedback is necessary in EWOD-based DMFS for accurate actuation of successive electrodes and guaranteed transport of droplets. Feedback control is also necessary for the control of temperature and concentration as well as for operations like droplet creation.

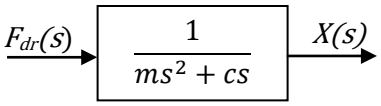


Figure 2.2: Block diagram of the open-loop droplet motion.

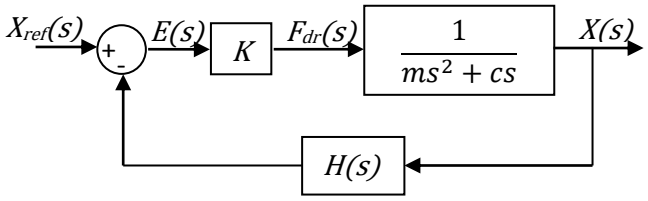


Figure 2.3: Block diagram for the closed-loop control of droplet position from one cell to an adjacent cell.

Hence, the feedback control of individual droplets is necessary for accurate positioning of the droplets and proper functioning of the DMFS. In a typical DMFS, a droplet can only be moved by one cell when actuated. To move a droplet from a starting cell to a destination cell along a path having multiple cells, the droplet needs to be actuated successively. The frequency of this successive actuation is defined as the droplet actuation frequency. The average droplet speed is defined as the total time taken by the droplet to travel the total distance between the start and destination cells. The study of transient response of a moving droplet in a feedback control system will be helpful in determining the actuation frequency and average droplet speed. Information on droplet position can help in detecting the malfunction of any particular bioassay operation (e.g. mixing) and the presence of faulty cells which are defined as the cells failing to actuate droplets further because of manufacturing flaws and degradation of materials. For example, if a droplet is stuck between two cells, this might indicate the presence of a faulty cell and the exact position of the droplet will be useful in identifying the faulty cell and thus saving those sample/reagent droplets which were programmed to use the cells now identified as faulty.

Droplet position can be sensed by using the visual feedback from a camera which must be capable of working at a high frames per second and a reasonably good resolution to detect the interface of the droplet (Gong and Kim, 2006). However, this method requires a transparent plate in a closed system and a fast image processing for real-time applications. Alternatively, the position of a droplet can be sensed from the electrical signals, such as impedance, resonant

frequency and capacitance (Armani et al. 2005). Sensing of an electrical signal requires integration of no additional device in EWOD-based DMFS or minimum additional device for a DMFS based on other droplet actuation principles. In an EWOD-based DMFS, the same electrodes can be used for both actuation and sensing the droplet. Electrical signals, generating from the system consisting of the electrodes, the droplet and the insulator, change in relation to the position of the droplet. Depending on the mechanism of position sensing, a transfer function may be present in the feedback path. The addition of a transfer function due to the position sensor in the feedback path will change the damping ratio (defined as the ratio of the damping coefficient of the system to its critical damping coefficient) and natural frequency of oscillation (defined as the frequency with which an undamped 2nd order system oscillates when excited by a step input), but both the type and the order of the system will remain unchanged. Clearly, accurate and fast sensing of droplet position in DMFS is essential for closed-loop control. For the demonstration of the basics of the DMFS control system, it is assumed that a position sensor with unity feedback is available for the control system. The closed-loop control block diagram of the position of a droplet moving from its current cell to the adjacent cell is shown in Figure 2.3. The controller shown in Figure 2.3 is a simple proportional gain. It represents the model of the hardware that compares the actual position with command value and generates the driving force for the droplet according to the error signal. The closed-loop transfer function with unity feedback (*H(s) =1*) of this system is given by:

$$G_c(s) = \frac{X(s)}{X_{ref}(s)} = \frac{K/(ms^2+cs)}{1+K/(ms^2+cs)} = \frac{K}{ms^2+cs+K} \tag{2.3}$$

It is noted that the effect of position feedback and proportional gain is similar to adding stiffness to the original system. More precisely, a DMFS with position feedback will resemble a 2nd order dynamic system represented by mass, spring and damper. Depending on the values of $m$, $c$ and $K$, the dynamic response of the system can be evaluated in terms of percentage overshoot, rise-time and settling time that play an important role in the performance of a DMFS. For example, the percentage overshoot must be controlled to avoid unintentional mixing between two droplets. The later can be a common control problem since a droplet residing in one cell may also cover a certain portion of adjacent cells due to variation in the dispensed droplet volume from the reservoir. To understand the effect of overshoot on the bioassay operation let us consider two droplets A and B in the two dimensional array (7×5) of cells shown in Figure 2.4. Droplets A and B are commanded to move from cell $(x_6,y_4)$ to cell $(x_5,y_4)$ and from cell $(x_2,y_4)$ to cell $(x_3,y_4)$, respectively. In moving multiple droplets simultaneously, fluidic constraints must be maintained at all times in order to avoid unintentional merging of two or more droplets (Griffith 2005). The

fluidic constraints say that both the current and next destination cell of a droplet must have all the adjacent cells empty. Therefore, the two movements mentioned above are permissible as there will be one empty cell between the new positions of the two droplets which are shown by dotted circles. If the overshoots of the droplets are large enough, their front end may come into contact. This will lead to inaccurate results of the chemical/biological analyses involving droplets A and B if their mixing is prohibited.

The rise-time and settling-time are also important in determining the average speed of droplet motion which in turn affects the overall throughput of the DMFS. In case of successive displacement of a droplet in one direction, which is the case for droplet C in Figure 2.4, the frequency of droplet actuation can be related to the rise-time in order to achieve maximum possible droplet speed for given values of other system parameters. When a droplet needs to change the direction of motion, as is the case for droplet A in Figure 2.4, it must be actuated only after the acceptable settling time has elapsed. If the droplet is actuated before acceptable settling time the droplet may have excessive inertia in the direction of motion. As the actuation force is applied in a transverse direction, the droplet may follow an unpredictable trajectory. This combined effect of droplet momentum in one direction and actuation force in a perpendicular direction can be avoided by actuating the droplet only after acceptable settling time. Thus, the droplet A in Figure 2.4 must be actuated to move from cell ($x_5$,$y_4$) to cell ($x_5$,$y_5$) only after the settling time has elapsed since it started from cell ($x_6$,$y_4$).

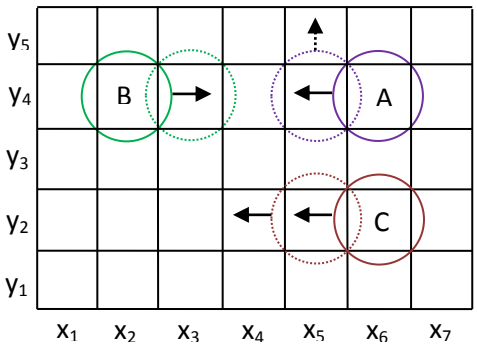

Figure 2.4: The effect of transient response in droplet motion.

### 2.1.2 Detailed Model of Droplet Dynamic System:

In developing the block diagrams and transfer functions of open-loop and closed-loop droplet position control systems it is assumed that the resistive force against droplet motion can be modeled by viscous damping where the resistive force is proportional to velocity. The coefficient of friction, *c*, used in the transfer functions in Equations 2.2 and 2.3, is the constant of proportionality. However, previous analytical and experimental study suggests that the resistance

to droplet motion results from different sources. The three sources of resistance reported in the literature (Ren et al. 2002, Bahadur and Garimella 2006) are (i) viscous dissipation inside the droplet, (ii) viscous drag due to droplet moving through filler-fluid, and (iii) slippage of contact-line (between the droplet and hydrophobic surface). These resistive forces can be nonlinear functions of velocity and time-dependent due to the change in fluidic properties arising from microfluidic operations, cross-contamination and deterioration. These three sources of resistance are used to estimate the total resistance to droplet motion only and research on developing the exact model of the underlying physics is still ongoing. Moreover, uncertainties in droplet motion and positioning, resulting from surface imperfection and variations in dimensions of material layer introduced at the fabrication and assembly stage, cannot be modeled. The purpose of a closed-loop control of droplet position is to compensate for the imperfections in the device and the error in modeling. However, addition of such a controller to the DMFS will increase the cost significantly and the feasibility of having a controller should be studied considering the application of the DMFS. A general purpose DMFS where the precise positioning and tracking of individual droplets are not crucial may not have a closed-loop controller for droplet position. On the other hand, a DMFS has the potential to be used as a high throughput and highly sensitive lab-on-a-chip (e.g., in drug discovery) where the investment of a robust controller for droplet position can be economically justified.

In this study, the models of the resistive forces proposed in the literature (Ren et al. 2002, Bahadur and Garimella 2006, Berthier et al. 2007, Chen and Hsieh 2006) are used to analyze and simulate the transient response of a droplet. The total plate shear force (assuming a parabolic velocity profile far from the liquid-liquid interface) is approximately modeled by (Bahadur and Garimella 2006, Yuh et al. 2006)

$$F_d = \left(\frac{6\mu_d U}{D}\right)(2\pi r^2) \tag{2.4}$$

where, $D$ is the spacing between the upper and lower plate, $r$, $\mu_d$ and $U$ are the droplet radius, viscosity and velocity, respectively. This assumption may not represent the exact flow pattern inside the droplet, but considering the fact that in a typical DMFS the plate separation is much smaller compared to droplet diameter, the above model serves as a good approximation for lumped parameter study of droplet dynamics (Kuo et al. 2003). In addition, experiments on EWOD-based DMFS revealed that plate shear force accounts for a smaller fraction of the total resistive force (Ren et al. 2002). Under the assumption that droplet as a rigid body is moving through filler fluid, the viscous drag is estimated by

$$F_f = \frac{1}{2}\left(C_D \rho_f U^2\right)(2rD) \tag{2.5}$$

where $C_D$ is the drag coefficient of a cylinder in a cross-flow and $\rho_f$ is the density of filler fluid. In general, for low Reynolds number ($R_e = \frac{\rho_d UL}{\mu_d} < 10^3$) flows,$C_D$ is a function of $\frac{1}{R_e}$, and for moderate Reynolds number flows ($10^3 < R_e < 10^5$), $C_D$ remains relatively constant (Munson et al. 2008). The contact-line friction is modeled by

$$F_c = \zeta U(4\pi r) \tag{2.6}$$

where $\zeta$ is the coefficient of contact-line friction defined in molecular kinetics and *n* varies from 0 to 2 (Chen and Hsieh 2006). The contact-line friction accounts for a larger fraction of the total friction force (Ren et al. 2002). Chen and Hsieh (2006) and Kuo et al. (2003) found that the model without considering contact-line friction overestimates the motion. Hence, an accurate model of the contact-line friction is necessary for the prediction of droplet dynamic behavior. In many studies, a linear relationship between the contact-line friction and droplet velocity could adequately verify experimental results (Ren et al. 2002, Chen and Hsieh 2006). In this paper, we also use the linear relationship in simulating droplet motion. It can noted that, for a certain range of Reynolds number ($R_e < 10$), $C_D$ can be a linear function of $\frac{1}{R_e}$ making the $F_f$ linear with *U*. Under this special condition, the total resistive force to droplet motion will be a linear function of droplet velocity and an exact solution of the droplet response can be derived.

The contact angle hysteresis, defined as the difference between the advancing and receding contact angle of a droplet in motion, is another factor that needs to be considered in order to model the droplet motion accurately. This implies that a portion of the driving force is used to overcome the contact angle hysteresis and below this threshold of force a droplet cannot be moved (Berthier et al. 2007). Thus, the equation of droplet motion, in a DMFS based on a general actuation mechanism, can be written as

$$m\frac{d^2x}{dt^2} = F_{dr} - F_{thresh} - F_d - F_f - F_c \tag{2.7}$$

where $F_{thresh}$ is the threshold of driving force. Although equation 2.7 represents the approximate dynamic model of a droplet in a general DMFS, the exact model may have additional terms specific to the actuation method. For instance, the total actuation force on a droplet in an EWOD-based DMFS is the resultant of the force acting on the tri-phase contact-line and that acting on the interface between the droplet and medium. The total force depends on the conductance and permittivity of the droplet and the magnitude and frequency of the applied voltage. The deviation of the droplet from circular shape (i.e., reduction of contact-angle on the advancing side) due to the energy stored in the droplet-insulator interface and the effect of the release of that energy upon withdrawal of voltage may be neglected considering their weaker influences. As droplets in a typical DMFS flow with low $R_e$, the scaling law suggests that the inertial effect of the droplet is

not dominant. However, consideration of droplet mass is not unusual for the analysis of transient and steady-state responses of a system modeled in terms of lumped parameters (Bahadur and Garimella 2006). The oversimplified model, derived by ignoring the droplet mass, may result in inaccurate estimation of parameters characterizing the dynamic response. For example, Kuo et al. (2003) have reported significant overshoot of a droplet driven by electrowetting force that can only be explained by the effect of the inertial force. The overshoot and the associated oscillations of the droplet result in a longer settling time. However, the calculated settling time using the droplet dynamic model without the mass term will result in a shorter time.

The block diagram of the closed-loop control of the droplet position considering the detailed resistances to motion is similar to Figure 2.3 except that the transfer function is replaced by a subsystem called 'Droplet'. Figure 2.5 shows the details of the subsystem 'Droplet' defined based on the nonlinear dynamics of droplet motion defined by equation 2.7.

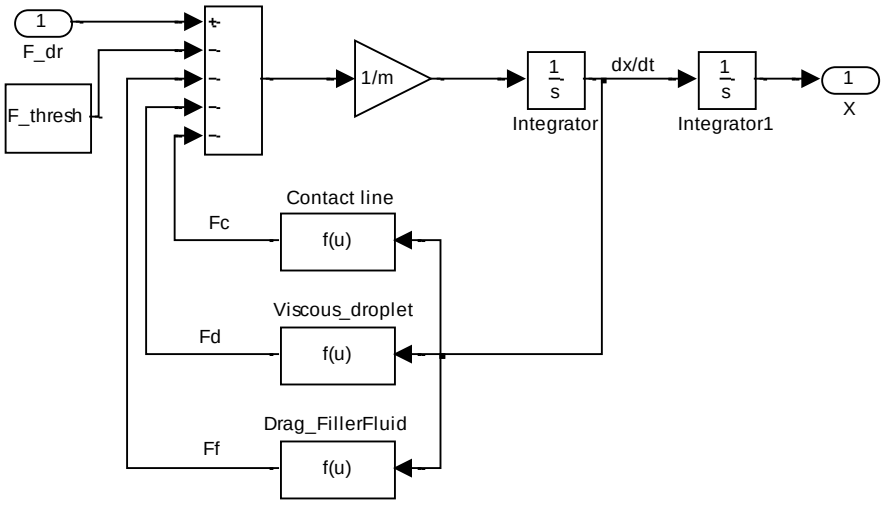


Figure 2.5: The 'Droplet' subsystem using resistive forces proposed in the literature.

### 2.1.3 Simulation Results and Discussion:

The dynamic response of a droplet can be obtained numerically by solving the differential equation of motion. For the present study, the dynamic response of the closed-loop position control system is simulated using SIMULINK®. It is assumed that the footprint of a droplet on both the top and bottom plate remains circular from the start to the end of motion and that the radius of the circular footprint is slightly greater (assumed 5%) than the half-length of a cell so that a droplet also overlaps the adjacent cells. Droplet mass, *m*, can be estimated by that of a cylinder with height equal to the plate spacing. Although the governing equation of droplet

motion is nonlinear, we make no attempt to design a controller for this system. Instead, this paper focuses on the necessity of feedback control and the effect of transient and steady-state responses on the performance of a DMFS. That is why a simple proportional controller is used in the simulation. The value of proportional gain can be adjusted to achieve desired transient response. Simulation is performed using ODE45 solver with a maximum step-size of 0.0001 and an absolute tolerance of 0.0001. The input to this system is a step command for position which is equal to the electrode pitch and is applied at the start of simulation. The position of the centre of the droplet is the output of the system. The geometric and fluidic parameters used in the simulation are summarized in Table 2.1. The droplet (water with 0.1 M KCl) and filler fluid (silicone oil) considered here are those used in the experiment performed by Pollack et al. (2002). The threshold driving force which is related to the contact angle hysteresis is taken to be $5\times10^{-6}$ N (Berthier et al. 2007).

Table 2.1: The values of fluidic, geometrical and other parameters used in simulation.

| | |
|---|---|
| Droplet viscosity, $\mu_d$, (1 μL Water with 0.1M KCL) | $1.9\times10^{-3}$ Pa.s |
| Droplet density, $\rho_d$ | 1000 kg/m$^3$ |
| Filler-fluid (Silicone oil) viscosity, $\mu_f$ | $1.7\times10^{-3}$ Pa.s |
| Filler-fluid density, $\rho_f$ | 760 kg/m$^3$ |
| Electrode (cell) pitch, $L_{nom}$ | $1500\times10^{-6}$ m |
| Plate spacing, $D_{nom}$ | $300\times10^{-6}$ m |
| Surface-tension between droplet & filler, $\gamma_{LM}$ | $40\times10^{-3}$ N/m |
| Coefficient of Drag, $C$ | 30 |
| Contact-line friction coefficient, $\zeta$ | 0.04 N.s/m$^2$ |
| Droplet radius, $r$ (Assuming 5% overlap of adjacent electrodes) | $(L/2) + 0.05(L)$ |
| Droplet mass, $m$; | $1.77\text{x}10^{-6}$ kg |
| Threshold of driving force, $F_{thresh}$ | 5 μN |

The results of simulation for two different values of proportional gain are shown in Figures 2.6-2.7 and are summarized in Table 2.2. The droplet response is similar to a typical 2$^{nd}$ order system. For the given values of fluidic and geometric parameters the system behaves as an underdamped one with the proportional gains of 1 and 10. For this simulation, the rise time is defined as the time taken by the system to attain the command value for the first time. Thus, the simulated rise time can be considered as the earliest time a droplet (e.g., droplet C) can be

actuated to move from its current destination cell (e.g., cell ($x_5y_2$)) to the new destination cell (e.g., cell ($x_4y_2$)). For example, a rise time of 5.659 millisecond (for $K$ = 1) implies that the actuation frequency cannot exceed 177 Hz resulting in a maximum obtainable average droplet speed of 26.55 cm/sec, where the average speed is calculated from dividing cell pitch by the rise time. The droplet speed thus calculated can be used in determining the transportation time for multiple droplets along different paths and consequently the assay completion time as well as optimal scheduling.

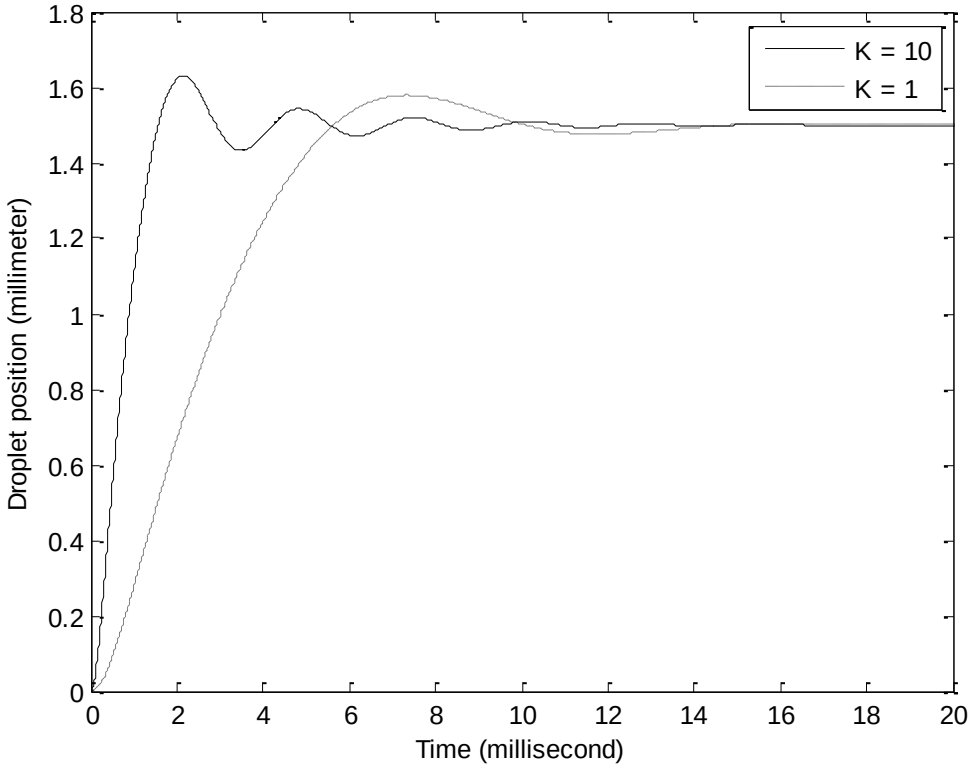


Figure 2.6: Simulation results showing droplet response to a step command.

Table 2.2: Simulation results for two different values of proportional gain.

| Proportional Gain ($K$) | Rise time (ms) | Peak time (ms) | % Overshoot | Settling time (ms) |
|---|---|---|---|---|
| 1 | 5.649 | 7.349 | 5.27 | 12.719 |
| 10 | 1.565 | 2.145 | 8.71 | 6.275 |

The percentage overshoot indicates how close a droplet can get to a nearby droplet while they are not allowed to contact each other. A critical situation arises when two droplets approach

each other, which is depicted in Figure 2.4 where droplets A and B are moved to their new cells simultaneously. From simulation with $K$ = 10, a 8.71% (0.1306 mm) overshoot added to the normal 5% (0.075 mm) overlap results in a total overlap of 13.71% (0.2056 mm) of cell ($x_4$,$y_4$) for droplet A . An equal overlap of 13.71% on the left side of cell ($x_4$,$y_4$) is also caused at the same time by droplet B. Therefore, at the time of peak displacement (i.e., at 2.145 millisecond) of the two droplets, there is a gap of 1.09 mm (72.58% of $L$) between the advancing edges of the droplets A and B. This is safe as far as the unwanted contact between two droplets is concerned. Thus, simulation results provide information on critical parameters which are helpful in identifying unwanted situations within the DMFS.

The settling times (defined as the time required for the response to remain within 2% of the steady-state value) obtained are 9.219 millisecond for $K$ = 1 and 5.195 millisecond for $K$ = 10. If the predetermined path of the droplet is such that there are changes in the direction along which it must move, then sufficient time should be allowed for the droplet to settle down in each destination cell before it is commanded again to move to the next destination cell along the path. The simulated settling time should be used as the period after which another actuation cycle can begin to move such a droplet (e.g., droplet A in Figure 2.4) from its current destination cell (e.g., cell ($x_5y_4$)) to an adjacent destination cell (e.g., cell ($x_5y_5$)). Thus, using the settling times obtained from simulation, the maximum allowable frequencies of actuating a droplet are found to be ~108 Hz and ~192 Hz for $K$ = 1 and $K$ = 10 respectively. The average speeds of a droplet are calculated by dividing the cell pitch by settling time and the speeds are found to be 16.3 cm/sec and 28.9 cm/sec for $K$ = 1 and $K$ = 10, respectively.

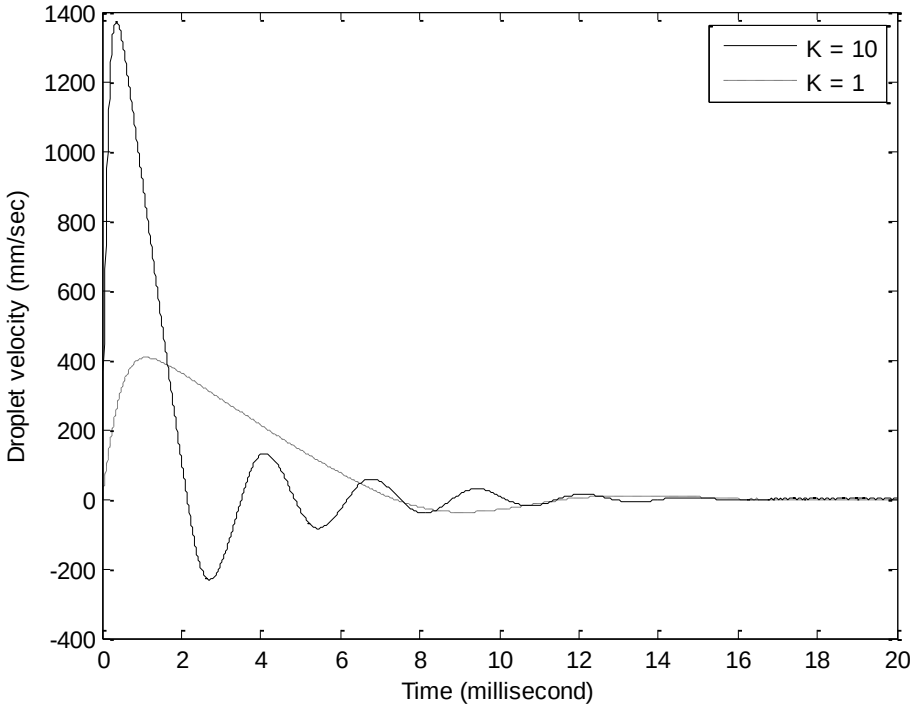


Figure 2.7: Simulation results showing droplet response (velocity) to a step command.

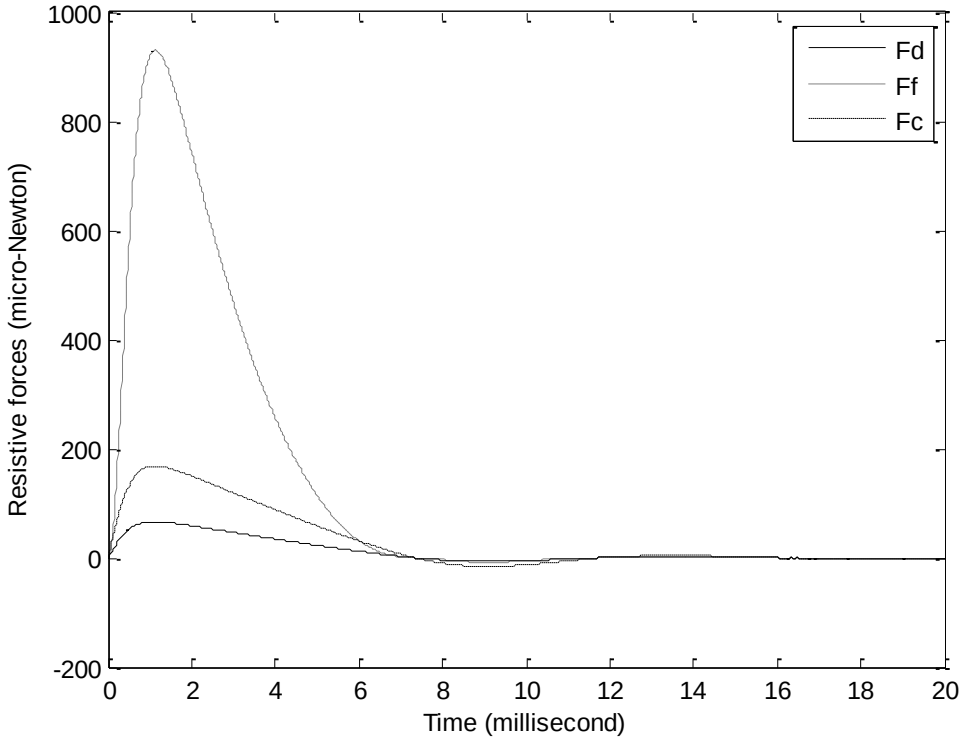


Figure 2.8: Resistive forces against droplet motion.

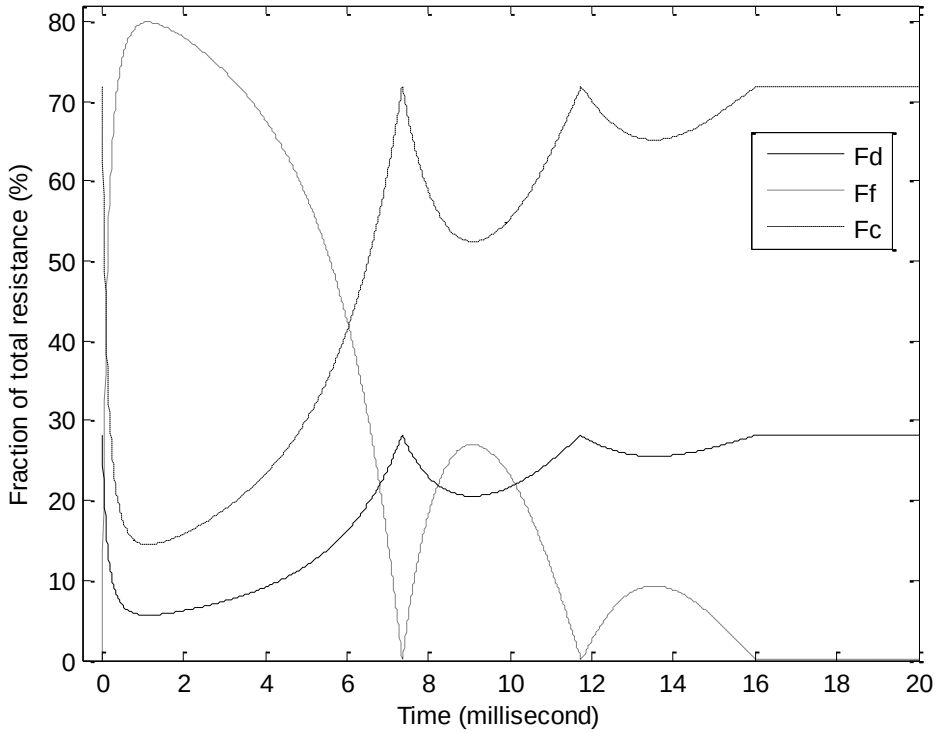


Figure 2.9: Resistive forces as fractions of total resistance.

Figure 2.8 shows the variation of different resistive forces (for K = 1) as the droplet moves to the adjacent cell. Individual resistances as percentages of the total resistive force are shown in Figure 2.9. At very low velocity of the droplet contact-line friction is most dominant (71.85 %) and the drag force due to the filler-fluid is least significant (~0%). As the droplet attains speed, contributions of each of the resistive forces change greatly. After 1.13 milliseconds, the droplet velocity becomes maximal. At this point, the percentage contributions of resistance due to viscous shear, drag and contact-line are 5.67%, 79.88% and 14.46% respectively. The drag force dominates until the droplet reaches the adjacent cell. The contact-line friction starts to dominate again as the droplet speed decreases.

The relation between the dynamic response of a droplet and geometric parameters of the DMFS has been studied. Simulations are performed by varying the electrode size, L (600 μm – 2000 μm), varying the gap between top and bottom plates, D (100 μm – 500 μm) and varying both L and D (200 μm – 600 μm) such that the L/D = 5. The rise time, settling time and percent overshoot are plotted against dimensionless $L' = L/L_{min}$ and $D' = D/D_{min}$ in Fig. 10, 11 and 12 respectively. It is assumed that the droplet radius is 5% greater than the size of the electrode and the droplet is in contact with both the top and bottom plate in each case of the simulation. The

total mass of the droplet and the resistance increase at greater rates with electrode size than with gap between two plates. Thus, the rise time increases at a faster rate with increasing L than with increasing D, shown in Figure 2.10. For similar reasons, the rise time increases at the fastest rate when both D and L are varied. Figure 2.11 shows that the settling time decreases at a higher rate with increasing L due to the fact that as the droplet becomes larger the response approaches that of a damped system. Interestingly, the settling time shows a local minimum for the range of values when both D and L are increased. This can be explained with the help of Figure 2.12 which shows that overshoot decreases at the fastest rate when both D and L are increased. With less overshoot and hence shorter duration of oscillations, the settling time decreases. With D>400 μm and L>2000 μm, the droplet response approaches that of a critically damped system and the settling time starts to increase again.

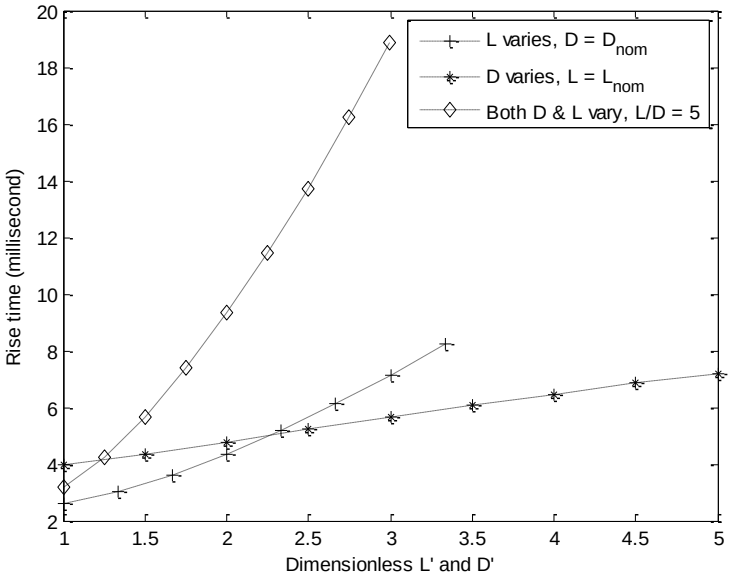


Figure 2.10: Rise time as a function of dimensionless L' and D'; $L'=L/L_{min}$, $D'=D/D_{min}$, $L_{nom}$=1500 μm, $D_{nom}$=300 μm.

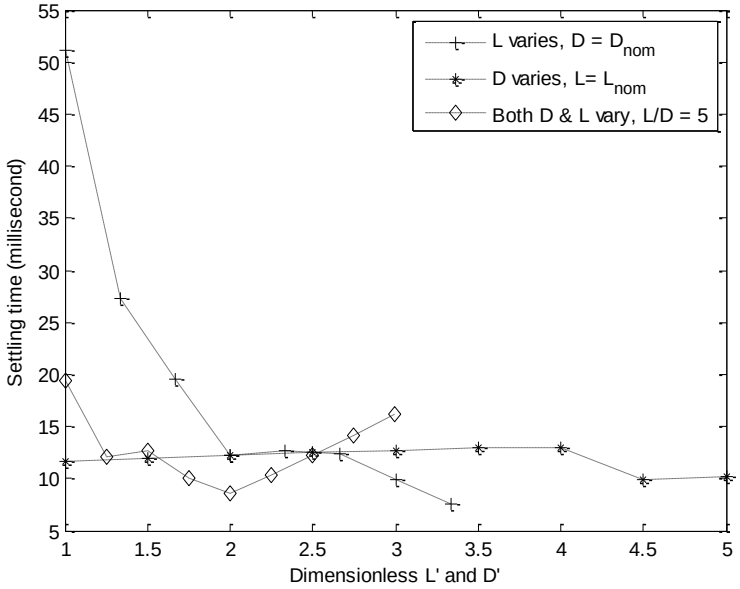


Figure 2.11: Settling time as a function of dimensionless L' and D'; $L'=L/L_{min}$, $D'=D/D_{min}$, $L_{nom}$=1500 μm, $D_{nom}$=300 μm.

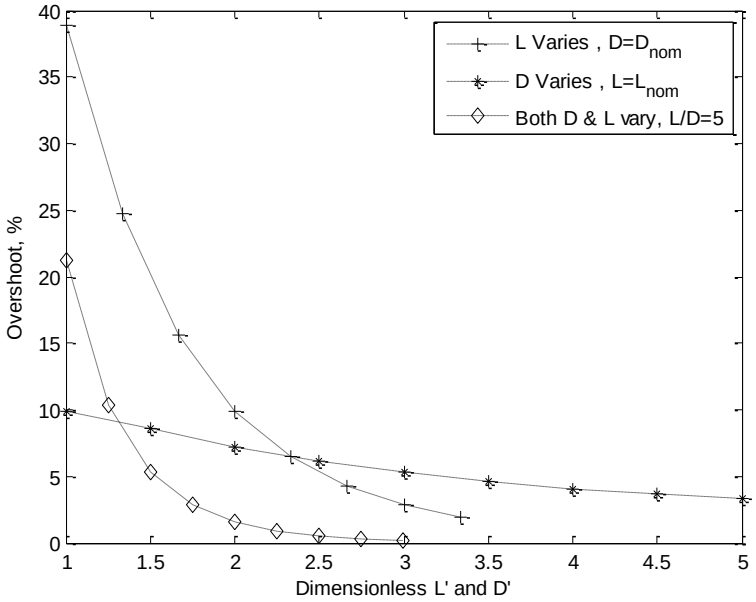


Figure 2.12: Percentage overshoot as a function of dimensionless L' and D'; $L'=L/L_{min}$, $D'=D/D_{min}$, $L_{nom}$=1500 μm, $D_{nom}$=300 μm.

## 2.2 Droplet sensing

Traditional droplet position sensing utilizes both the upper and lower plates to measure the capacitance. This prohibits the integration of any other feature, which might add to the functionality of the DMFS, to the upper plate. The new method of capacitance measurement proposed here relies on the capacitance measurement between the electrodes only on the lower plate.

### 2.2.1 Coplanar capacitance

A schematic of the side view of a droplet positioned between two electrodes is shown in Figure 2.13 (i). Electric field lines between the electrodes in the lower plate and the ground electrode in the upper plate are parallel over the entire area of the electrodes except in a small region near the midpoint. The equivalent parallel plate capacitances are shown in Figure 2.13 (ii).

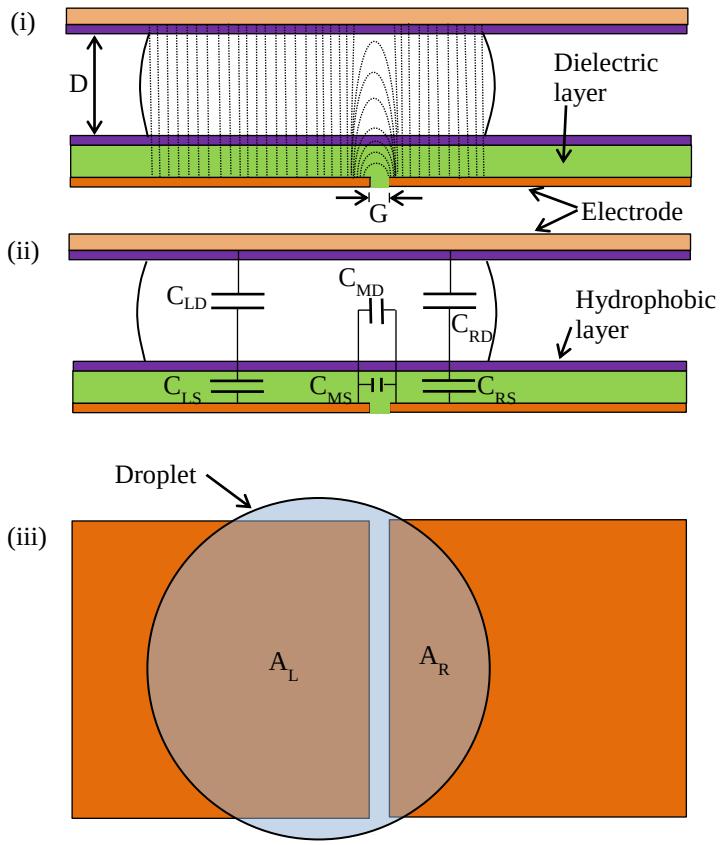


Figure 2.13: Electric field lines, equivalent capacitances and overlapped areas; (i) Electric field lines formed between the coplanar electrodes, (ii) Equivalent parallel plate capacitances, (iii) Top view of the droplet, showing areas of overlap on the two coplanar electrodes.

Electric field lines originating from a small region of one electrode near the midpoint in the corresponding region of the other electrode. The equivalent capacitances due to these elliptic field lines inside the liquid and the solid dielectric layer, identified as $C_{MD}$ and $C_{MS}$, are typically less than a picofarad. The total capacitance of the dielectric layer and the droplet between the two coplanar electrodes in lower plate is given by

$$C_{meas} = C_{eq} + C_{MD} + C_{MS} \tag{2.8}$$

where $C_{MD}$ and $C_{MS}$ are the equivalent capacitances due to the elliptic field lines in the droplet and the solid layer, respectively; $C_{eq}$ is the equivalent capacitance of the series connected capacitances $C_R = \frac{C_{RS}C_{RD}}{C_{RS}+C_{RD}} = \frac{\varepsilon_0\varepsilon_S\varepsilon_D A_R}{\varepsilon_D t_S+\varepsilon_S D}$ and $C_L = \frac{C_{LS}C_{LD}}{C_{LS}+C_{LD}} = \frac{\varepsilon_0\varepsilon_S\varepsilon_D A_L}{\varepsilon_D t_S+\varepsilon_S D}$; $\varepsilon_S$ is the equivalent relative permittivity of solid layers, $\varepsilon_D$ is the relative permittivity of the solid layer, $t_S$ is the total thickness of the solid layers, $D$ is the height of the droplet; $A_R$ and $A_L$ are the areas of overlap on the right-side and left-side electrodes respectively. $C_{eq}$ is given by

$$C_{eq} = \frac{\varepsilon_0\varepsilon_S\varepsilon_D}{\varepsilon_D t_S+\varepsilon_S D}\left(\frac{A_R A_L}{A_R+A_L}\right) = \frac{\varepsilon_0\varepsilon_S\varepsilon_D}{\varepsilon_D t_S+\varepsilon_S D}(A_R + A_L)\left(f_{AR} - {f_{AR}}^2\right) \tag{2.9}$$

where $f_{AR} = \frac{A_R}{A_R+A_L}$ is the overlap area on the right-side electrode normalized by the total area of overlap. Theoretically, the values of $f_{AR}$ can range between 0 and 1, corresponding to the droplet positions at the centers of the left-side and the right-side electrodes. In practical situations, however, the droplet is usually large enough to have non-zero values of $A_R$ and $A_L$ at the initial and final position, and hence $0 < f_{AR} < 1$. The capacitance, $C_{eq}$, is a quadratic function of the area fraction, $f_{AR}$, and has the maximum value at $f_{AR} = 0.5$ corresponding to the droplet positioned at the midpoint between the two coplanar electrodes. As the droplet moves away from the midpoint towards either direction, the value of capacitance decreases. Equation (2.9) shows that $C_{eq}$ varies linearly with the total overlap area on the coplanar electrodes. A larger droplet will form larger capacitance than a smaller droplet. It should be noted that due to the circular or elliptic shape, as observed in top-view, of the droplet, the total overlap area is not constant for the whole duration of translocation from one electrode to the adjacent one. The total overlap area remains constant except for the beginning and final parts of the travel distance equal to the length of initial droplet overlap on the adjacent electrodes. A droplet with smaller height generates higher capacitance since $C_{eq}$ is inversely related to droplet height.

### 2.2.2 Numerical investigation

Three dimensional finite element analyses were performed in COMSOL® to investigate the variation of capacitance between two coplanar electrodes. Geometry of the model included

two electrodes, each 1.4 mm × 1.4 mm, the dielectric layer of thickness 1.23 μm and the droplet. These dimensions are chosen to represent those of a DMFS used in experiments. The inter-electrode gap is adjusted depending on the type of investigation. A portion of the electrode on each side of the two sensing electrodes is also incorporated so as to model the actual device more closely. Along the transverse direction, the dielectric layer is extended sufficiently beyond the droplet-air interface. In all simulations, the diameter of the cylindrical droplet of deionized water is 1.6 mm. The error in the capacitance due to the assumption of a $90^o$ contact angle is expected to be insignificant, since the dynamic contact angle during droplet motion typically varies from ~$80^o$ to ~$110^o$. Since the thickness of the hydrophobic layer in typical designs is an order of magnitude lower than that of the dielectric layer in the lower plate, the hydrophobic layer is not modeled separately to avoid complexities in mesh generation. However, the relative permittivity of the dielectric layer is set equal to the equivalent permittivity calculated by considering the individual capacitances of cyanoethyl pullulan ($\varepsilon_r = 20$) and Teflon® connected in series. Moreover, the Teflon layer in the upper plate was neglected since the capacitance of this layer can also be considered as connected to the dielectric layer in series and the equivalent permittivity was assigned to the dielectric layer in the computational model. The capacitance between the coplanar electrodes is obtained by defining the governing physics as electrostatics and solving for the electric field distribution in the computational domain according to

$$-\boldsymbol{\nabla}\varepsilon_0\varepsilon_r\boldsymbol{E} = \rho_f \tag{2.10}$$

where $\varepsilon_0$ and $\varepsilon_r$ are the permittivities of vacuum and material respectively, $\rho_f$ is the free charge per unit volume, and $\boldsymbol{E} = \boldsymbol{\nabla}$V is the electric field and V is the electric potential. The boundary conditions for the internal surfaces between two different materials are set to continuity of electric displacement field, $\boldsymbol{D} = \varepsilon_0\varepsilon_r\boldsymbol{E}$. The coplanar electrodes for the computation of capacitance are defined as ports while the other electrodes are set to floating potentials. Likewise, the upper surfaces of the droplet and the surrounding medium are set to floating potentials implying that these surfaces attain virtually the same potential as that of the electrode in the upper plate. A zero charge boundary condition, defined as $\hat{n}.\boldsymbol{D} = 0$, is set for each of the outer surfaces of dielectric materials. The capacitance between coplanar electrodes is calculated according to

$$C = \frac{2U_e}{V^2} \tag{2.11}$$

where V is the potential difference between the electrodes and $U_e$ is the electrical energy stored in the domain. COMSOL® calculates the stored energy according to

$$U_e = 0.5\ \varepsilon_0\varepsilon_r\int_\Omega|\boldsymbol{E}|^2 d\Omega \tag{2.12}$$

where $\Omega$ denotes the entire computational domain in the model.

Capacitances were computed for droplet positions at 100 µm increments in either direction from the midpoint between the coplanar electrodes. Figure 2.14 shows the values of coplanar capacitance obtained from simulation as well as from Equation 2.9 as a function of the fraction of overlap area on the right-side electrode. Results verify that coplanar capacitance is indeed a quadratic function of the overlap-area fraction. In addition, the capacitances are significantly lower for a droplet of 80 µm height than those for a droplet of 40 µm height. The capacitances calculated using the analytical model follows closely the trend of those from a finite element analysis, yet the analytical model fails to capture a small portion of the total capacitance corresponding to the contributions of fringe fields in the droplet and in the dielectric layer between the coplanar electrodes. The value of capacitance, unexplained by the analytical model, ranges from ~400 fF to ~650 fF. The effect of inter-electrode gap was also investigated and the results are shown in Figure 2.15 for three inter-electrode gaps while the droplet height was kept constant at 80 µm. The coplanar capacitance is increased when a narrower gap between the electrodes is used. This is evident more in the results obtained from the numerical analysis than those from the analytical model. A 14% increase in the total capacitance is achieved by reducing the gap from 145 µm to 20 µm. The major contribution in this change is from the capacitances corresponding to the fringing electric field lines. Since these capacitances are not accounted for in Equation 2.9, the change in capacitance due to change in inter-electrode gap is significant only when the droplet is near the midpoint between the electrodes. This change in capacitance

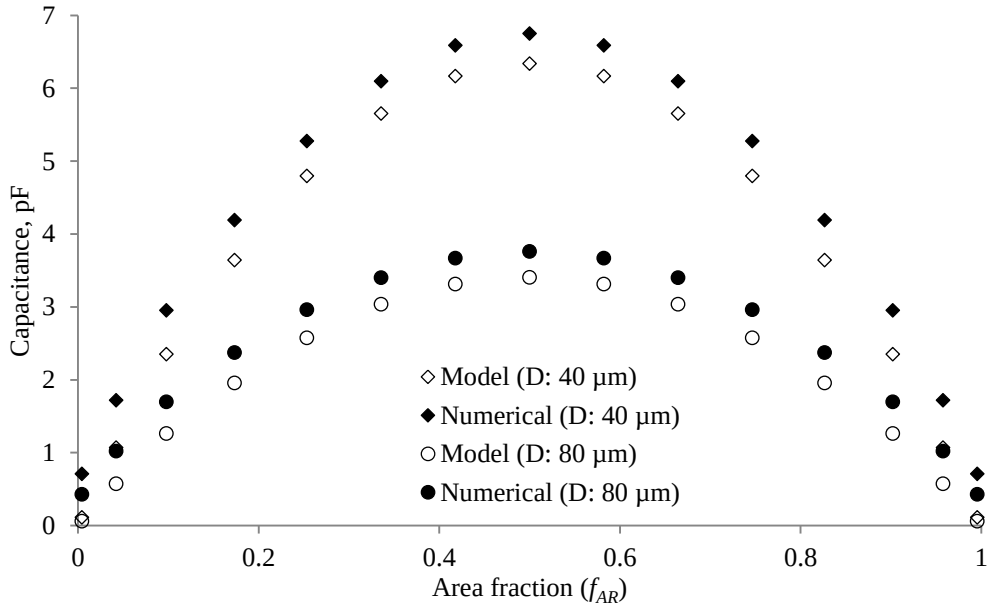


Figure 2.14: Capacitance between coplanar electrodes for two droplet heights

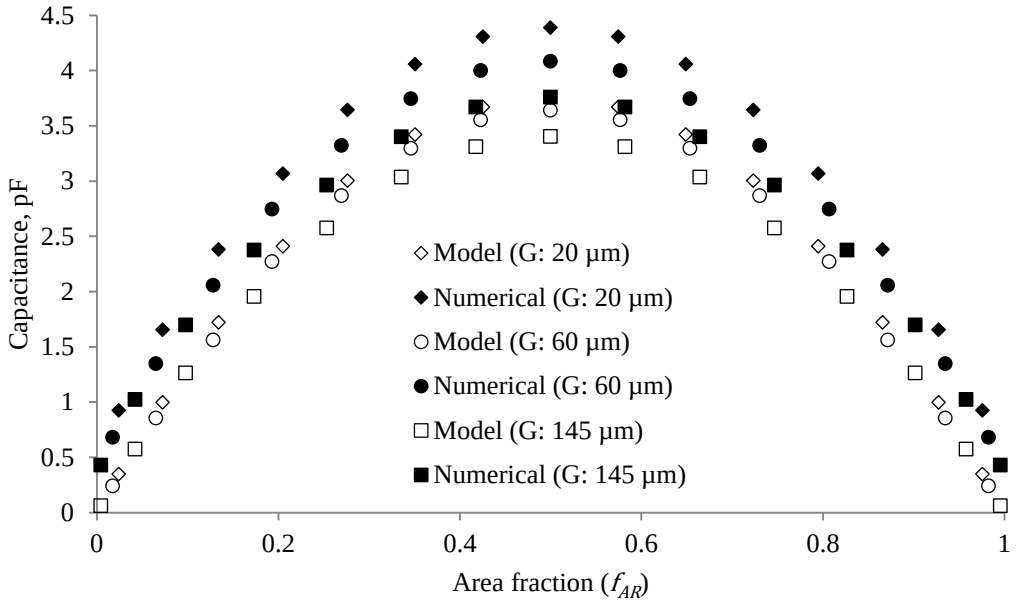


Figure 2.15: Capacitance between coplanar electrodes for three inter-electrode gaps

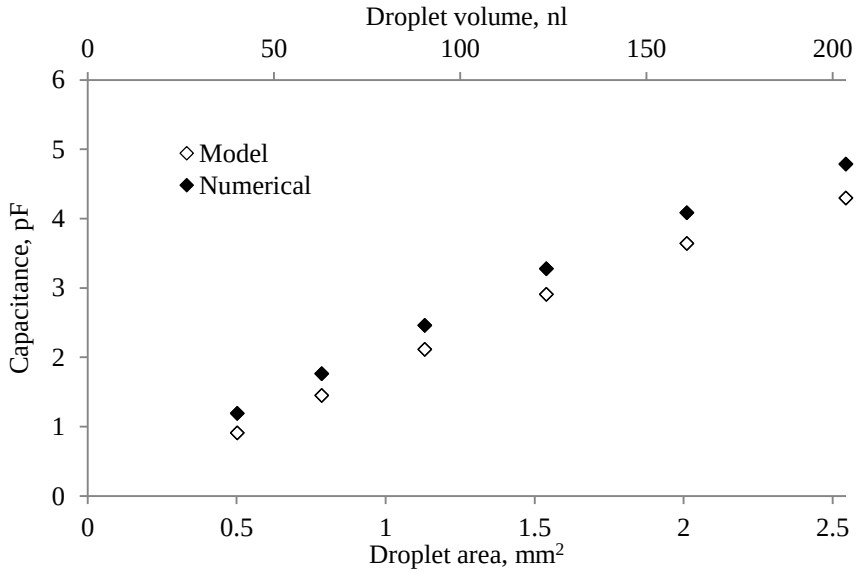


Figure 2.16: Maximum capacitance between coplanar electrodes in a DMFS with inter-electrode gap of 60 µm and droplet height of 80 µm.

originates from the increase in the total overlap area as a result of a smaller gap. The dependence of coplanar capacitance on the total area of droplet overlap on the adjacent electrodes is illustrated in Figure 2.16. Coplanar capacitances were computed for droplets of different volumes by positioning them at the midpoint between the electrodes. Simulations were performed

considering an inter-electrode gap of 60 µm and a droplet height of 80 µm. Results verify that the maximum capacitance between two coplanar electrodes increases with droplet size. However, the change in maximum capacitance occurs at a high rate for droplets with diameters smaller than the electrode size.

### 2.2.3 Experimental

#### 2.2.3.1 Sensing electronics

Capacitance measurement was performed by counting the resonant frequency of an oscillator. The stable and sensitive oscillator circuit was formed by three Schmitt trigger inverters out of the six in a MM74HC14N IC, two 2 KΩ resistors and the capacitance formed between the coplanar electrodes. The frequency of oscillation with 50% duty cycle is given by (Fairchild Semiconductor Corporation)

$$f_{meas} \cong \frac{0.559}{RC_{meas}} \tag{2.13}$$

Thus, the capacitance of the system can be calculated based on the knowledge of the resonant frequency and the resistor. The IC was connected to a 5 Vdc output from a PXI 4110 power supply and the frequency was measured through the PXI 6224 data acquisition (DAQ) system, shown in Figure 2.17. The sampling time and the number of samples for the counters in the DAQ

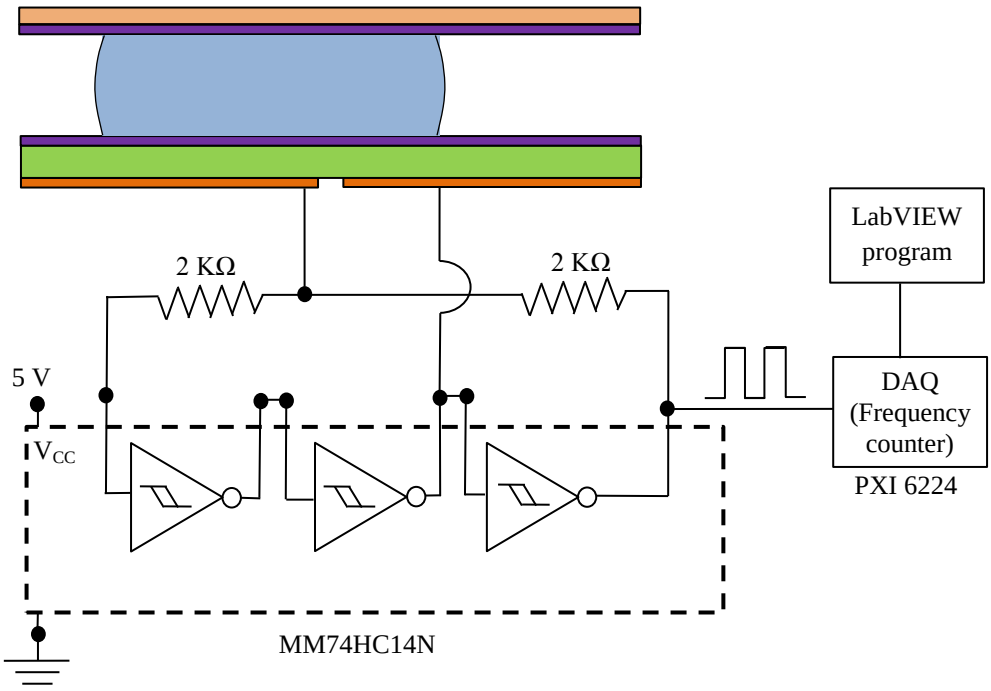


Figure 2.17: Schematic diagram showing the capacitance measurement circuitry

were configured through a LabVIEW program. Figure 2.18 shows the experimental setup used to verify the efficacy of the proposed sensing method. Droplets of the desired volume were dispensed at appropriate positions using the PipeJet P9 Nanoliter Dispenser. Images of droplets were acquired using HiSpec 5 monochromatic camera with a resolution of 1696 × 1710 and each pixel is 8 µm × 8 µm. The areas of overlap on the side electrodes were calculated through image analysis in MATLAB. In each top-view image of the, the meniscus was identified first and then the total number of pixels were calculated. The accuracy of meniscus detection in MATLAB was 1~2 pixels, determined by enlarging the region of the image containing the meniscus, corresponding to a lateral accuracy of 4~8 µm considering the magnification by the lens. This results in an error less than 2% in the calculation of overlap area.

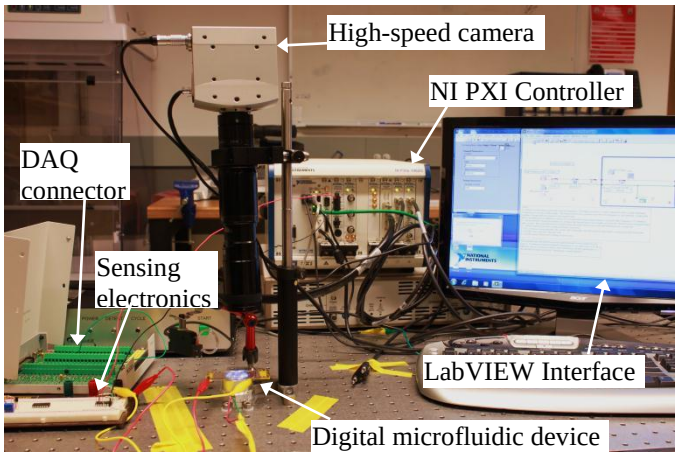


Figure 2.18: Photograph of the experimental setup for capacitance measurement

### 2.2.3.2 Results

Investigation of the capacitance between coplanar electrodes was performed on DMFS fabricated following the procedure as outlined in chapter 5. Droplets of approximately equal volume were deposited using the droplet dispenser at various positions between two adjacent electrodes, shown in Figure 2.19. Figure 2.20 shows the capacitance measured in a DMFS with a gap of 40 µm between the upper and lower plates. The values of capacitance shown are obtained by subtracting the parasitic capacitance from the capacitances measured in presence of droplets. The parasitic capacitance results from the capacitances between the connecting wires, the electrodes and the neighboring substances and the capacitance due to the dielectric layer in the inter-electrode gap. Results verify Equation 2.9 that the coplanar capacitance is a quadratic function of the fraction of overlap of the droplet. A maximum value of ~ 18 pF results when the droplet is at the midpoint between the adjacent electrodes. Although the variability in experimental data is quite high, the dominant characteristic of data can be explained by the

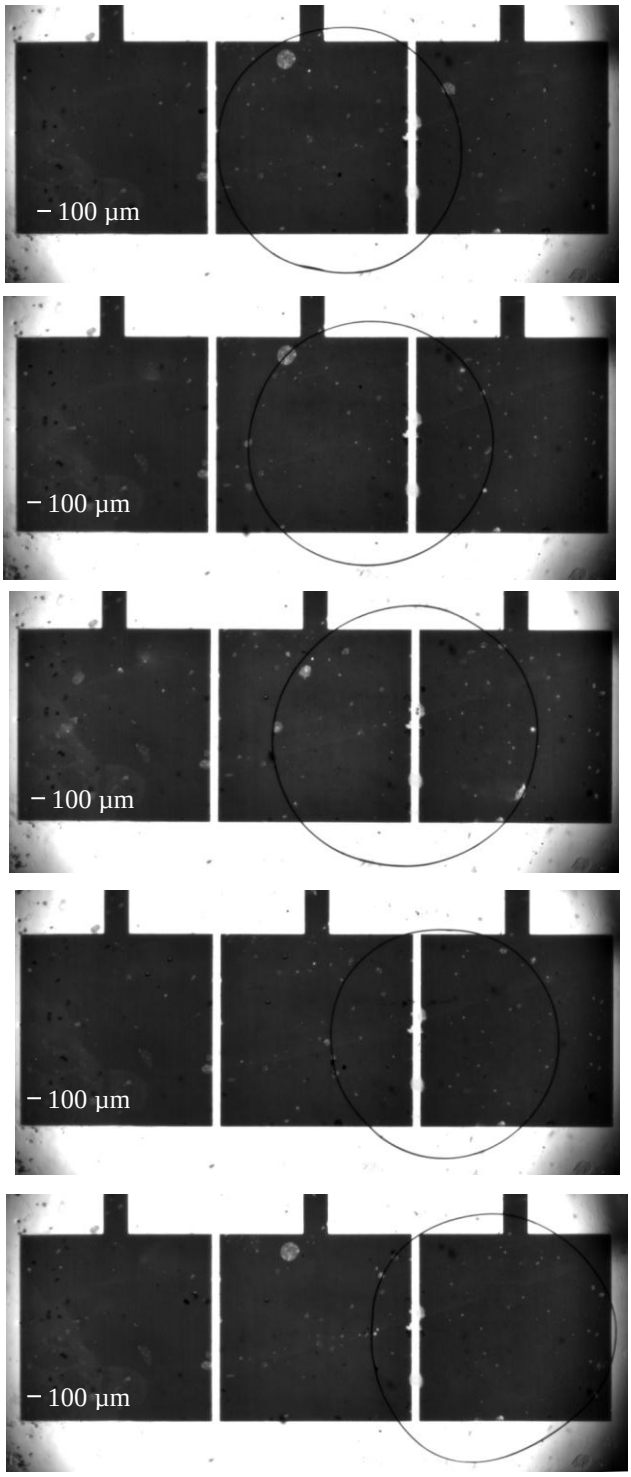


Figure 2.19: Images of droplet at five different positions between the two adjacent coplanar electrodes connected to measure capacitance. Electrode size: 1.4 mm × 1.4 mm, Inter-electrode gap: 60 µm, Droplet height: 80 µm.

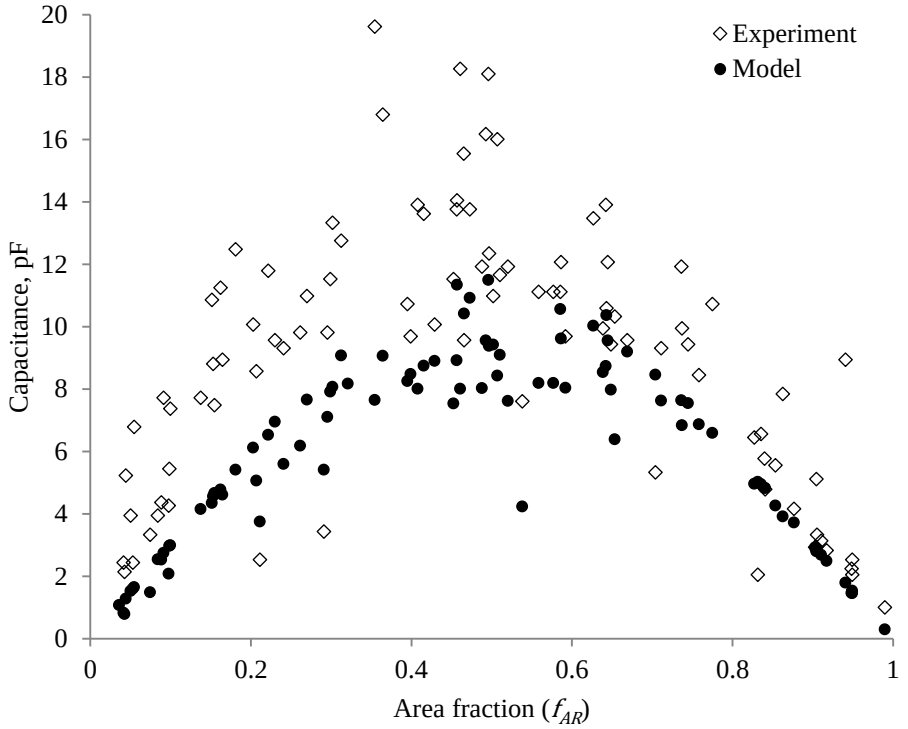


Figure 2.20: Measured capacitance in a DMFS with 40 μm gap between the upper and lower plates.

analytical model given by Equation 2.9. The capacitances obtained from the analytical model were calculated based on the overlap areas in the images corresponding to the experimental data points. As expected, the variability of data obtained from the analytical model is low compared to that of the experimental data. The capacitance measurement is highly sensitive to the tolerance of circuit elements, imperfections in material property as well as geometry of the device and noise from the environment external to the active area of measurement. In a microdevice involving a droplet of volume less than a microliter, the capacitance measurement is especially sensitive to the condition of the instrumentation as well as of the device, and the measurement is more susceptible to noise. As such, variations were unavoidable even though the setup was prepared according to guidelines for minimizing measurement error. The measured frequency often varied within a few seconds even though the position of the droplet was not changed. This variation was not always unidirectional disproving the reasoning that only the reduction of volume due to evaporation results in the change in system capacitance. Although evaporation could affect the measurements, a significant change in the resonant frequency due to evaporation in our device required a much longer period than a few seconds. Moreover, the variations in experimental data originated from those of dispensed volumes of droplets. Investigation of the effect of increasing

the droplet height was conducted by measuring the capacitances at different droplet positions between the coplanar electrodes. It is worth mentioning that the scatter in data points for the model originates from the fact that measured capacitance depends on the volume of the droplet. This means that droplets of different sizes will result in different capacitances even though the overlap area-fractions are equal. Figure 2.21 shows the capacitances measured for a droplet height of 80 µm along with those obtained from analytical model. The measured values of capacitance are significantly lower than those for a device with a plate gap of 40 µm. The analytical model results in overestimated values of capacitance which indicates the possibility of a limit of droplet height within which the analytical equation is applicable. The experimental data shows skewness with maximum capacitance corresponding to droplet position at an offset from the midpoint. The most probable source of this skewness is the gradual decrease in the thickness of the dielectric layer over the right-side electrode. Since the dielectric layer was deposited by spin coating, the thickness of the layer was not uniform all over the device surface. However, the variability of data points is lower than that for 40 µm plate spacing.

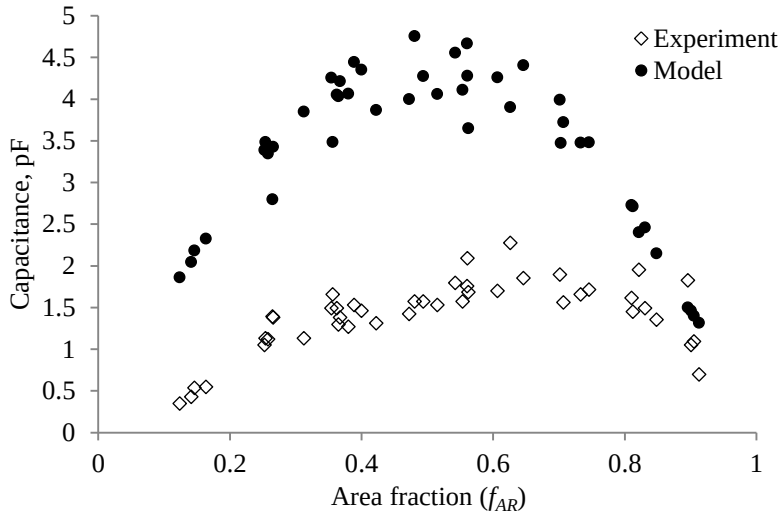


Figure 2.21: Measured capacitance in a DMFS with 80 µm gap between the upper and lower plates.

The relation between coplanar capacitance and the size of the droplet was studied by depositing droplets of different volume at the midpoint between the electrodes, shown in Figure 2.22. The measured capacitances of droplets of different volume are shown in Figure 2.23 to verify the dependence of capacitance on the total area of overlap on the electrodes. Droplets were positioned at the midpoint between the coplanar electrodes having an inter-electrode gap of 60 µm while the gap between the upper and lower plates was fixed at 80 µm. Results validate the

theory, as discussed in previous sections, that the capacitance between the coplanar electrode for a given position of the droplet is linearly dependent on the total area of overlap. In other words, the value of maximum capacitance corresponding to the droplet at midpoint is higher for larger droplets. It is worth noting that obtaining the accurate value of the maximum capacitance is quite difficult by placing the droplet manually at the midpoint. Any misalignment of the droplet with respect to the midpoint results in a capacitance lower than the maximum value. The maximum value of capacitance increases with the total droplet area at a high rate until up to ~1.5 $mm^2$. For droplets having diameters greater than the size of an electrode, the droplet overlap area increases at a lower rate owing to larger radii of curvature.

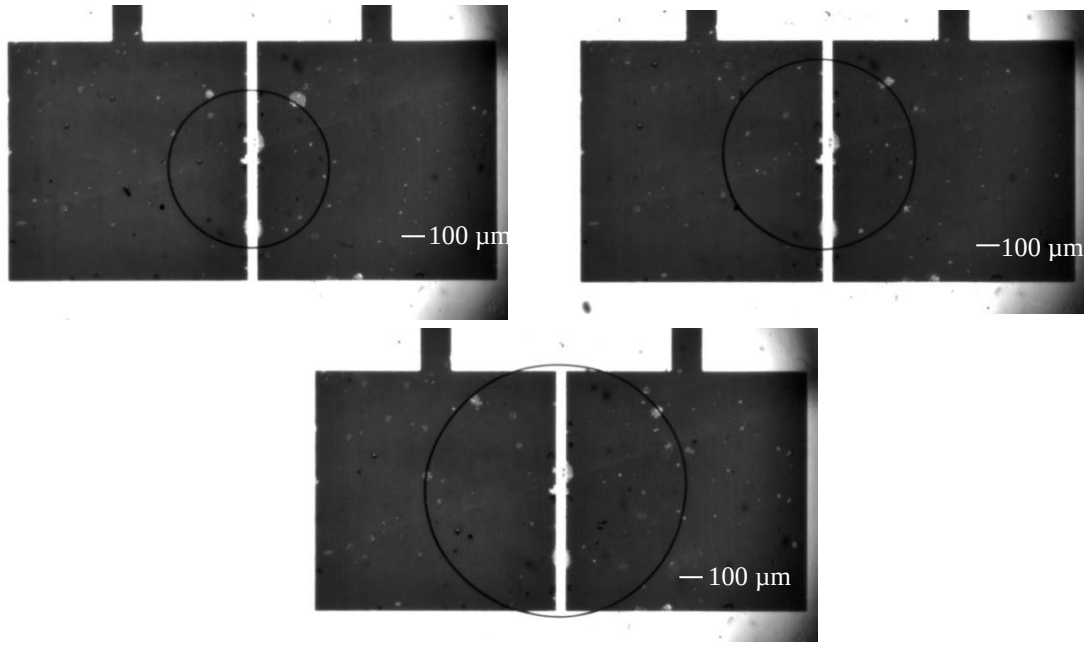


Figure 2.22: Droplets of different volumes placed at the center of two coplanar. Electrode size: 1.4 mm × 1.4 mm, Inter-electrode gap: 60 µm, Droplet height: 80 µm.

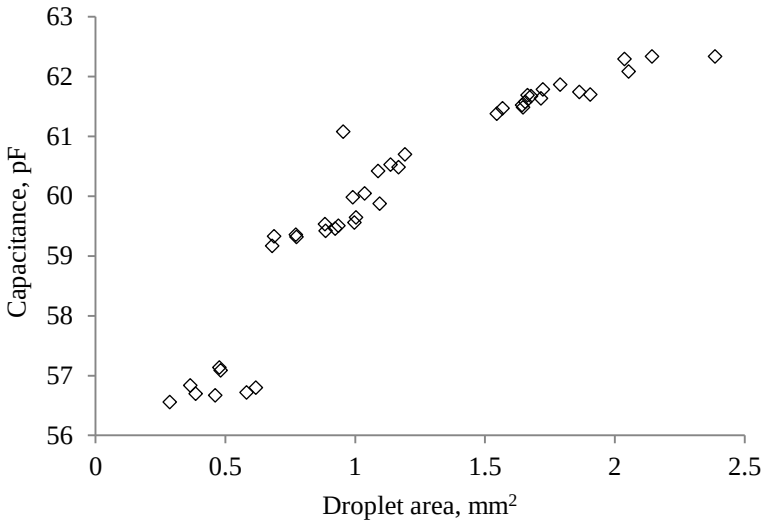


Figure 2.23: Maximum capacitance measured when the droplet is at the midpoint between electrodes (1.4 mm 1.4 mm); Inter-electrode gap: 60 µm, Droplet height: 80 µm.

This section presented a novel method of droplet position sensing by measuring the capacitance between two coplanar electrodes. The total capacitance consists of a network of capacitances due to the presence of the droplet and the overlapped portions of the dielectric and hydrophobic layers. The capacitance is a nonlinear function of the position of the droplet and a maximum capacitance is developed when the droplet is at the midpoint between the two adjacent electrodes. Results of simulation performed in a finite element-based software package, COMSOL®, verify that the analytical model predicts the capacitance very well. Experiments were conducted to test the new method of capacitance measurement as well as to verify the analytical model. Experimental results verify that the total capacitance is a nonlinear function of the droplet position and is maximal when the droplet is at the midpoint. Moreover, both numerical and experimental results show that the total capacitance depends on the diameter and height of the droplet, and the gap between the electrodes. This new method of droplet position sensing through capacitance measurement between electrodes on the lower plate significantly enhances the functionality of a DMFS by setting the upper plate free to accommodate other features, e.g. a photodetector. Since the proposed method relies on the droplet overlap on the adjacent electrodes, a feedback control system for splitting a droplet can be developed by measuring two coplanar capacitances from the three electrodes involved in the splitting process. In the traditional method of droplet sensing through capacitance measurement, both the upper and lower plates are electrically connected and hence, adding any desirable feature to the upper plate is impossible. Moreover, the capacitance measurement for one operation might affect the measurement for

another operation at a nearby location due to the common connection to the upper plate. This is especially important in sensing liquid accumulation over the electrodes during splitting. Therefore, the measurement of capacitance between coplanar electrodes is particularly advantageous for feedback control of splitting, which is the main motivation for the development of new capacitance measurement method. The applicability and effectiveness of this method in the control of splitting will be verified through experiments in future research.

## 2.3 EWOD droplet actuation

As discussed in chapter 1, EWOD is the most suitable actuation method for manipulating droplets on a planar surface and capable of performing all the basic fluidic operations efficiently. Low power consumption, ease of fabrication and programmable generation of control signals are the main advantages of EWOD-based DMFS. Moreover, splitting a droplet, which is the focus of this thesis, is not feasible with other actuation methods. Therefore, EWOD is chosen as the most appropriate method of actuation for splitting droplets. However, the investigation of the underlying physics of and the parameters affecting the EWOD is fundamental to the implementation and proper use in a DMFS to control the complex process of droplet splitting accurately.

### 2.3.1 EWOD force

Figure 2.24 shows the side view of a conductive droplet in an EWOD driven DMFS. It is assumed that the curvature of the spherical surface of the droplet is small and hence the droplet between the two hydrophobic surfaces can be approximated by a cylinder with a height equal to the gap between two plates. Furthermore, the deviation of the footprint of the droplet from circular shape during transition is also assumed to be negligible. The two assumptions are justified by the fact that most practical systems have small gap between two plates and the contact angles of droplets on commonly used hydrophobic surfaces are around $90^0$. The droplet of aqueous solution is considered as a perfect conductor. When the electrode on the bottom plate, over which the droplet is residing, and that on the top plate are electrically grounded and an adjacent electrode is energized by applying a voltage, a capacitor is formed between the droplet and the energized electrode. The materials of both hydrophobic and dielectric layers act as the dielectric layer of the capacitor. Although the hydrophobic layer between the droplet and the top ground electrode forms another capacitor, the capacitance is very high compared to the bottom one as the thickness of the hydrophobic layer is usually very small compared to that of the dielectric layer on the bottom plate. As a result, the potential drop across the top hydrophobic layer is negligible and almost all of the applied voltage is dropped at the bottom capacitor. In other words, the droplet can be considered as the virtual ground of the bottom capacitor. As the droplet is usually quite flat in typical designs, the fringe-field effects of the parallel-plate capacitor are ignored in this paper.

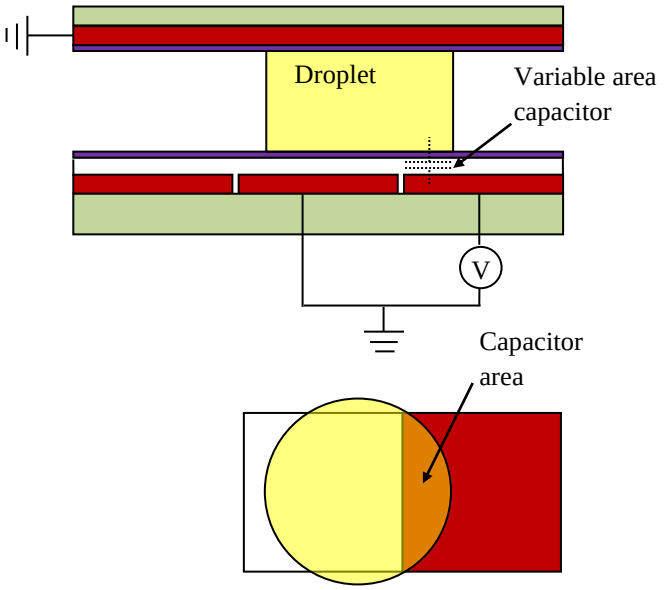


Figure 2.24: Capacitance formed between the conductive droplet and the energized electrode.

The effective area of the capacitor shown in Figure 2.24 is identified in the top view. The energy stored in the system is not minimal since the surface area of the capacitor is not maximal. Thus, the system will try to reach the minimum energy state by inducing a force on the movable conductor and thereby, maximize the area on the activated electrode on which the droplet resides. According to the above discussion, the EWOD force on the droplet is given by

$$F_{EWOD} = -\frac{dE}{dx} = \frac{d}{dx}\frac{CV^2}{2} = \left(\frac{\varepsilon_{rd}\varepsilon_{rh}}{t_h\varepsilon_{rd}+t_d\varepsilon_{rh}}\right)\frac{\varepsilon_o V^2}{2}\frac{dA_p}{dx} \tag{2.14}$$

where $V$ is the applied voltage, $x$ is the droplet position, $t_d$ is the thickness of the dielectric layer, $t_h$ is the thickness of the hydrophobic layer, $\varepsilon_{rd}$ is the dielectric constant of dielectric layer, $\varepsilon_{rh}$ is the dielectric constant of hydrophobic layer, $\varepsilon_o$ is the permittivity of vacuum and $A_p$ is the area of the droplet over the activated electrode. According to this model, a certain amount of overlap of the droplet towards the activated electrode is necessary for the generation of a nonzero driving force.

The relative size of the droplet with respect to the electrode can vary depending on the requirements of the assay operation, accuracy and precision of the droplet generation and any other intermediate manipulation of the droplet, such as division and merging. On the other hand, the overlapped area, $A_p$, is a function of the droplet position as well as the size of the droplet relative to that of the electrode. More precisely, for a given size of the droplet, $A_p$ changes at different rates at different positions of the droplet. Different rate of change of $A_p$ results in

different magnitude and direction of the actuating force. In general, the droplet size with respect to that of the square electrode can form a total of five distinct configurations. Three primary configurations can be identified as a droplet with a diameter (i) greater than the length of the electrode but less than the diagonal length of the electrode, (ii) equal to the diagonal length and (iii) greater than the diagonal length. A closer investigation of configuration (i), as depicted in Figure 2.25 (i) reveals that this configuration can appear in three different configurations. The relative magnitude of the dimensions *p* and *q* determines the sequence of different magnitudes and directions of the actuating force as the droplet moves from its current electrode to the adjacent electrode. If the droplet diameter is closer to the diagonal length of the electrode, *p* is greater than *q*; if the diameter is closer to the length of the electrode, *p* is less than *q*; and finally, for $r = 5L/8$, where *r* is the radius of the droplet and *L* is the length of the electrode, *p* and *q* are equal. Hence, the droplet size can be classified into five groups: (1) $L/2<r<5L/8$, (2) $r=5L/8$, (3) $5L/8<r<L/\sqrt{2}$, (4) $r=L/\sqrt{2}$ and (5) $r>L/\sqrt{2}$.

Figure 2.25 (i) shows a droplet ($L/2<r<5L/8$) in its initial position with the center of mass coincident with the center of the electrode. The displacement of the droplet, *x*, is defined as the distance between the center of the electrode and that of the droplet. The droplet starts to move towards the adjacent electrode as soon as a sufficient voltage is applied to that electrode. The magnitude and direction of the driving force depends on the rate at which the area of the droplet footprint over the activated electrode changes. From the beginning of droplet motion to a displacement of $\frac{L}{2}-\sqrt{r^2-\frac{L^2}{4}}$, the driving force is proportional to the rate of change of the area *abj*, shown by the shaded area in Fig. 3(i), which is given by

$$A_p = r^2 cos^{-1}\frac{\frac{L}{2}-x}{r} - \left(\frac{L}{2}-x\right)\sqrt{r^2-\left(\frac{L}{2}-x\right)^2} \tag{2.15}$$

and the rate of change of this area is given by

$$\frac{dA_p}{dx} = \sqrt{4r^2 - L^2 + 4Lx - 4x^2} \tag{2.16}$$

The initial value of the driving force is proportional to $\sqrt{4r^2-L^2}$ and acts in favor of the desired direction of droplet motion. It can be noted that the initial magnitude of the driving force is higher with larger droplet sizes.

For $\frac{L}{2}-\sqrt{r^2-\frac{L^2}{4}} \le x < \frac{L}{2}+\sqrt{r^2-\frac{L^2}{4}}$, the overlapped area *ackli*, shown by the orange area in Fig. 3(iii), is given by

$$A_p = \left(x-\frac{L}{2}+\sqrt{r^2-\frac{L^2}{4}}\right)L + \left(r^2 cos^{-1}\frac{L}{2r} - \frac{L}{2}\sqrt{r^2-\frac{L^2}{4}}\right) \tag{2.17}$$

where the rate of change of this area is given by $\frac{dA_p}{dx} = L$. Hence, the driving force within this range of droplet displacement is constant and is the maximum force that can be generated where the other factors remain constant. Thus, a droplet with diameter close to the diagonal length of the electrode will be subjected to the maximum amount of driving force for the most part of the travel time from one electrode to the next. For the special case with droplet radius, $r = \frac{L}{\sqrt{2}}$, the maximum driving force acts on the droplet from the start of transition up to a distance of $\frac{3L}{2} - r \cong 0.79L$.

For $\frac{L}{2} + \sqrt{r^2 - \frac{L^2}{4}} \leq x < \frac{3L}{2} - r$, the overlapped area *acdefghi*, shown by the shaded area in Figure 2.25 (v), is given by

$$A_p = 2\left(r^2 cos^{-1}\frac{L}{2r} - \frac{L}{2}\sqrt{r^2 - \frac{L^2}{4}}\right) - \left[r^2 cos^{-1}\frac{x-\frac{L}{2}}{r} - \left(x - \frac{L}{2}\right)\sqrt{r^2 - \left(x - \frac{L}{2}\right)^2}\right] + 2L\sqrt{r^2 - \frac{L^2}{4}} \tag{2.18}$$

and the rate of change of this area is given by

$$\frac{dA_p}{dx} = \sqrt{4r^2 - L^2 + 4Lx - 4x^2}\ . \tag{2.19}$$

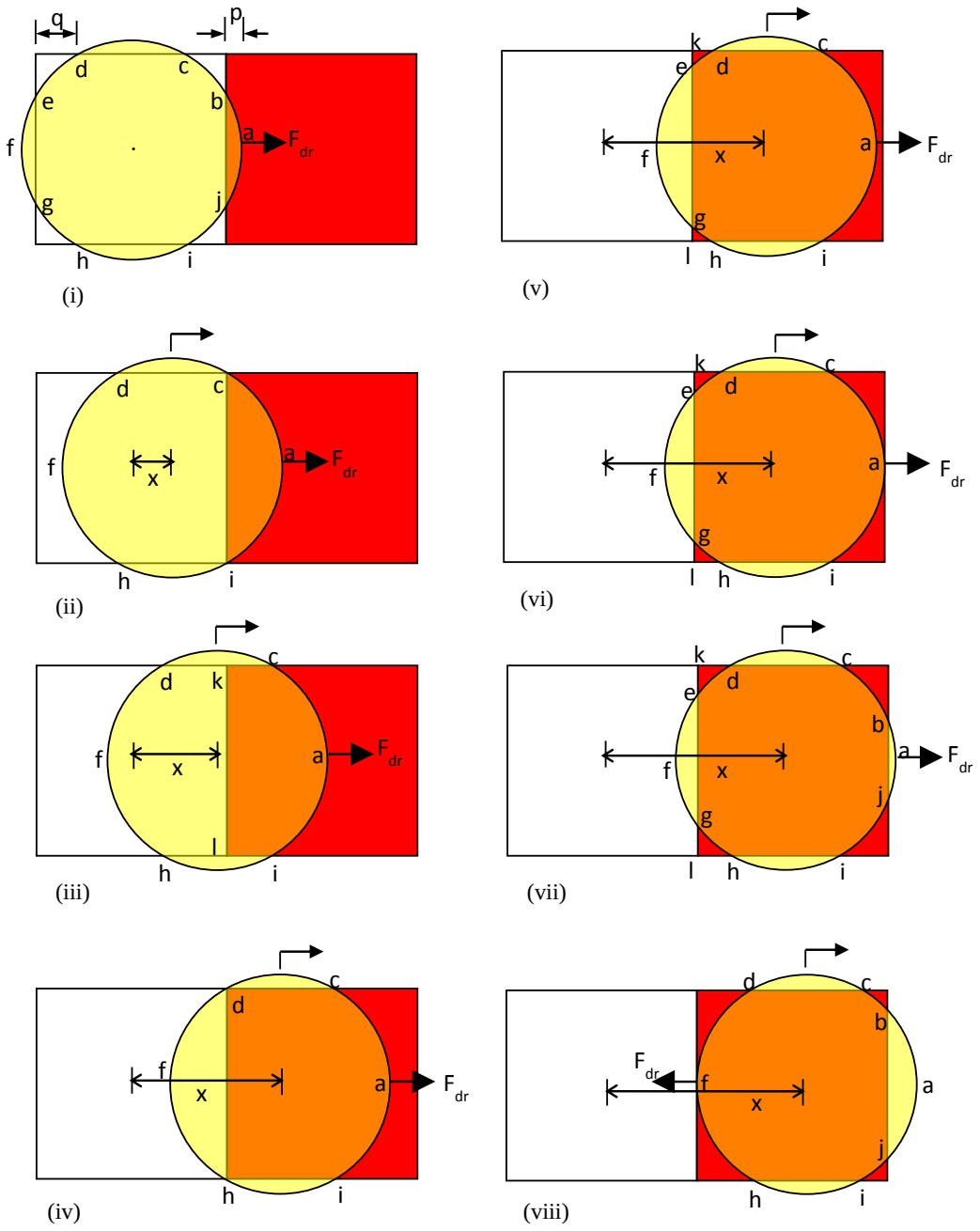


Figure 2.25: Sequential positions and the corresponding overlapped areas of a droplet ($L/2<r<5L/8$) in transition

This rate is always positive for the stated range of displacement resulting in a positive driving force towards the destination electrode. However, as the rate of change of the overlapped area decreases (exposed areas *dke* and *hlg* increase) with displacement of the droplet, the magnitude of the driving force decreases proportionally causing the droplet to decelerate.

For $\frac{3L}{2} - r \leq x < \frac{L}{2} + r$, the overlapped area *acdefghi*, shown by the shaded area in Figure 2.25 (vii), is given by

$$A_p = 2\left(r^2 cos^{-1}\frac{L}{2r} - \frac{L}{2}\sqrt{r^2 - \frac{L^2}{4}}\right) - \left[r^2 cos^{-1}\frac{x - \frac{L}{2}}{r} - \left(x - \frac{L}{2}\right)\sqrt{r^2 - \left(x - \frac{L}{2}\right)^2}\right] - \left[r^2 cos^{-1}\frac{\frac{3L}{2} - x}{r} - \left(\frac{3L}{2} - x\right)\sqrt{r^2 - \left(\frac{3L}{2} - x\right)^2}\right] + 2L\sqrt{r^2 - \frac{L^2}{4}} \quad (2.20)$$

and the rate of change of this area is given by

$$\frac{dA_p}{dx} = \sqrt{4r^2 - L^2 + 4Lx - 4x^2} - \sqrt{4r^2 - 9L^2 + 12Lx - 4x^2}\,. \quad (2.21)$$

As the droplet continues to move towards the destination electrode, the droplet area *baj*, which is not over the activated electrode, increases in addition to the increase of areas *dke* and *hlg*. Consequently, the rate of change of the overlapped area decreases at a faster rate and the resulting driving force diminishes quickly. This is also evident from equation 2.21, having two terms on the right side, which are always positive for the given range of *x*. When the droplet displacement is equal to *L* (i.e., the droplet is centered over the destination electrode), both the terms are equal resulting in no driving force acting on the droplet. In case the droplet has sufficient momentum (capable of overcoming the resistive forces) towards the direction of its motion, the droplet will be displaced from its desired position. As the droplet moves away from the center of the destination electrode towards the next electrode, the second term on the right side of equation 2.21 becomes greater than the first term making the rate of change of the overlapped area negative. As a result, a negative driving force is generated that acts against the motion of the droplet. This force will not only retard the droplet, it will also drive the droplet in the opposite direction in an attempt to position the droplet at the center of the destination electrode. If the droplet overshoots again to the left of the desired final position, a driving force will be generated which will oppose the motion and bring the droplet to the center.

The simulation block diagram, shown in Figure 2.26, implements the EWOD driven droplet actuation with inherent position feedback of unity gain. The 'Droplet' subsystem, shown in Figure 2.27, is the realization of the droplet dynamics described by Equation 2.7. The 'EWOD-Force' subsystem incorporates the mechanism of electrowetting force generation, explained in Section 2.3.1, for all the possible droplet sizes.

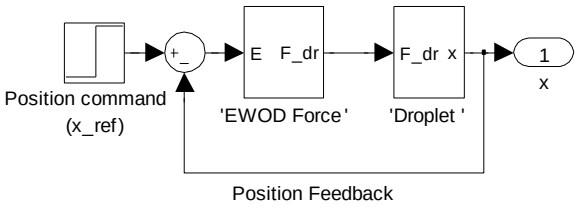


Figure 2.26: Simulation model of droplet motion.

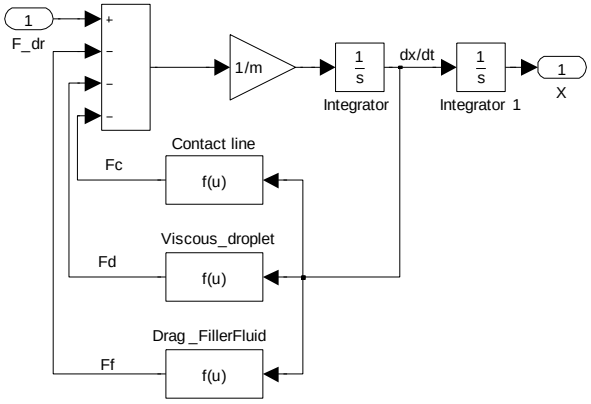


Figure 2.27: The 'Droplet' subsystem using resistive forces proposed in the literature.

### 2.3.2 Simulation Results:

The dynamic response of the EWOD-driven droplet is simulated in SIMULINK® using ODE45 solver with a maximum step-size of 0.0001 and an absolute tolerance of 0.0001. The input to this system is a step command for position which is equal to the electrode pitch and is applied at the start of the simulation. The position of the centre of the droplet is the output of the system. The geometric and fluidic parameters used in the simulation are summarized in Table 2.3. The droplet (water with 0.1 M KCl) and filler-fluid (silicone oil) considered here are those used in the experiment performed by Pollack et al. (2000).

Table 2.3: The values of fluidic, geometrical and other parameters used in simulation.

| | |
|---|---|
| Droplet viscosity, $\mu_d$; (1 μL Water with 0.1M KCL) | $1.9\times10^{-3}$ Pa.s |
| Droplet density, $\rho_d$ | 1000 kg/m$^3$ |
| Filler-fluid (Silicone oil) viscosity, $\mu_f$ | $1.7\times10^{-3}$ Pa.s |
| Filler-fluid density, $\rho_f$ | 760 kg/m$^3$ |
| Electrode pitch, $L$ | $1500\times10^{-6}$ m |
| Contact-line friction coefficient, $\zeta$ | 0.04 N.s/m$^2$ |
| Surface-tension between droplet & filler-fluid, $\gamma_{LM}$ | $40\times10^{-3}$ N/m |
| Plate spacing, $D$ | $300\times10^{-6}$ m |
| Dielectric (Parylene C) layer thickness, $t_d$ | $0.8\times10^{-6}$ m |
| Hydrophobic (Teflon) layer thickness, $t_h$ | $60\times10^{-9}$ m |
| Dielectric constant of dielectric material, $\varepsilon_{rd}$ | 3.15 |
| Dielectric constant of hydrophobic material, $\varepsilon_{rh}$ | 2.1 |

Figures 2.28, 2.29 and 2.30 show the instantaneous position, velocity and driving force for droplets of different sizes relative to that of the electrode (1.5 mm) driven by 50 volts. Droplets with radii 0.8 mm, 0.9375 mm, 1.0 mm, 1.0607 mm and 1.1 mm are considered in simulation having overlapped areas, on the adjacent electrode, of 0.8302%, 6.3868%, 10.0736%, 14.2729% and 20.95%, respectively. The responses of droplets with radii 0.8 mm and 0.9375 mm are similar to that of a typical underdamped second order system while others show overdamped behavior. All the droplets, except the largest one ($r$ = 1.1 mm), can attain the desired final position. The larger the droplet, the later it reaches the adjacent electrode. It is found that the largest droplet stops before the final position. The whole area of the destination electrode is covered before the center of the largest droplet coincides with that of the destination electrode. Further displacement of the droplet does not change the overlapped area and hence the driving force becomes zero. The smallest droplet shows a low acceleration during the first 2-3 milliseconds. It continues to accelerate for a longer period of time resulting in a maximum velocity (~10.5 cm/s in Figure 2.29) which is the highest velocity among all the droplets. This high velocity together with the low frictional resistances resulting from less amount of mass can be attributed to the overshoot by the smallest droplet. The maximum rate of change of the area on the destination electrode overlapped by the droplet is equal to the width of the electrode. Hence, the maximum driving force that can be generated with the given geometrical and material properties is found to be 58.75 μN, shown in Figure 2.30. The larger the droplet, the higher the

initial driving force until the droplet size fully covers an electrode for which the initial force is equal to the maximum value.

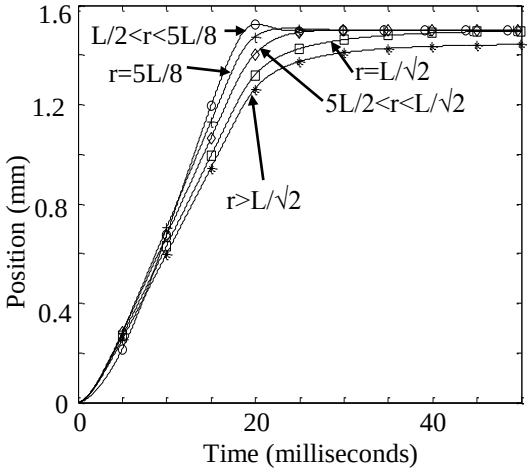


Figure 2.28: Dynamic response (position) of droplets of different sizes relative to the electrode.

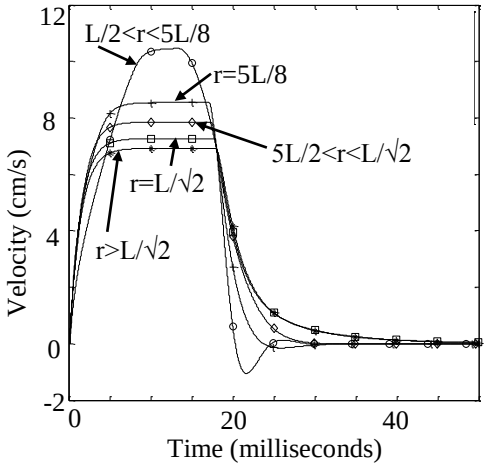


Figure 2. 29: Dynamic response (velocity) of droplets of different sizes relative to the electrode.

Among the three resistive forces, the contact-line friction is the most dominant one, shown in Fig. 2.31. The drag force on the droplet from the filler-fluid is not significant. Thus, a more realistic model of the contact-line motion should be incorporated into the dynamic model of droplet motion in order to perform accurate simulation of the actual system. Figure 2.32 shows the position of droplets for five consecutive cycles of actuation and demonstrates the usefulness of simulation in studying the continued transition of droplets. The frequency of successive actuation of the electrodes is determined from the time a droplet takes to travel a distance equal to the electrode pitch. However, droplets of diameter equal to or greater than the diagonal length of the electrode take either extremely long time or cannot cover the commanded distance at all. It is noted that a droplet can have sufficient overlap on the electrode adjacent to the destination electrode before completing the total displacement. Considering this, the time to cover 96% of the electrode pitch is considered as the period of successive actuation of electrodes for a droplet of diameter greater than the diagonal length of the electrode. For the droplets of other sizes, the period of electrode actuation is considered as the time needed for a droplet to cover 98% of the electrode pitch. The resulting actuation frequencies (average droplet speed) for droplets of increasing sizes are 53 Hz (7.94 cm/s), 46 Hz (6.9 cm/s), 34 Hz (5.2 cm/s), 31 Hz (4.7 cm/s) and 22 Hz (3.3 cm/s). Simulations performed with shorter period of successive electrode actuation

also shows successful continued motion of droplets provided that the period in each cycle allowed sufficient time for the droplet to have certain amount of overlap on the next adjacent electrode.

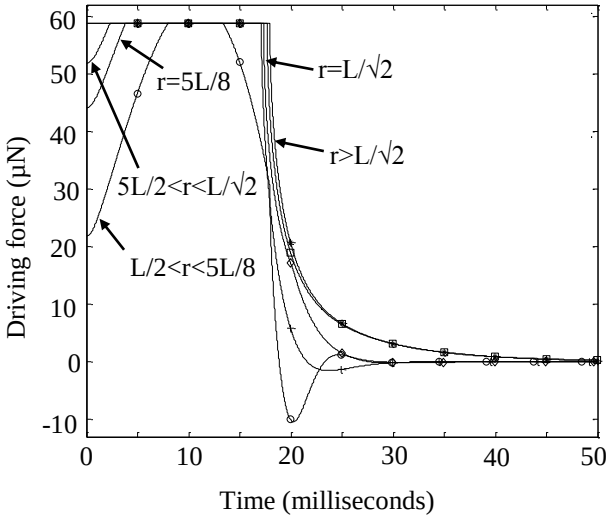


Figure 2.30: Electrowetting driving force for droplets of different sizes.

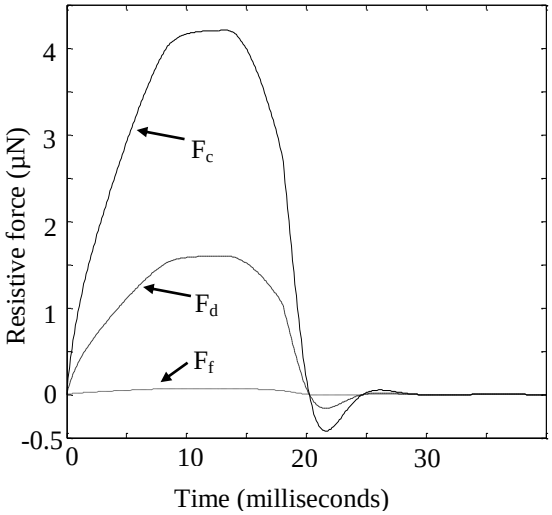


Figure 2.31: Resistive forces against droplet motion.

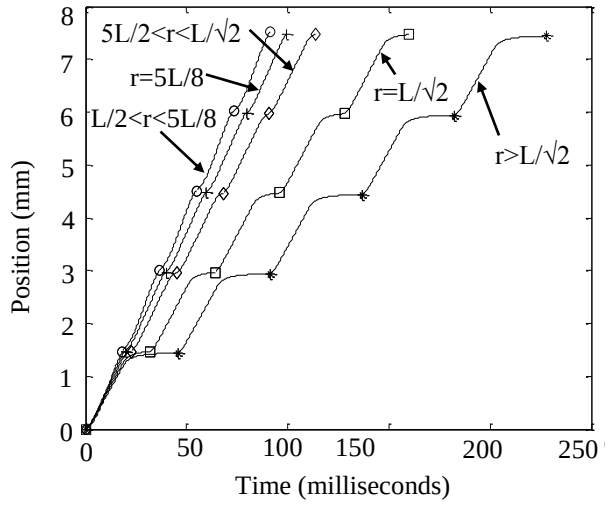


Figure 2.32: Dynamic response (position) of droplets of different sizes due to successive actuation of electrodes.

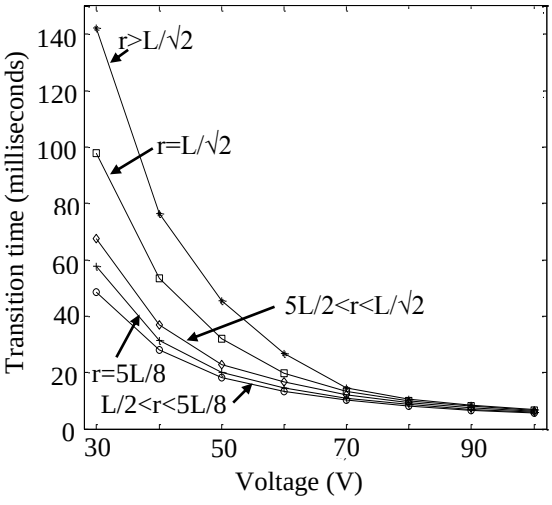


Figure 2.33: Droplet transition times for different actuation voltages.

The actuation voltage, geometric parameters and material properties are related to the driving as well as the resistive forces which in turn affects the dynamic response of an individual droplet and the overall throughput of the chemical/biological analysis. Experimental investigation of all the effects and interactions will be expensive and time consuming. In this study, several simulations are performed to identify how the droplet response is influenced by actuation voltage, spacing between the top and bottom plates, electrode size, dielectric thickness and dielectric constant and the results are shown in Figures 2.33, 2.34, 2.35, 2.36 and 2.37. The transition time decreases with higher voltage, shown in Figure 2.33, since the driving force is quadratically related to the actuation voltage. For weaker driving force, corresponding to lower voltages, the variations in transition times among droplets of different sizes are significant. The variations in transition times among droplets of different sizes are not significant for actuation voltages greater than 70 volts.

Figure 2.34 shows the transition times of droplets of different sizes as a function of the spacing between two plates. Viscous friction inside the droplet is inversely related to the plate spacing resulting in higher transition times for smaller spacing. Although the drag force due to the filler-fluid increases with plate spacing, the transition times are not affected as the drag force is the weakest resistive force. However, the droplet mass also increases with plate spacing and for larger spacing the transition times increase. One of the crucial geometrical parameters in a DMFS which should be determined for optimal performance of the device is electrode size. Figure 2.35 shows the variations of droplet transition times with the size of the electrode. Droplet sizes are changed so that the percentages of overlap on the adjacent electrodes are the same for all the electrode sizes considered in the simulation. The plate spacing is also changed proportionately in order to simulate practical systems. The results show that the response is faster with smaller electrodes because of smaller droplets and resulting lower resistive forces. As the variations in droplet size relative to a given electrode size is greater for larger electrodes, the variations in transition times increases with electrode size.

The thickness of the dielectric layer is another design parameter that should be carefully selected. Equation 2.14 suggests that the driving force increases with thinner dielectric layer. Figure 2.36 shows that the transition times are less for smaller thicknesses of the dielectric layer than those for thicker dielectric layers. The variations of transition times among different droplet sizes are higher for thicker dielectric layers. Although higher driving force can be generated with thinner dielectric layer, the dielectric breakdown strength should also be considered so that there is no electric short between the electrode and the droplet during operation. The electrowetting driving force increases with dielectric constant of the material in the dielectric layer.

Consequently, the droplet transition time is shorter for higher dielectric constant, shown in Figure 2.37. For low dielectric constant, corresponding to weak driving force, the variations in the transition times of droplets of different sizes are significant compared to that with high dielectric constant. However, the reduction in transition time becomes insignificant with higher dielectric constants.

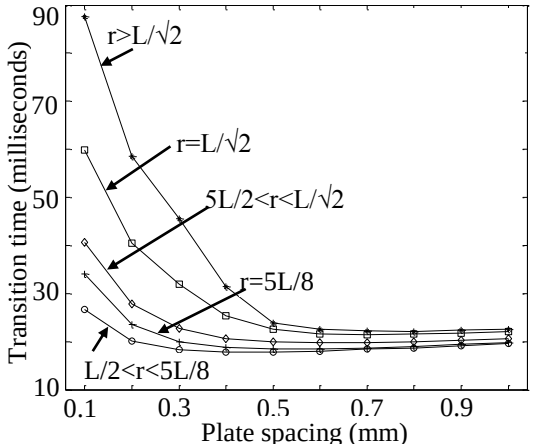


Figure 2.34: Droplet transition times for different plate spacing.

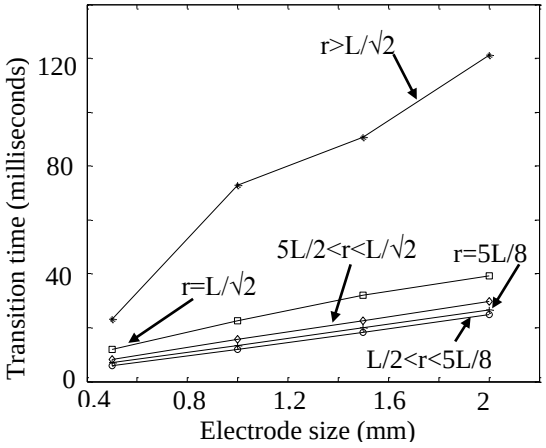


Figure 2.35: Droplet transition times for different electrode sizes.

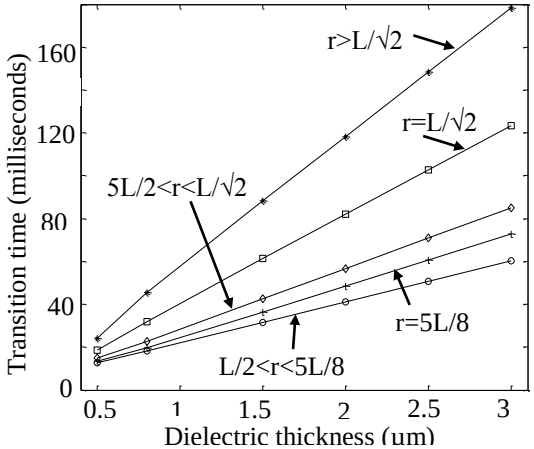


Figure 2.36: Droplet transition times for different dielectric thicknesses.

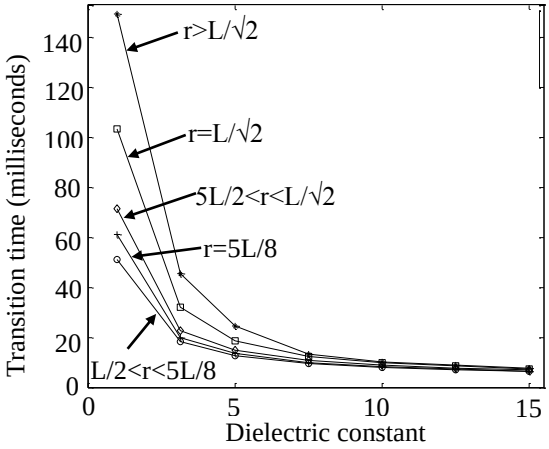


Figure 2.37: Droplet transition times for different dielectric constants.

Equation 2.14 can be used only when the applied voltage is DC. Application of AC voltage results in a lower actuation force due to the voltage drop across the droplet. The intensity of electric field generated inside the droplet depends on the conductivity of the liquid as well as the frequency of applied voltage and can be explained with the help of complex permittivity, defined as (Chatterjee et al. 2006)

$$\varepsilon^* = \varepsilon_0(\varepsilon_r - j\frac{\sigma}{\omega\varepsilon_0}) \tag{2.22}$$

where $\sigma$ is the electrical conductivity, $\omega$ is the angular frequency of the applied voltage, $j$ is the imaginary unit defined as $j^2 = -1$. A liquid having moderate to high conductivity ($\sigma > 10^{-9}$ S/m) behaves as a conductor ($\varepsilon^* \ll \varepsilon_0\varepsilon_r$) at low frequency. The voltage drop occurs in the dielectric layer only and thus the actuation force, approximately equal to that in DC case, acts on the tri-phase contact line. This corresponds to the classical EWOD force. However, as the frequency increases, the contribution of conductivity reduces resulting in the penetration of electric field inside the droplet. In addition to the force on the tri-phase line, a force acts on the droplet-air interface also originating from the voltage drop across the droplet. This force on the interface is known as the dielectrophoresis force. It should be noted that the total actuation force is lower than that in DC case due to the weakening of the dominating portion, acting on the tri-phase line, of the actuation force. The droplet acts as an insulator ($\varepsilon^* \approx \varepsilon_0\varepsilon_r$) at a sufficiently high frequency determined by the conductivity and size of the droplet. Following the energy minimization approach which considers the maximization of the total capacitance of the droplet and dielectric layer, the general expression of the total actuation force was derived by Kumari et al. (2008) and is given by

$$F_d = \frac{1}{2t_s}\varepsilon_s\varepsilon_0 V^2 \frac{dA_p}{dx}\left(\frac{(1+\omega^2\frac{D\varepsilon_s\varepsilon_D\varepsilon_0^2}{t_s\sigma_D^2}+\left(\omega\frac{\varepsilon_0\varepsilon_D}{\sigma_D}\right)^2)(1+\left(\omega\frac{\varepsilon_0\varepsilon_D}{\sigma_D}\right)^2)}{(1+\omega^2\frac{D\varepsilon_s\varepsilon_D\varepsilon_0^2}{t_s\sigma_D^2}+\left(\omega\frac{\varepsilon_0\varepsilon_D}{\sigma_D}\right)^2)^2+\left(\omega\frac{D\varepsilon_0\varepsilon_D}{t_s\sigma_D}\right)^2}\right) \tag{2.23}$$

where $V$ is the root-mean-square of the applied voltage, $t_s = t_h + t_d$and $\varepsilon_s = \frac{t_s\varepsilon_{rd}\varepsilon_{rh}}{\varepsilon_{rd}t_h+\varepsilon_{rh}t_d}$ are the total thickness and the equivalent dielectric constant of the solid layers in the lower plate, $D$ is the droplet height, $\varepsilon_D$ and $\sigma_D$ are the dielectric constant and conductivity of the liquid. It is noted that the above relation was developed under the assumption of no voltage drop across the hydrophobic layer in the upper plate. Furthermore, the effects of fringing fields due to the droplet interface and the conductivity of dielectric layers were neglected. Nevertheless, the above relation can be conveniently used to estimate the actuation force since the instrumentation for measuring the force in digital microfluidics is yet to be developed. The actuation force in the special case of DC voltage can be obtained from Equation 2.23 by plugging in $\omega = 0$. Moreover, the weakening of actuation force at higher frequencies, corresponding to the decrease in value of the term within parenthesis, can be compensated by increasing the conductivity of the liquid.

The actuation force, given by Equation 2.23, accounts for the longitudinal component of the total force generated without taking the deformation of the droplet into account. Although it is the longitudinal component of actuation force that moves the droplet, the transverse and the

vertical component also contributes in deforming the interface. The deformation of the droplet is related to the size, viscosity of the droplet as well as the magnitude of the total force. Droplet shape deviates more from circular, as seen in top-view, to elliptical at higher speed of motion between electrodes. The longitudinal actuation force is proportional to the rate of change of liquid overlap area on the energized electrode with respect to droplet position. If the droplet is large enough to cover the electrode, the longitudinal force is proportional to the width of the electrode during transport of the droplet from one electrode to the next and is given by

$$F_d = \frac{1}{2t_s}\varepsilon_s\varepsilon_0 V^2 L\left(\frac{(1+\omega^2\frac{D\varepsilon_s\varepsilon_D\varepsilon_0^2}{t_s\sigma_D^2}+\left(\omega\frac{\varepsilon_0\varepsilon_D}{\sigma_D}\right)^2)(1+\left(\omega\frac{\varepsilon_0\varepsilon_D}{\sigma_D}\right)^2)}{(1+\omega^2\frac{D\varepsilon_s\varepsilon_D\varepsilon_0^2}{t_s\sigma_D^2}+\left(\omega\frac{\varepsilon_0\varepsilon_D}{\sigma_D}\right)^2)^2+\left(\omega\frac{D\varepsilon_0\varepsilon_D}{t_s\sigma_D}\right)^2}\right). \quad (2.24)$$

However, the estimation of longitudinal force in droplet splitting requires careful observation of the process dynamics. Figure 2.38 shows the outline of the liquid at an instant during splitting. The maximum width of liquid overlap on the energized electrode is typically equal to the width of the electrode. However, the width of overlap along the edge of the energized electrode near the center electrode is less than the electrode width due to the presence of the neck. Hence, a force acts against the elongation of the droplet whose magnitude is proportional to the total width of uncovered edge of the electrode by the neck. The net longitudinal force is thus proportional to *W* instead of the electrode width, *L.* Continued accumulation of liquid over the electrode results in the front of the droplet reaching the farthest edge of the electrode. In this state, the net positive longitudinal force is further reduced owing to the overlap of liquid on the edge of the electrode where no electrostatic force exists anymore. Therefore, the longitudinal component of actuation force is proportional to *W-We* and can be calculated from Equation 2.24 using *W-We* in place of *L.*

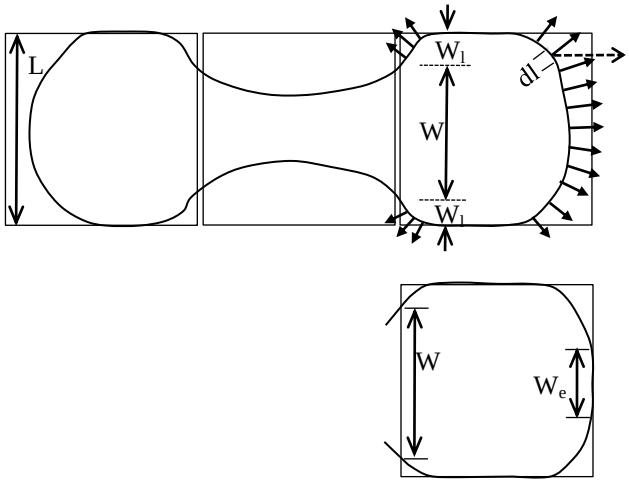


Figure 2.38: Schematic top-view of a droplet during splitting.

## 2.4 Investigation of the effects of dielectric material

The traditional EWOD theory centers on the idea that wettability dependent contact angle change acts as the driving force for the droplet motion. The Lippmann-Young equation that relates the contact angle change to the applied voltage, corresponding to Figure 2.39, is given by

$$\cos\theta(V) - \cos\theta(0) = \frac{\varepsilon_0 \varepsilon_{rh} \varepsilon_{rd} V^2}{2\gamma_{lg}(t_h \varepsilon_{rd} + t_d \varepsilon_{rh})} \tag{2.25}$$

where $V$ is the applied voltage, $\theta(V)$ and $\theta(0)$ are the contact angles with and without applied voltage, $\gamma_{lg}$ is the surface tension at the liquid-gas interface, $\varepsilon_0$ is the permittivity of vacuum, $\varepsilon_{rh}$, $t_h$ and $\varepsilon_{rd}$, $t_d$ are the dielectric constants and thicknesses of the hydrophobic layer and the dielectric layer, respectively. This model requires the droplet to be conductive and exhibits a considerable amount of contact angle change for actuation. That is why the traditional theory fails to explain some of the characteristics of electric-field driven droplet manipulation, for example the motion of dielectric liquid, low-surface tension liquid with no apparent change in contact angle, and the contact angle saturation (Abdelgawad and Wheeler 2008, Chatterjee et al. 2006). Recent studies based on the electromechanical analysis revealed that the EWOD and DEP are the low and high frequency limits of electromechanical response of the droplet, respectively (Jones et al. 2003).

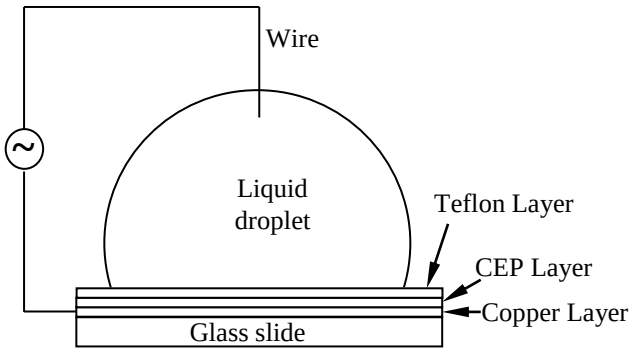


Figure 2.39: Schematic diagram of open EWOD.

### 2.4.1 Materials and fabrication

Copper-coated glass slides (25 mm × 75 mm × 1 mm) with 45 nm of coating thickness were obtained from EMF Corporation. Before adding the dielectric layer on to the Copper surface it was degreased with Acetone, cleaned with deionised water and subsequently dried in Nitrogen gas. Granular CEP obtained from Biddle Sawyer Corporation, USA, was dissolved in N, N-Dimethylformamide to produce a 10% (wt/wt) solution. An approximately 1 μm thick layer of

CEP was added by spin-coating at 2000 rpm for 30 seconds. The slide was dried in a vacuum chamber for about 3 hours and then annealed at 100$^{o}$C for 60 minutes. This annealing temperature has been reported to result in a dielectric constant of 20 (Na and Rhee 2006). To form the hydrophobic layer, a 1% (wt/wt) solution of Teflon® AF1600 (obtained from DuPont) in Fluoroinert FC-40 (obtained from 3M) was prepared. Teflon® layer (~50 nm) was then added on top of the dielectric layer by spin-coating at 2000 rpm for 60 seconds. Next, the slide was baked at 160$^{o}$C for 10 minutes. For the testing of actuation potential, a two-dimensional array of electrodes was prepared following the same procedure as outlined in Chapter 5.

### 2.4.2 Experimental results

#### 2.4.2.1 Contact angle

For contact angle measurement, Leica System was used to capture the gray-scale images of the droplets. A general purpose free image processing package, *ImageJ*, coupled with the *Drop Analysis* plugin was used to determine the contact angles (Stalder et al. 2006). DI water droplets, each having a volume of 5 μL, were deposited manually on the test slide using a pipette. The square-wave AC signal, generated from the National Instrument Function Generator, was amplified by a Trek Amplifier (PZD 700). One end of the power supply was connected to the copper layer on the slide and the other end was connected to a vertical wire. This wire was lowered gradually to make contact with the droplets. Figures 3 (a) and (b) show the photographs of a droplet of DI water without and with applied voltage, respectively. In order to minimize the effects of natural evaporation of liquid a new droplet was deposited for each voltage level.

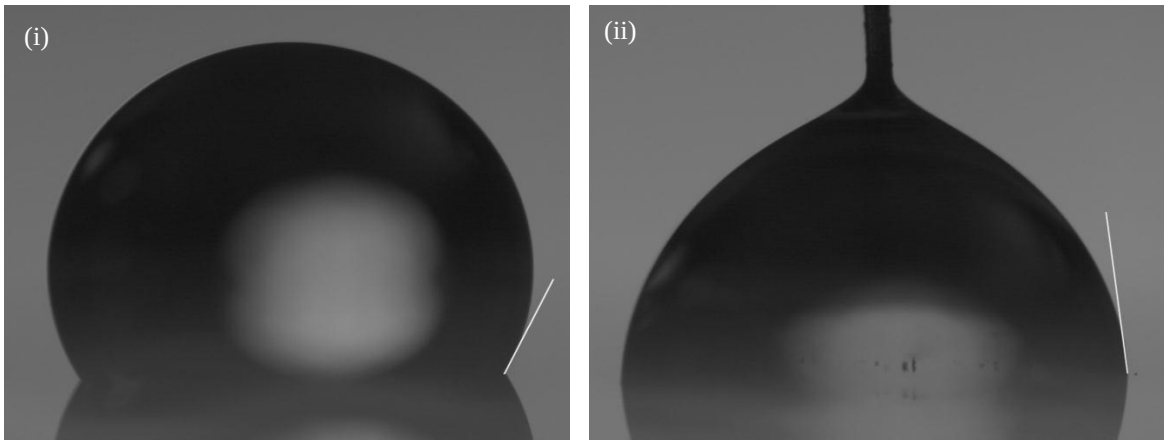


Figure 2.40: Photographs of a 5 μL droplet of DI water when (i) no voltage is applied; (ii) voltage is applied.

The measured values of contact angle in relation to the applied voltage of 30 Hz and 1 kHz are plotted in Figure 2.41 (i) and (ii), respectively. The static contact angle of DI water with zero applied voltage was measured to be 119$^o$ which is very close to the values reported in the literature (Cho et al. 2003, Hong et al. 2008Moon et al. 2002,). The minimum contact angle of 73$^o$ was measured at an applied voltage of 30 V, shown in Figure 2.41 (i). The resulting contact angle change (46$^o$) is higher than that obtained with anodic $Ta_2O_5$ (Li et al. 2008). It has been reported that a contact angle change of 40$^o$ is required to move droplets with reasonable speed in typical DMFS. The experimental results using CEP as the dielectric material suggest that around 22 V is required to generate the needed contact angle change. The results also suggest that the required contact angle change can be achieved with much lower voltages if the deposited CEP layer is made thinner. The thickness of CEP layer can be reduced by using higher spin speed and low concentration solution. However, as the thickness of the dielectric layer is reduced the effect of Teflon layer becomes more and more dominant in addition to the adverse effects of the roughness of underlying metallic layer and pores in the dielectric layer.

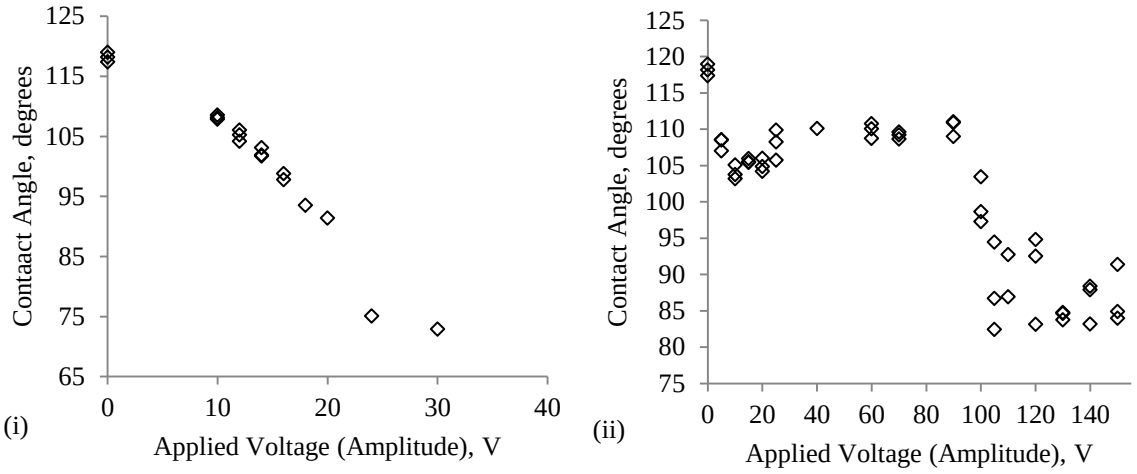


Figure 2.41: Results of contact angle measurement, applied voltage is square wave with (i) 30 Hz, (ii) 1 kHz.

The effect of signal frequency in electrowetting-on-dielectric phenomenon was also studied where a higher frequency (1 kHz) signal was applied to the DI water droplets. According to the electromechanical theory, the effect of electrowetting becomes weaker at higher applied frequencies. The results of our experiment support this theory. Figure 2.41 illustrates that with a 1 kHz signal higher voltages are required to achieve considerable amount of contact angle change. However, we observed that the distance between the bottom electrode and the tip of the wire electrode plays an important role in the results. The contact angle change due to an applied

voltage of given magnitude was found to be greater with smaller distance than that when the distance was greater. This is most probably due to the fact that as the wire electrode is brought closer to the slide the voltage drop across the capacitor formed by the CEP and Teflon layer is increased. Consequently, the electrowetting-on-dielectric effect becomes stronger resulting in a greater change in contact angle. Another observation is that at lower frequencies, droplets start to shake considerably. This can be attributed to the hydrodynamic time-scale being comparable to the period of applied frequency.

Droplets of aqueous solution require lower voltage for sufficient electrowetting effect. In our preliminary investigation 0.1 mM KCl was used as a conductive liquid. We observed significant amount of contact angle change at 15~17 V. As mentioned earlier, the thickness of CEP layer can be reduced using high spin-speed and low concentration solution. However, we observed electrolysis inside the conductive droplet when subject to prolonged application of voltage. This can be attributed to the surface impurities which were either coated with very thin CEP or not coated at all. Consequently, the droplet was in contact with copper or the thin CEP could not sustain the applied voltage and resulting in a short between the droplet and the copper layer.

It can be mentioned here that researchers have also investigated the use of PDMS in digital microfluidics since it serves as both dielectric and hydrophobic material and can be coated using a spinner. Although PDMS possesses good dielectric property ($\varepsilon_r = 2.75$), its lower break-down strength (21V/ μm) imposes the limit of how thin the layer can be in order to avoid electrolysis caused by the short between the electrode and the droplet. Kuo et al. (2003) reported that the contact angle of a droplet of DI water, placed on top of a 38 μm thick PDMS layer, changes from $102^o$ to $60^o$ when 700 V is applied between the droplet and the bottom electrode. Furthermore, droplet movement was also observed under the application of 500 V. Recently, Abdelgawad and Wheeler (2008) found that ac voltage higher than 300 $V_{rms}$ is required to perform microfluidic operations on DI water droplets in a DMFS having a PDMS layer of 9 μm thick. Thus, CEP seems to be a better choice as the dielectric material for a DMFS due to its high dielectric constant, breakdown strength and ease of fabrication.

#### 2.4.2.2 Droplet actuation

The results of contact angle measurement using the CEP as dielectric material indicate that typical operations in a DMFS can be performed at lower voltages. Hence, to test the effectiveness of the use of CEP a droplet of ~300 nl DI water was deposited at the center of an electrode (1.5 mm × 1.5 mm) by using a pipette. An 80 μm gap between the bottom and top

surfaces was created by two layers of scotch tape. The sandwiched droplet slightly overlapped the adjacent electrodes in addition to covering the host electrode completely. The top-view of a portion of the assembled DMFS is shown in Figure 2.42 (i). One of the adjacent electrodes was connected to one end of the DC power supply while the ITO layer on the top slide was connected to the other end. The host electrode was electrically floating. Successful droplet transition from the host electrode to the adjacent electrode was observed with an applied voltage of 20 V, shown in Figure 2.42 (ii).

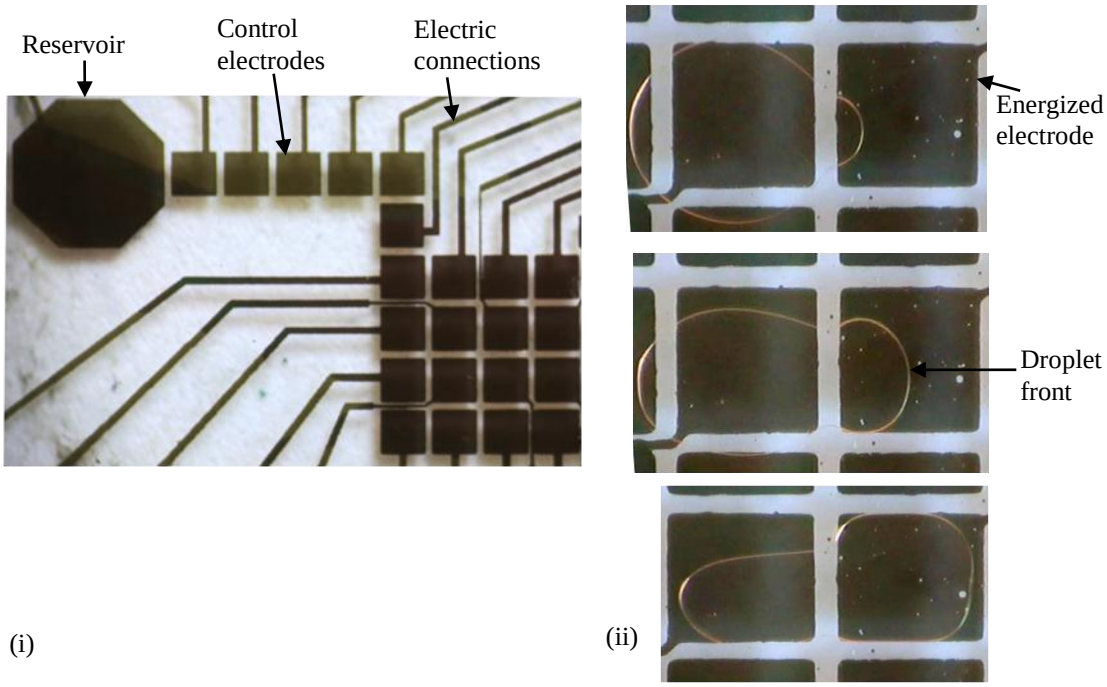


Figure 2.42: Fabricated device (i) and snapshots of droplet motion at 20 Vdc (ii)

Since the EWOD actuation force is directly related to the properties of the dielectric material, a material possessing high dielectric constant is desirable to operate a DMFS at lower voltages. For a DMFS to serve as a hand-held and disposable lab-on-a-chip, it must have three qualities, namely, low-power, low-cost and easy to fabricate. CEP is a polymeric dielectric material ($\varepsilon = 20$) that can be deposited by spin-coating obviating the need for expensive deposition facilities. Thus, a DMFS can be fabricated quickly in a resource limited situation, yet the device can be operated at voltages as low as 20V. This research was conducted considering CEP as the dielectric material. All the simulations were performed incorporating the properties of CEP into the models. Experimental study of droplet sensing as well as splitting was performed in DMFS fabricated using CEP as the dielectric material. Therefore, this thesis not only introduces

the attractive features of CEP but also verifies the advantages through extensive use in device fabrication and reliable operation.

# CHAPTER 3

# SYMMETRIC SPLITTING: SIMULATION

This chapter discusses the general aspects of computational fluid dynamics as applied in microfluidics involving free surface. The advantages and limitations of popularly used software packages are briefly mentioned in relation with the problem of droplet splitting in digital microfluidic systems. Next, the electromechanics of droplet splitting is explained based on the simulation results along with the limitations of and assumptions in modeling for simulation. Parameters and properties that play the central role in characterizing the splitting as well as determining the result of splitting are introduced. Finally, results of successful and unsuccessful splitting are presented and interpreted based on the concepts of previous sections.

## 3.1 Computational fluid dynamics in droplet splitting

The realization of an accurate and reliable lab-on-a-chip device for one or more biomedical/chemical tasks requires a properly designed digital microfluidic system (DMFS). This means that the geometric parameters and the materials are carefully chosen such that the total combination allows successful operations of all the necessary fluidic functions. The basic fluidic functions must be performed within the normal operating range defined by the combination of material properties and geometric parameters. For instance, the material for the dielectric layer and its thickness should be so chosen as to prevent dielectric failure and electrolysis of the liquid sample while the voltage levels meet the lower and upper limit imposed by the fluidic operation and available power supply, respectively. Thus, an optimally designed DMFS demands in-depth understanding of the dominant physics and detailed modeling and analysis taking into account critical system parameters. In a DMFS, the fluidic operations involve fluid motion and deformation of liquid-air or liquid-liquid interface of a discrete droplet governed by the bidirectional coupling between electrostatics and fluid dynamics in three dimensions. It is well-known that a reasonably accurate reduced-order model, if it exists or is deducible, is often more intuitive and saves a lot of time for the investigation during predevelopment stage. This kind of model is very hard to develop for complex phenomena like droplet generation and merging. Moreover, the probable inaccuracies in capturing the dominant physics might not justify the level of efforts and time required for developing such model instead of a rigorous one. Since this thesis focuses on droplet splitting, a phenomenon involving free-surface fluid dynamics and topological

change, a part of the investigation is performed through computational fluid dynamic (CFD) simulations.

There are mainly two families of numerical methods for handling the unique challenges of evolution of free-surface and topological change. The Lagrangian approach distributes computational nodes are on the droplet interface and the evolution of the droplet interface is explicitly tracked by using interface-adaptive meshes (Furlani and Hanchak, 2011, Chakrabarty et al., 2010). While this approach provides accurate description of the droplet interface, the major drawback is that the mesh can be severely deformed in many applications necessitating frequent checking of mesh quality and remeshing. In simulating droplet splitting or merging, this approach faces the ultimate challenge and may not be the best option to choose. The finite element method and the boundary integral method are the two examples of this category of numerical scheme. The Arbitrary Lagrangian-Eulerian (ALE) method attempts to remedy this problem by allowing the nodes to move independent of fluid velocity thereby maintaining mesh quality and minimizing remeshing. However, the difficulty in implementing ALE for complex flows as well as developing interface reconstruction scheme poses the major challenge. In the Eulerian approach, the mesh is fixed and the interface is defined according to the solution of an unknown scalar function. The value of this function in each computational cell determines the presence of interface within the cell. Examples of this category of numerical scheme include marker-and-cell, level-set, phase field and volume-of-fluid (VOF). The most attractive feature of this category is the capability of simulating topological changes, e.g., droplet splitting and merging. Although the level-set method has been used for simulating electrowetting actuated contact-angle change and droplet operations in two dimensions, it was found that simulations of coupled electrohydrodynamics in three dimensions is extremely challenging due to the need for high level of customization and trial-and-error method with a number of numerical parameters. Besides, the level-set method has the drawback of incapable of conserving the mass in areas of high curvature. While the VOF method has the advantages in implementation and computation time, the major disadvantage is that complexities may arise from interface reconstruction procedures. If lower order interface reconstruction schemes are used, errors in the curvature of the free-surface may be introduced resulting in inaccuracies in fluid pressure in certain regions within the droplet.

All the simulations of droplet splitting were performed using commercial CFD software, FLOW-3D®. FLOW-3D® solves the governing partial differential equations by a control-volume-based finite-difference technique while an improved volume-of-fluid method, TruVOF®, is employed to track the droplet-medium interface accurately and with stability. In order to track the interface, a scalar function F specifying the volume fraction of the liquid in each computational

cell is introduced. The value of F ranges between 0 and 1, where a value of 0 in a given cell indicates surrounding medium (e.g., air) and 1 indicating that the cell resides in the interior of droplet. Any other value of F signifies the presence of droplet-medium interface in the given cell. The evolution of the interface is tracked by solving the passive transport equation

$$\frac{\partial F}{\partial t} + \nabla . \bar{v} F = 0 \tag{3.1}$$

where $t$ is time, $\bar{v}$ is the velocity vector, and $\nabla$ is the gradient operator. The interface is reconstructed taking into account the values of F in the neighboring cells. FLOW-3D® also allows the coupling of other physics, e.g. electromechanics, heat transfer, phase change etc., with the fluid dynamics module.

### 3.2 Simulation model

In general, the purpose of any simulation is to understand the main characteristics of the process taking into account the essential inputs, available mathematical models of the physics involved and a representation of the geometry. Simulations of electrowetting force based droplet splitting process were also carried out with a view to understand the mechanism and identify the conditions when splitting is feasible. However, a major challenge was the development of the simulation model that represents the real device as close as possible while keeping the complexity within reasonable limits for the solver thereby reducing computation time. For instance, modeling the Teflon® layer, having a thickness of 100 nm as compared to 1 μm for the dielectric layer and 70 μm for the droplet, imposes difficulty in meshing the computational domain. For the lower plate, Teflon® layer thickness is added to that of the dielectric layer and the equivalent dielectric constant is used as the material property. The Teflon® layer on the upper plate is not modeled in simulations since the voltage drop across this layer is close to zero, as found from both numerical and experimental studies (Bahadur and Garimella, 2006, Kumari et al. 2008). Consequently, the boundary condition for the upper wall was set to zero potential. The gap between adjacent electrodes is not taken into consideration in order to avoid the complexity in meshing the dielectric layer and the potential inaccuracy originating from multiple mesh blocks. The common inputs having fixed values in all the simulations are presented in table 3.1.

Table 3.1: Material properties and dimensions used in simulations

| | |
|---|---|
| Liquid | Deionized water ($\varepsilon_r$ = 78) |
| Droplet Conductivity | $2.5\times10^{-5}$ S/m |
| Equivalent dielectric constant | $\varepsilon_r$ = 15 |
| Dielectric layer thickness | 1 μm |
| Static contact angle | $117^o$ |
| Surface tension (Water-air) | 0.072 N/m |
| Ambient medium | Air |

Since the splitting process is symmetric about the vertical plane passing through the center of the droplet, only half of the domain, shown in Figure 3.1, is modeled in FLOW-3D® in order to save computation time. The computational domain was divided into a mesh consisting of cubic cells. Jang et al. (2007) reported simulation results of EWOD-actuated droplet operations using a volume-of-fluid based CFD code and found that the pressure difference between the sides of a moving droplet stabilizes at a grid density of 74,286 cells/mm$^3$. Since the dimensions of the computational domain in our investigation varied significantly, the grid density ranged between

64000 cells/mm$^3$ to 296296 cells/mm$^3$ and 64000 cells/mm$^3$ to 186589 cells/mm$^3$ for electrode sizes of 1 mm and 1.5 mm, respectively. The dielectric surface and the upper plate in contact with the droplet were set as no-slip walls. The gravitational effects were not considered since the bond number (Chakrabarty et al. 2010) for typical applications is very low. On the electromechanics side, appropriate potential boundary conditions were set for the left and right electrodes. The potentials for the center electrode as well as the upper surface were set to zero. Simulations were limited to DC potentials as FLOW-3D® does not provide a direct way of incorporating AC potentials. Although one can input values of potential and time in a tabular form, the total number of entries in the table is limited to 500 only. This means that the complete simulation of a splitting process actuated by high frequency AC requires a number of restarts of the fractionally complete parts. Contact-line pinning, contact angle hysteresis and saturation are the typically observed behavior in electrowetting force actuated droplet dynamics. Contact-line pinning results from molecular dynamics near the tri-phase contact-line in response to the applied electric stress and the surface roughness. The consequent translocation of the contact-line is less smooth than the way a CFD package implements that. The contact angle hysteresis reduces the effective driving force generated by the applied electric field and contact angle saturation places an upper limit of the deformation along the vertical plane. Therefore, the combined effect of these phenomena is to slow down the fluidic process. However, they were not modelled in FLOW-3D® due to absence of universally accepted theories.

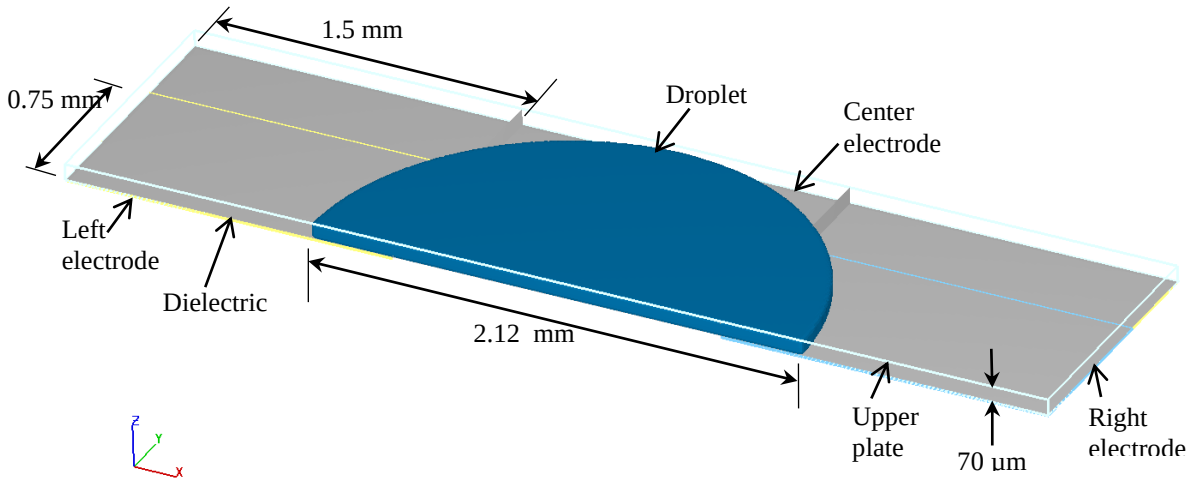


Figure 3.1: Isometric view of the computational domain in FLOW-3D®

### 3.3 Symmetric splitting of droplet

#### 3.3.1 General theory

Symmetric splitting of a droplet is defined as the process of liquid flows in two opposing directions at equal rate and ultimately forming two droplets of equal volume. In a DMFS, symmetric splitting of a droplet is accomplished by applying necessary voltages to the two adjacent electrodes, one to the left and another to the right, of the center/host electrode. The electrode on the top plate is grounded and the center electrode is usually either grounded or kept at floating potential. A schematic of the symmetric splitting of a droplet confined between two plates in a DMFS is shown in Figure 3.2. It is noted that for successful splitting by EWOD the droplet must be large enough to have some overlap on the adjacent electrodes while residing at the center electrode with proper alignment. As soon as voltages are applied to the appropriate electrodes, the droplet starts elongating longitudinally. More and more liquid accumulates over the actuated electrodes while the amount of liquid on the center electrode reduces to keep the total volume constant. Thus, the width of the deformed droplet, measured along the transverse direction through the center decreases as the process continues. Eventually, there appear two concave regions (negative radius of curvature) in the droplet over the center electrode and thereby, initiating the phase known as necking. Although the neck formation is crucial for splitting, this does not guarantee successful completion of the splitting process due to reasons discussed in the following sections. Only when the combination of material properties, geometric parameters and applied voltages is such that the radii of curvature of the neck continue to decrease, the splitting of the droplet can be completed following pinch-off of the neck. Otherwise, the droplet deformation stops and the elongated droplet retains the deformed shape even though the electrodes remain activated.

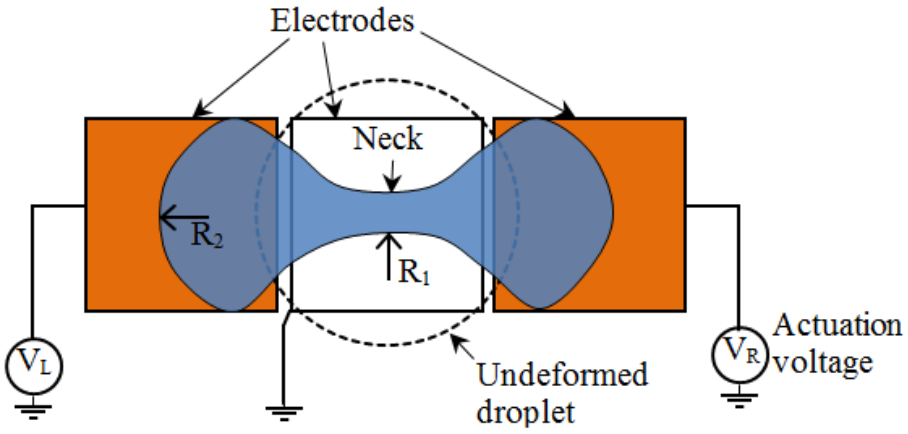


Figure 3.2: Schematic of the splitting of a droplet using electrowetting actuation

In an attempt to understand the interrelation between the parameters and the condition necessary for successful splitting, a static analysis was performed by Cho et al. (2001). Considering Laplace's equation for pressure difference across the liquid-air interface and the Lippmann-Young's relation between the contact angle and voltage, the following relation was derived

$$\frac{R_2}{R_1} = 1 - \frac{R_2}{d}\frac{\varepsilon_o \varepsilon_r {V_d}^2}{2t\gamma_{LG}} \tag{3.2}$$

where $R_1$ and $R_2$ are the respective radii of curvature of the neck and the front of a droplet along the X-Y plane (i.e. parallel to the plane of hydrophobic surface), $d$ is the gap between upper and lower plates, $V_d$ is the voltage across the dielectric and hydrophobic coatings in the lower plate, $t$ and $\varepsilon_r$ are the combined thickness and equivalent dielectric constant of the dielectric and hydrophobic coating respectively. Equation (3.2) can be used to understand the key parameters and their interrelation that control the process of splitting a droplet. As discussed above, since the initiation of a neck (i.e. a negative $R_1$) over the center electrode is essential for splitting, the second term on the right-hand side of the equation must be greater than one. This means that the ratio between the radius of curvature at the front of a droplet ($R_2$) and the plate gap ($d$) must be large. $R_2$ can be approximated by the size of the electrode. Thus, splitting is easier for a droplet on larger electrodes with smaller gap between the plates assuming that the droplet size is consistent with that of the electrode. Alternatively, splitting can be facilitated by increasing the value of the electrowetting number ($EWN = \frac{\varepsilon_o \varepsilon_r {V_d}^2}{2t\gamma_{lg}}$). This can be achieved by using a dielectric material possessing a high dielectric constant, thinner dielectric layer, a liquid having low surface tension, and a higher actuation voltage. However, the upper limit of applicable voltage imposed by the dielectric breakdown strength should also be taken into consideration during designing the device. It can also be noticed that the surface tension between the liquid and the surrounding medium is an important determinant for splitting unlike droplet transport, where surface tension plays a role only in defining the dynamic shape of a moving droplet. Droplets having lower value of surface tension between liquid and medium will require lower actuation voltages in comparison with those having higher values of surface tension.

Another usefulness of Equation (3.2) is that the minimum ratio between the electrode size and plate gap required for successful splitting can be approximately calculated. This is done by applying the equation for the instant just before the pinch-off and approximating $R_1$ by half of the electrode size. It should be mentioned here that the above equation serves as a guideline qualitatively only since the actual dynamics of the process including the viscous resistance and energy needed for the deformation, is not modeled. It has been found that reorganizing the

equation, in an attempt to find the minimum voltage for splitting, results in a highly underestimated value. Therefore, a more accurate model capable of explaining the dynamics of splitting is necessary for a deeper understanding as well as a reliable estimate of the design parameters and operational variables.

### 3.3.2 Electrohydrodynamic response

Investigation of the results of three-dimensional CFD simulation of droplet splitting in terms of electric potential and field, fluid pressure, velocity and flow rates etc. reveals the characteristics of the process. Figure 3.3 shows the distribution of induced charges, electric field and pressure along the vertical plane of symmetry (X-Z plane at Y = 0) after 1 ms of the start of splitting a DI water droplet by applying 52 Vdc to the electrodes on either side. Electric dipoles are induced inside the droplet due to the application of voltages to the electrodes and they tend to migrate towards the droplet-dielectric and the droplet-medium interfaces where there are discontinuities of electric field. As a result, there exists a high concentration of induced negative charges at those interfaces shown in Figure 3.3 (i). The norm of electric field is zero in the bulk of the liquid while it is non-zero along the length of the energized electrodes overlapped by the elongated droplet due to the z-component of electric field. The norm of electric field is maximal near the tri-phase contact line due to the additional horizontal components of electric field originating from the presence of charges on the droplet-medium interface. The norm of electric field decreases rapidly along the positive z-direction and ultimately approaches zero. The pressure field inside the droplet, shown in Figure 3.3 (iii), is directly related to the electric field distribution through the following relation

$$P_{el} = 0.5\varepsilon_0 E^2 \tag{3.3}$$

where $P_{el}$ is the electrostatic pressure. Liquid pressure is higher near the energized electrodes due to the presence of electric field. It is the electrostatic pressure ($0.5\varepsilon_0 E^2.\hat{n}$) on the droplet-medium interface which causes the contact angle reduction by reducing the liquid pressure and thereby increasing the radius of curvature of the interface on the vertical plane.

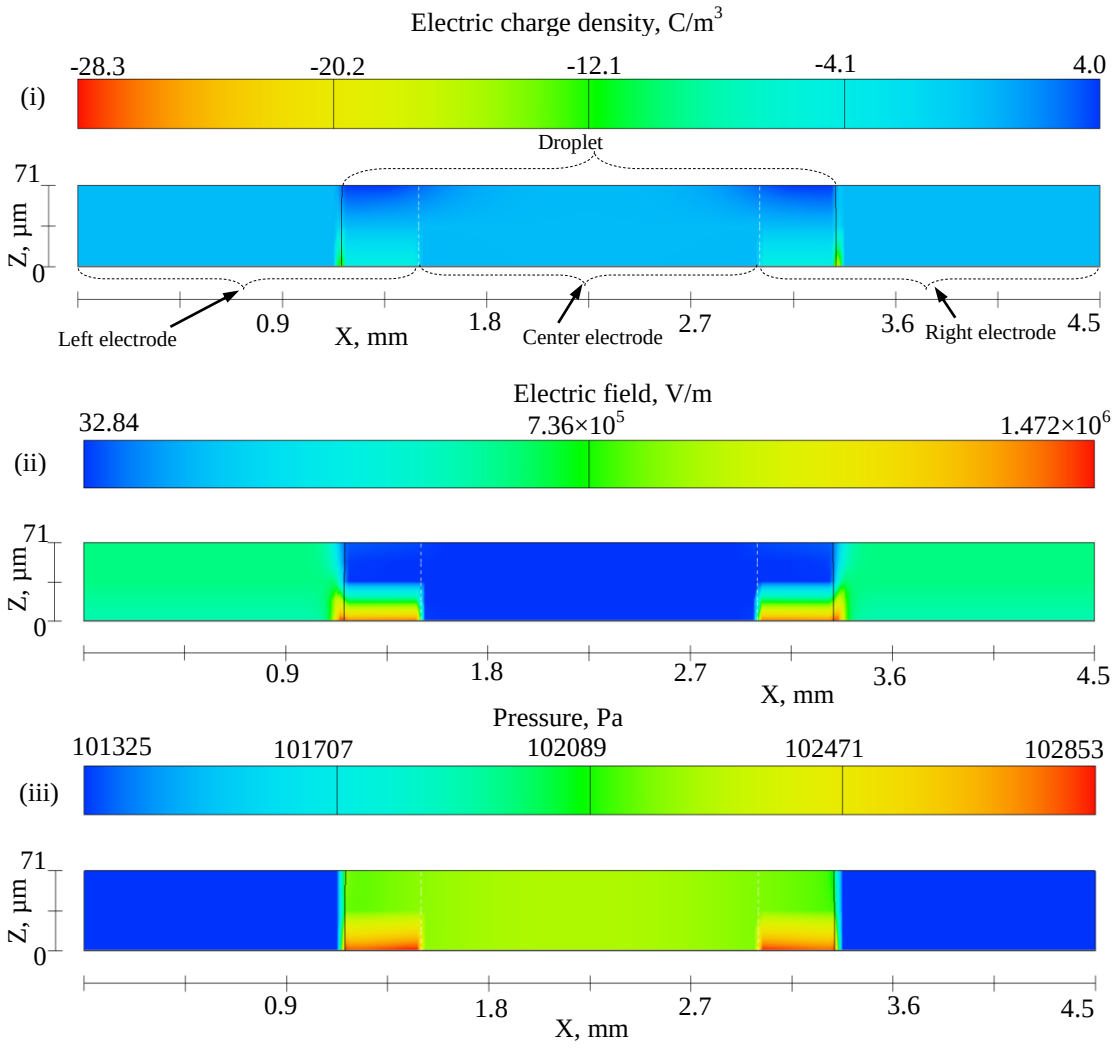


Figure 3.3: Distribution of (i) Electric charge, (ii) Electric field, and (iii) Pressure along the vertical plane of symmetry (X-Z plane at Y = 0) after 1 ms of start of splitting. Electrode: 1.5 $mm^2$, Droplet: DI water (2.12 mm diameter), Plate gap: 70 µm.

The pressure contours and velocity vectors along the X-Y plane just above the hydrophobic surface during splitting a droplet are shown in Figure 3.4. The higher pressure over the energized electrodes is due to the vertical electric field, as discussed above. Since there is no pressure gradient inside the droplet along X-direction, the deformation and stretching of the droplet is solely due to the change of pressure at the droplet-medium interface including the region near the tri-phase contact line. The velocity vectors reveal the characteristic pattern of liquid flow during splitting. The flow rates towards the energized electrodes are higher during the early stage of splitting as evidenced by the scales of velocity vectors. Flows over the energized electrodes are mainly longitudinal (i.e. X-direction) while those over the center electrode are due

to combinations of longitudinal and transverse (i.e. Y-direction) velocities. Along the longitudinal centerline, velocity field has the x-component only. However, the magnitude of velocity decreases with distance from the front of the droplet and decays to zero near the center of the droplet. The contribution of y-component of the velocity field increases with distance from the centerline towards the droplet interface. Velocity field consists of y-component only along the centerline in transverse direction. Since the formation of a neck is critical in splitting, the magnitude of velocity along the transverse centerline determines the rate at which neck is formed and the width of this neck is reduced. The distribution of electric potential in the droplet and the surrounding medium along with the velocity field along the vertical plane passing through the longitudinal centerline is shown in Figure 3.5. Except near the droplet-air interface, the velocity distribution is similar to that of a poiseuille flow between two plates. Near the interface and close to the tri-phase contact line, there exists a strong contribution of z-component of velocity resulting from the strong electric field. This explains how the interface moves over the solid surface where a no-slip boundary condition is set. Continuous displacement of liquid from above the tri-phase contact line and filling the corner of the wedge result in the continuous advancement

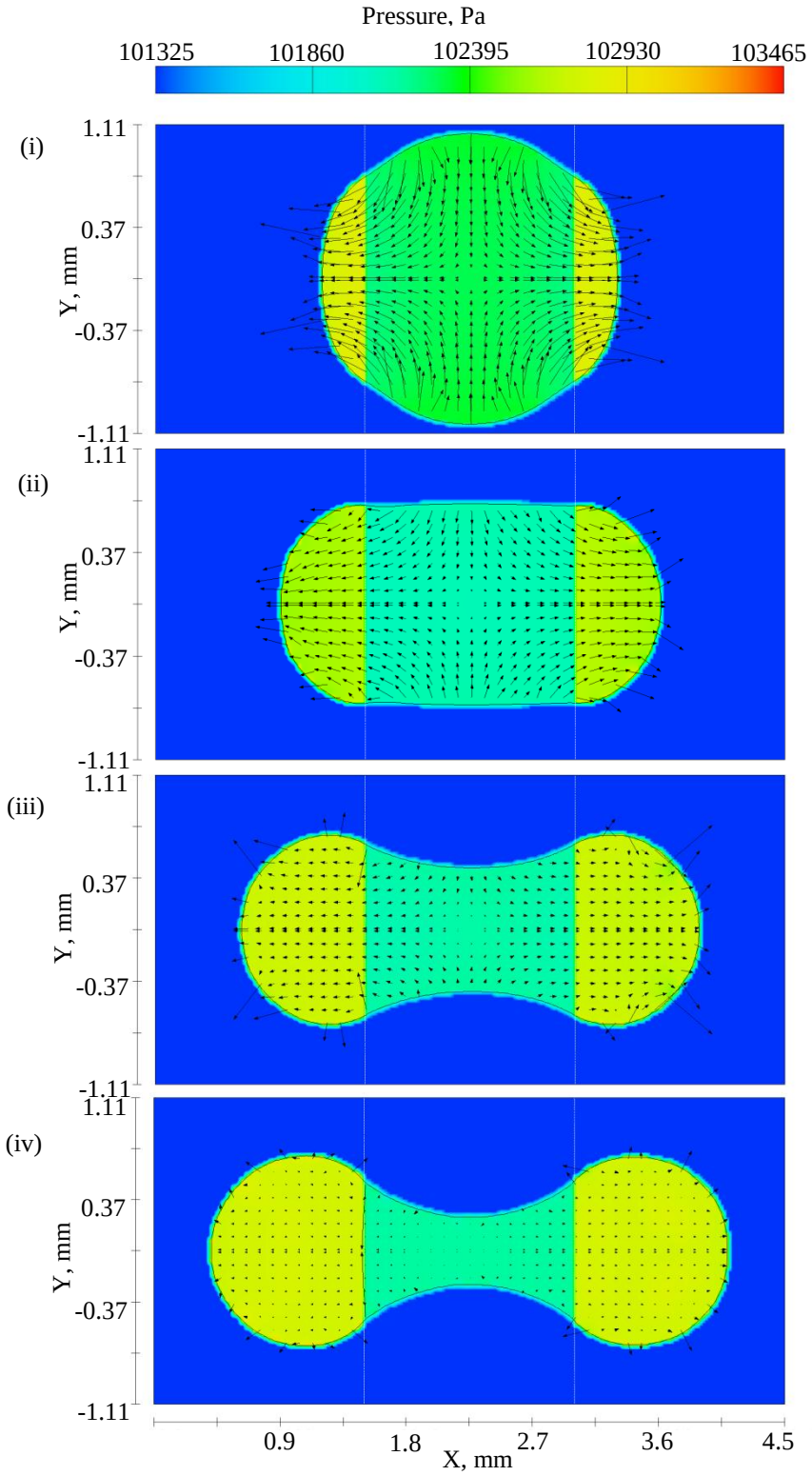


Figure 3.4: Pressure (color) and velocity (vector) distribution during splitting at (i) 0.5 ms, (ii) 5 ms, (iii) 15 ms, and (iv) 35 ms. Electrode: 1.5 $mm^2$, Droplet: DI water (2.12 mm diameter), Plate gap: 70 µm.

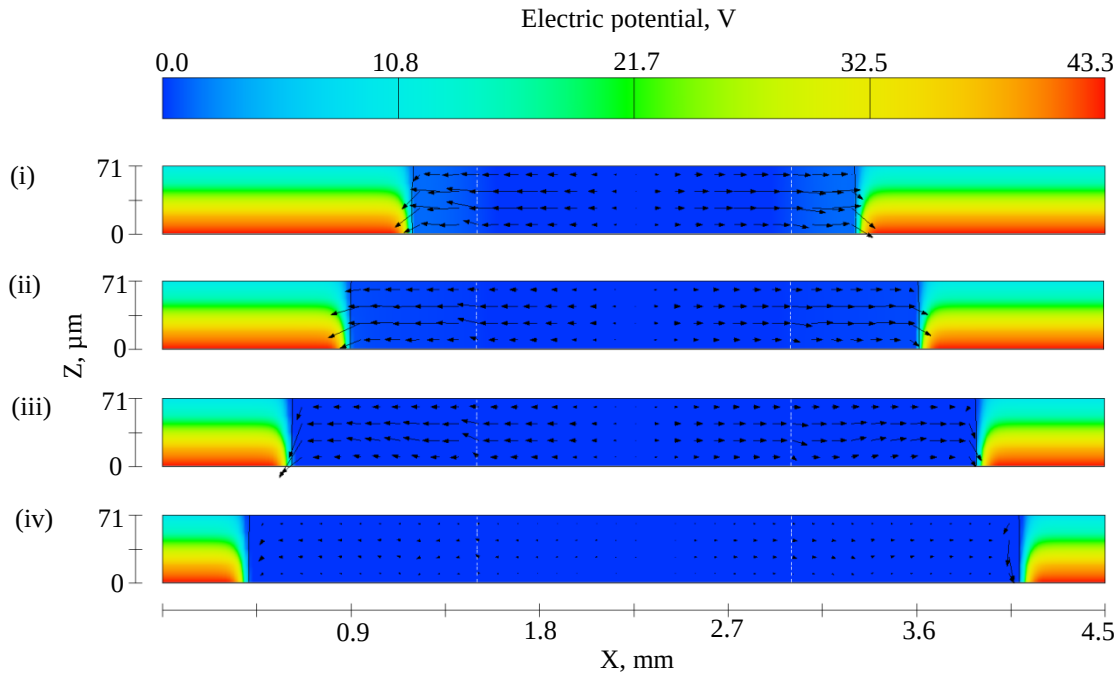


Figure 3.5: Electric potential (color) and velocity (vector) distribution along the vertical plane of symmetry (X-Z plane at Y = 0) at (i) 0.5 ms, (ii) 5 ms, (iii) 15 ms, and (iv) 35 ms. Electrode: 1.5 $mm^2$, Droplet: DI water (2.12 mm diameter), Plate gap: 70 µm.

of the interface. It is worth mentioning here that for an approximate model describing the motion of a droplet from electrode to electrode a poiseuille flow is commonly assumed. This conservative model accounts for the viscous dissipation far from the interface reasonably well. However, in case of developing a simple model of the flow rates in splitting a droplet, the above assumption would be result in highly inaccurate values due to the dominant two-dimensional velocity field inside the droplet. In any case, the z-component of velocity close to the droplet-air interface is not modeled. The strong field along the horizontal direction originates from the gradient of electric potential existing near the tri-phase contact shown in the figure as the densely packed potential contours. Even though the liquid is DI water (non-conductive), the potential inside the droplet is zero since the applied voltages were DC. This is fully in line with the theory in that as long as the applied voltage is DC or AC with frequency lower than a critical value the droplet will behave like a conductive liquid and the potential of the droplet will remain zero.

### 3.3.3 Successful and unsuccessful splitting

Investigation of symmetric droplet splitting was conducted for two commonly used sizes of electrode (1.5 mm × 1.5 mm and 1 mm × 1 mm). The size of the droplet in each case was such

that the diameter of the footprint on the hydrophobic surface is equal to the diagonal length of the underlying electrode. The aspect ratios, defined as the ratio between the diameter of the droplet footprint and the gap between upper and lower plates, were equal in both cases. The geometric and material properties used in CFD simulation are shown in Table 3.1. In order to simulate successful droplet splitting, the actuation voltages to the electrodes were increased stepwise in each simulation run while all other inputs were kept constant. If the simulation showed unsuccessful splitting, the actuation voltages would be increased by magnitudes proportional to the width of the neck existing during the final stage of droplet deformation. If the width of the neck in an unsuccessful splitting was found to be very narrow, this would indicate that successful splitting is possible with only a small increase in actuation voltage. Therefore, in this case, the actuation voltages were increased by small steps (e.g. 1 or 2 volts) and simulations were repeated until successful splitting was achieved. Results of CFD simulation were exported into text files and then, processed using MATLAB and Microsoft Excel. Specifically, the volumetric flow rates, the capillary numbers towards the left-side and right-side electrodes and the total wall shear from the upper and lower plates were extracted with a view to understand the mechanism of splitting. Flow rates were calculated by defining two porous surfaces with 100% porosity at the junctions between the center electrode and the two side electrodes. FLOW 3D® keeps record of volumetric flow rates through these surfaces at every time instants specified by the user. The capillary number, which expresses the relative strength of viscous forces with surface tension, is given by the following relation

$$Ca = \frac{\mu U}{\gamma_{lg}} \tag{3.3}$$

where $\mu$ is the viscosity, $U$ is the velocity and $\gamma_{lg}$ is the surface tension between liquid and air. This dimensionless number has been extensively studied in droplet microfluidics of channel based systems where droplets of a primary phase are manipulated in a continuously flowing secondary phase ([a]Christopher and Anna 2007). In those systems, the calculation of $Ca$ is simple as the $U$ can be approximated by the velocity of the continuous phase. However, finding the $Ca$ in droplet splitting on a digital microfluidic platform is not as straightforward as in channel-based systems. The reason is that the droplet deforms and the two ends advances during splitting and the magnitude of velocity field varies with longitudinal and transverse position. In this thesis, the average of the longitudinal components of velocity (i.e. X-component) along the vertical plane of symmetry passing through the longitudinal centerline was calculated in order to find the $Ca$. For the calculation of $Ca$ to the left-hand and right-hand sides, the velocity components starting from the junctions of the center and the side electrodes to the instantaneous positions of droplet fronts

on respective sides were considered. Since the droplet front along the longitudinal centerline represents best the speed of splitting, the above mentioned method of calculation results in good approximation of the values of $Ca$ in droplet splitting. The total wall shear for a given time instant was calculated by integrating the shear stresses for all the cells adjacent to the two solid surfaces over the droplet footprint area.

In the simulation of splitting in a DMFS with 1.5 mm × 1.5 mm square electrodes, the diameter and height of the droplet were 2.12 mm and 70 μm respectively. Successful droplet splitting was achieved with 52 V applied to the left-hand and right-hand side electrodes. Figure 3.6 shows simulation results in terms of flow rates and capillary numbers for 50 V and 52 V. Splitting was not possible with 50 V. The volumetric flow rates to either side reach maximum values within the first 2 milliseconds (ms) from the start of splitting. Thereafter, flow rates drop quickly showing exponential decays and beyond 50 ms, flow rates rarely exceed 1 nl/ms. Eventually, the deformation of droplet comes to an end. Although very low flow rates exist due to the presence of capillary waves, the net increase in liquid accumulation over the side electrodes becomes zero. The exponentially decreasing pattern in flow rate is also observed in successful splitting of a droplet with 52 volts. In this case, the peak flow rates exceed 6 nl/ms as compared to peak flow rates of ~5.86 nl/ms with 50 volts. The neck breaks up at about 92 ms and the flow rates suddenly increases up to a value of 6.5 nl/ms. This increase in flow rate is due to the release of surface tension force which had been opposing droplet deformation until the neck broke up. When the remaining portions of liquid from the center electrode are completely accumulated to the side electrodes, the two newly created droplets gradually move to the equilibrium position and achieve equilibrium shape. Since the flow rate is determined by the fluid velocity for a fixed geometry, the capillary numbers during splitting a droplet are also expected to follow similar pattern. As shown in Figures 3.6 (ii) and 3.6 (iv), the $Ca$ value reaches a peak within the first 2 ms and decays exponentially approaching zero value. Values of $Ca$ are expected to be smaller for simulation runs with lower voltages since fluid velocity depends on the applied voltage. This signifies that for a given liquid, dielectric material and geometry, there exists a minimum $Ca$ below which splitting is not possible. Beyond the minimum $Ca$, viscous forces dominate over the surface tension forces and the deformation of droplet can be sustained up to the point of neck break-up. Thus, the minimum voltage required for successfully splitting a droplet can be estimated from the critical $Ca$, provided there exists an appropriate model relating fluid velocity to applied voltage. The critical $Ca$ can also be useful in estimating the required voltage for splitting droplets of other liquids. Both experimental and numerical studies show that liquid velocity decreases with increase of viscosity. However, the extent to which velocity is

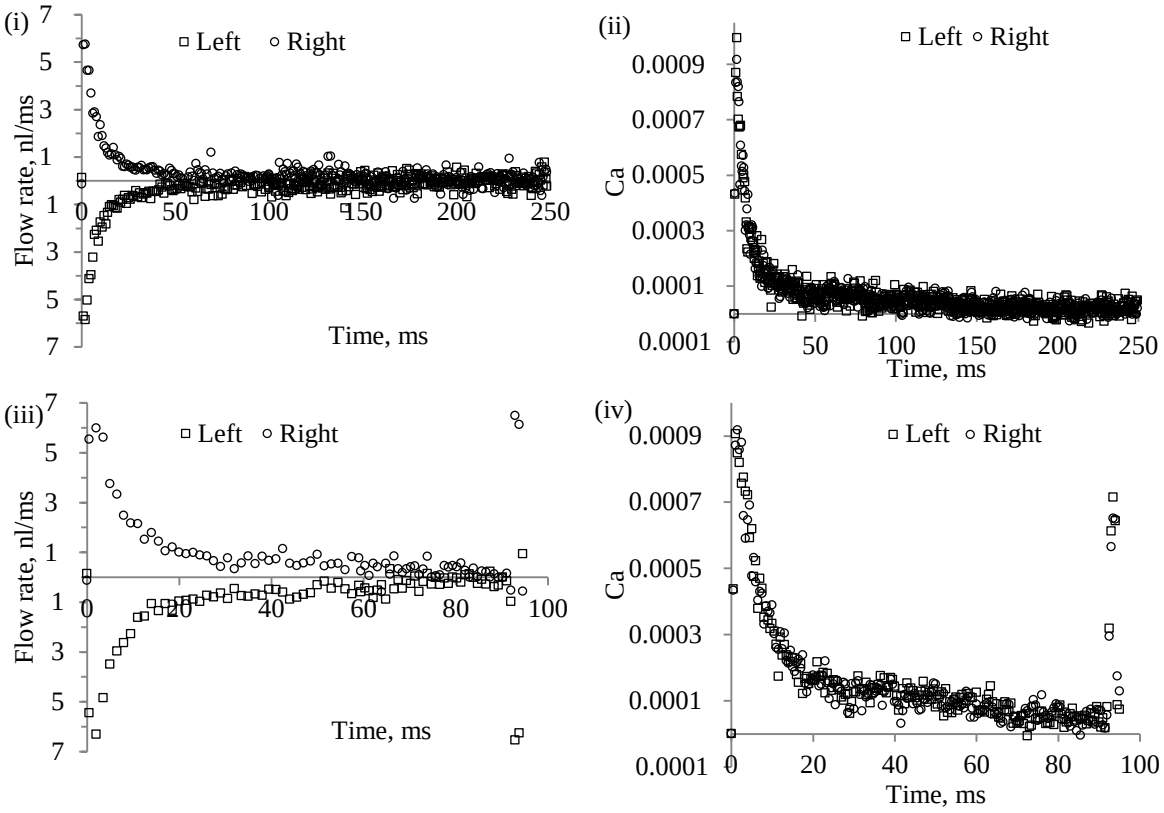


Figure 3.6: Results of splitting in a DMFS with 1.5 mm × 1.5 mm electrodes; (i) Flow rate, and (ii) Capillary number in unsuccessful splitting with 50 V; (iii) Flow rate, and (iv) Capillary number in successful splitting with 52 V.

reduced depends on whether the resistance to flow is determined by viscous shear alone or a combination of contact line friction and shear. The denominator in the definition of $Ca$, the surface tension between the liquid and the surrounding medium increases with viscosity. Consequently, higher voltages are required in order to achieve a $Ca$ greater than the critical value and thereby successfully split a droplet with high viscosity. It is noted in Figure 3.6 that the peak values of $Ca$ with 50 V are slightly greater than those with 52 V. This might have been due the fact that $Ca$ was calculated based on the X-component of velocity only. Calculation of velocity magnitude taking into account the other two components may result in $Ca$ values consistent with applied voltages.

Simulation results of splitting a droplet, having a diameter of 1.414 mm and a height of 46 µm, in a DMFS with 1 mm × 1 mm electrodes are shown in Figure 3.7. Droplet splitting

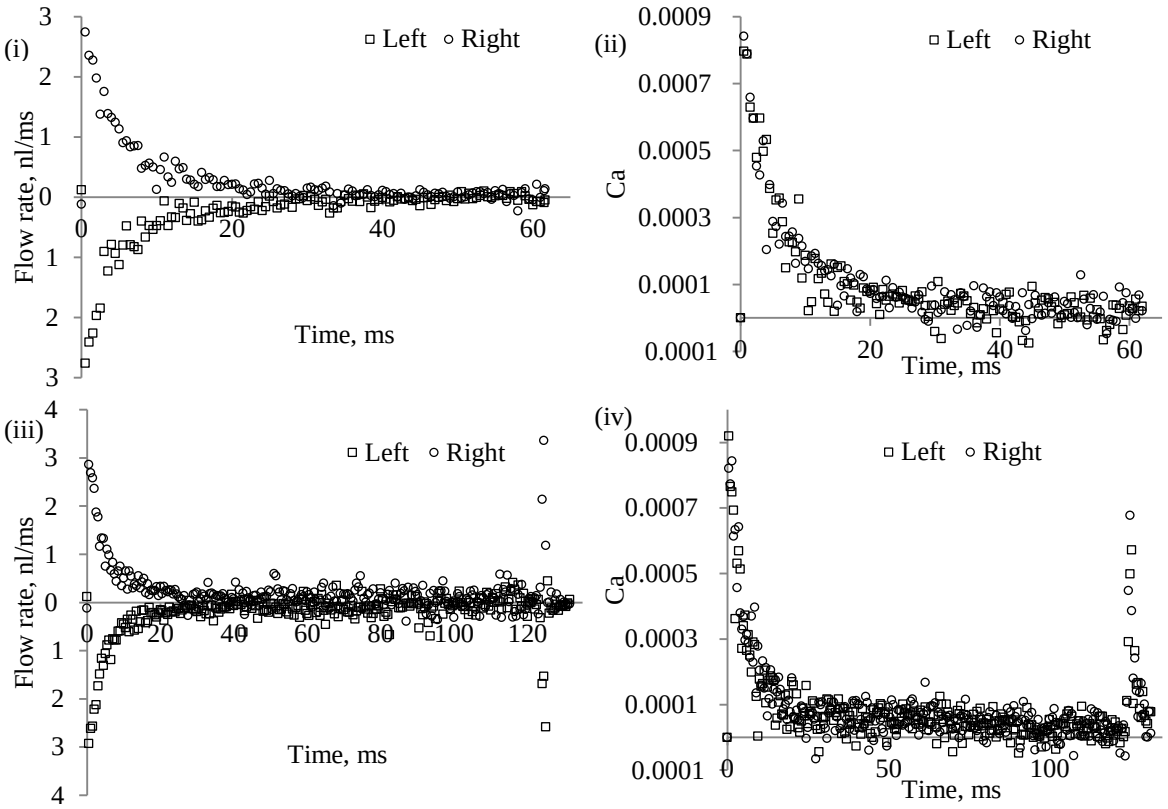


Figure 3.7: Results of splitting in a DMFS with 1 mm × 1 mm electrodes; (i) Flow rate, and (ii) Capillary number in unsuccessful splitting with 45 V; (iii) Flow rate, and (iv) Capillary number in successful splitting with 47 V.

was possible with 47 V applied to the side electrodes and the duration of the process was 124 ms. Thus, splitting a droplet in a DMFS with smaller electrodes requires lower voltages assuming the aspect ratio and droplet size to electrode size remain constant. This is quite intuitive since a smaller droplet means lower resistance originating from viscous shear, solid and liquid surfaces and inertia. The peak flow rates are also lower in magnitude because of lower actuation voltages and smaller gap between the plates. As a result, the total time to completely split a droplet on smaller electrodes is greater than the time needed on larger electrodes. The flow rates and the capillary numbers show the typical pattern consisting of a peak value followed by exponential decay. It can also be noticed that the peak values resulting from 47 V are greater than those from 45 V. The peak values of $Ca$ resulting from 1 mm$^2$ electrodes are nearly the same values resulting from 1.5 mm$^2$ electrodes. However, the values of $Ca$ decay faster and reduce to values below 0.0001 after ~20 ms, which explains the reason for longer duration of splitting process in the DMFS with 1 mm$^2$ electrodes.

The general pattern of exponential decay in liquid flow rate and velocity can be explained qualitatively by considering the sources of energy dissipation during the process of splitting a droplet. In case of splitting a droplet having air as the surrounding medium, the drag from air can be neglected since the density of air is much lower compared to that of water. Thus, energy is required to overcome the viscous shear and the contact line friction. In addition, splitting involves working against the surface tension that resists any deformation of the interface and thereby, exploiting additional energy. At the beginning, the electrowetting force applies to the small portion of the droplet residing over the energized electrode on either side. The actuation force acts strongly on the small mass of liquid while the viscous shear, which is proportional to the footprint area of the effective liquid, is low. The change in liquid-air interface area is also small during the early stage of splitting as the droplet deforms from a circular shape to an elliptical shape (when seen from top). Consequently, the liquid flows at a high rate towards the energized left- and right-side electrodes. As more liquid accumulates over the side electrodes, the mass of effective liquid upon which the same actuation force acts increases. The viscous shear also increases due to increase in liquid area. With continued deformation of the droplet, the radius of curvature at the neck decreases while the total liquid-air interface area increases at a higher rate. As a result, the amount of input energy converted to surface energy increases with advancement in splitting. Thus, the applied electrostatic energy cannot maintain the same flow rate as time advances. Deceleration of liquid caused by increased resistance to splitting results in the exponential decay in the flow rate and the velocity.

Droplet splitting is a process which involves not only the electrostatic force induced liquid flow but also the continuous deformation of the liquid-air interface near the center of the droplet. And according to the discussion in the previous sections, successful splitting requires continued necking until the pinch off. Thus, a competition exists between the viscous shear and the surface tension. Total shear forces originating at the upper and lower solid surfaces were calculated in order to investigate the impact of applied voltages to viscous shear as well as to feasibility of splitting. Figure 3.8 shows the total wall shear along with the force of surface tension with different voltages for two electrode sizes. Surface tension acts in containing the liquid within a total surface that minimizes energy and resists any deformation of the interface. Hence, any attempt to split a droplet by pulling liquid from both sides needs to work against the surface tension force. This opposing surface tension force is from multiplying the surface tension

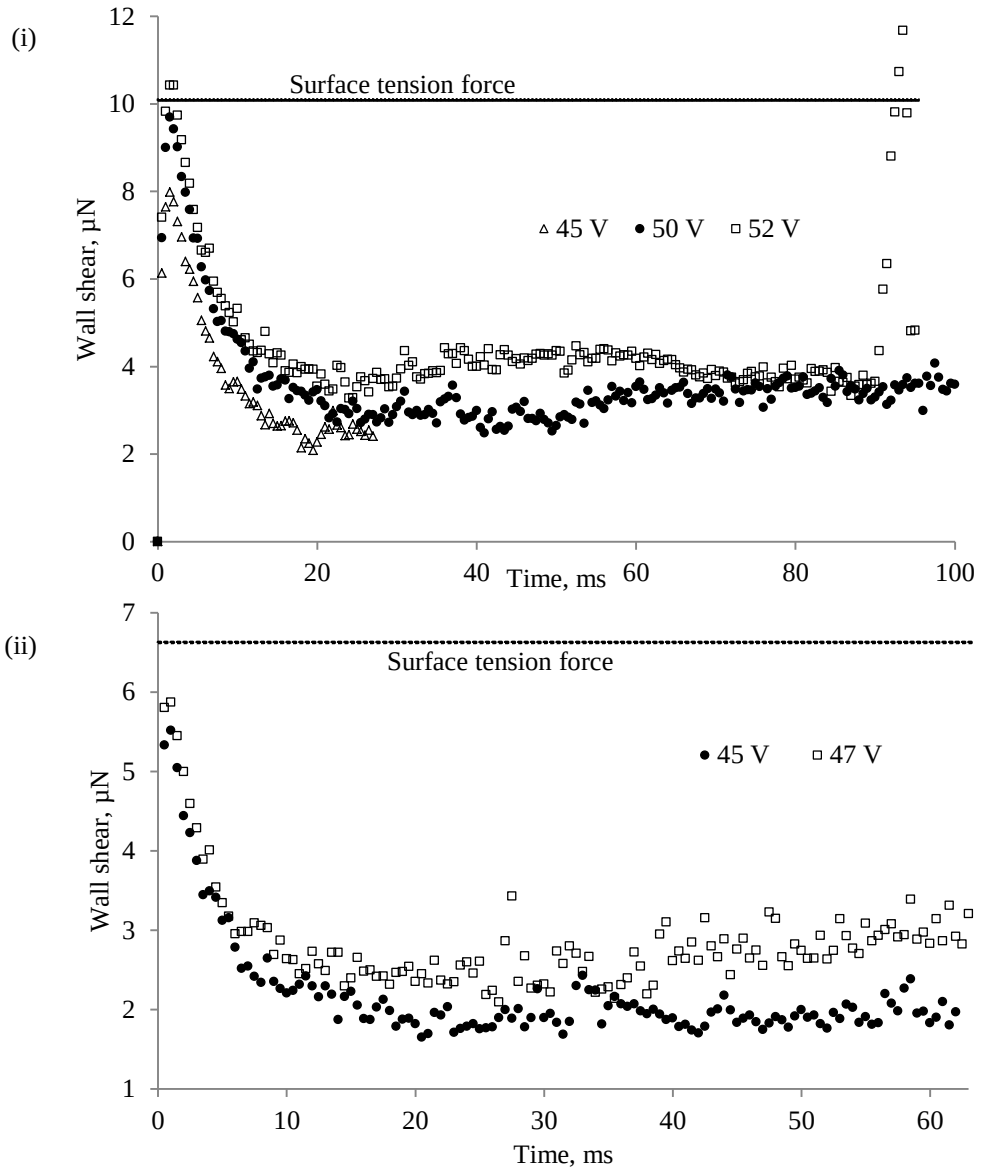


Figure 3.8: Total shear from the upper and lower hydrophobic surfaces during splitting in DMFS with (i) Electrode: 1.5 mm × 1 mm, and (ii) Electrode: 1 mm × 1 mm.

between water and air by the length of the gap between the two plates. This results in an approximate value of the force since the exact length of the droplet-air interface along the vertical plane is not considered here. However, the resulting values serve as good approximations of the exact values especially in the current case of comparative study. The shear forces reach maximum values within the one or two milliseconds of the application of actuation voltages. These maximum values determine the ultimate chance of successful splitting since the extent to which the magnitude of shear is reduced by the immediate decay depends on the maximum values. As

noticed in Figure 3.8 (i), the wall shear resulting from 52 V exceeds the surface tension force, reaches 10.4 μN and does not go below 3.3 μN throughout the splitting process. The peak values of shear in unsuccessful splitting are smaller than the surface tension force of 10.08 μN. However, the peak values of shear, both for successful and unsuccessful cases, in a DMFS with 1 $mm^2$ electrodes are lower than the surface tension force. Therefore, even though the peak of shear is lower than resistance from the surface, a droplet can be successfully split if the sustained value of shear during the necking phase is high enough for continuing the thinning of the neck.

# CHAPTER 4
# ASYMMETRIC SPLITTING: SIMULATION

In this chapter, the concepts of asymmetric splitting are described in relation with results obtained from CFD simulations. The first section explains how the level of applied voltage, the ratio between the voltages to the electrodes, and droplet size and aspect ratio influence asymmetric splitting. Next, the results of splitting with different aspect ratios of the droplet are presented. The final section presents the simulation results of asymmetric splitting with different ratios of voltages.

## 4.1 Preliminary concepts of asymmetric splitting

Asymmetric splitting is the process of dividing a droplet into two unequal droplets. In a DMFS, asymmetric splitting is performed by applying voltages of different magnitudes to both sides of the droplet. Ideally, a droplet residing over the center electrode and positioned at the centroid of the electrode has equal overlapped areas on the left- and right-side electrodes. These overlapped areas are prerequisites for the electrowetting force to be effective in starting liquid flows. Also, the perfect alignment of the droplet with the center electrode is necessary for an unbiased initial condition for splitting process. Any misalignment of the droplet results in unequal overlapped areas to both sides and in unequal actuation forces at the beginning of splitting even if the applied voltages are equal. Assuming a proper initial condition, application of unequal voltages to the electrodes will generate liquid flows of unequal magnitude towards the energized electrodes. Liquid from the center of the droplet will flow towards the front causing the formation of a neck over the center electrode. Under the favorable condition resulting from the combination of the properties of liquid and solid materials and the geometrical parameters, actuation forces on both sides continue to deform the droplet and the width of the neck continues to decrease. Ultimately, the neck pinches off and two sister droplets of unequal volumes are created. If the actuation force from the electrode with lower voltage is not strong enough, the liquid flow rate to the corresponding direction gradually decreases and at one point, liquid flow completely stops before the neck pinch-off. On the other side, liquid continues to flow since the voltage, and hence the actuation force, is stronger than the side with lower voltage. The radius of curvature of the neck does not decrease anymore. As a result, liquid from the weak side flows back towards the neck in order to maintain the supply of liquid towards the stronger side. Eventually, the splitting

of the droplet asymmetrically fails and the total liquid accumulates over the electrode with higher voltage.

### 4.1.1 Minimum voltage

Multiple CFD simulations were performed in FLOW 3D® in order to investigate the dynamics of asymmetric splitting and to identify the conditions necessary for successful splitting. In the preliminary investigation, simulations were repeated for a DMFS with 1.5 mm × 1.5 mm electrodes and having a gap of 70 μm between the upper and lower plate. Other inputs to the software were as described in Table 3.1. The droplet of DI water, having a diameter of 2.12 mm, was assumed to be aligned with the center electrode. In all the simulations, the voltage to the left-side electrode is always lower than the right-side electrode. Here, the main objective was to find the minimum voltage to the left-side required for successful asymmetric splitting. A typical scenario of unsuccessful splitting is shown in Figure 4.1 along with the potential color contours. Simulation results in terms of volumetric flow rates, capillary numbers and longitudinal components of electrowetting force for two cases of unsuccessful splitting – (a) Left: 40 V, right: 45 V and (b) Left: 45 V, right: 50 V, are shown in Figure 4.2. Flow rates in both cases reach their maximum values at about 2 ms from the instant voltages are applied. The maximum flow rate on the left side is lower than that on the right side due to weaker actuation force. Following the characteristic pattern, flow rates decay at exponential rates; although to the right-hand sides, the flow rates never drop below a positive value. On the left-hand sides, liquid flow diminishes continuously and after a certain time (23 ms for (a) and 30 ms for (b)), flow reverses to maintain the supply of liquid to the right-hand sides. The reverse flow from the left-side electrode continues with increased rate and after some time (e.g. 85 ms for case (a) as in Figure 4.2 (i)) no liquid remains over the left-side electrode. The plot of $Ca$ with time shows similar pattern of having a peak followed by an exponential decay. In general, the value of maximum $Ca$ is higher for higher voltages. The maximum $Ca$ on the right-hand side (45 V) for case (a) is approximately equal to that on the left-hand side (45 V) for case (b). Hence, there exists a strong correlation between the applied voltage and the $Ca$ through liquid velocity. The negative values of $Ca$ indicate reverse flow of liquid from the left-side electrodes for the above cases of unsuccessful splitting. The longitudinal component of electrowetting force on the right-hand side remains fairly constant whereas that on the left-hand side decreases slowly. When the rate of liquid flow to the right from left-side electrodes increases, the width of overlap along the edge of electrode decreases rapidly and thus, the actuation force to resist the flow to the right also decreases

rapidly. Consequently, liquid flows from the left-side electrode at accelerated rates towards the center electrode.

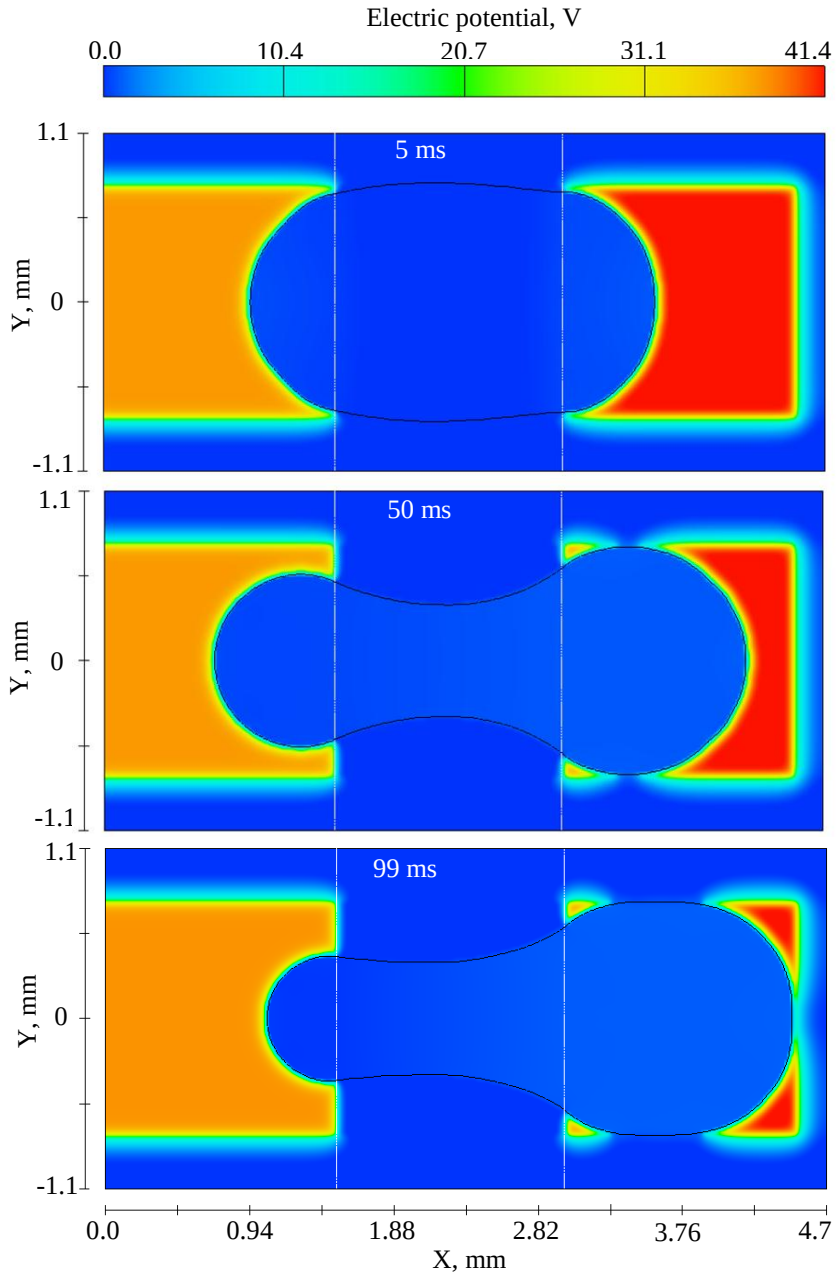


Figure 4.1: Unsuccessful droplet splitting with 45 V and 50 V applied to the left-side and right-side electrodes; Droplet dia.: 2.12 mm, droplet height: 70 µm, Dielectric thickness: 1 µm, $\varepsilon_r$: 15.

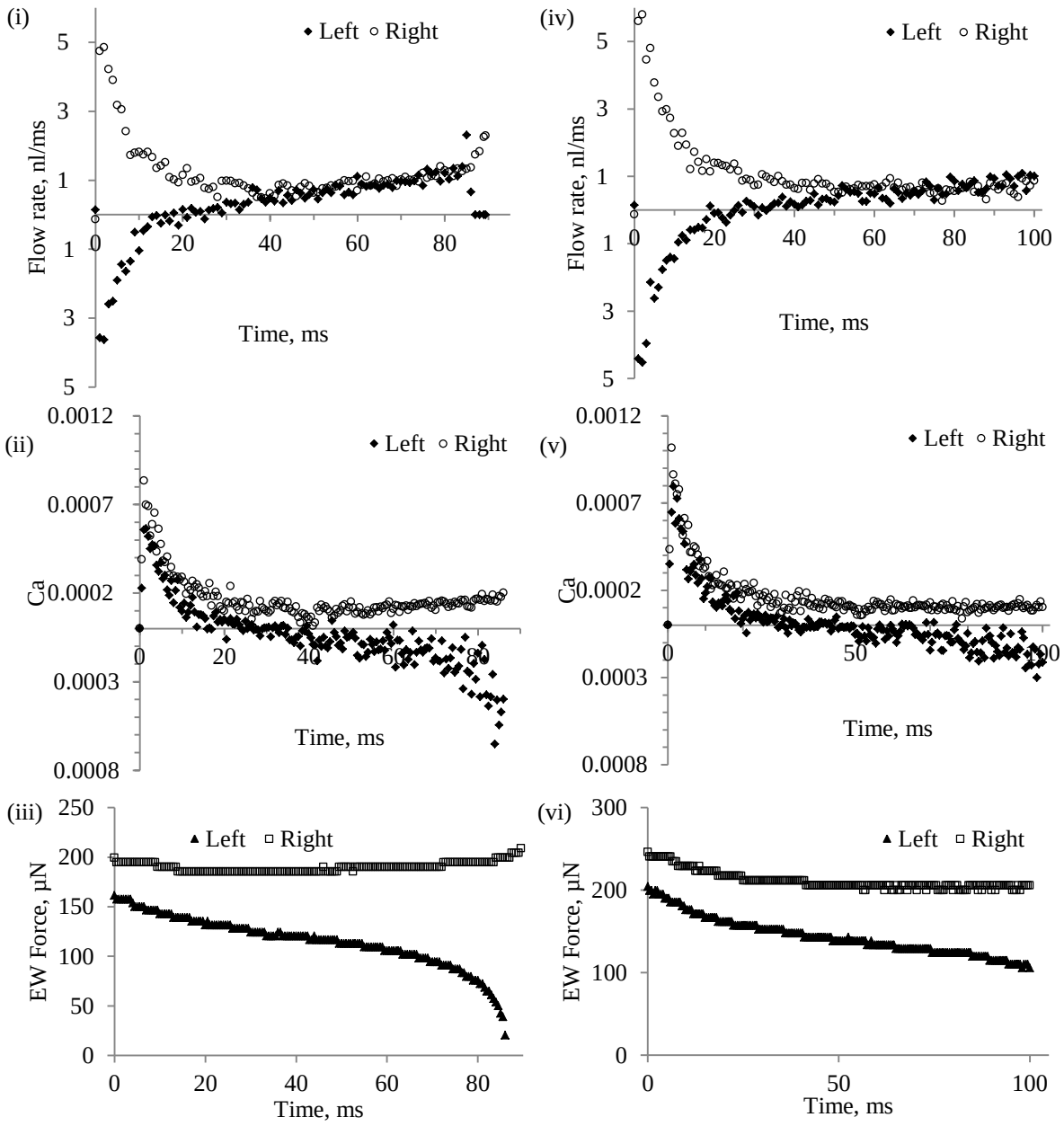


Figure 4.2: Simulation results (flow rates, capillary numbers ($Ca$) and electrowetting forces) of unsuccessful asymmetric splitting. 1st column: Left-side electrode: 40 V, right-side electrode: 45 V; 2nd column: Left-side electrode: 45 V, right-side electrode: 50 V.

When the applied voltages to the left-side and the right-side electrodes were increased from 45 V to 50 V and from 50 V to 60 V, the droplet was split into two unequal sister droplets. Simulation results are shown in Figure 4.3. Flow rate and $Ca$ plots represent the typical characteristics except that both have higher absolute peak values. The actuation force to the left is

now sufficient to generate liquid flow at a rate of 5.4 nl/ms within 1 ms since the start of the process. Due to a stronger force than the previous two cases, non-zero flow rates to the left can be maintained till the break-up of the neck at 71 ms. Consequent release of the opposing surface tension force causes the flow rates to increase sharply. The maximum $Ca$ on the left-side is 0.00083 as compared to 0.00052 and 0.00081 for 40 V and 45 V, respectively. Thus, successful asymmetric splitting requires that viscous forces be of certain level relative to the surface tension effects for a given size of the droplet. In other words, there exists a minimum voltage for a given droplet size and liquid property since velocity is dependent on the applied voltage. Figure 4.3 (iii) shows that the longitudinal component of electrowetting force on both sides decreases gradually. Initially, the overlap width across an electrode is equal to the width on either side. During the formation of neck and subsequent increase of the radius of neck, the overlap width decreases and as a result, the actuation force also decreases. The liquid front on the right-side reaches the end of right-side electrode at 40 ms owing to higher flow rate. The more the liquid covers the edge of right-side electrode, the less is the effective actuation force to the right. As the actuation force on the left-side becomes greater than the other side and continues to pull the liquid, the neck is pinched off eventually.

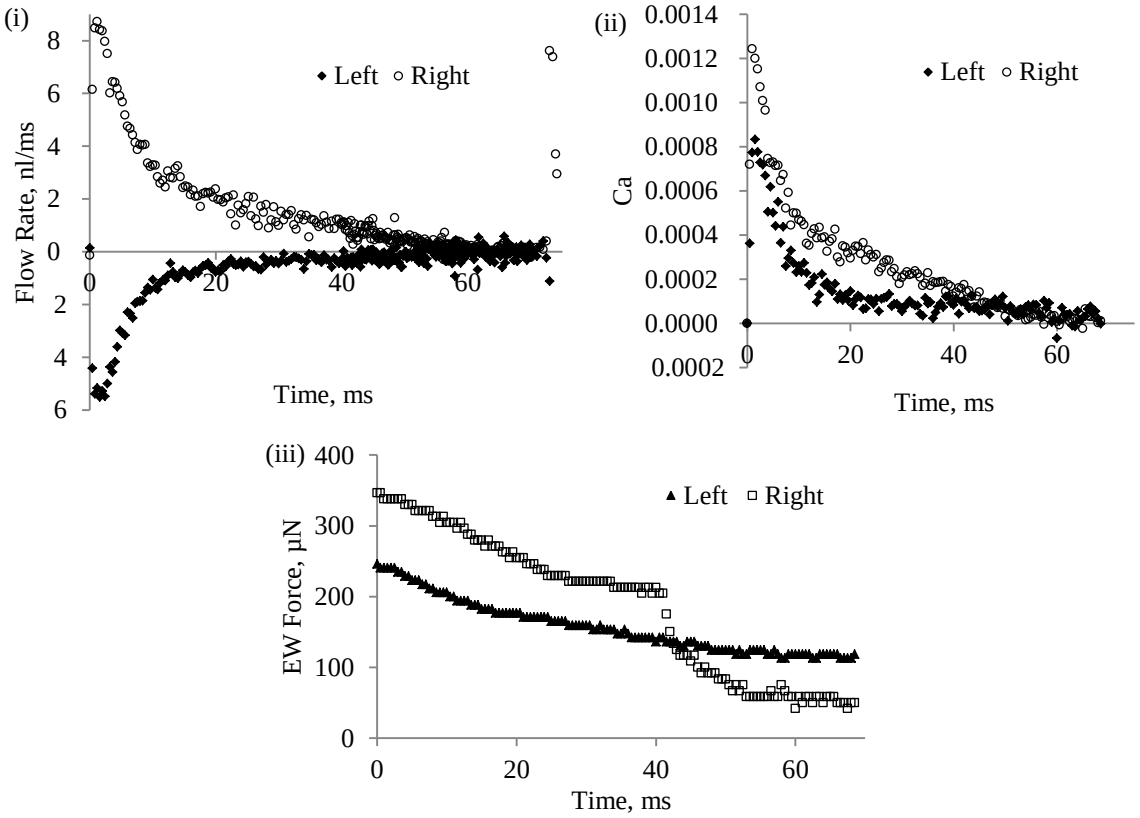


Figure 4.3: Simulation results (flow rates, capillary numbers ($Ca$) and electrowetting forces) of successful asymmetric splitting; left-side electrode: 50 V, right-side electrode: 60 V.

### 4.1.2 Voltage ratio and aspect ratio

In this section, the role of applied voltage ratio and droplet aspect ratio in asymmetric splitting is discussed. To split a droplet having an aspect ratio of 30.3 (diameter: 2.12 mm) in a DMFS with 1.5 mm × 1.5 mm electrodes, a minimum of 50 V to the left-side electrode was necessary. Now, if the diameter of the droplet is reduced to 1.7 mm in the same device, the aspect ratio decreases to 24.3. This also results in a reduction of overlap area as well as width of overlap on the side electrodes. Simulation with 50 V and 60 V to the left- and right-side electrodes showed that the droplet cannot be split asymmetrically and the results are shown in Figures 4.4 (i)-(iii). The maximum flow rates on either side are smaller than those in case of the larger droplet. The smaller width of overlap on the side electrodes results in weaker actuation forces at the beginning. However, due to smaller effective mass of liquid, the velocity along the vertical plane passing through the longitudinal centerline is higher, as found in Figure 4.4 (ii). The maximum values of $Ca$, i.e. 0.0012 and 0.002, are higher than those in the case of larger droplet. This indicates that even with a higher capillary number droplet may not be split if the size of the droplet (hence, the aspect ratio) is reduced. Liquid flow to the left stops at about 18 ms and a reverse flow towards the center electrode begins as the radius of curvature at the neck ceases to decrease further.

Asymmetric splitting of the droplet was possible when the voltage to the right-side electrode was increased to 70 V while the voltage to the left-side was kept at 50 V. The maximum flow rate and $Ca$ to the right is higher than those with 60 V due to stronger actuation force, shown in Figure 4.4. Moreover, the flow rate to the right decays at a slower rate. As a result, the neck on the center electrode becomes narrower at a higher rate and ultimately, pinches off at about 33 ms. The longitudinal component of electrowetting force increases during the first 2-3 ms due to increasing width of overlap of the droplet on the side electrode. However, as the radius of curvature at the neck becomes negative (i.e. concave) and continues to decrease, the widths of droplet overlap on the electrodes gradually decreases until the pinch-off. The wall shear originating from the hydrophobic surfaces on the upper and lower plates along with the surface tension forces are shown in Figure 4.5 for the successful and unsuccessful splitting. Wall shear on the lower plate is greater due to higher gradient in the X- and Y-component of velocity in the vertical direction compared to the shear on the upper plate. In general, the value of total shear reaches a maximum within ~2 ms and then decreases exponentially owing to the decrease in average fluid velocity. In case of unsuccessful splitting shown in Figure 4.5 (i), wall shear decays at a higher rate to a certain minimum value corresponding to the cessation of flow to the left. As liquid begins flowing to the right from the left-side electrode the total wall shear starts increasing

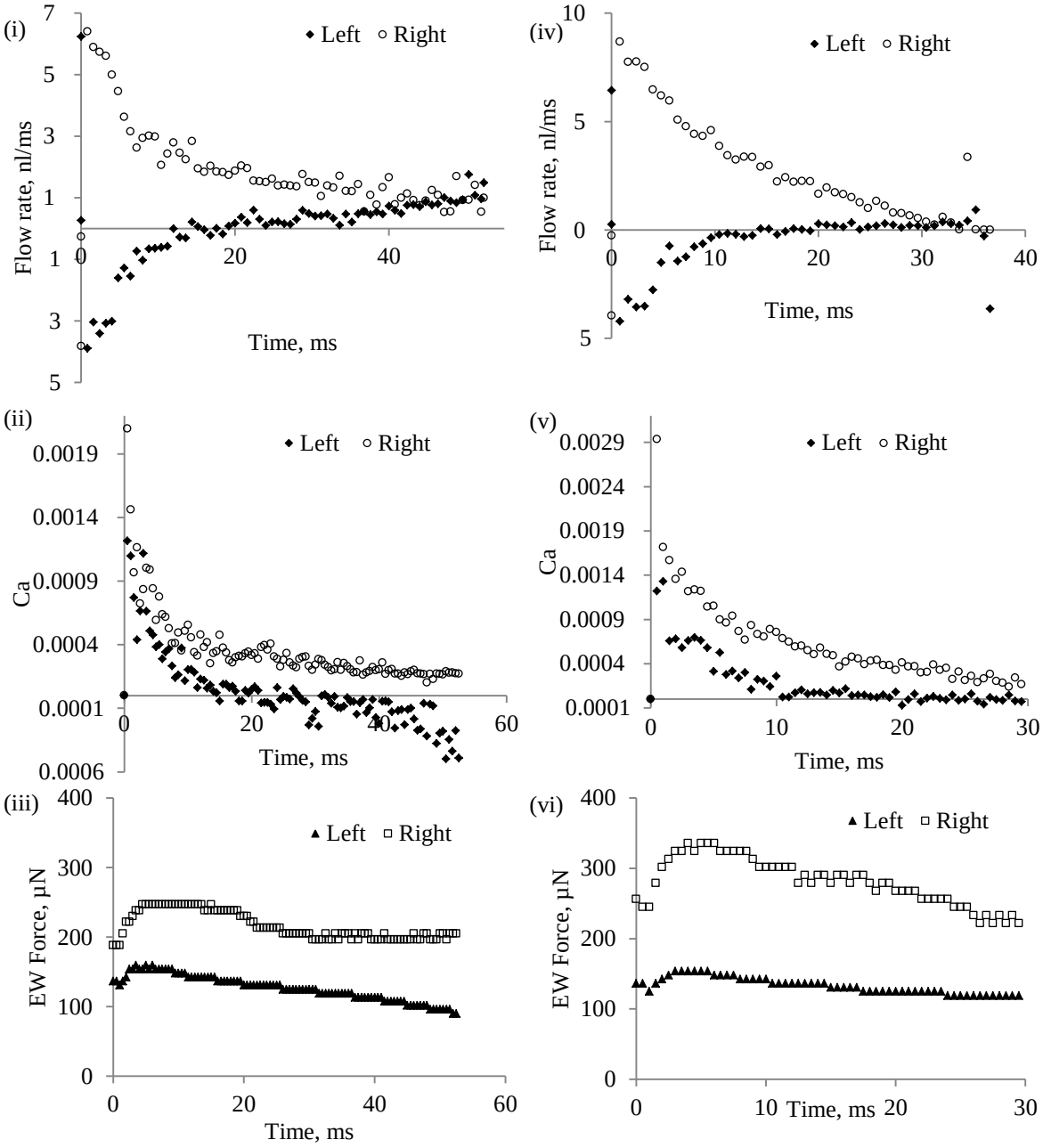


Figure 4.4: Flow rates (i, iv), Capillary numbers (ii, v), electrowetting forces (iii, vi) for asymmetric splitting of a DI water droplet having 1.7 mm dia. and 70 µm height; 1st column: Unsuccessful with 50 V to left and 60 V to right, 2nd column: Successful with 50 V to left and 70 V to right.

again. Figure 4.5 (ii) shows that the total shear in case of successful splitting decreases at a lower rate and this continues till the pinch-off of the neck occurs. It is noted that the total wall shear (10.87 µN) exceeds the surface tension force (10.08 µN) signifying that viscous stress is stronger than interfacial stress resulting in continuous deformation of the droplet-air interface. The

maximum wall shear (8.8 μN) in case of unsuccessful splitting is lower than the surface tension force and thus, viscous effects failed to overcome the interfacial resistance resulting in the end of narrowing of the neck.

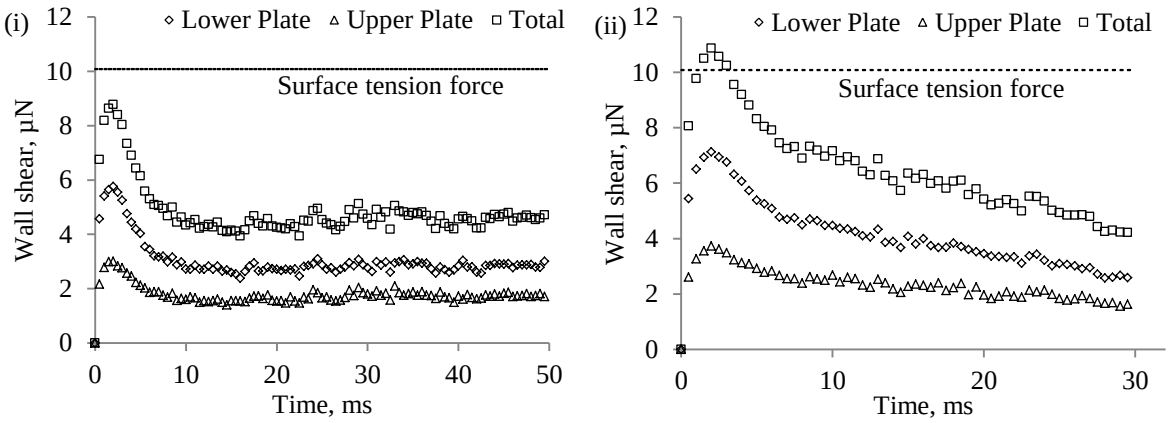


Figure 4.5: Wall shear in splitting a droplet having aspect ratio of 24.3 with (i) 50 V, 60 V (unsuccessful), (ii) 50 V, 70 V (successful)

The relative strength of viscous shear to surface tension determines the ultimate success in splitting a droplet asymmetrically. Since the total shear depends on viscosity, velocity and total area of the droplet, the applied voltages and the aspect ratio of the droplet are the two critical parameters in splitting a droplet of given viscosity. The area over which shear stress applies increases with the aspect ratio of the droplet, assuming that the gap between two plates remain constant. The average velocity of liquid increases with higher actuation voltages. A droplet of DI water having an aspect ratio of 24.3 could not be split with applied voltages of 50 V to left and 60 V to right, whereas a droplet having an aspect ratio of 30.3 was successfully split with the same voltage. The higher aspect ratio, provided the height of the droplet is constant, corresponds to a larger area of liquid-solid surface and stronger viscous effects with respect to surface tension. However, the droplet with an aspect ratio of 24.3 could be split when 50 V and 70 V were applied to the left-side and right-side electrodes. In this case, the higher voltage to the right yields higher average velocity and the consequent stronger viscous shear capable of deforming the interface till the break-up of the neck. If the droplet aspect ratio is reduced further, the above voltage pair will not be sufficient for successful splitting anymore. This is verified by the simulation results, shown in Figure 4.6, of splitting a droplet having aspect ratio of 22.86 (diameter: 1.6 mm) in the same DMFS with 50 V and 70 V applied to the left-side and right-side electrodes respectively. Due to smaller width of overlap on the side electrodes the electrowetting force is weaker than those for a

droplet of higher aspect ratio. As a result, the maximum flow rate to the left is lower compared to the previous cases and the liquid begins to flow towards the center electrode after around 10 ms. By 30 ms, no liquid remains in the space over the left-side electrode. Absence of actuation force to the left results in higher average velocity of liquid towards the right-side. This is depicted in all the Figures 4.6 (i), (ii) and (iii) as rapid increase in the data points. The maximum wall shear is less than the surface tension force implying that viscous effects are not strong enough to maintain the continuous deformation of droplet-air interface.

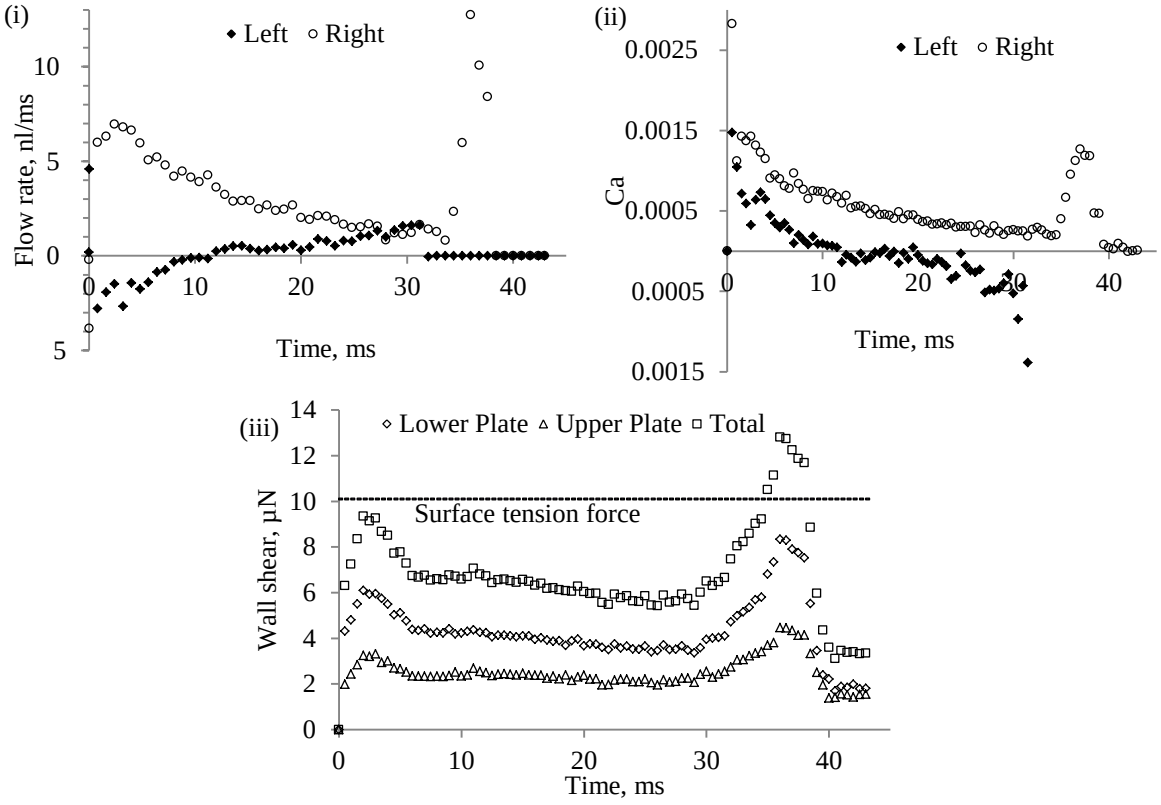


Figure 4.6: (i) Flow rates, (ii) capillary numbers, and (iii) wall shear in splitting a droplet having aspect ratio 22.86 with 50 V and 70 V

Larger ratio between applied voltages favors splitting as demonstrated above by showing the results of asymmetric splitting of a droplet having aspect ratio of 24.3. Applied voltages of 50 V and 70 V (ratio: 1.4) led to successful splitting while voltages of 50 V and 60 V (ratio: 1.2) failed to split. This implies that increasing the ratio between applied voltages while keeping the left-side voltage constant increases the average velocity and thereby, the total wall shear. In order to split the same droplet asymmetrically with voltages, of which the ratio is 1.2, the magnitude of voltage to the left-side must be increased. Higher voltages to either side of the droplet will

generate higher average velocity and consequently, the viscous shear will be stronger enough to overcome the resistance to deformation of the droplet-air interface. With 53 V and 63.6 V (ratio: 1.2) applied to the left-side and right-side electrodes, a droplet of DI water having an aspect ratio of 24.3 was successfully split and the results are shown in Figure 4.7. Due to higher voltages the maximum flow rates are greater than in the case of splitting a droplet having the same aspect ratio with 50 V and 60 V. The capillary numbers on the vertical plane of symmetry are also higher than those for aspect ratios of 24.3 as well as 30.3 with 50 V and 60 V to the electrodes. The maximum value of wall shear is slightly less than the surface tension force indicating that the viscous shear is just strong enough to cause continuous increase of the droplet-air interface till the neck breaks up at about 40 ms.

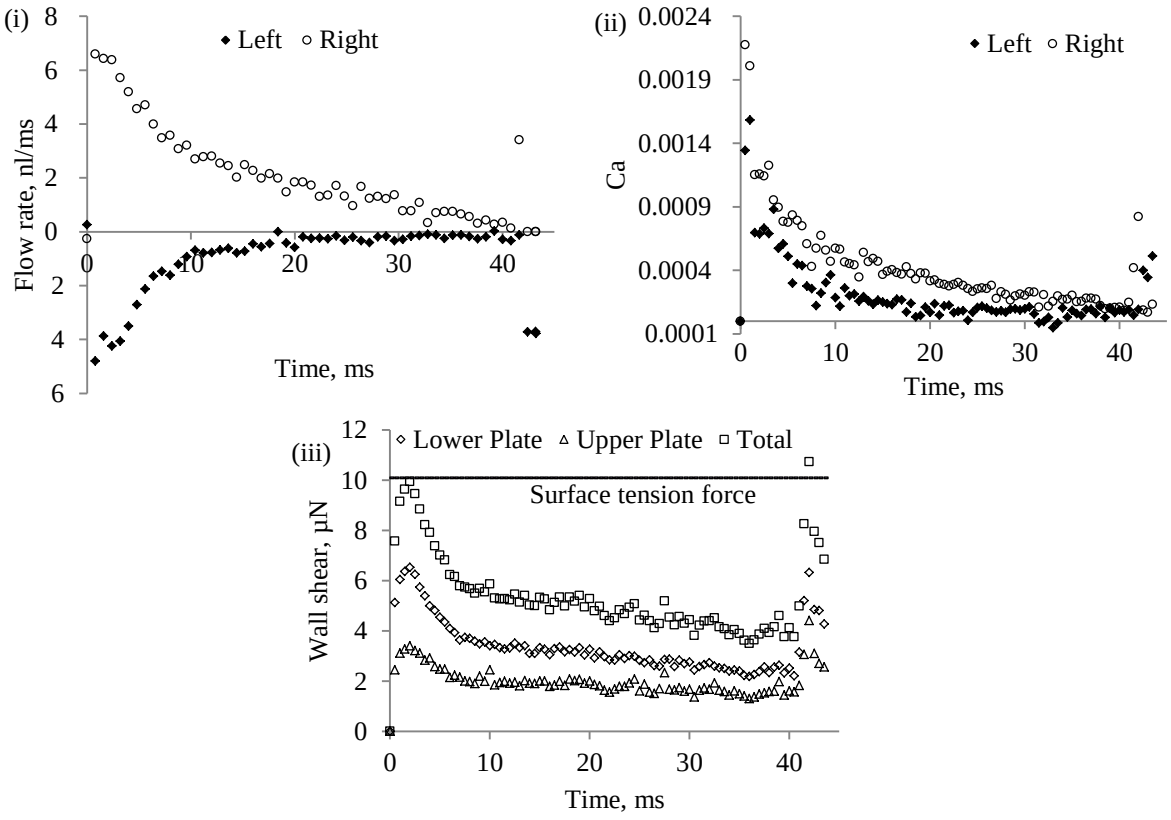


Figure 4.7: (i) Flow rates, (ii) capillary numbers, and (iii) wall shear in splitting a droplet having aspect ratio 24.3 with 53 V and 63.6 V

### 4.2 Variation of droplet aspect ratio

In this section, simulation results of studies in asymmetric splitting by varying the aspect ratio are presented. Droplet aspect ratio, defined as the ratio between the diameter and the height of a droplet, determines the relative strength of viscous shear to surface tension. For a given liquid and aspect ratio, the applied voltages must be high enough to increase the total shear. Thus, there exists a minimum required voltage for the left-side electrode, assuming that right-side voltage is higher, for successful asymmetric splitting. Moreover, the above minimum voltage will increase with lower ratios of applied voltages (right-side to left-side). The main goal of this section is to identify the minimum required voltages to the left-side electrode for different aspect ratios. This study considered two electrode sizes, i.e. 1.5 mm × 1.5 mm and 1 mm × 1 mm. Aspect ratios were changed by changing the gap between the upper and lower plates. Droplet size was chosen such that the diameter equals the diagonal length of the electrode in both cases. In addition, the ratio between the applied voltages was fixed at 1.41 for all the simulations. That is, whenever a change was made to the voltage for left-side, a corresponding change was also made to the other voltage so that the ratio remains constant at 1.41. The dimensions of computational domain and the properties of liquid and solid materials used as inputs for all the simulations are presented in Table 3.1.

The minimum voltage required for successful splitting of a droplet with a given aspect ratio was found by repeating simulations with different voltages. The appropriate voltage was determined through the method of bracketing. The first step in bracketing involved applying a high enough voltage, that can split the droplet and a lower voltage to the left-side electrode that fails to split. This process was iterated several times to narrow down the range of voltages in each iteration. Increment or decrement in voltage was also dependent on the dynamics of splitting observed through the plots of droplet deformation. In case of failed splitting, a large width of the neck remaining at the end of simulation time indicated a large increment in voltage required. In case of successful splitting, a slow rate of droplet deformation and a longer time to pinch-off the neck towards the last stage of splitting indicated that a small or no decrement of voltage would be necessary. Once the required voltage had been identified, a simulation with a marginally different voltage was performed in order to verify that the identified voltage was indeed the correct minimum voltage. Table 4.1 shows the parameters used in simulations and the results for the two electrode sizes.

Table 4.1: Properties of the droplet and the device used in study of aspect ratio variation and summary of results.

| Electrode size (mm × mm) | Droplet diameter (mm) | Droplet height (μm) | Droplet volume (nl) | Left-side voltage (V) | Right-side voltage (V) | Time to split (ms) |
|---|---|---|---|---|---|---|
| 1.5 × 1.5 | 2.12 | 50 | 176.5 | 45 | 63.6 | 35.5 |
| | | 70 | 247 | 50 | 70 | 38 |
| | | 90 | 317.5 | 64 | 90.5 | 11 |
| | | 110 | 388.28 | 74 | 104.65 | 7.5 |
| | | 130 | 458.66 | 78 | 110 | 12 |
| | | 150 | 529.48 | 87 | 123 | 10 |
| | | 170 | 600.08 | 96 | 135.76 | 9 |
| | | 200 | 705 | 105 | 148.5 | 7.5 |
| | | 250 | 882.46 | 108 | 152 | 8 |
| 1 × 1 | 1.414 | 46 | 72.23 | 47 | 66.5 | 24.5 |
| | | 72 | 113.06 | 63 | 89 | 10.5 |
| | | 100 | 157.03 | 74 | 104.6 | 6 |
| | | 133 | 204.14 | 91 | 128 | 9 |
| | | 165 | 259.1 | 107 | 151 | 7 |
| | | 200 | 314.06 | 112 | 158 | 4.5 |

Results of asymmetric splitting of droplets of varying aspect ratios with the minimum voltages to the left-side electrode (1.5 mm × 1.5 mm) are shown in Figures 4.8, 4.9, 4.10 and 4.11. Flow rates in all cases, shown in Figure 4.8, follow the same characteristics – the maximum flow rates occur within a few milliseconds from the time voltages are applied. Subsequently, flow rates decay at various rates until the pinch-off occurs. In general, the value of maximum flow rate increases with droplet height. However, the duration of high flow rates also increases with droplet height as a result of increasing mass moment of inertia. Figure 4.9 shows accumulation of liquid on the side electrodes with time. Since the amount of liquid accumulated is obtained from the integration of flow rates with respect to time, the results resemble the response of first order systems. In each case, equal amounts of liquid exist on both sides due to the droplet being larger than the electrode. As the gap between the plates is increased, the initial volume of liquid residing over the side electrode is also increased with droplet height. Towards the end of splitting before the pinch-off, the accumulated liquid increases by very small amounts. As soon as the neck pinch-off occurs, the remaining liquid from the center electrode is distributed between the side electrodes depending on the position of pinch-off. Hence, the volume of accumulated liquid quickly increases by a few nanoliters to tens of nanoliters. It is noted that the amount of liquid joining the low voltage side after the pinch-off increases with droplet height. The capillary numbers, shown in Figure 4.10, follow the characteristics similar to those of flow rates. Maximum values of $Ca$ are obtained between 1.5 ms to 2 ms from the beginning of splitting. The values of $Ca$ to the left-side for the droplet having a height of 150 μm are smaller than those for

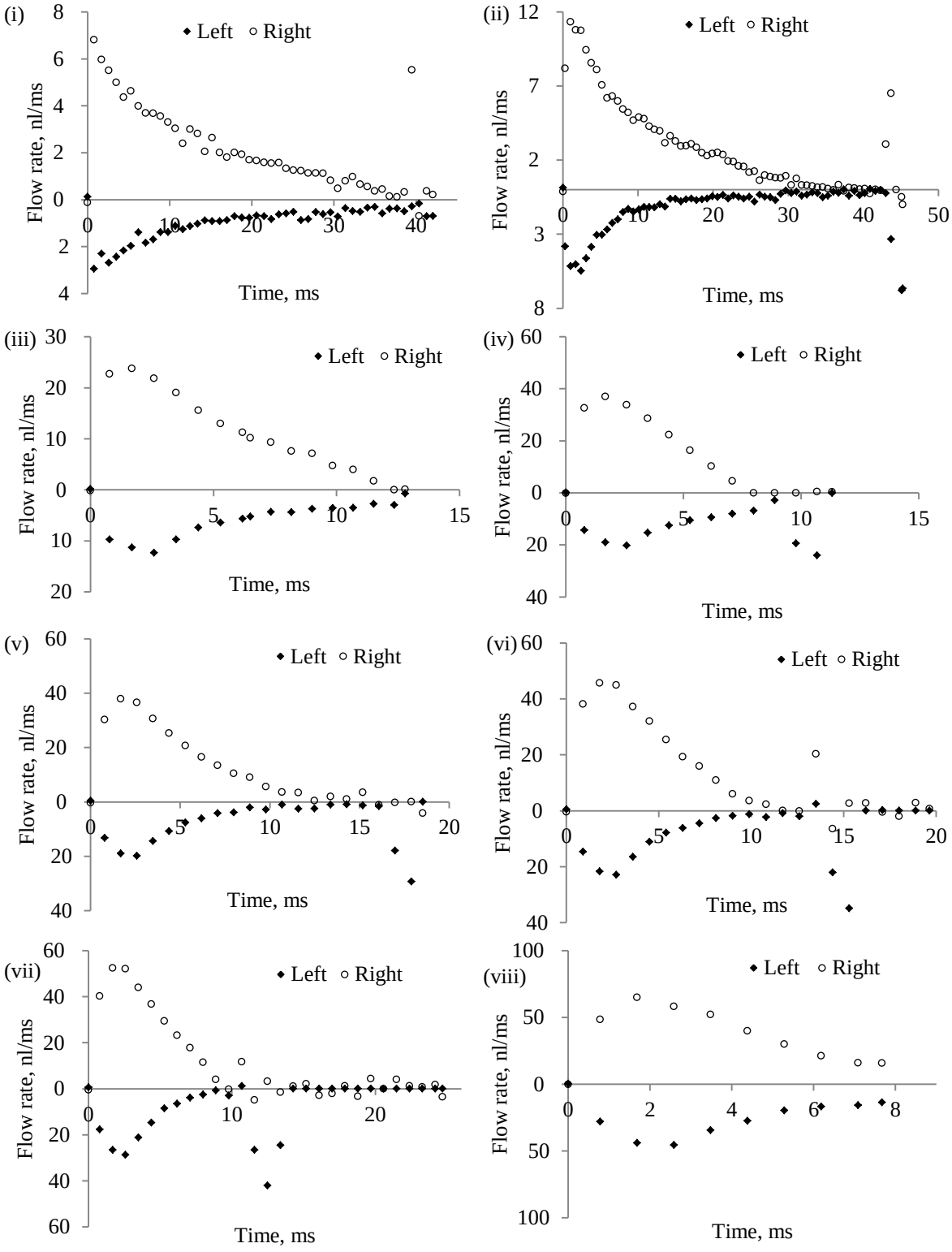


Figure 4.8: Flow rates in asymmetric splitting of a droplet having a diameter of 2.12 mm and heights of (i) 50 µm, (ii) 70 µm, (iii) 90 µm, (iv) 110 µm, (v) 130 µm, (vi) 150 µm, (vii) 170 µm, (viii) 200 µm.

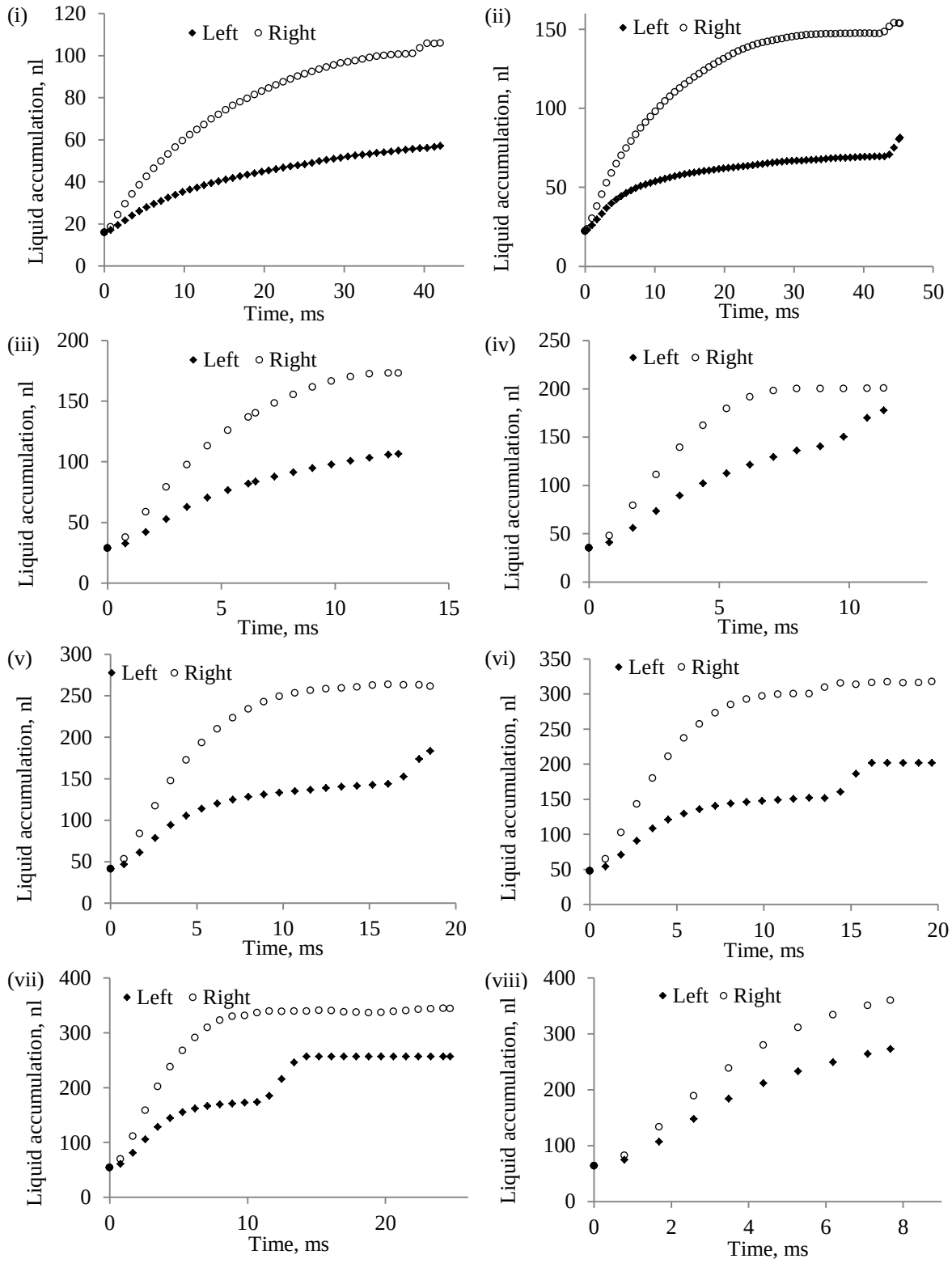


Figure 4.9: Liquid accumulation in asymmetric splitting of a droplet having a diameter of 2.12 mm and heights of (i) 50 µm, (ii) 70 µm, (iii) 90 µm, (iv) 110 µm, (v) 130 µm, (vi) 150 µm, (vii) 170 µm, (viii) 200 µm.

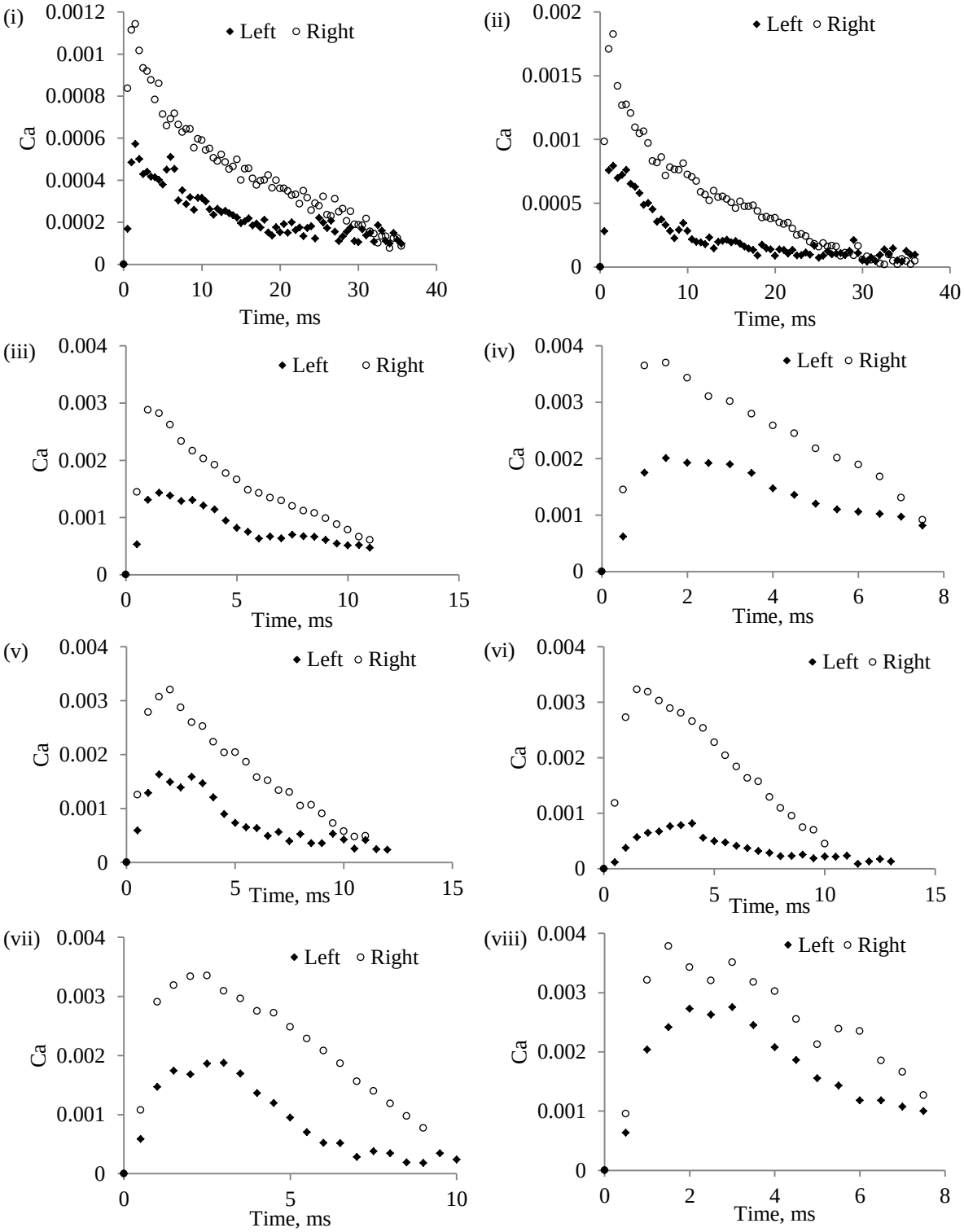


Figure 4.10: Capillary numbers in asymmetric splitting of a droplet having a diameter of 2.12 mm and heights of (i) 50 µm, (ii) 70 µm, (iii) 90 µm, (iv) 110 µm, (v) 130 µm, (vi) 150 µm, (vii) 170 µm, (viii) 200 µm.

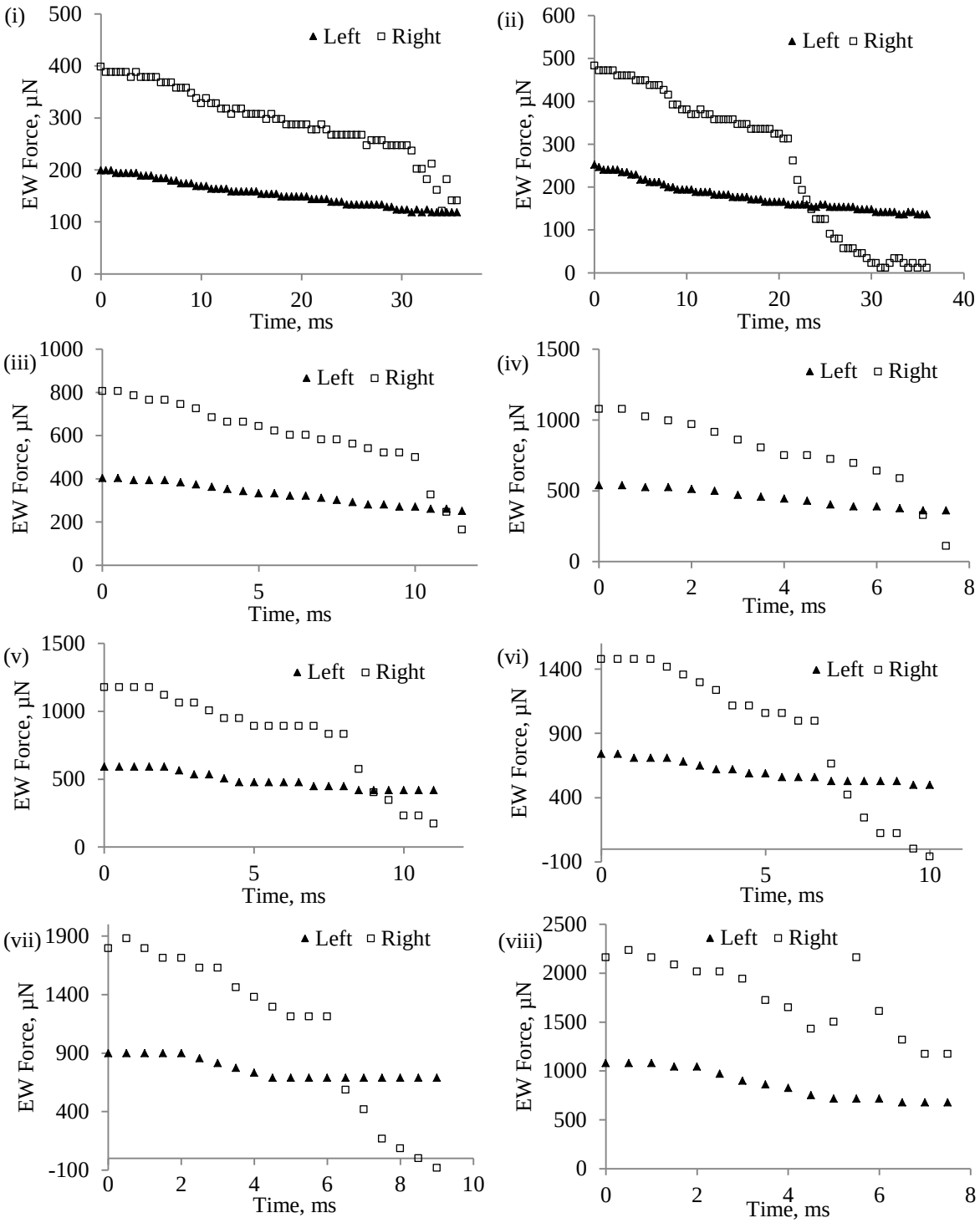


Figure 4.11: Longitudinal component of electrowetting force in asymmetric splitting of a droplet having a diameter of 2.12 mm and heights of (i) 50 µm, (ii) 70 µm, (iii) 90 µm, (iv) 110 µm, (v) 130 µm, (vi) 150 µm, (vii) 170 µm, (viii) 200 µm.

any other case. Contrarily, the values of $Ca$ to the left are not significantly lower than those to the right for the droplet having 200 µm. Figure 4.11 shows that the longitudinal components of electrowetting force in all the cases are of maximum values at the beginning of splitting. Since the magnitude of force is proportional to the width of overlap of the droplet across the junction of center and side electrodes, the magnitude decreases with narrowing of the neck. However, the magnitude of electrowetting force to the right decreases at a much higher rate when the liquid front reaches the end of right-side electrode.

The volume of liquid and the length of droplet-air interface along the vertical plane increases with droplet height. Also, the droplet deformation and the break-up of neck are the results of competing forces originating from surface tension and shear stress. Therefore, the relative strength of total shear in each case of varying aspect ratio must be sufficient to overcome the force of surface tension. The total wall shear for successful asymmetric splitting with minimum voltage to the left-side electrode is shown in Figure 4.12 for a droplet height of (i) 50 µm, (ii) 70 µm, (iii) 90 µm and (iv) 110 µm. The maximum shear occurs at 1.5 - 2.5 ms and the magnitude exceeds that of surface tension force in all cases. The values of maximum shear as well as the difference between the surface tension force and total shear increase with droplet height. Moreover, the total shear remains greater than the surface tension force for a significant portion of the total splitting time.

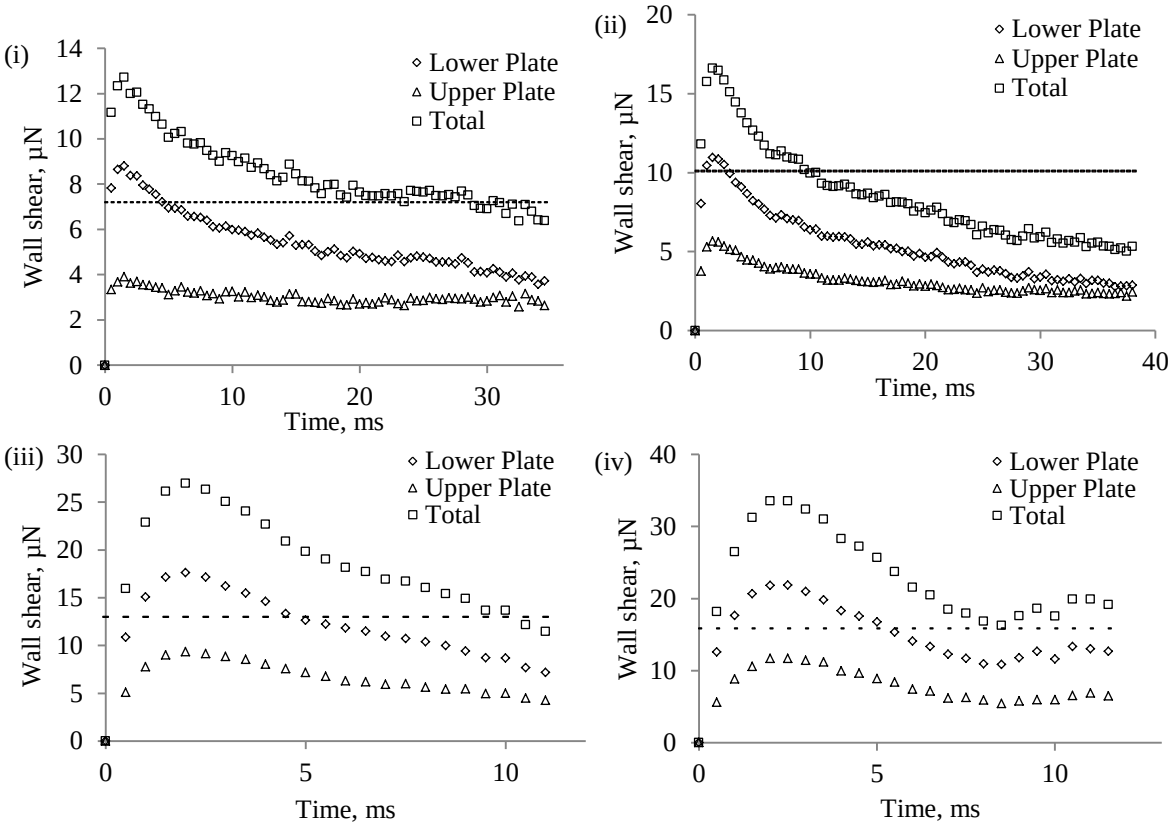


Figure 4.12: Wall shear in asymmetric splitting of a droplet having a diameter of 2.12 mm and heights of (i) 50 µm, (ii) 70 µm, (iii) 90 µm, and (iv) 110 µm

Results of asymmetric splitting are presented in Figure 4.13. The minimum voltage to the left-side electrode required for successful splitting is plotted against droplet height for the two electrode sizes. Increase in droplet height increases resistance from surface tension as well as increases droplet mass. As a result, higher voltages are required to generate stronger actuation forces so that the resistance to deformation originating from surface tension as well as inertia can be overcome. Also, splitting a droplet of same height requires higher voltage in a DMFS with smaller electrodes than in case of larger electrodes. The reason for this is the reduction of droplet footprint area on the solid surface. As the surface tension force does not change, higher velocity must be generated by applying higher voltage so that the viscous shear overcomes interfacial resistance. By utilizing the dimensionless electrowetting number (EWN) and the aspect ratio, the same result is shown in Figure 4.13 (ii) which will be useful for selecting the appropriate voltages for real experiments. The aspect ratio decreases with droplet height provided that the diameter remains constant. Hence, lower voltages, and thereby smaller EWNs, are required to successfully split droplets of higher aspect ratio. A number of guidelines can be derived from the above

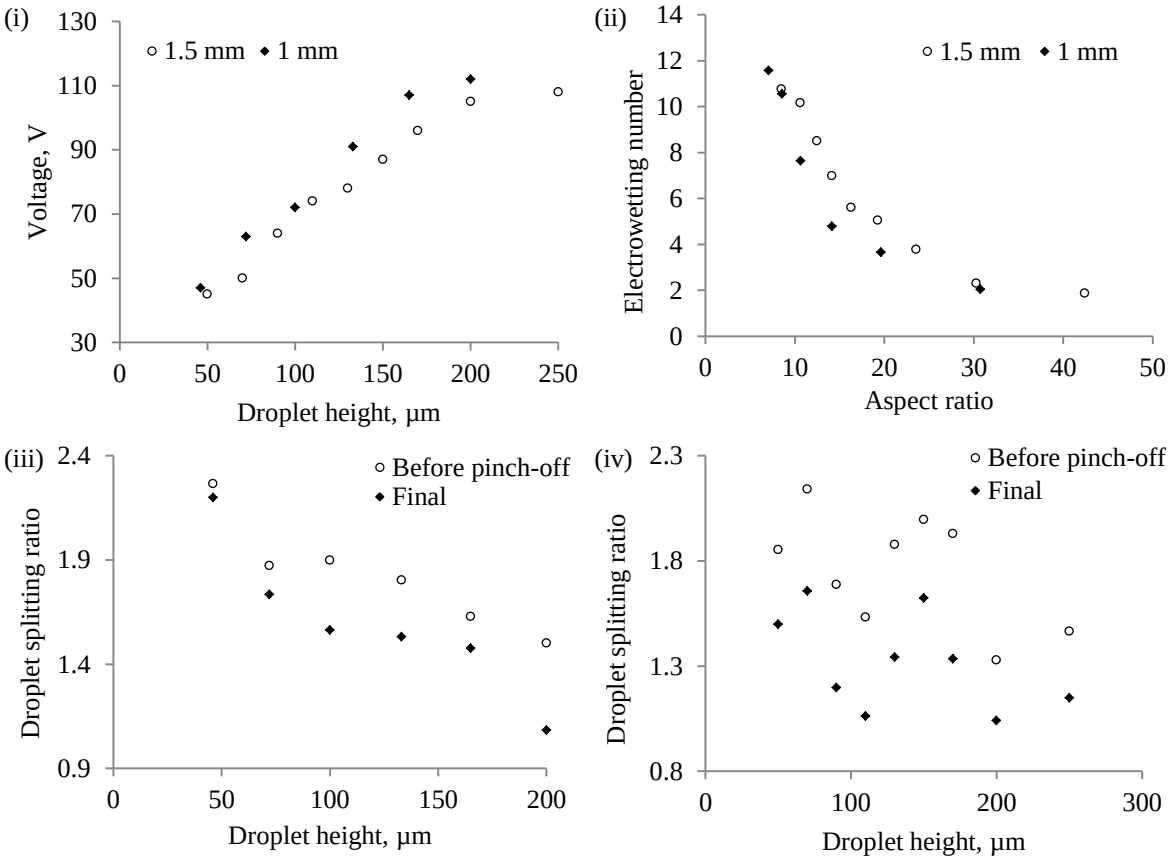


Figure 4.13: Summary of asymmetric splitting with aspect ratio variation; (i) minimum voltage vs. droplet height, (ii) electrowetting number vs. aspect ratio, (iii) Droplet splitting ratio vs. droplet height for 1 mm × 1 mm electrode, and (iv) Droplet splitting ratio vs. droplet height for 1.5 mm × 1.5 mm electrode

relation since the EWN includes the thickness and property of dielectric layer and the surface tension of the liquid. Any change of material or dimension will have to be accompanied by a necessary change in the voltage. For instance, if a liquid with surface tension lower than DI water is to be used, the corresponding EWN will be greater than the minimum value required for splitting. Therefore, the applied voltage can be reduced such that the appropriate EWN is obtained. This is quite intuitive since a liquid with lower surface tension introduces weaker resistance to deformation of the interface. The ratio between the volumes of accumulated liquid on both sides just before the neck pinch-off and after completion of the process is shown in Figures 4.13 (iii) – (iv) for the two electrode sizes. The liquid ratios are always higher before pinch-off than those after completion of splitting due to unequal amounts of liquid distribution towards the side electrodes. Generally, liquid ratios decrease with increasing droplet height although this correlation is weaker in case of 1.5 mm electrodes. The reason for this variation is

not properly understood and further investigation is required taking into account the numerical aspects as well as the other physics which were not modeled in this investigation.

### 4.3 Variation of voltage ratio

Both the dynamics and the outcome of asymmetric splitting are directly related to the magnitudes of voltage and the ratio between the voltages applied to the side electrodes. There exists a voltage level for the left-side electrode, assuming that voltage on the right-side is higher, below which asymmetric splitting fails. This level shifts upwards for splitting the same droplet with a lower ratio between the voltages. Since splitting involves a complex process governed by nonlinear transient equation, there is no simple method of determining the final ratio between the volumes of sister droplets in relation to that between the applied voltages. The effects of variation of the ratio between voltages were investigated through CFD simulations performed in FLOW-3D® and this section presents the simulation results in terms of flow rates, liquid accumulation, splitting ratio and time to split. All the simulations were performed considering a DMFS with 1.5 mm × 1.5 mm electrodes, a gap of 70 μm between the upper and lower plates and the properties of dielectric layer and liquid shown in Table 3.1. A sequence of snapshots from simulation, shown in Figure 4.14, portrays the typical characteristics in successful splitting with asymmetric voltage application. Figure 4.15 shows the results of asymmetric splitting of a droplet having a diameter of 2.12 mm for the voltage ratios of 1.2 to 2 while the voltage to the left-side electrode was fixed at 50 V. The maximum values of flow rates to the right-side are higher for larger voltage ratios, shown in Figure 4.15 (i). However, the rate of increase in flow rates gradually diminishes at higher ratios. High flow rate results in quick accumulation of liquid and fill up of the space over the right-side electrode. As the front of the liquid covers the end of that electrode, the longitudinal component of actuation force starts to vanish. As a result, the rate of increase in the volume of liquid to the right-side approaches zero before the pinch-off of the neck, shown in Figure 4.15 (ii). After the pinch-off, the flow rates go up significantly for a few milliseconds until the remaining portions of liquid from over the center electrode completely moves to the side electrodes. Consequently, the volume of liquid in the newly created droplet on the right-side electrode increases. This increase in liquid volume to the left-side is greater for higher voltage ratios, as noticed in Figure 4.15 (iii). Since the voltage to the left-side electrode is 50 V in all the cases, flow rates follow the same trajectory until the pinch-off.

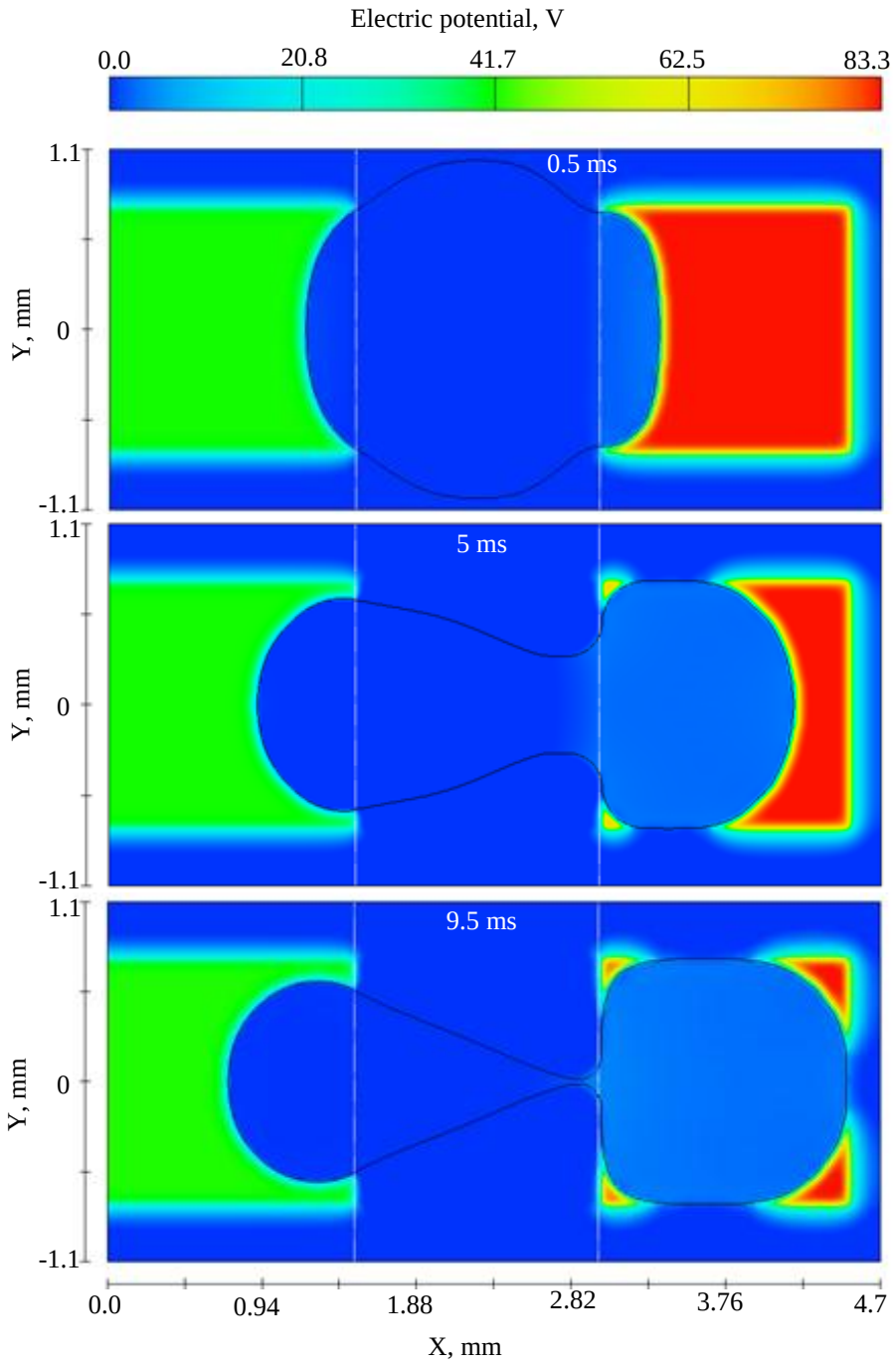


Figure 4.14: Asymmetric splitting of a droplet (dia: 2.12 mm, height: 70 µm) with 50 V and 100 V applied to left-side and right-side electrodes (1.5 mm × 1.5 mm); Dielectric layer: 1 µm, $\varepsilon_r$: 15.

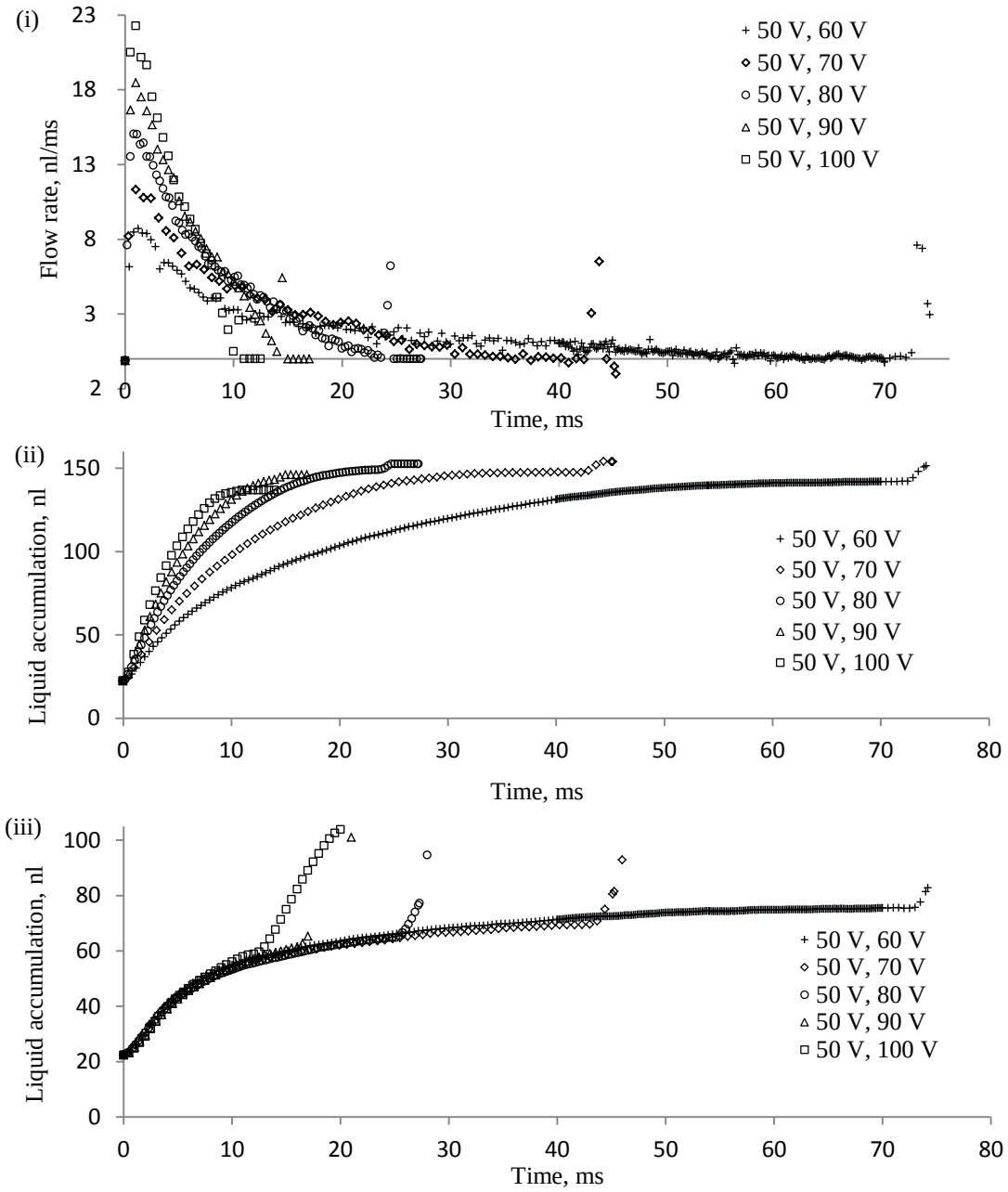


Figure 4.15: Results of voltage ratio variation with constant left-side voltage of 50 V; (i) Flow rates to the right-side, (ii) liquid accumulation to the right-side, and (iii) liquid accumulation to the left-side; Droplet dia.: 2.12 mm, height: 70 µm, electrode: 1.5 mm × 1.5 mm.

The effect of varying the ratio between applied voltages in asymmetric splitting of the droplet was investigated with higher levels of voltage. The voltage to the left-side electrode was constant at 65 V, while that to the right-side electrode was increased from 74 V to 105 V. The dimensions and properties of materials were the same as above. Figure 4.16 (i) depicts that the

maximum flow rates are higher resulting in faster splitting and fill up of the space to the right. However, the change in the total liquid volume after pinch-off is very small and cannot be identified in Figure 4.16 (ii).

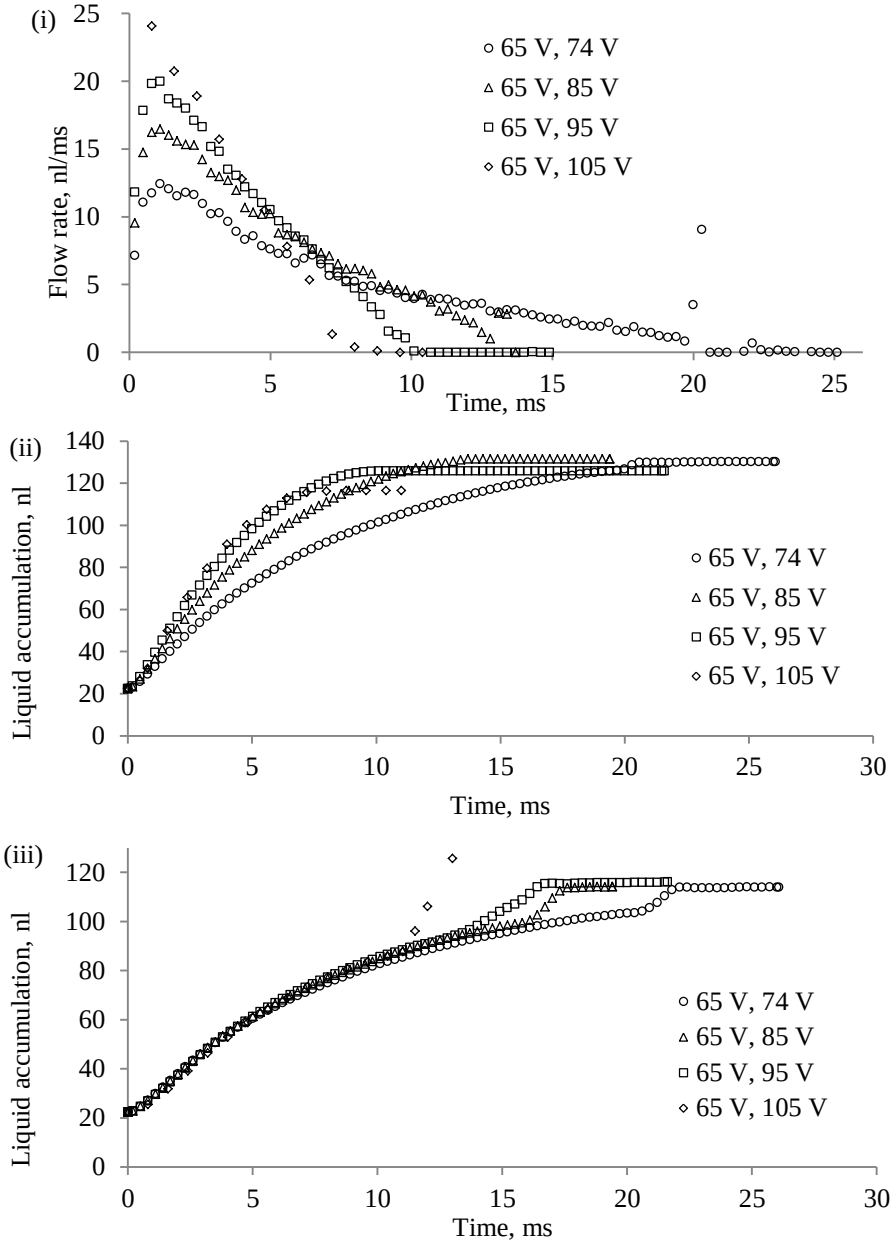


Figure 4.16: Results of voltage ratio variation with constant left-side voltage of 65 V; (i) Flow rates to the right-side, (ii) liquid accumulation to the right-side, and (iii) liquid accumulation to the left-side; Droplet dia.: 2.12 mm, height: 70 µm, electrode: 1.5 mm × 1.5 mm.

It is noted that when the voltage to the right-side electrode was increased to 105 V, the final volume of the corresponding droplet was smaller compared to those in the other cases. The flow patterns on the left-side, shown in Figure 4.16 (iii), in each of the cases were similar due to the voltage level being constant. However, the volume of liquid added to the left after the pinch-off is higher for higher voltage ratios.

Asymmetric splitting by varying the voltage ratio was also investigated for a different aspect ratio in the same the same DMFS. The diameter of the droplet was decreased to 1.7 mm resulting in an aspect ratio of 24.3. The voltage to the left-side electrode was fixed at 60 V while that to the right-side electrode was increased from 70 V to 100 V. Simulation results are shown in Figure 4.17. The flow rates to the right-side follow the characteristic pattern, however, with oscillations near the peak. This might have resulted from the capillary waves generated due to high rate of deformation coupled with the fact that the droplet-air interface area is smaller compared to the larger droplets in previous two cases. Figure 4.17 (ii) shows that the increase in the volume of liquid on the right-side electrode is not very significant. Besides, the final volume of accumulated liquid on the right-side is lower for higher ratios of voltages. This implies that the position where the neck pinches off is very close to the right-side electrode and hence, almost the entire volume of liquid from the center electrode joins the droplet on the left-side. However, the rate of liquid accumulation on the left-side is same for all the cases due to the voltage being constant.

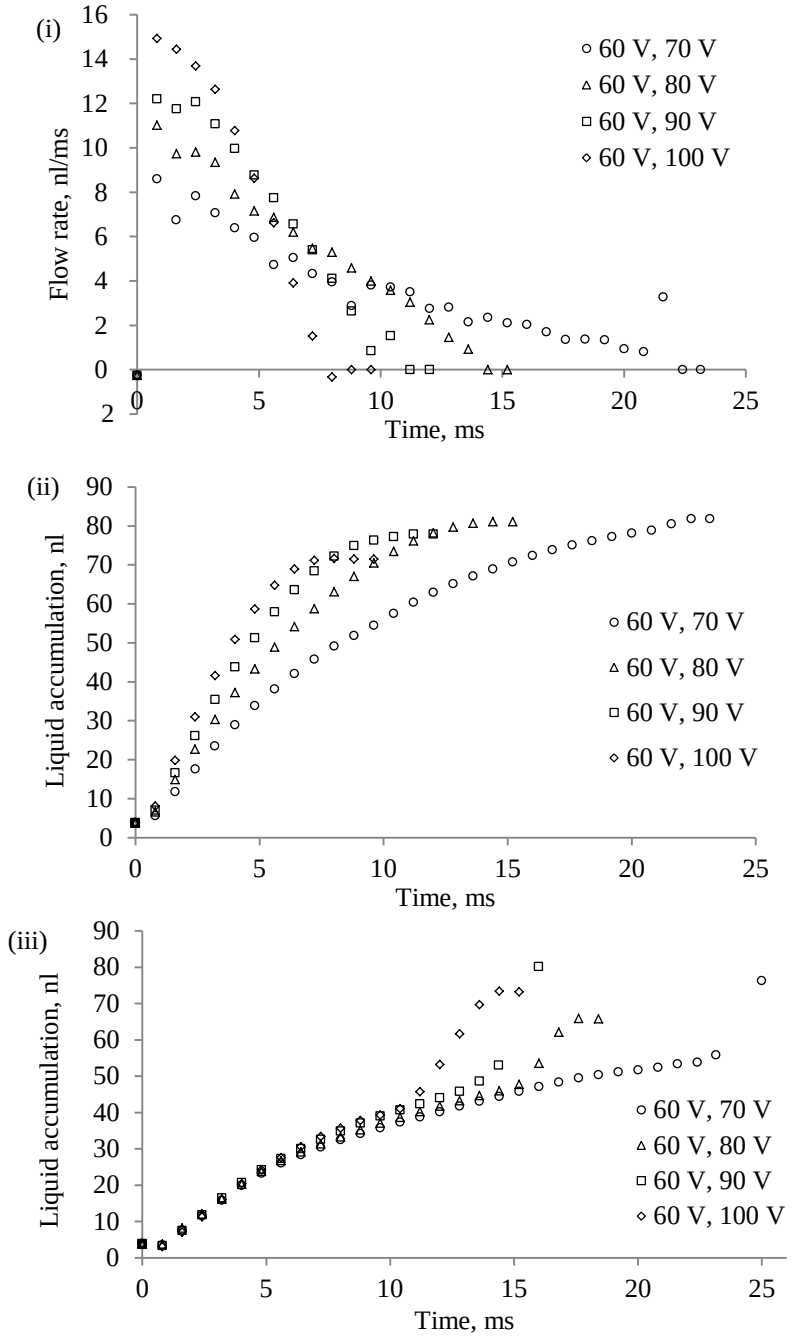


Figure 4.17: Results of voltage ratio variation with constant left-side voltage of 60 V; (i) Flow rates to the right-side, (ii) liquid accumulation to the right-side, and (iii) liquid accumulation to the left-side; Droplet dia.: 1.7 mm, height: 70 µm, electrode: 1.5 mm × 1.5 mm

Simulation results of asymmetric splitting with variation of the ratio between applied voltages are summarized in Figure 4.18. The ratio between the volumes of accumulated liquid on both sides before the pinch-off and that between the two sister droplets are shown in Figures 4.18

(i), (ii), (iii) for the base voltages of 50 V, 65 V and 60 V respectively. The ratio, before pinch-off, increases with higher voltage to the right-side electrode. However, beyond a limit of voltage ratio (1.8 and 1.46 for 50 V and 65 V respectively) the ratio between accumulated liquid does not increase anymore. The ratio between the final volumes of droplets, however, decreases with increasing voltage ratio except for voltage ratios up to 1.19 with base voltage of 65 V. This is the consequence of asymmetric position of the neck pinch-off. In symmetric splitting, the neck always pinches off at the center of the droplet. Application of unequal voltages to the electrodes results in higher flow rates towards the higher voltage side which in turn results in a displacement of the position where the concavity in the neck begins. The higher the voltage ratio, the more is the displacement of the position of maximum concavity in the neck towards high voltage side. As the voltage ratio increases, a level of higher voltage is reached which results in the position of maximum concavity to be adjacent to the edge common to both center and side electrodes. Subsequently, the neck pinches off at the point of maximum concavity where the radius of curvature is minimal. Thus, effectively the entire volume of liquid, remaining over the center electrode just before pinch-off, contributes to the volume of the droplet on the lower voltage electrode. This characteristic poses a limit to asymmetric splitting. It is worth mentioning that simulations performed in FLOW 3D did not incorporate some of the experimentally observed phenomena in contact-line motion at micro to nanoscale. For instance, contact-line pinning and contact angle saturation are typical in droplet motion for which theoretical models are yet to be developed. Also, the roughness parameters of the hydrophobic surfaces need to be characterized and taken into account in CFD simulations. Consideration of all these phenomena, which are not dominant however, not trivial either, may result in closer approximation of the experimental splitting process. Figure 4.18 (iv) and (v) shows that the time needed to complete splitting of a droplet decreases with higher ratios between voltages. Also, the time needed to split is reduced further if a higher level of base voltage is applied. As higher voltages result in higher velocities in liquid, higher values of the capillary numbers are generated. This is depicted in Figure 4.18 (vi) showing the maximum values of $Ca$ resulting from different voltage for three aspect ratios. The maximum $Ca$ varies linearly with the voltage within the range considered in this study. Besides, the values of $Ca$ are higher for droplets with lower aspect ratio. The rise in $Ca$ is due to smaller liquid volumes resulting from decreasing the diameter of the droplet while the height remains constant. Smaller diameter corresponds to smaller area of solid-liquid interface that contributes to the total shear stress. Therefore, liquid velocity increases in response to a given voltage owing to smaller inertia and lower viscous shear.

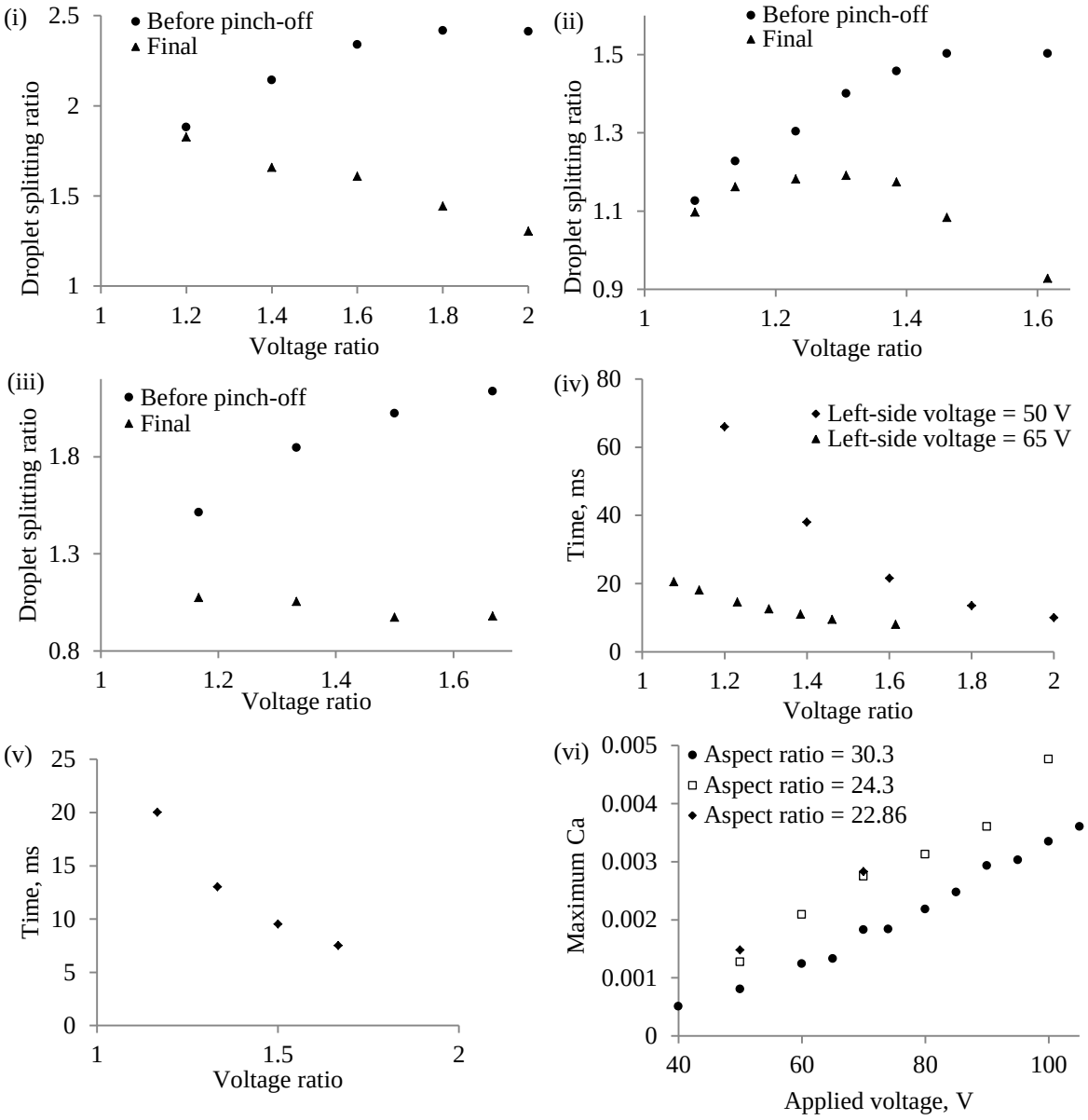


Figure 4.18: Summary of asymmetric splitting with voltage ratio variation; Droplet splitting ratio vs. voltage ratio with left-side voltage of 50 V (i), 65 V (ii), 60 V (iii); Splitting time vs. voltage ratio with 50 V and 65 V (iv), 60 V (v); Maximum capillary number vs. applied voltage (vi).

# CHAPTER 5
# EXPERIMENTS

In this chapter, the materials, methods and equipment used for the experimental study of droplet splitting and results are described. First, the design and fabrication of the DMFS are explained. Next, the experimental setup is shown along with the description of the equipment and their purpose and specifications. In the next section, experimental results of preliminary investigation of symmetric splitting are presented and explained. The final section shows the results of asymmetric splitting with various ratios of applied voltages followed by a few comments on the limitations and sources of error in results.

**5.1 Fabrication**

A simple DMFS with lower plate having multiple 1 × 3 electrode (1.5 mm × 1.5 mm) arrays was fabricated to investigate droplet splitting. The fabrication process is schematically shown in Figure 5.1. Copper-coated glass slides (25 mm × 75 mm × 1 mm) with 45 nm of coating thickness were obtained from EMF Corporation. At first, the copper surface was degreased with acetone, cleaned with deionized water and subsequently dried in Nitrogen gas. A thin layer of positive Photoresist (Shipley S1813) was spin-coated on the copper-coated slide at 4000 rpm for 30 seconds and baked at 60$^{o}$C for 10 minutes. The photoresist layer was then exposed in UV (OAI 200 Mask Aligner) for 7 seconds. After the exposure, the designed pattern of electrodes was transferred to the photoresist layer by developing in sodium hydroxide for 10 – 30 seconds. Next, the exposed area of copper was etched away using ferric chloride etchant. The remaining photoresist was washed away using photoresist thinner. For the dielectric layer, granular cyanoethyl pullulan (CEP) obtained from Biddle Sawyer Corporation, USA, was dissolved in N, N-Dimethylformamide to produce a 20% (wt/wt) solution. A 1.23 μm thick layer of CEP was added by spin-coating at 1500 rpm for 30 seconds. The slide was dried in a vacuum chamber for about 3 hours and then annealed at 100$^{o}$C for 60 minutes. This annealing temperature has been reported to result in a dielectric constant of 15-20 (Na and Rhee 2006). To form the hydrophobic layer, a 1% (wt/wt) solution of Teflon AF1600 (obtained from DuPont) in Fluoroinert FC-40 (obtained from 3M) was prepared. A Teflon layer (~51 nm) was then added on top of the dielectric layer by spin-coating at 1000 rpm for 60 seconds. Next, the slide was baked at 160$^{o}$C for 10 minutes. The top plate of the DMFS was formed by an indium-tin-oxide coated glass slide

having a Teflon layer of 51 nm thickness. The CEP and Teflon layers from above the connecting electrodes located around the periphery of the slide were scratched away gently using a sharp scalpel in order to have access to external electrical wires.

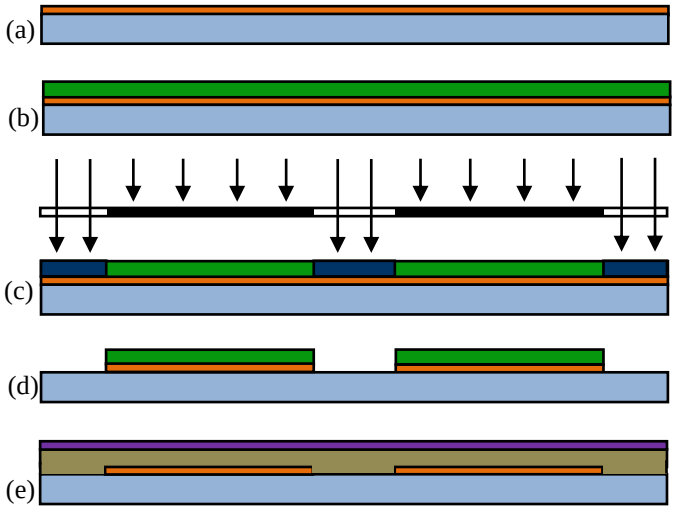


Figure 5.1: Fabrication of DMFS; (a) Copper coated glass slide, (b) Photoresist deposition, (c) UV exposure, (d) Development and etching, and (e) Coating of CEP and Teflon®.

## 5.2 Experimental setup

The fabricated lower plate of the DMFS containing the actuation electrodes was securely placed on top of an upward facing LED lamp, shown in Figure 5.2. This lamp provided the extra amount of light needed for proper exposure of images during high speed recording by HiSpec 5 camera (523 frames per second at full resolution of 1696 × 1710, Pixel size: 8 μm × 8 μm). With sufficient intensity of light and reduced resolution, the images can be recorded at higher rates. During the experiments performed in this investigation, images were recorded at a maximum rate of 400 frames per second. Beyond this rate images were underexposed and hence, the droplet meniscus was not easily identified. The DMFS was positioned such that the selected group of three electrodes to be used for splitting was within the field of view of the camera. The camera was attached to a Navitar 12X (0.58 - 7X) zoom lens through a 1.33X adapter. The field of view of the camera and the zoom level were adjusted for maximum resolution and thereby, maximum accuracy in the results of image analysis. Throughout all the experiments in droplet splitting, the scale ring of the lens was fixed at 1.5X position resulting in an ultimate magnification of 2.02. The coarse focusing was performed by adjusting the position of the fixtures in the vertical post supporting the camera while the focusing ring at the front of the lens was used for fine focusing. Images were acquired in a laptop through HiSpec Control Software as JPEG format and analyzed in MATLAB®.

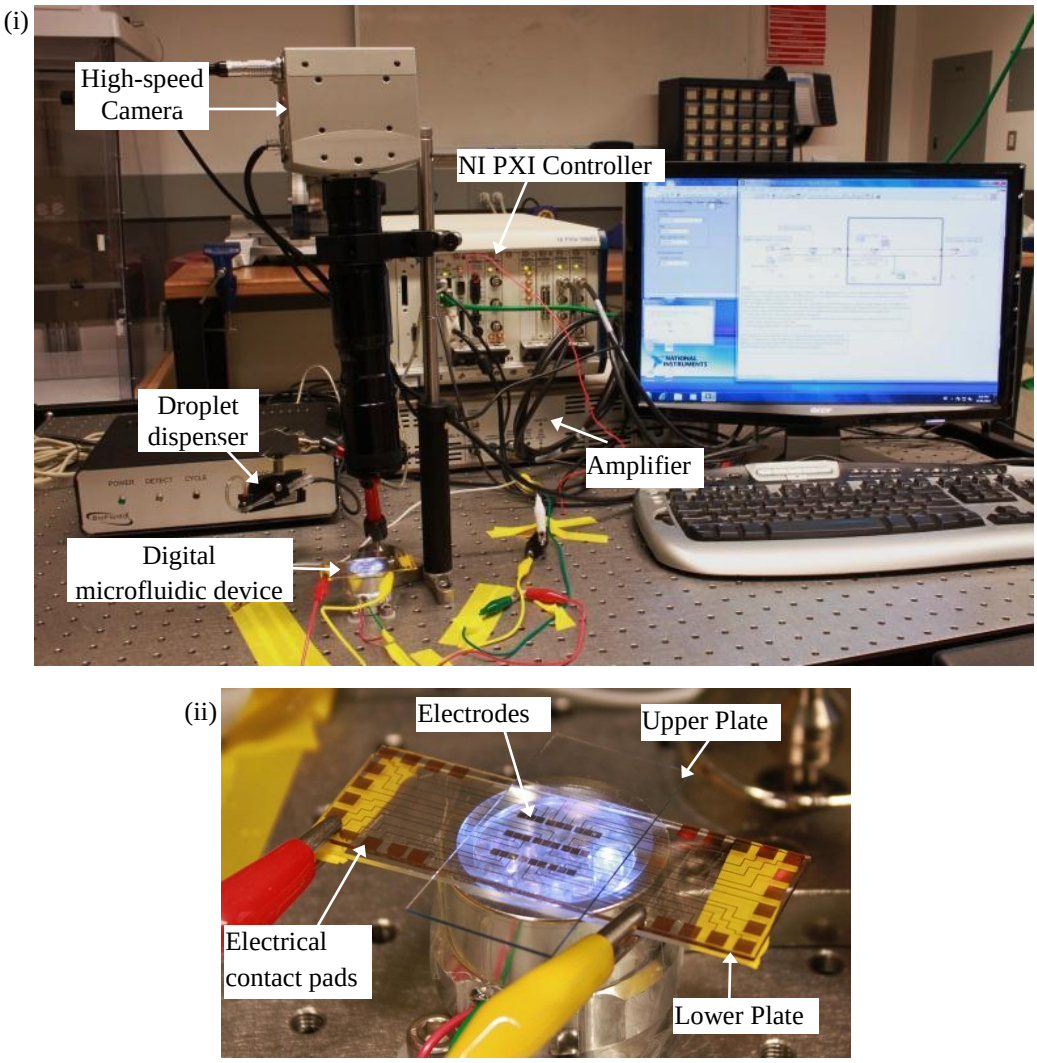


Figure 5.2: (i) Photograph of experimental setup, (ii) Enlarged view of the DMFS.

The gap between the upper and lower plates was created by placing single sided 3M scotch tape having a thickness of 40 µm. A gap of 80 µm was created by placing two layers of tape for all the experiments performed. Since the volume of droplet in the designed DMFS is smaller than 400 nl, a pipette could not be used in dispensing due to smaller volume of droplet and hydrophobicity of the solid surface. This problem was resolved by using a nanoliter droplet dispenser PipeJet$^{TM}$ P9 (Biofluidix Inc.) capable of dispensing a droplet of 2 nl to 60 nl. The stroke length of the piezoelectric actuator can be adjusted in the accompanying software to change the droplet volume. In order to dispense a droplet of volume greater than 60 nl, multiple droplets can be generated at a rate of 50 Hz. However, the accuracy of volume of the final droplet resulting from multiple dispensing of liquid was very high owing to several factors. Even though the landing accuracy of the droplets in case of multiple dispensing can be controlled by reducing

the distance between the tip and the DMFS surface, occasional disintegration of droplets during detachment from the tip would result in variation of the final volume. Besides, the first few droplets were also observed to bounce away from the Teflon surface due to impact at an angle less than $90^{o}$. Nevertheless, droplets were dispensed after bringing the tip of the dispenser above the target electrode and aligning manually with the center as accurately as possible. Next, the upper plate was brought down slowly, while keeping it parallel to the lower plate, and placed on the tapes in such a careful manner that the position of the droplet was not changed. If the alignment of the droplet was interrupted, a new droplet was dispensed and the upper plate was assembled again.

The actuation voltages to the electrodes were generated by two identical function generators (NI PXI 5402) controlled by embedded PXI controller. LabVIEW programs were written for the controller to generate desired voltages through the function generators. Synchronous generation and application of necessary voltages are extremely critical in splitting since the fluidic process involves simultaneous actuation of the droplet on both sides. Although the typical duration of splitting process is a few tens of milliseconds to less than a second, the first few milliseconds are very important as the maximum velocity occurs during this time. Therefore, any difference in timing of the generation of voltages between the two function generators, even by fractions of a millisecond, will lead to inaccurate results of splitting. Moreover, asymmetric splitting is even more sensitive to timing due the process involving application of unequal voltages from the beginning. Experiments without synchronous application of voltages revealed that success in droplet splitting was uncertain and in the successful cases, the end results were highly inaccurate. Therefore, a LabVIEW program was written for the synchronous voltage generation and was used for all the experiments. Voltages from the function generators were amplified by Trek PZD700 Piezo driver/amplifier (0 - ±700 V) having two independent channels with adjustable gains. For all the experiments, sinusoidal voltage signal of 15 KHz was applied to the electrodes.

### 5.3 Symmetric splitting

Experimental investigation of symmetric splitting of DI water droplets involved the determination of the minimum voltage required for splitting. Initially, a low voltage was applied to each of the side electrodes simultaneously in an attempt to split the droplet. If splitting turned out to be unsuccessful, the amplitude of voltage was increased. These steps were repeated until a level of voltage was found that could successfully split the droplet. The total volume of droplet in every repetition was adjusted so as to cover the center electrode completely. However, perfect alignment of the droplet was not possible due to manual positioning of the dispenser tip and assembling of the upper plate, and variation in the droplet volume stemming from faulty dispensing as well as uncertainties inherent to the dispenser.

Splitting experiments revealed that a 110 $V_{p\text{-}p}$ (38.9 $V_{rms}$) was necessary to successfully split a droplet into equal portions and the sequence of images during splitting is shown in Figure 5.3. The initial position of the droplet was not ideal as the centroid of the droplet was slightly off to the lower right from that of the electrode. Application of equal voltages results in liquid flows in both direction and continued deformation of droplet meniscus over the center electrode. The radius of curvature of the neck decreases with time although the neck is not exactly parallel to the longitudinal axis due to surface imperfections. Eventually, the neck pinches-off at about 155 ms producing two droplets on both side electrodes. However, the volume of droplet on the left-side is smaller than that on the right-side because of the larger initial overlap of the droplet on the right-side electrode.

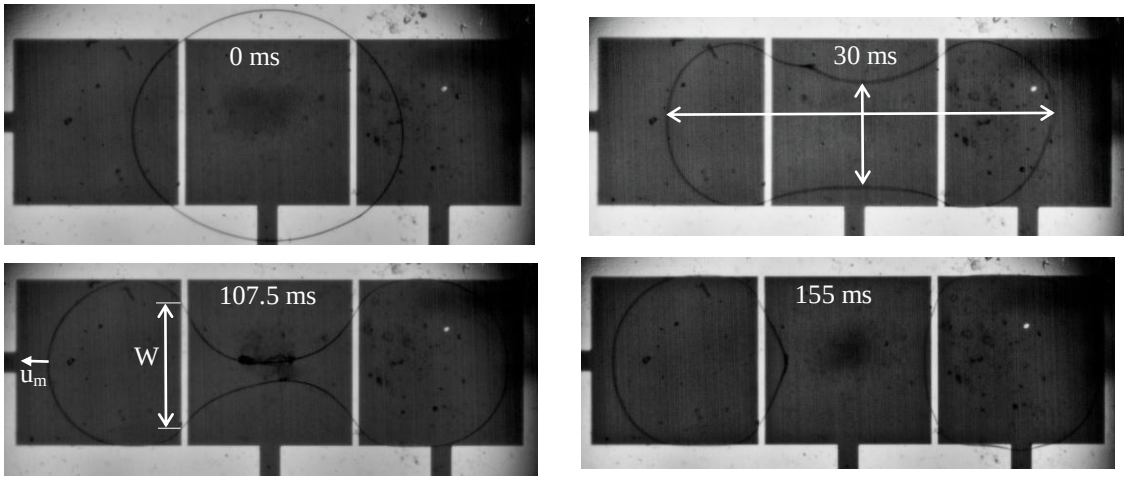


Figure 5.3: Sequence of images in symmetric splitting of a droplet of DI water with 110 $V_{p\text{-}p}$.

The response of a droplet upon application of voltages and the dynamics of splitting in both successful (110 $V_{p\text{-}p}$) and unsuccessful cases (100 $V_{p\text{-}p}$, 105 $V_{p\text{-}p}$) are portrayed in Figures 5.4

and 5.5 in terms of electrowetting force, capillary number ($Ca$), and deformation of the droplet. The longitudinal component of electrowetting force was estimated using equation 2.24 taking the width (W in Figure 5.3) of droplet overlap along the junction of center and side electrodes into account. Although the transverse and the vertical component of actuation force are in no way negligible, their contribution towards elongating the droplet is not significant. The transverse component

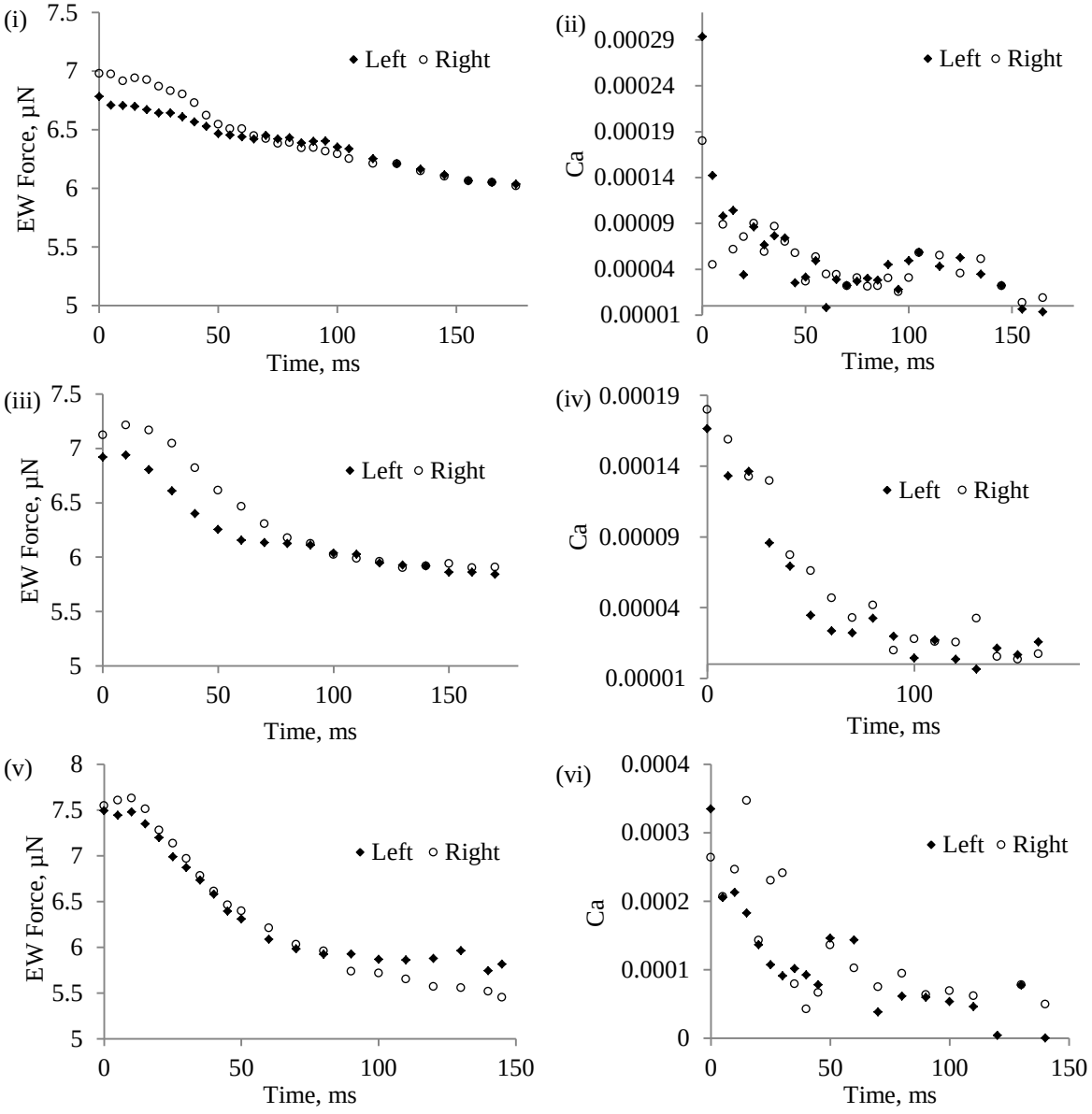


Figure 5.4: Longitudinal component of electrowetting force and capillary number ($Ca$) in symmetric splitting with 100 $V_{p\text{-}p}$: (i), (ii); 105 $V_{p\text{-}p}$: (iii), (iv); and 110 $V_{p\text{-}p}$: (v), (vi).

mainly contributes to the velocity in transverse direction. Figures 5.4 (i), (iii) and (v) show that the actuation force is maximum at the beginning since the width of overlap (W) is equal to that of the electrode. As the droplet starts to deform, a neck is formed which narrows with time. Thus, the magnitude of actuation force gradually decreases. However, for unsuccessful splitting the narrowing of neck slows down and eventually, the droplet no longer deforms. This implies that the longitudinal component of actuation force decreases at a low rate and after a certain period the force stops decreasing any further. In other words, the actuation force fails to deform the droplet. $Ca$ was calculated by considering the velocity of droplet meniscus along the longitudinal centerline ($u_m$ in Figure 5.3). The value of $Ca$ is maximum at the beginning of splitting due to the actuation force acting on a smaller effective mass of liquid. With time, the mass of liquid over the side electrodes increases. As a result, the liquid velocity estimated through the meniscus velocity decreases owing to higher resistance from shear and inertia. The maximum $Ca$ for 110 $V_{p-p}$ was above 0.0003, shown in Figure 5.4 (vi), and higher than the corresponding values for 100 $V_{p-p}$ and 105 $V_{p-p}$. It is noted that, although the values of $Ca$ indicates the relative strength of viscous effects to surface tension, the effect of size and aspect ratio of the droplet is not included. The magnitude of shear in a given droplet is well represented by the deformation of the droplet in splitting, shown in Figure 5.5. Here, the deformation is defined as the ratio between the length of the droplet and width of the neck. Deformation is plotted on a semi-logarithmic graph since the values are an order of magnitude higher during the later phase of splitting than at the beginning. The rate of deformation is higher for higher voltages and for unsuccessful splitting, the rate of deformation approaches zero after a certain period of time. The total shear is higher when the rate of deformation is higher as the rate of deformation is a measure of viscous effects. In case of successful splitting, the total shear is high enough to overcome the resistance to deformation of the interface.

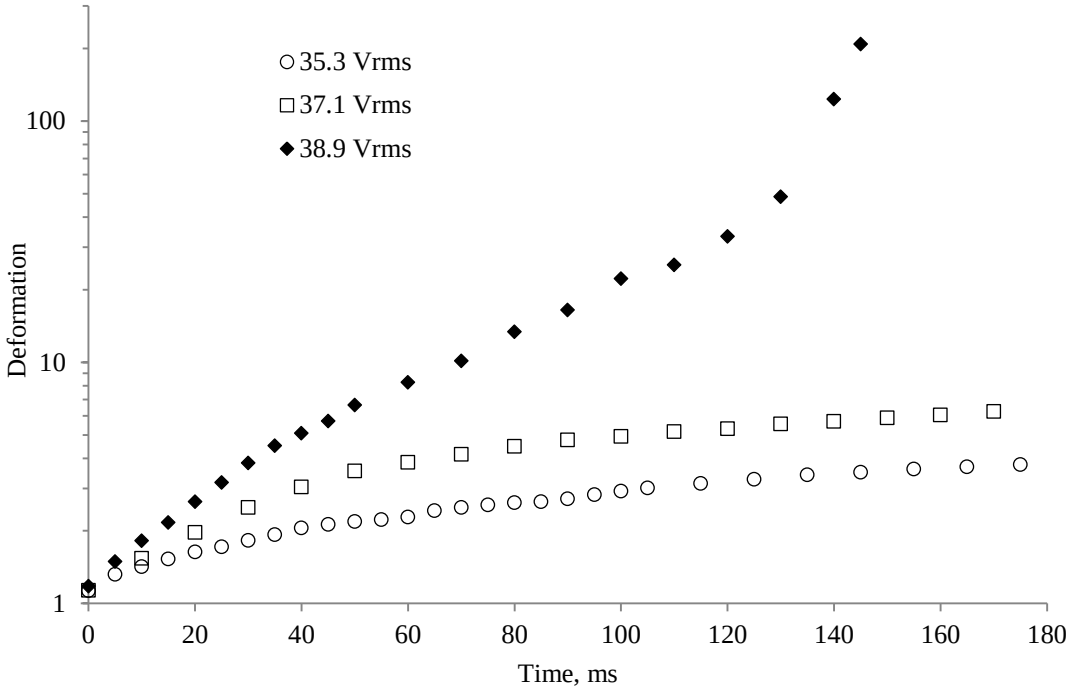


Figure 5.5: Droplet deformation in symmetric splitting

## 5.4 Asymmetric splitting

### 5.4.1 Preliminary investigation

The primary objective of experiments in asymmetric splitting was to determine the minimum voltage level required for successful splitting and investigate the dynamics of splitting. Figure 5.6 shows the sequence of images while attempting to split the droplet with 80 $V_{p-p}$ (28.3 $V_{rms}$) and 84 $V_{p-p}$ (29.7 $V_{rms}$), and 80 $V_{p-p}$ (28.3 $V_{rms}$) and 108 $V_{p-p}$ (38.2 $V_{rms}$). In this investigation, the lower voltage was always applied to the left-side electrode. Thus, the ratio between the voltages applied to the right-side and left-side electrodes for the first case was 1.05

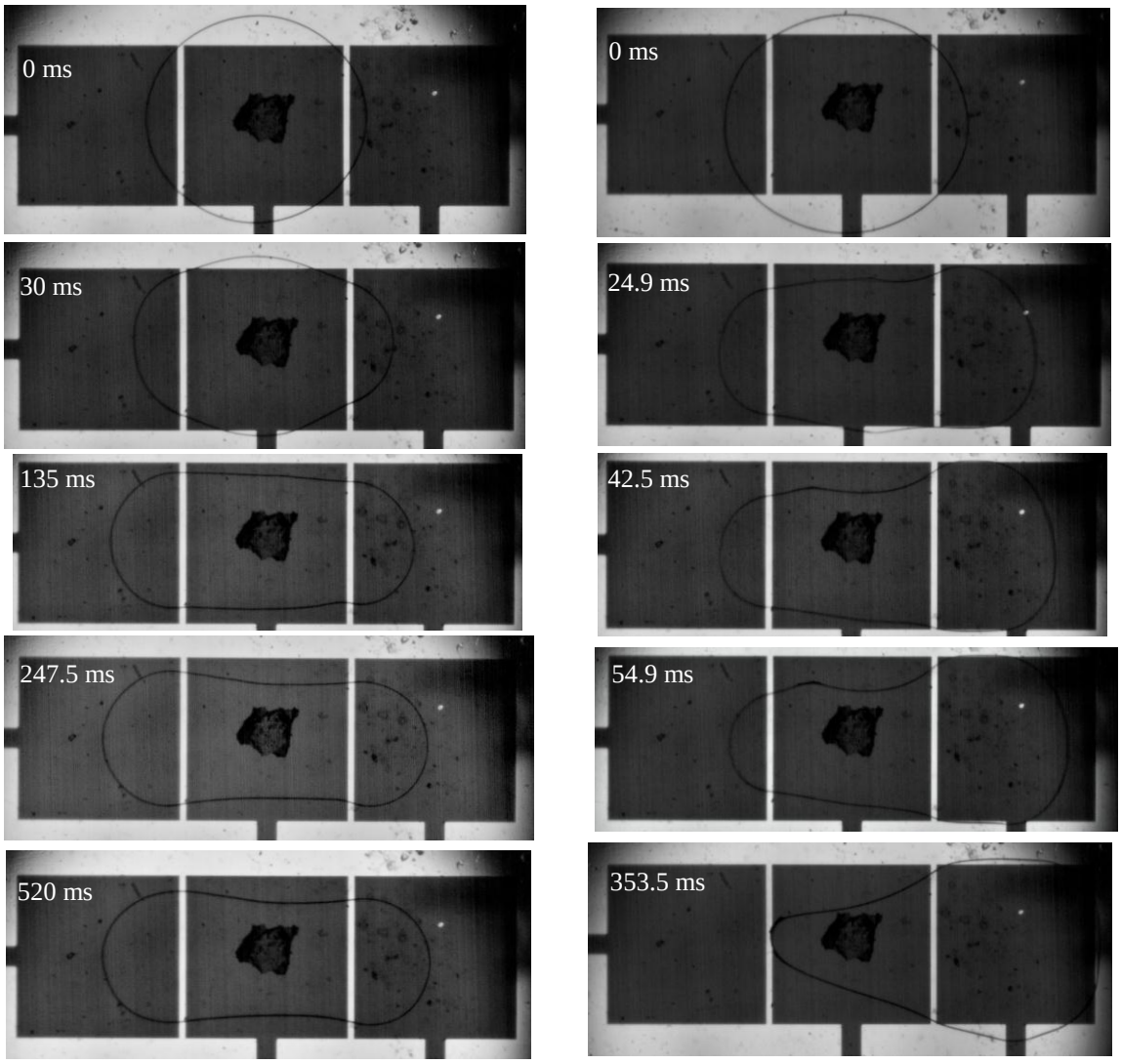


Figure 5.6: Sequence of images in asymmetric splitting with voltage ratios of 1.05 (left column: 28.3 $V_{rms}$, 29.7 $V_{rms}$) and 1.35 (right column: 28.3 $V_{rms}$, 38.2 $V_{rms}$).

while that for the second case was 1.35. With 28.3 $V_{rms}$ to the left-side electrode, the droplet deformed at a very low rate due to weaker actuation forces. A neck was formed over the center electrode; however, continuation of the radius of curvature was not possible. As a result, the droplet retained the deformed shape without further elongation even though the electrodes were left with voltages. The total volume of liquid accumulated on the right-side electrode was not much higher than that on the left-side electrode, although the voltage applied to left-side was higher. This was the consequence of misalignment of the droplet at the beginning of splitting process. A higher ratio between the applied voltages results in a higher average velocity and a higher total shear. Thus, a higher voltage ratio has more potential to split a droplet. In order to verify this concept, a higher ratio of voltages was applied while keeping the voltage to left-side constant. Attempt of splitting asymmetrically with 28.3 $V_{rms}$ and 38.2 $V_{rms}$ was also unsuccessful, however, a different dynamics was observed. The droplet was pulled towards right with a relatively high actuation force as evidenced by large volume of liquid accumulated to the right-side within 25 ms of the process. A neck was formed whose width on the right-side electrode could not be reduced owing to stronger electrowetting effect. However, the liquid continued to flow to the right-side at a high rate and hence, the volume of liquid on the center and left-side electrode reduced at a rate faster than the actuation force on the left-side could generate. Consequently, the width of neck along the edge of left-side electrode decreased which, in turn reduced the actuation force to the left. Finally, the entire volume of liquid was accumulated on the right-side electrode.

The result of increasing the voltage of the left-side electrode to 100 $V_{p-p}$ (35.4 $V_{rms}$), while maintaining the ratio between applied voltages at 1.05, is shown in Figure 5.7. During the early phase of splitting, liquid flowed to both directions at rates determined by the corresponding actuation forces. As a result, the neck was formed of which the concavity gradually increased. After a certain period, the radius of curvature at the neck ceased to decrease further due to the actuation force on the left-side failing to overcome the total resistance provided by the surface tension force and accumulated mass of liquid. In contrast, the liquid continued to flow to the right. This, together with the fact that the neck stopped deforming, resulted in the reduction of liquid volume on the left-side and ultimately, in pulling the total liquid over the right-side electrode. The second column of Figure 5.7 shows the sequence of images of a successful splitting with 110 $V_{p-p}$ (38.9 $V_{rms}$) and 115 $V_{p-p}$ (40.8 $V_{rms}$) to the electrodes (i.e. the ratio was 1.05). This time the levels of voltages on both sides were high enough to generate high flow rates and thereby, a high rate of droplet deformation. The radius of curvature at the neck was reduced

fast indicating the dominance of viscous shear over the surface tension. The contraction of neck continued and ultimately, pinched off at ~120 ms producing two droplets of unequal volumes.

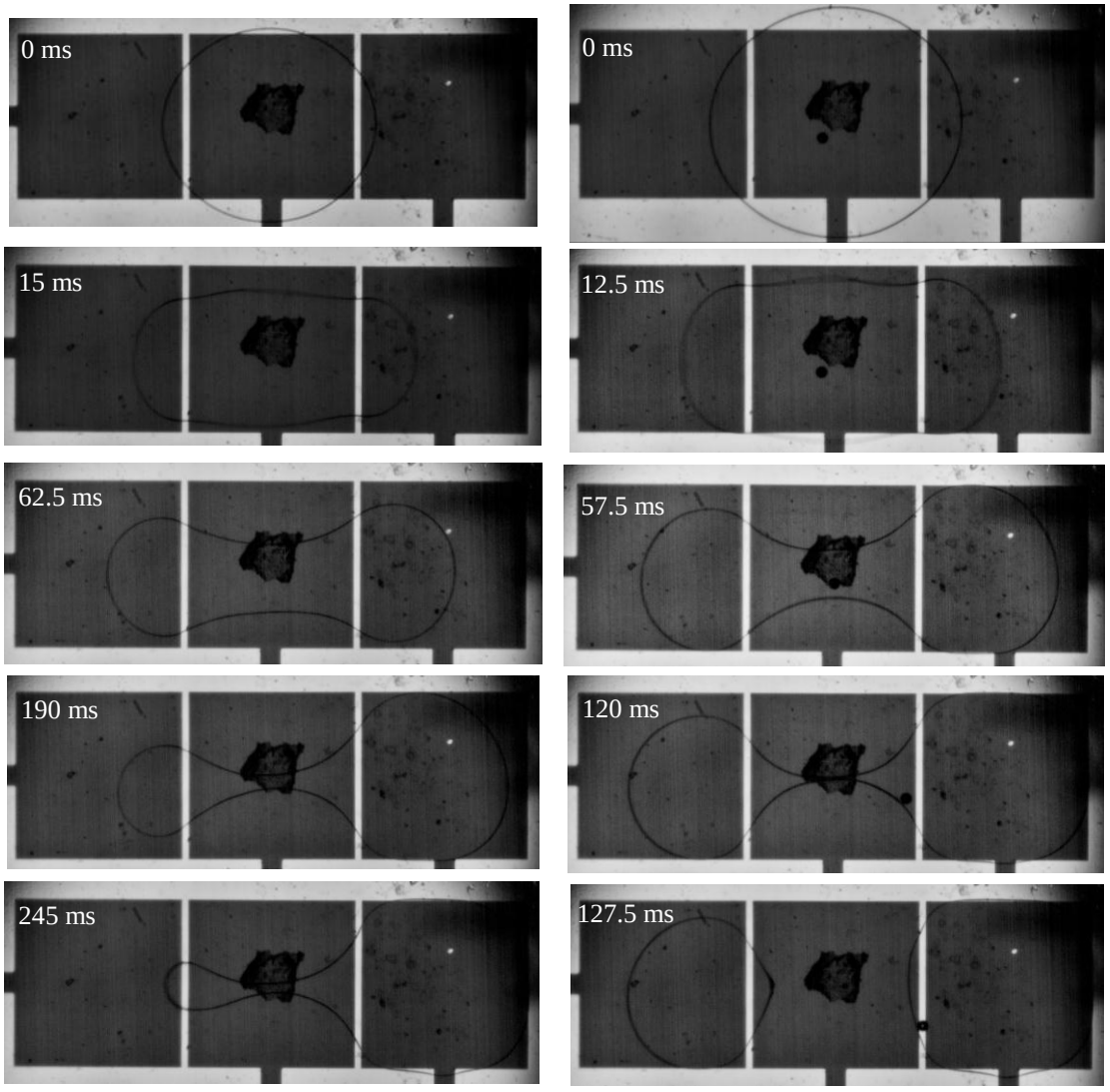


Figure 5.7: Asymmetric splitting with voltage ratio of 1.05; Left column- 35.4 $V_{rms}$, 37.1 $V_{rms}$, Right column- 38.9 $V_{rms}$, 40.8 $V_{rms}$

### 5.4.2 Variation of voltage ratio

This section presents the results of asymmetric splitting obtained for different voltage ratios. The voltage to the left-side electrode in all the experiments performed in one DMFS was kept constant at 140 $V_{p-p}$ (49.5 $V_{rms}$) while that to the other side was varied according to the selected voltage ratios. A high enough voltage for the left-side was selected in order to minimize the chance of unsuccessful splitting at any ratio. The sequences of images during asymmetric splitting of droplets with voltage ratios of 1.1 and 1.3 are shown in Figure 5.8. The ratio between


Figure 5.8: Asymmetric splitting with voltage ratios of 1.1 and 1.3; the voltage to the left-side electrode in both cases: 140 $V_{p-p}$ (49.5 $V_{rms}$)

the volumes of the sister droplets is higher for higher ratios between applied voltages. The flow rate towards left-side is affected by the level of voltage to the right-side electrode. A voltage of 49.5 $V_{rms}$ to the left-side induced higher flow rate to the left when the voltage ratio was 1.1 compared to that when the ratio was 1.3. However, the flow rate towards right-side is not strongly dependent on the corresponding voltage and is not affected by the level of voltage to the left-side. Higher voltage to the right-side generates higher flow rates and the electrode is covered by liquid faster than in splitting with lower voltages. Generally, the right-side electrode is covered by liquid before the neck pinch-off for high ratios of voltages. This imposes a limit on the ratio between the volumes of created droplets due to the fill up of space to the right for further accumulation of

liquid. The volume of accumulated liquid on the left-side increases slowly for higher ratio of voltages, although, the liquid front the on the left-side continues to advance. This is due to the contraction of neck across the length of the center electrode at higher rate resulting from the combined effect of high flow rate to the right and surface tension. The position where the neck pinch-off occurs was observed to be closer to the center of the middle electrode for lower ratios between voltages. However, for higher ratios of applied voltages, the point of minimum radius of curvature on the neck shifts towards the right-side electrode until the electrode is completely filled with liquid and no more liquid can accumulate. Beyond this point, the point of minimum curvature starts to move towards left-side since the liquid is being pulled actively from the left-side only.

Characterization of asymmetric splitting of droplets at different ratios involves detailed investigation of the process dynamics. Specifically, the response of a droplet measured by velocity and flow rates of liquid in relation with time-dependent actuation forces are analyzed in this research. Table 5.1 summarizes the experimental parameters and results for the investigation of variation of applied voltages. Flow rates, volumes of accumulated liquid, capillary numbers and longitudinal components of electrowetting force are shown in Figures 5.9, 5.10, 5.11 and 5.12. Flow rates are calculated based on the area of liquid overlap on either side obtained from image analysis in MATLAB. Liquid volume was estimated via multiplication of the area of liquid by the gap between the upper and lower plates of the DMFS. The identification of droplet meniscus in MATLAB was accurate within 1-2 pixels resulting in an accuracy of ± 8 μm in the position of meniscus. The conservative estimation of the maximum error in liquid volume resulted in a value less than 2% considering the dimensions of the DMFS used in the experiment.

Table 5.1: Voltages, droplet volume and splitting time for asymmetric splitting with constant left-side voltage of 49.5 $V_{rms}$

| Left-side voltage, p-p (rms) | Right-side voltage p-p (rms) | Voltage ratio | Droplet volume (nl) | Time to split (ms) |
|---|---|---|---|---|
| 140 (49.5) | 147 (52) | 1.05 | 232.792 | 70 |
| | 154 (54.4) | 1.1 | 262.512 | 100 |
| | 161 (56.9) | 1.15 | 251.896 | 67.5 |
| | 168 (59.4) | 1.2 | 214.344 | 55 |
| | 175 (61.9) | 1.25 | 228.872 | 50 |
| | 182 (64.3) | 1.3 | 237.88 | 70 |
| | 189 (66.8) | 1.35 | 264.328 | 62.5 |
| | 196 (69.3) | 1.4 | 243.816 | 40 |

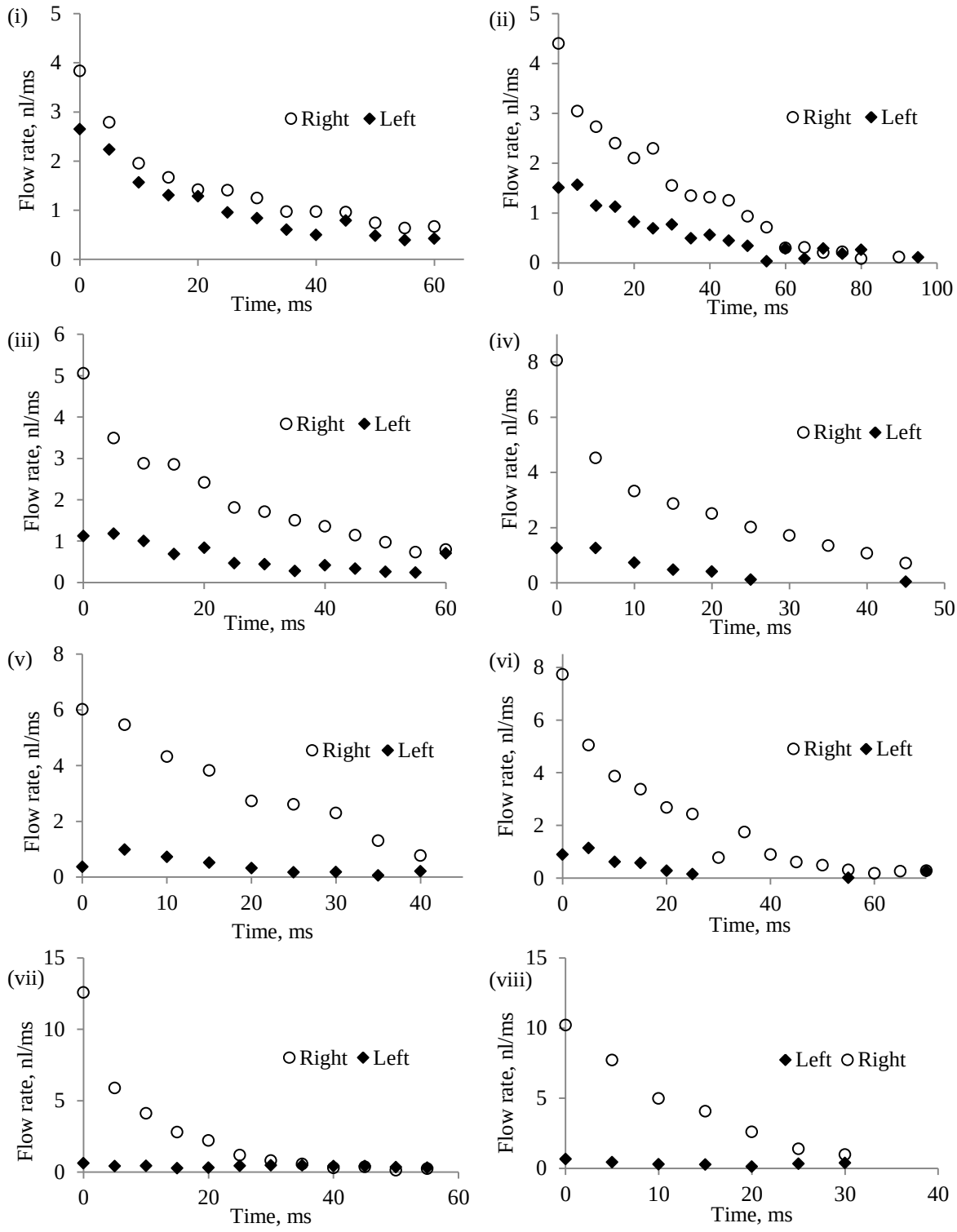


Figure 5.9: Flow rates in asymmetric splitting with ratios of (i) 1.05, (ii) 1.1, (iii) 1.15, (iv) 1.2, (v) 1.25, (vi) 1.3, (vii) 1.35, and (viii) 1.4 between applied voltages; The constant voltage to the left-side electrode: 49.5 $V_{rms}$.

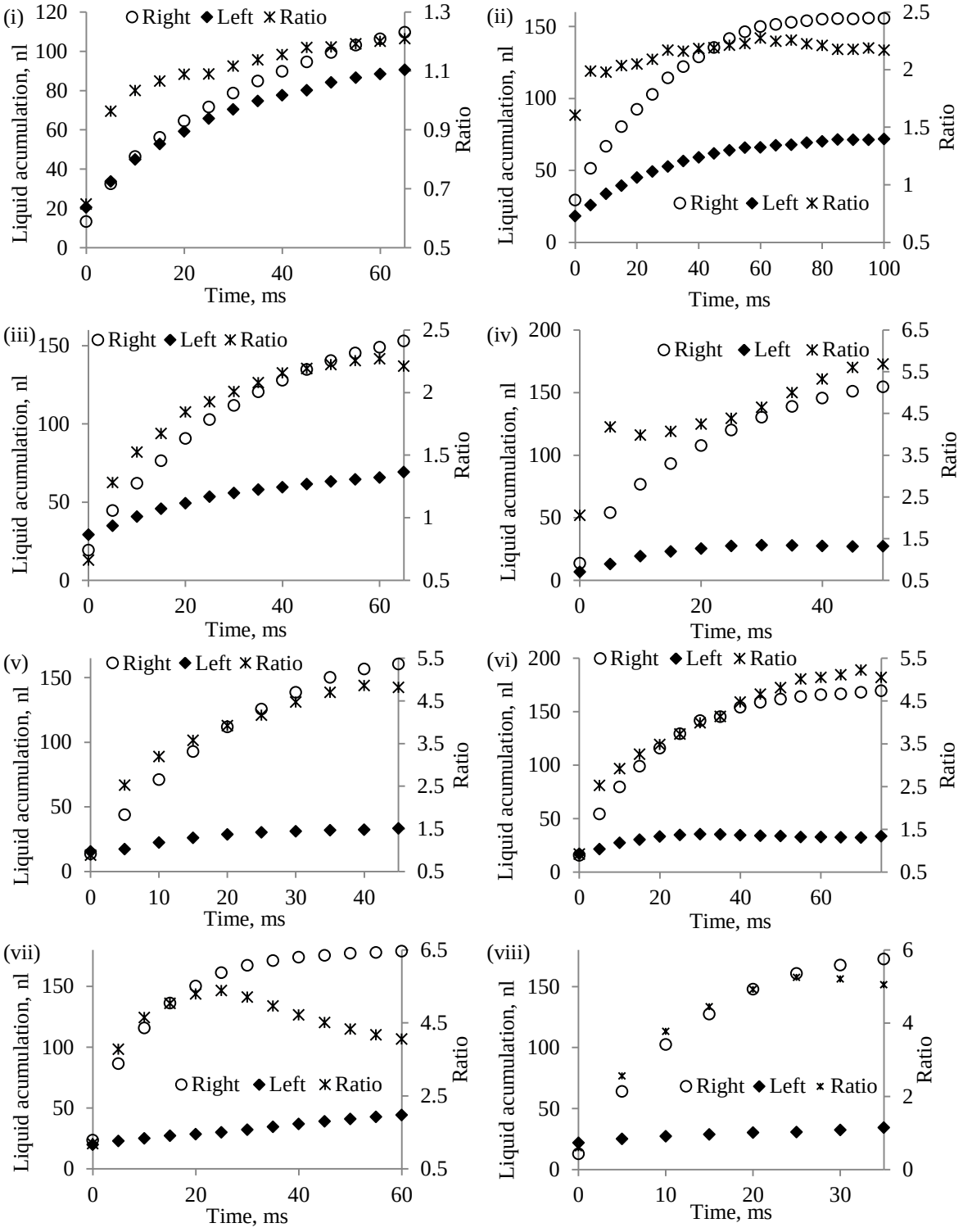


Figure 5.10: Liquid accumulation in asymmetric splitting with ratios of (i) 1.05, (ii) 1.1, (iii) 1.15, (iv) 1.2, (v) 1.25, (vi) 1.3, (vii) 1.35, and (viii) 1.4 between applied voltages; The constant voltage to the left-side electrode: 49.5 $V_{rms}$.

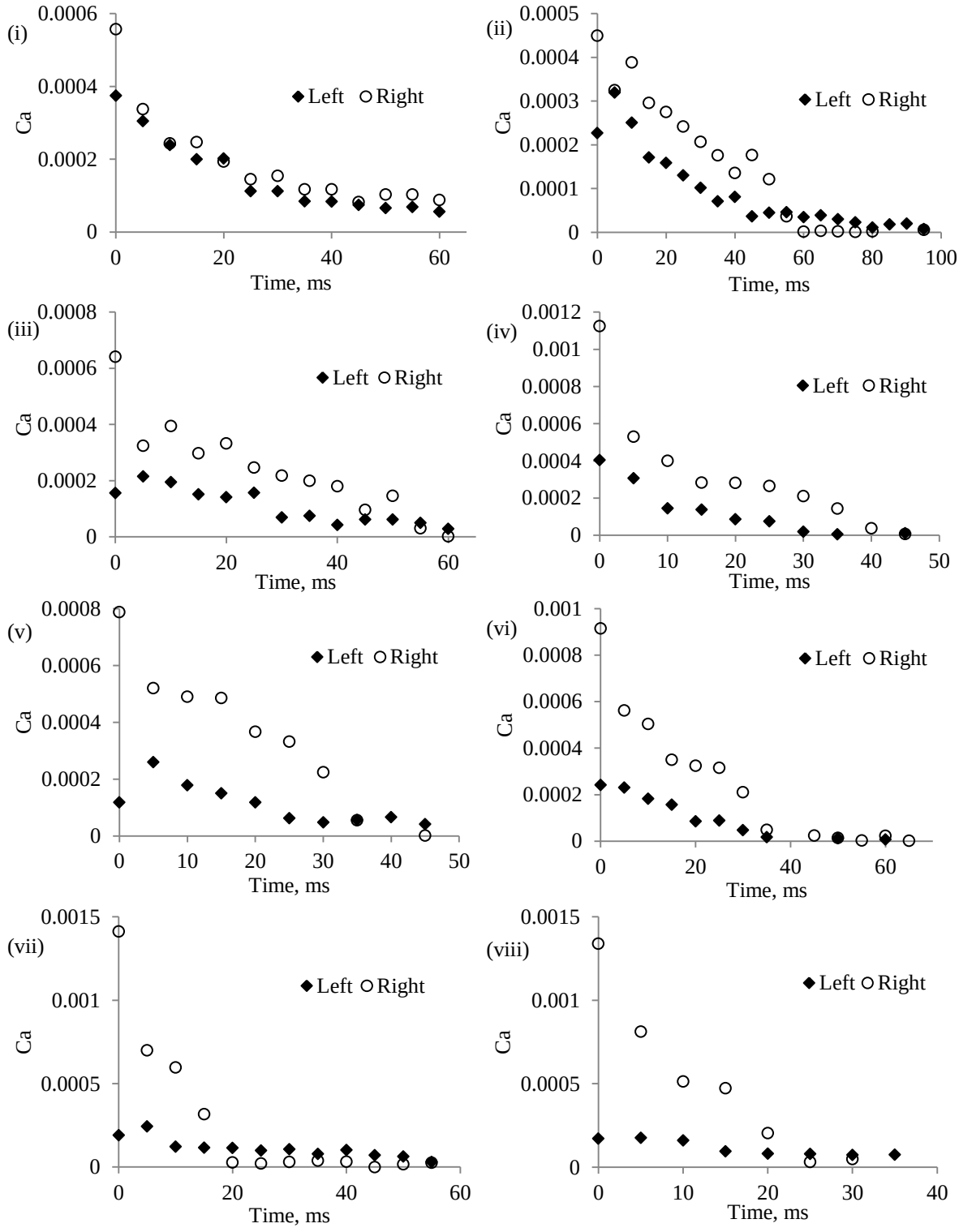


Figure 5.11: Capillary numbers in asymmetric splitting with ratios of (i) 1.05, (ii) 1.1, (iii) 1.15, (iv) 1.2, (v) 1.25, (vi) 1.3, (vii) 1.35, and (viii) 1.4 between applied voltages; The constant voltage to the left-side electrode: 49.5 $V_{rms}$.

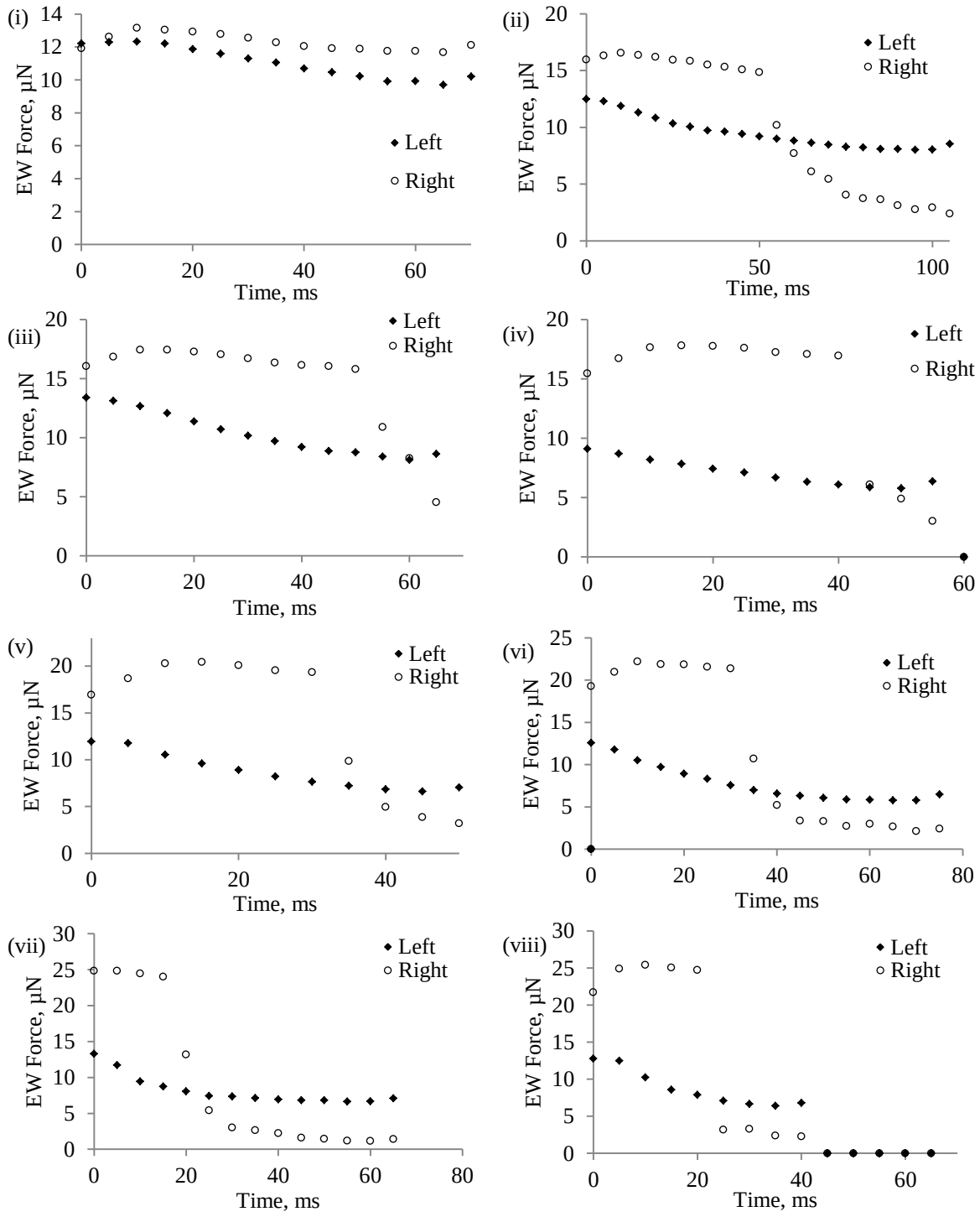


Figure 5.12: Longitudinal component of electrowetting force in asymmetric splitting with ratios of (i) 1.05, (ii) 1.1, (iii) 1.15, (iv) 1.2, (v) 1.25, (vi) 1.3, (vii) 1.35, and (viii) 1.4 between applied voltages; The constant voltage to the left-side electrode: 49.5 $V_{rms}$.

Figure 5.9 shows that maximum flow rates occurred at the beginning of splitting. The difference in the values of maximum flow rates on left- and right-side generally increased with higher ratio between voltages. The maximum flow rate to the left-side decreases with higher voltage ratios although the voltage to the left-side electrode was constant in all the cases. Eventually, flow rates dropped to several tens of picoliter per millisecond to a few hundred picoliter per millisecond before the neck pinch-off. The volumes of accumulated liquid on both sides and their ratios as a function of time are shown in Figure 5.10. Since the volume of liquid on the side electrodes is the cumulative result of liquid flow, the slopes of curves are proportional to respective flow rates. The rate of increase in liquid volume on the right-side falls significantly when the liquid completely fills the space over the electrode. Conversely, the liquid accumulation continues to increase on the left-side till the neck pinch-off. As a result, the curves of ratio between accumulated volumes have a downward trend before pinch-off. It is noted that results immediately after the pinch-off are not shown; therefore, the value of ratio between accumulated liquid corresponding to the last time instant is not the final ratio between the volumes of sister droplets. In general, the final ratio between droplet volumes is smaller than those at the time of pinch-off. The $Ca$, calculated as explained in section 5.3, are shown in Figure 5.11. The general characteristics of $Ca$ in all cases were similar to those of flow rates. The value of $Ca$ on the right-side was always maximum at the beginning whereas that on the left-side occasionally reached the maximum at ~5 ms. Besides, the $Ca$ showed a positive correlation with applied voltage to the right-side electrode. However, the values fluctuated occasionally originating from the fact that $Ca$ was calculated based on the velocity of meniscus which showed stick-slip behavior. Nonetheless, the results agreed with theoretical expectations and are useful since the maximum values are of most concern. Figure 5.12 shows the estimated values of the longitudinal components of actuation forces obtained by considering the width (W in Figure 5.3) of liquid overlap along the inner edges of the side electrodes. In absence of appropriate instrumentation for measuring the actual electrowetting forces during splitting, estimated values serve well in understanding the process dynamics. The results shown are well within the expected range of the force magnitude. For a droplet large enough to cover the electrode completely and residing with perfect alignment with the center of the electrode, a maximum force in the longitudinal direction is generated as soon as voltages are applied. In practice, perfect alignment was impossible to achieve, especially if deposited and positioned manually. In addition, droplet volume varied from trial to trial giving rise to variations in the initial value of W. For these reasons, the values of actuation forces increased for the first 10 – 15 ms corresponding to the increase in liquid overlap across electrode width. Owing to stronger forces, liquid accumulated and covered the right-side electrode before

the neck pinch-off except for the ratio of 1.05. The magnitude of force decays at high rates as soon as the front of the liquid reaches the outer edge of the electrode. The relaxation of the neck resulting from the sudden large drop of pull towards right-side increases the width of the neck along the inner edge of left-side electrode. Hence, the actuation force to the left increases towards the end of splitting process. The deformation of droplet, defined in section 5.3, as a function of time at different voltage ratios are shown in Figure 5.13. The rate of deformation is indicative of the intensity of viscous shear. Results depict the exponential rate of droplet deformation during splitting. It is noticed that the rate increases with increase in voltage ratio for most cases. Moreover, the rate of deformation increases during the later phase of splitting for all the cases except for ratios of 1.1 and 1.3.

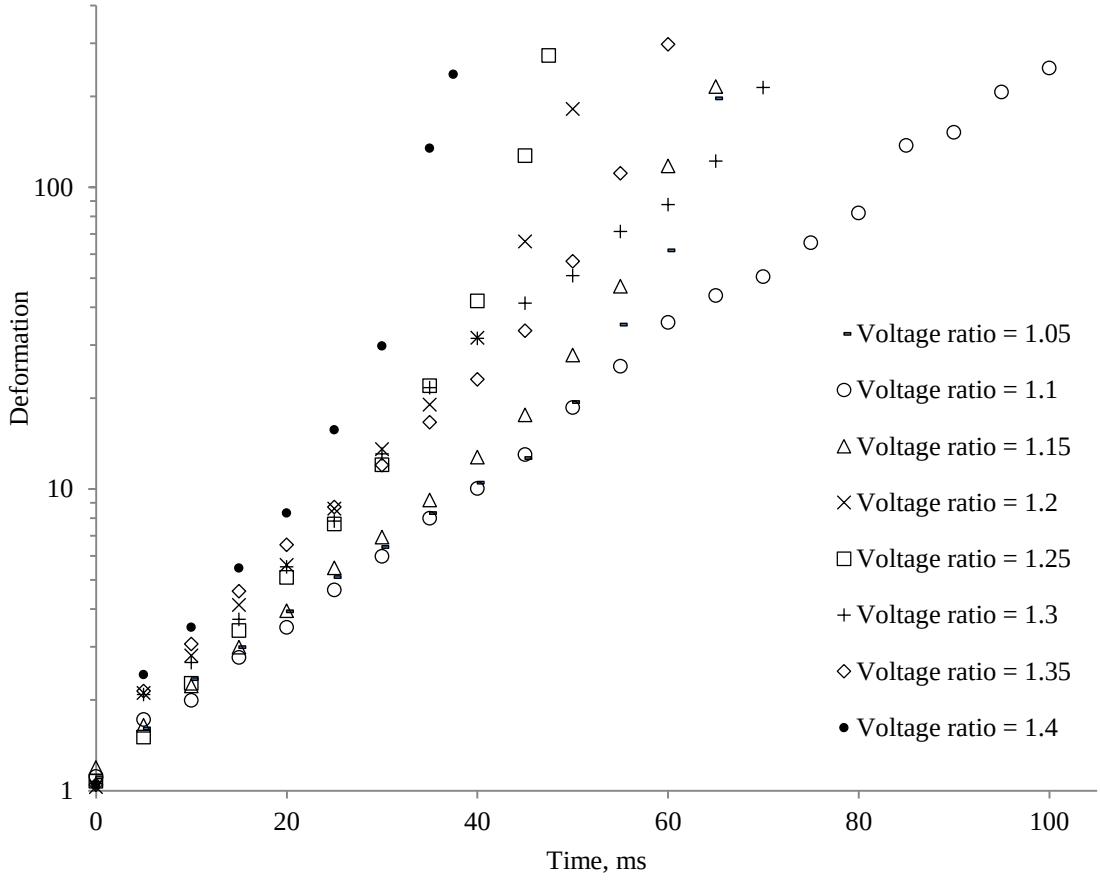


Figure 5.13: Droplet deformation in asymmetric splitting

Investigation of asymmetric splitting was also conducted for various ratios of applied voltages while the left-side voltage was kept constant at 120 $V_{p-p}$ (42.4 $V_{rms}$). The DMFS used in this set of experiments was fabricated according to the same method and under exactly same conditions in order to make the device identical to the one used for 140 $V_{p-p}$. Table 5.2 shows the

experimental parameters and results. Results of successful splitting in terms of flow rates and accumulated liquid are shown in Figures 5.14 and 5.15.

Table 5.2: Voltages, droplet volume and splitting time for asymmetric splitting with constant left-side voltage of 42.4 $V_{rms}$

| Left-side voltage, p-p (rms) | Right-side voltage p-p (rms) | Voltage ratio | Droplet volume (nl) | Time to split (ms) |
|---|---|---|---|---|
| 120 (42.4) | 126 (44.5) | 1.05 | 265 | 65 |
| | 132 (46.7) | 1.10 | 251 | 55 |
| | 138 (48.8) | 1.15 | 282.648 | 65 |
| | 144 (51) | 1.20 | 277.624 | 65 |
| | 150 (53) | 1.25 | 290.184 | 110 |
| | 156 (55.2) | 1.30 | 264.976 | 40 |
| | 162 (57.3) | 1.35 | 294.696 | 115 |

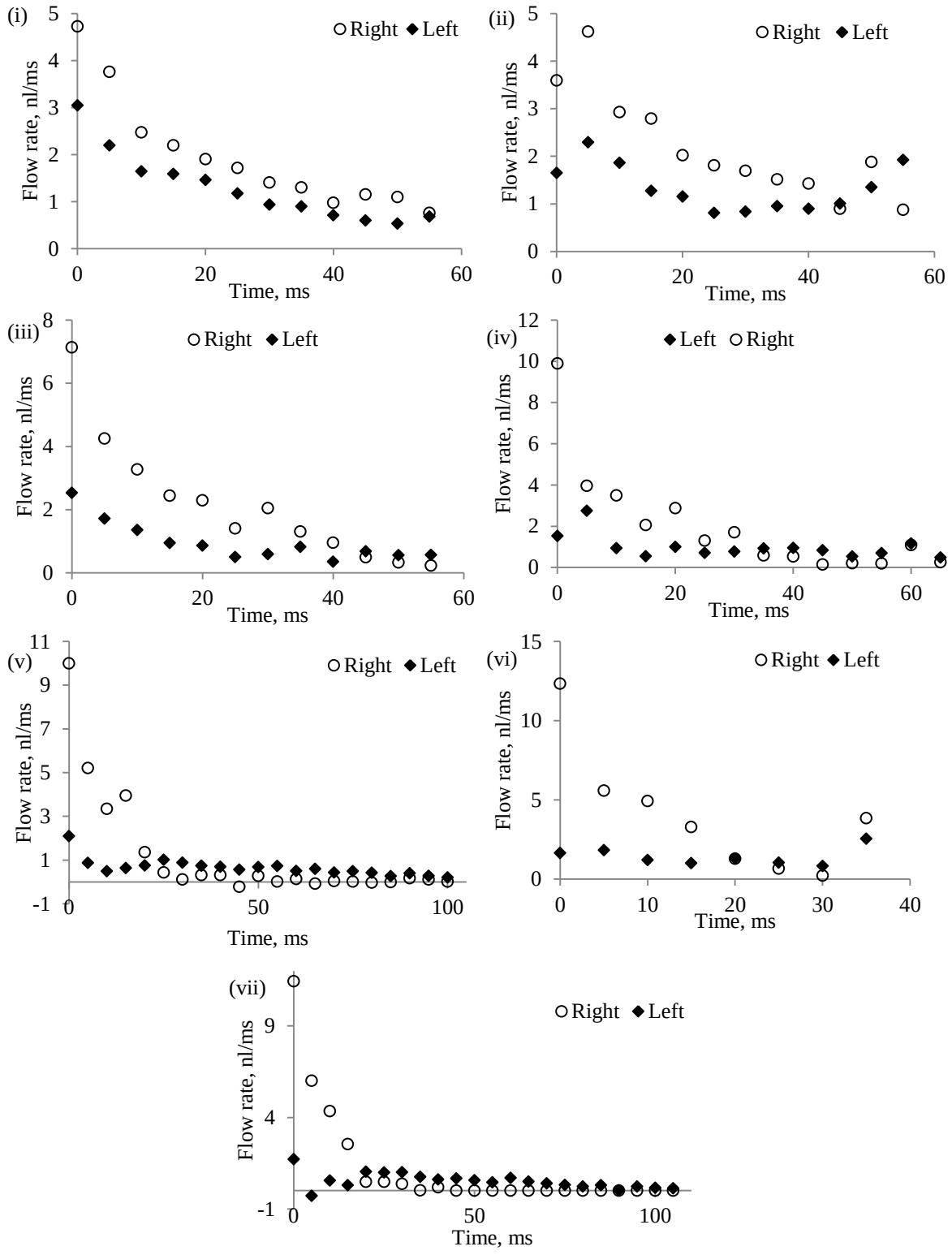


Figure 5.14: Flow rates in asymmetric splitting with ratios of (i) 1.05, (ii) 1.1, (iii) 1.15, (iv) 1.2, (v) 1.25, (vi) 1.3, and (vii) 1.35, between applied voltages; The constant voltage to the left-side electrode: 42.4 $V_{rms}$.

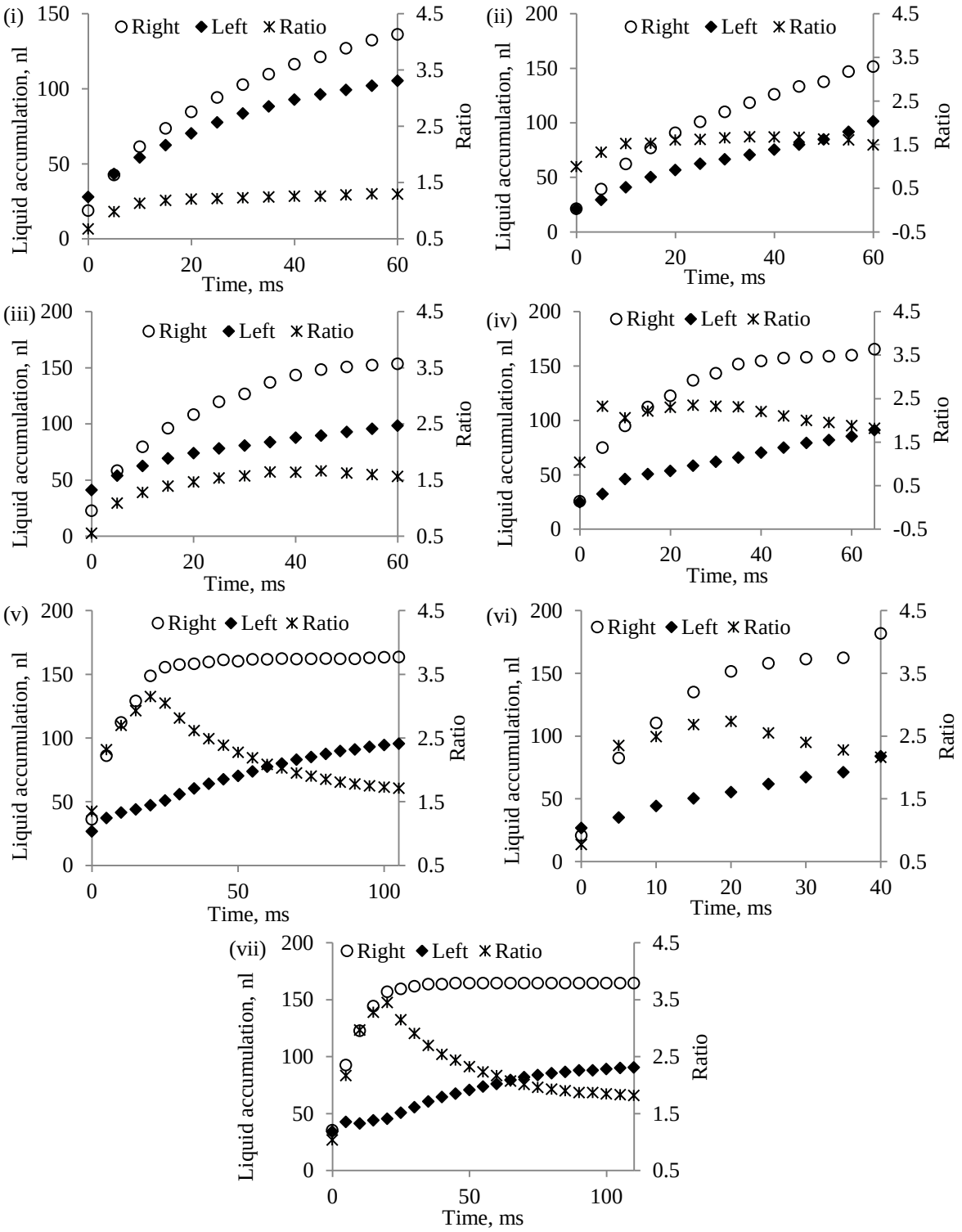


Figure 5.15: Liquid accumulation in asymmetric splitting with ratios of (i) 1.05, (ii) 1.1, (iii) 1.15, (iv) 1.2, (v) 1.25, (vi) 1.3, and (vii) 1.35, between applied voltages; The constant voltage to the left-side electrode: 42.4 $V_{rms}$.

One of the major objectives of this research was to investigate the relation between applied voltages and the final outcome of splitting. Figure 5.16 shows the relation between the voltage ratio and the splitting ratio for the two levels of base voltages investigated in this research. The achieved splitting ratio increases with the ratio between applied voltages. Also, the splitting ratio increases with higher base voltage. The variability in data-points is greater for voltage ratio of 1.2 and beyond. For the base voltage of 48.5 $V_{rms}$, the ratio between the volumes of created droplets did not increase for voltage ratios higher than 1.3. Nevertheless, results shown here are expected to serve well in predicting the splitting results in open loop operations of the DMFS.

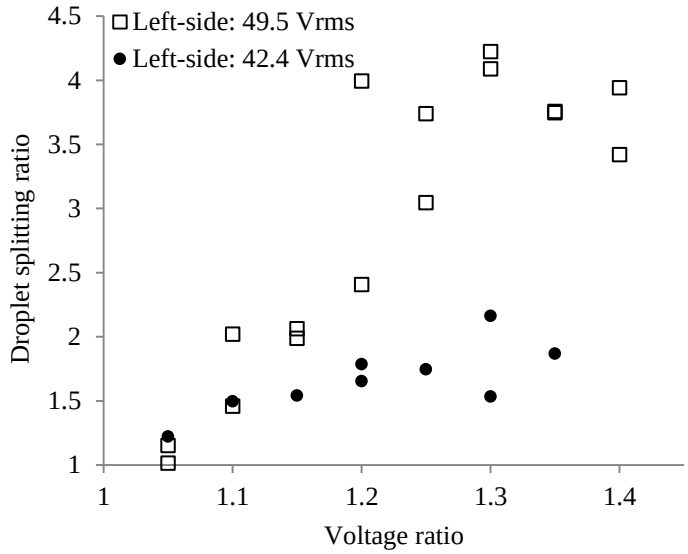


Figure 5.16: Droplet splitting ratio as a function of ratio between applied voltages

The variability and inconsistency in the experimental results can be attributed to several sources of errors. The main contributor is undoubtedly the fabrication method and associated inaccuracies. The surface quality of copper slides varied between samples and minor imperfections, which were not visible to human eyes, acted as potential sites of dielectric breakdown and consequent electrolysis.

Dimensions in the design were not exactly transferred to the fabricated device due to variations resulting from etching the copper and developing the photoresist. For instance, the electrode size, designed as 1.5 mm × 1.5 mm, was found from image analysis to be ~ 1.4 mm × 1.4 mm and the interelectrode gaps were ~ 100 µm as opposed to 60 µm in the design. The wider gap necessitated larger droplets, affecting the actuation. Also, the position and dimensions of the connecting lines to the actuation electrodes influenced the results. The flow of liquid towards the connecting line on the high voltage biased the results of splitting. Better design incorporating the

proper position of connecting lines can minimize overlap of liquid outside of the energized electrodes.

The dielectric layer was a major source of variations and uncertainties in experiments. Since the material used in experiments, CEP, was coated using spinning, the thickness of the layer was not uniform throughout the desired area. Any difference between the thicknesses over left-side and right-side electrodes results in a significant error in splitting. Frequently electrolysis would occur even at lower voltages indicating the imperfections in the CEP coating and/or the copper surface.

The variation in dispensed liquid was common from trial to trial even though the desired volume was set in the software for the dispenser. Manual assembly of the upper plate on the tapes resulted in misalignment of the droplets. Moreover, the elasticity of the tapes could affect the parallelism of the upper plate with respect to the lower plate. Collectively, all these could have introduced abnormal response of the droplet upon application of voltages.

# CHAPTER 6
# CONCLUSIONS AND FUTURE RESEARCH

## 6.1 Conclusions

This thesis is focused on the splitting of droplets in electrowetting-on-dielectric (EWOD) based digital microfluidic systems (DMFS). The research started with the preliminary concepts of EWOD actuation and the simplified dynamics of droplet motion to identify important material properties and geometric parameters. DMFS prototypes were fabricated using a proposed dielectric material that not only simplified the fabrication but also enhanced the operational efficiency by lowering the required voltage for droplet manipulation. Detailed investigation of symmetric and asymmetric splitting was conducted through numerical simulations as well as experiments. The following paragraphs briefly state the discoveries of this research.

Energy minimization based investigation of the electrowetting actuated droplet motion reveals that the magnitude of actuation force is related to the position of the droplet between two adjacent electrodes. Thus, the dynamic system can be considered as a closed-loop system with unity position feedback. Also, the variation of actuation force during the translocation of a droplet from one electrode to the adjacent one is related to the size of the droplet. Since the actuation force is proportional to the area of liquid overlap on the energized electrode, a droplet large enough to cover the electrode will be subject to maximum actuation force throughout the motion. A droplet with a diameter smaller than the diagonal length of the electrode will be subject to low actuation force at the beginning of motion. The magnitude of force increases with the droplet overlap as it moves closer to the center of the destination electrode. Simulation of the droplet dynamic system, modeled as a lumped parameter mass and considering the semi-empirical relations of resistances to droplet motion, was performed in SIMULINK for different droplet sizes and geometry of the device. The results also showed that the actuation force increases with the permittivity and decreases with the thickness of the dielectric layer. Finally, it is shown that the transition time from one electrode to the adjacent one increases with electrode size and viscosity of the liquid, and hence lower switching frequencies can be achieved.

Since the properties of the dielectric material plays a vital role in the fabrication process and operational efficiency of the DMFS, a part of this research concentrated on finding a suitable dielectric material that can be processed using simple fabrication recipes and basic facilities. The material selected for and investigated in this research is cyanoethyl pullulan (CEP), possessing a

dielectric constant of ~15. The high dielectric constant facilitates the actuation of droplets by imparting the capability of generating stronger electric field near the tri-phase contact line. Thus, a lower voltage is sufficient to bring about a significant change in the contact angle. Experimental results show that ~40$^{o}$ change in contact angle is possible with a voltage of about 30 V. Moreover, droplets can be transported between electrodes with a voltage of 20 V in a DMFS fabricated using CEP. In addition to reducing the level of voltage required for droplet actuation, the fabrication process is also simplified by CEP which can be deposited using a spin-coater. Although PDMS–a commonly used dielectric material–can be deposited using a spin-coater, the viscosity limits the minimum achievable thickness. A low-thickness coating is possible using parylene-C, however, the deposition requires a sophisticated device. Thus, the total time and cost of fabrication is significantly reduced using CEP in comparison with other common materials requiring expensive deposition facilities.

In view of a need for a closed-loop control system for repeatable splitting, a novel coplanar droplet sensing method is proposed in this research which can enhance both the capability and flexibility of a DMFS. Among many methods of droplet sensing, measurement of the capacitance has been considered as the simplest yet most effective method. In a typical configuration of the DMFS, where droplets are confined between two plates, the traditional approach utilizes both the upper and lower plates to measure the capacitance. The proposed approach utilizes the lower plate only resulting in a simpler design and more flexible structure. The variation of coplanar capacitance originating from the droplet position between two adjacent electrodes is investigated both numerically and experimentally. The results show that the capacitance is at the peak when the droplet is at the midpoint between two adjacent electrodes. The results verify that the total capacitance can be modeled as the equivalent of the two series connected capacitances. The equivalent capacitance decreases as the droplet moves away from the midpoint in either direction. Furthermore, the measured capacitance decreases when the gap between the electrodes as well as the plates is increased. The value of maximum capacitance is also found to be linearly dependent on the total overlap area of the droplet. The followings highlight the findings.

Numerical investigation of droplet splitting was conducted using the commercial CFD software FLOW-3D®. Multiple simulations were performed to understand the electrohydrodynamics of droplet splitting and to identify the parameters that determine the success in both symmetric and asymmetric splitting.

- The results verify the idea that droplet splitting is a process where the relative strength of competing forces of viscous shear and of surface tension determines the

success of splitting. There exists a threshold voltage for successful symmetric splitting of a droplet for a given geometry. Results verified that the level of total wall shear in comparison with the force of surface tension determines the success of the splitting process.

- In asymmetric splitting, there exists a minimum voltage required for successful splitting of a droplet of given the aspect ratio (i.e., diameter to height ratio) and electrode size. If the aspect ratio of the droplet is reduced keeping the electrode size constant, the level of required voltage shifts upwards. Also, the required voltage to the left-side electrode increases with smaller ratios of voltages.
- Asymmetric splitting of droplets of different aspect ratios was investigated for two electrode sizes. For a given electrode size, the required voltage for successful asymmetric splitting increases with droplet height. The reason for this is the increase in the length of droplet surface along the vertical plane as well as in the total mass of the droplet. The required voltage is higher for smaller electrode compared to that for larger electrode for the same droplet aspect ratio.
- Asymmetric splitting of droplets was also investigated for different ratios of applied voltages while keeping the device geometry and droplet aspect ratio constant. The voltage to the right-side electrode was always higher than the left-side. The results suggest that the ratio between flow rates to right-side and left-side increase with voltage ratio. However, the ratio between volumes of final droplets does not correspond to that of the applied voltage due to the shifting of the point of pinch-off towards the high voltage electrode. The pinch-off of the neck from near the right-side electrode result in a large portion of liquid on the center electrode joining the liquid on the left-side electrode. Consequently, the final ratio between the volumes of sister droplets decreases as opposed to the increase in the voltage ratio.

Symmetric and asymmetric splitting of DI water droplets were investigated experimentally in a two-plate DMFS fabricated using CEP as the dielectric material. Results in terms of flow rates, liquid accumulation and capillary numbers were derived from the analysis of images. The typical pattern of volumetric flow rate consists of a peak and subsequent exponential decay. The maximum flow rate occurs within ~2 ms of the application of voltages. Other observations that characterize the process of droplet splitting are as follows:

- Experiments on symmetric splitting revealed that the required minimum voltage for successful splitting is 38.9 $V_{rms}$ in the fabricated DMFS (electrode: 1.4 mm × 1.4

mm, thickness of CEP layer: 1.23 µm, thickness of Teflon: 51 nm, plate gap: 80 µm). The rate of deformation of the droplet indicates the magnitude of total viscous shear. Thus, the rate of deformation must be high enough, corresponding to the required voltage, to successfully split a droplet.

- For successful asymmetric splitting, the required voltage for the left-side electrode was found to be equal to that for symmetric splitting. If a lower voltage is applied to the left-side electrode, the droplet either assumes a deformed shape and continues to hold that shape or ultimately accumulates on the right-side electrode depending on the magnitude of voltage to the right-side.
- Ratio between the applied voltages to the right-side and left-side electrodes was varied from 1.05 to 1.4 for two different levels of left-side voltages while keeping all other parameters constant. The ratio between the volumes of two sister droplets depends on the ratio between the applied voltages, although the variation in the results are greater for higher ratios. With higher voltage ratio, the liquid quickly accumulates and completely covers the right-side electrode before the neck break-up. In general, the volume ratios are lower in case of a lower base voltage than those in case of higher base voltage. Moreover, the volume ratio does not increase significantly beyond the voltage ratios of 1.25-1.3.

## 6.2 Future research

Further research is necessary to improve the results of simulations performed in FLOW-3D®. The simulation models in this research were developed under some assumptions to keep the duration of each run within a reasonable limit. Results were satisfactory in terms of revealing the dominant characteristics of the process dynamics. However, the following modifications and/or inclusions are expected to make the simulation models more realistic and the results comparable to experimental observations:

- The surface roughness of both hydrophobic layers and the contact line pinning are expected to add damping effects to the motion of liquid. Thus, the duration of splitting a droplet will be extended and be comparable to those in experiments.
- The incorporation of contact angle hysteresis will affect the response of the droplet at lower voltages. The contact angle saturation determines the limit of deformation of the droplet interface over the energized electrode. Although an appropriate theoretical model of saturation is yet to be developed, there are empirical models which can be considered for incorporation into simulation models in FLOW-3D®.
- The hydrophobic layers were not considered in simulation models. The effect of hydrophobic layer in the lower plate was added by considering the equivalent dielectric constant and the total thickness of the dielectric and hydrophobic layers. However, modeling the upper hydrophobic layer can be challenging owing to the difficulties related to large variations in the scale of mesh sizes.
- In practice, AC voltages are also used for the actuation droplets in order to minimize the risk of electrolysis. Future research can also be directed towards the application of AC voltages in simulation models.

Further experimental investigation is needed to develop the comprehensive relation between the ratios of applied voltages and the ratios of droplet volumes. The experimental conditions can be improved to minimize the sources of inaccuracies in the results. For instance, the fabrication of device and experiments must be performed in a cleaner environment to eliminate any settlement of dust on the hydrophobic surfaces. The coating thickness of dielectric layer is not very uniform over a large area of surface featuring multiple electrodes. Hence, alternative methods capable of producing conformal coating can be considered for the deposition of dielectric material. The results presented in this thesis can be extended by considering liquids with varying conductivities and viscosities. Moreover, future experiments may also be performed

in DMFS with different electrode sizes and droplet heights as well as with closed-loop control of droplet splitting.

# BIBLIOGRAPHY


Abdelgawad M. and Wheeler A. R., 2008, "The digital revolution: A new paradigm for microfluidics", *Advanced Materials*, **20**, 1-6.

Ahmadi A., Holzman J. F., Najjaran H., Hoorfar M., 2011, "Electrohydrodynamic modeling of microdroplet transient dynamics in electrocapillary-based digital microfluidic devices", *Microfluidics and Nanofluidics*, **10**, 1019-1032.

[a]Armani M., Walker S. and Shapiro B., 2005, "Modeling and control of electrically actuated surface tension driven microfluidic systems," *Proceedings of the 13th Mediterranean Conference on Control and Automation*, Limassol, Cyprus, 131-138.

[b]Armani M., Chaudhary S., Probst R., Walker S. and Shapiro B., 2005, "Control of microfluidic systems: two examples, results and challenges," *International Journal of Robust and Nonlinear Control*, **15**, 785-803.

Arzpeyma A., Bhaseen S., Dolatabadi A., Wood-Adams P., 2007, "A coupled electro-hydrodynamic numerical modeling of droplet actuation by electrowetting", *Colloids & Surfaces A*, **323**, 28-35.

Bahadur V. and Garimella S. V., 2006, "An energy-based model for electrowetting-induced droplet actuation," *Journal of Micromechanics and Microengineering*, **16**, 1494-1503.

Baird E., Young P., Mohseni K., 2007, "Electrostatic force calculation for an EWOD-actuated droplet", *Microfluidics & Nanofluidics*, **3**, 635-644.

Basu A. S. And Gianchandani Y. B., 2007, "A 128-pixel digitally-programmable microfluidic platform for non-contact droplet actuation using marangoni flows", *IEEE Conference on Solid-state Sensors, Actuators and Microsystems*, Lyon, France, 771-774.

Bennes J., Alzuaga S., Cherioux F., Ballandras S., Vairac P., Manceau J. F., Bastien F., 2007, "Detection and high-precision positioning of liquid droplets using SAW systems", *IEEE Transactions on Ultrasonics, Ferroelectrics and Frequency Control*, **54**, 2146-2151.

Berry, S., Kedzierski, J., and Abedian, B., 2006, "Low voltage electrowetting using thin fluoropolymer films," *Journal of Colloid and Interface Science*, **303**, 517-524.

Berthier J., Dubois P., Clementz P., Claustre P., Peponnet C., Fouillet Y., 2007, "Actuation potentials and capillary forces in electrowetting based microsystems", *Sensors and Actuators A*, **134**, 471-479.

[a]Bhattacharjee B. and Najjaran H., 2010, "Simulation of droplet position control in digital microfluidic systems," *Journal of Dynamic Systems, Measurement and Control*, **132**, 014501.

[b]Bhattacharjee B. and Najjaran H., 2010, "Droplet position control in Digital Microfluidic Systems", *Biomedical Microdevices*, **12**, 115-124.

[c]Bhattacharjee B. and Najjaran H., 2009, "Size dependent droplet actuation in digital microfluidic systems", *SPIE Conference on Micro- and Nanotechnology Sensors, Systems and Applications*, Orlando, FL, 73180H(1-12).

[d]Bhattacharjee B., Najjaran B., 2010, "Effects of the properties of dielectric materials on the fabrication and operation of digital microfluidic systems", *Proceedings of ASME IMECE*, Vancouver.

[e]Bhattacharjee B. and Najjaran H., 2011, "Modeling and simulation of unequal droplet splitting in electrowetting based digital microfluidics", *ASME ICNMM*, Edmonton.

Brennan D**.**, Jary D**.**, Peponnet C**.**, Cardosa F**.**, Freitas P**.**, Dinca M**.**, Aherne M**.** and Galvin P., 2011, "An integrated hybrid system for genetic analysis combining EWOD sample preparation and magnetic detection", *Journal of Physics: Conference Series*, **307**, 012022.

Carlson A., Do-Quang M., Amberg G., 2010, "Droplet dynamics in a bifurcating channel", *International Journal of Multiphase Flow*, **36**, 397-405.

Chang J.-H., Choi D.-Y., You X., Pak J. J. and Han S., 2010, "Low voltage electrowetting on atomic-layer-deposited aluminium oxide", *5th IEEE International Conference on Nano/Micro Engineered and Molecular Systems*, Seoul, South Korea, 612-615.

Chang Y.-H., Lee G.-B., Huang F.-C., Chen Y.-Y. and Lin J.-L., 2006, "Integrated polymerase chain reaction chips utilizing digital microfluidics", *Biomedical Microdevices*, **8**, 215-225.

Chakrabarty K., Fair R. B., Zeng J., 2010, "Design tools for digital microfluidic biochips: toward functional diversification and more than Moore", *IEEE Transactions on Computer-Aided Design of Integrated Circuits and Systems*, 29 (7), 1001-1017.

Chatterjee D., Hetayothin B., Wheeler A. R., King D. J., Garrell R. L., 2006, "Droplet-based microfluidics with nonaqueous solvents and solutions", *Lab on a Chip*, **6**, 199-206.

Chatterjee D., Shepherd H. and Garrell R. L., 2009, "Electromechanical model for actuating liquids in a two-plate droplet microfluidic device", *Lab on a Chip*, **9**, 1219-1229.

Chaudhury M. K. & Whitesides G. M., 1992, "How to make water run uphill", *Science*, **256**, 1539-1541.

Chen J. H., Hsieh W. H., 2006, "Electrowetting-induced capillary flow in a parallel plate channel", *Journal of Colloid and Interface Science*, **296** (1), 276-283

Chiou P. Y., Chang Z., Wu M.C., 2008, "Droplet manipulation with light on optoelectrowetting device", *Journal of Microelectromechanical Systems*, **17**, 133-138.

Chiou P. Y., Moon H., Toshiyoshi H., Kim C. J., Wu M. C., 2003, “Light actuation of liquid by optoelectrowetting”, *Sensors and Actuators A*, **104**, 222-228.

Cho S. K., Moon H., and Kim C.-J., 2003, "Creating, transporting, cutting, and merging liquid droplets by electrowetting-based actuation for digital microfluidic circuits", *Journal of Microelectromechanical Systems*, **12**, 70-80.

Cho S. K., Moon H., Fowler J., Fan S.-K., and Kim C.-J., 2001, “Splitting a liquid droplet for electrowetting-based microfluidics”, *ASME International Mechanical Engineering Congress and Exposition*, New York, NY, 1-7.

Cho S. K. and Kim C.-J., 2003, “Particle separation and concentration control for digital microfluidic systems”, *IEEE Conference on MEMS*, Kyoto, Japan, 686-689.

Choi K., Ng A. H. C., Fobel R. and Wheeler A. R., 2012, “Digital microfluidics”, *Analytical Chemistry*, **5**, 413-440.

Chuang H. S., Kumar A, Wereley S.T., 2008, “Open optoelectrowetting droplet actuation”, *Applied Physics Letters*, **93**, 064104.

Clime L., Brassard D., Veres T., 2009, “Numerical modeling of the splitting of magnetic droplets by multiphase lattice Boltzmann equation”, *Journal of Applied Physics*, **105**, 07B517 1-3.

Darhuber A. A., Valentino J. P., Troian S. M., Wagner S., 2003, “Thermocapillary actuation of droplets on chemically patterned surfaces by programmable microheater array”, *Journal of Microelectromechanical Systems*, **12**, 873-879.

Fair R. B., 2007, “Digital microfluidics: Is a true lab-on-a-chip possible?”, *Microfluidics and Nanofluidics*, **3**, 245-281.

Fan S.-K., Hashi C., and Kim C.-J., 2003, “Manipulation of multiple droplets on NxM grid by cross-reference EWOD driving scheme and pressure-contact packaging", *IEEE Conference on MEMS*, Kyoto, Japan, 694-697.

Fan S.-K., Huang P.-W., Wang T.-T. and Peng Y.-H., 2008, “Cross-scale electric manipulations of cells and droplets by frequency-modulated dielectrophoresis and electrowetting”, *Lab on a Chip*, **8**, 1325-1331.

Fouillet Y., Jary D., Brachet A.G., Berthier J., Blervaque R., Davous L., Roux J. M., Achard J. L. and Peponnet C., 2006, “EWOD digital microfluidics for lab on a chip”, *International Conference on Nanochannels, Microchannels and Minichannels*, Limerick, Ireland, 1-10.

Fowler J., Moon H.and Kim C.-J, 2002, “Enhancement of mixing by droplet-based microfluidics*”, IEEE Conference on MEMS*, Las Vegas, NV, 97-100.

Furlani E. P., Hanchak M. S., 2011, "Nonlinear analysis of the deformation and breakup of viscous microjets using the method of lines", *International Journal for Numerical Methods in Fluids*, **65** (5), 563-577.

Gallardo B. S., Gupta V. K., Eagerton F. D., Jong L. I., Craig V. S., Shah R. R., Abbott N. L., 1999, "Electrochemical principles for active control of liquids on submillimeter scale", *Science*, **283**, 57-60.

Gascoyne P. R. C., Vykoukal J. V., Scwartz J. A., Anderson T. J., Vykoukal D. M., Current K. W., McConaghy C., Becker F., Andrews C., 2004, "Dielectrophoresis-based programmable fluidic processor", *Lab on a Chip*, **4**, 299-309.

Gong J., Fan S. K., and Kim C. J., 2004, "Portable digital microfluidics platform with active but disposable lab-on-a-chip," *17th IEEE International Conference on Micro Electro Mechanical Systems*, 355-358.

Gong J., and Kim C. J., 2005, "Two-dimensional digital microfluidic system by multi-layer printed circuit board", *Proceedings of IEEE MEMS*, Miami, FL, 726-729.

Gong J. and Kim C.-J., 2006, "Real-time feedback control of droplet generation for EWOD digital microfluidics," *Proceedings of 10th International Conference on Miniaturized Systems for Chemistry and Life Sciences*, Tokyo, 1046-1048.

Gong J. and Kim C. J., 2008, "Direct-referencing two-dimensional-array digital microfluidics using multi-layer printed circuit board", *Journal of Microelectromechanical Systems*, **17**, 257-264.

Hong J. S., Ko S. H., Kang K. H., and Kang I. S., 2008, "A numerical investigation on AC electrowetting of a droplet", *Microfluidics and Nanofluidics*, **5**, 263-271.

Hunt T. P., Issadore D., Westervelt R. M., 2008, "Integrated circuit/microfluidic chip to programmably trap and move cells and droplets with dielectrophoresis", *Lab on a Chip*, **8**, 81-87.

Ichimura K., Oh S. K., Nakagawa M., 2000, "Light-driven motion of liquids on a photoresponsive surface", *Science*, **288**, 1624-1626.

Jang L.-S., Lin G.-H., Lin Y.-L., Hsu C.-Y., Kan W.-H. and Chen C.-H., 2007, "Simulation and experimentation of a microfluidic device based on electrowetting on dielectric", *Biomedical microdevices*, **9**, 777-786.

Jones T. B., 2005, "An electromechanical interpretation of electrowetting", *Journal of Micromechanics and Microengineering*, **15**, 1184-1187.

Jones T. B., 2008, "More about the electromechanics of electrowetting", *Mechanics Research Communications*, **36**, 2-9.

Jones T. B., Fowler J. D., Chang Y. S., and Kim C.-J., 2003, "Frequency-based relationship of electrowetting and dielectrophoretic liquid microactuation", *Langmuir*, **19**, 7646-7651.

Kawamoto H. & Hayashi S., 2006, "Fundamental investigation of electrostatic travelling-wave transport of a liquid drop", *Journal of Physics D*, **39**, 418-423.

Kim, N. Y., Hong, S. M., Park, S. S., and Hong, Y. P., 2006, "The movement of micro droplet with the effects of dielectric and hydrophobic surface treatment with R.F. atmospheric plasma in EWOD structure," *Journal of Physics: Conf. Series*, **34**, 650-655.

Krogmann F., Qu H., Mönch W., Zappe H., 2008, "Push/pull actuation using opto-electrowetting", *Sensors & Actuators A*, **141**, 499-505.

Kumari N., Bahadur V. and Garimella S. V., 2008, "Electrical actuation of electrically conducting and insulating droplets using ac and dc voltages", *Journal of Micromechanics and Microengineering*, **18**, 105015 (1-10).

Kuo J. S., Spicar-Mihalic P., Rodriguez I., Chiu D. T., 2003, "Electrowetting-induced droplet movement in an immiscible medium", *Langmuir*, **19**, 250-255.

Lebrasseur E., Al-Haq M. I., Choi W. K., Hirano M., Tsuchiya H., Torii T., Higuchi T., Yamazaki H., Shinohara E, 2006, "Two-dimensional electrostatic actuation of droplets using a single electrode panel and development of disposable plastic film card", *Sensors & Actuators A*, **136**, 358-366.

Lehmann U., Hadjidj S., Parashar V. K., Vandevyver C., Rida A., Gijs M. A. M., 2006, "Two-dimensional magnetic manipulation of microdroplets on a chip as a platform for bioanalytical applications", *Sensors & Actuators B*, **117**, 457-463.

Li, Y., Parkes, W., Haworth, L. I., Ross, A. W. S., Stevenson, J. T. M. and Walton, A. J., 2008, "Room-temperature fabrication of anodic tantalum pentoxide for low-voltage electrowetting on dielectric (EWOD)," *Journal of Microelectromechanical Systems*, **17**(6), 1481-1488.

Lu H. W., Bottausci F., Fowler J. D., Bertozzi A. L., Meinhart C., Kim C. J., 2008, "A study of EWOD-driven droplets by PIV investigation", *Lab on a Chip*, **8**, 456-461.

Luan L., Evans R. .D, Jokerst N. M. and Fair R. B., 2008, "Integrated optical sensor in a digital microfluidic platform", *IEEE Sensors Journal*, **8**, 628-635.

Miller E. M. and Wheeler A. R., 2009, "Digital bioanalysis", *Analytical and Bioanalytical Chemistry*, **393**, 419-426.

Moon H., Cho S. K., Garrell R. L., and Kim C.-J., 2002, "Low voltage electrowetting-on-dielectric", *Journal of Applied Physics*, **92**, 4080-4087.

Moon H., Wheeler A. R., Garrell R. L., Loo J. A., Kim C. J., 2006, "An integrated digital microfluidic chip for multiplexed proteomic sample preparation and analysis by MALDI-MS", *Lab on a Chip*, **6**, 1213-1219.

Morgan H., Hadwen B., Broder G., Morganti D., Jacobs A., Brown C., Kubota Y. and Hector J., 2012, "Programmable large area digital microfluidic array with integrated droplet sensing for bioassays", *Lab on a Chip*.

Mugele F., Baret J.-C., 2005, "Electrowetting: from basics to applications", *Journal of Physics: Condensed Matters*, **17**, R705.

Munson B. R., Young D. F., Okiishi T. H. and Huebsch W. W., 2008, "Fundamentals of fluid mechanics", Wiley Publishers, 6th Edition.

Murran M. A. and Najjaran H., 2012, "Capacitance-based droplet position estimator for digital microfluidic devices", *Lab on a Chip*, **12**, 2053-2059.

Na M., Rhee S.-W., 2006, "Electronic characterization of Al/PMMA[poly(methyl methacrylate)]/p-Si and Al/CEP(cyanoethyl pullulan)/p-Si structures," *Organic Electronics*, **7**, 205-212.

Nelson W. C. and Kim C. J., 2011, "Monolithic fabrication of EWOD chips for picoliter droplets", *Journal of Microelectromechanical Systems*, **20**, 1419-1427.

Nguyen N. T., Ng K. M., Huang X., 2006, "Magnetic actuation for microfluidics based on ferrofluid droplets", *Proceedings of SPIE*, **6414**, 64140T.

Niu X., Zhang M., Peng S., Wen W., and Sheng P., 2007, "Real-time detection, control and sorting of microfluidic droplets", *Biomicrofluidics*, **1**, 044101(1-12).

Paik P., Pamula V. K. and Fair R. B., 2003, "Rapid droplet mixers for digital microfluidic systems," *Lab on a Chip*, **3**, 253-259.

Pollack M.G., Fair R.B. and Shenderov A.D., 2000, "Electrowetting-based actuation of liquid droplets for microfluidic applications", *Applied Physics Letters*, **77**, 1725-1726.

Pollack M. G., Paik P. Y., Shenderov A. D., Pamula V. K., Dietrich F. S., and Fair R. B., 2003, "Investigation of electrowetting-based microfluidics for real-time PCR applications," *International Conference on Micro Total Analysis Systems, Squaw Valley*, CA, 619-622.

Pollack M.G., Shenderov A.D., Fair R.B., 2002, "Electrowetting-based actuation of droplets for integrated microfluidics", *Lab on a Chip*, **2**, 96-101.

Ren H., Fair R. B., Pollack M. G. and Shaughnessy E. J., 2002, "Dynamics of electro-wetting droplet transport," *Sensors and Actuators B*, **87**, 201-206.

Ren H., Fair R. B. and Pollack M. G., 2004, "Automated on-chip droplet dispensing with volume control by electro-wetting actuation and capacitance metering," *Sensors and Actuators, B*, **98**, 319–327.

Ren H., Srinivasan V., and Fair R. B., 2003, "Design and testing of an interpolating mixing architecture for electrowetting-based droplet-on-chip chemical dilution", *The 12th International Conference on Solid Stale Sensors, Actuators and Microsystem*, Boston, MA, 619-622.

Renaudin A., Tabourier P., Camart J. C., Druon C., 2006, "Surface acoustic wave two-dimensional transport and location of microdroplets using echo signal", *Journal of Applied Physics*, **100**, 116101.

Renaudin A., Sozanski J. P., Verbeke B., Zhang V., Tabourier P., Druon C., 2009, "Monitoring SAW-actuated microdroplets in view of biological applications", *Sensors & Actuators B*, **138**, 374-382.

Schertzer M. J., Ben-Mrad R., Sullivan P. E., 2010, "Using capacitance measurements in EWOD devices to identify fluid composition and control droplet mixing", *Sensors and Actuators B*,**145**, 340-347.

Shih S. C. C., Fobel R., Kumar P., Wheeler A., 2010, "A feedback control system for high-fidelity digital microfluidics", *Lab on a Chip*, **11**, 535-540.

Srinivasan V., Pamula V. K., and Fair R. B., 2004, "An integrated digital microfluidic lab-on-a-chip for clinical diagnostics on human physiological fluids", *Lab on a Chip*, **4**, 310-315.

Stalder A.F., Kulik G., Sage D., Barbieri L., Hoffmann P., 2006, "A snake-based approach to accurate determination of both contact points and contact angles", *Colloids And Surfaces A*, **286**, 92-103.

Taniguchi T., Torii T., Higuchi T., 2002, "Chemical reactions in microdroplets by electrostatic manipulation of droplets in liquid media", *Lab on a Chip*, **2**, 19-23.

Teh S. Y., Lin R., Hung L. H. and Lee A. P., 2008, "Droplet microfluidics," *Lab on a Chip*, **8**, 198-220.

Wang K.-L., Jones T. B. and Raisanen A., 2008, "DEP actuated nanoliter droplet dispensing using feedback control", *Lab on a Chip*, **9**, 901-909.

Washizu M., 1998, "Electrostatic actuation of liquid droplets for microreactor applications", *IEEE Transactions on Industry Applications*, **34**, 732-737.

Zeng J. & Korsmeyer T., 2004, "Principles of droplet electrohydrodynamics for lab-on-a-chip", *Lab on a Chip*, **4**, 265-277.

Zhao P., Li Y., Zeng X., Zhou J., Huang Y., Liu R., 2009, "EWOD using P(VDF-TrFE)", *4th IEEE International Conference on Nano/Micro Engineered and Molecular Systems*, 202-205.

Zhao Y., Yi U.-C., and Cho S. K., 2007, "Highly efficient in-droplet particle concentration and separation by twDEP and EWOD for digital microfluidics", *IEEE MEMS Conference*, Kobe, Japan, 537-540.